MEASUREMENT OF THE DIFFERENTIAL DIJET PRODUCTION CROSS SECTION IN PROTON-PROTON COLLISIONS AT $\sqrt{s}$= 7 TeV

by

Bora Işıldak

B.S., Physics, Boğaziçi University, 2005

Submitted to the Institute for Graduate Studies in
Science and Engineering in partial fulfillment of
the requirements for the degree of
Doctor of Philosophy

Graduate Program in Physics
Boğaziçi University

2011

MEASUREMENT OF THE DIFFERENTIAL DIJET PRODUCTION CROSS SECTION IN PROTON-PROTON COLLISIONS AT $\sqrt{s}$= 7 TeV

APPROVED BY:

Prof. Erhan Gülmez (Thesis Supervisor)	.....
Prof. Metin Arık	.....
Assoc. Prof. Kerem Cankoçak	.....
Prof. Serkant Ali Çetin	.....
Prof. Osman Teoman Turgut	.....

DATE OF APPROVAL: 7.12.2011

To my dearest wife Ceren and beautiful daughter Birce,

ACKNOWLEDGEMENTS

I would like to express my deeply-felt gratitude to my thesis advisor Prof. Erhan Gülmez for his guidance and endless support throughout my studies. His well-known patience and prudence eased my graduate life.

I would also like to thank Dr. Konstantinos Kousouris who has shared his profound knowledge with me. This thesis would be impossible without his help and wisdom. He taught me all aspects of a high energy experimental physics analysis. His coherent teaching and wide intelligence always pushed me forward in the past two years.

I am also grateful to Dr. Niki Saoulidou for her invaluable support during my thesis writing process. I am also happy to work with Dr. Klaus Rabbertz who gave his time and consideration for my studies.

I want to express my thanks to both Prof. Yaşar Önel and Prof. Mithat Kaya who played important roles in my life at CERN. They were very encouraging and sincere. I specially thank Serhat Işıtın, Cemile Ezer, Özlem Kaya and Kazım Çamlıbel for their friendships.

I specially thank my mother and father Çiğdem, Mehmet Işıldak, my grandmother Melahat Elma, my sister Banu and brother Barış for their support throughout my life. They have always been behind me in every decision I have made. I sincerely thank my family-in-law, Gülümser, Vecihi and Yiğit Yavuz. Without their encouragement, it would be hard to pursue my graduate studies abroad. They have always helped me to think positively whenever I met with obstacles.

I gratefully acknowledge the Bogazici University Research Fund (No: 09B302P and 5883) for their kind support in this work.

ABSTRACT

MEASUREMENT OF THE DIFFERENTIAL DIJET PRODUCTION CROSS SECTION IN PROTON-PROTON COLLISIONS AT $\sqrt{s}$= 7 TeV

A measurement of the double-differential inclusive dijet production cross section in proton-proton collisions at $\sqrt{s}$ = 7 TeV is presented as a function of the dijet invariant mass and jet rapidity. The data correspond to an integrated luminosity of 36 pb^{-1}, recorded with the CMS detector at the LHC in 2010. The measurement covers the dijet mass range 0.2 TeV to 3.5 TeV and jet rapidities up to $|y| = 2.5$. It is found to be in good agreement with next-to-leading-order QCD predictions.

ÖZET

$\sqrt{s}$ = 7 TeV'DEKİ PROTON-PROTON ÇARPIŞMALARINDA JET ÇİFTİ OLUŞUMUNUN DİFERANSİYEL TESİR KESİTİ ÖLÇÜMÜ

7 TeV kütle merkezi enerjisinde çarpışan protonlardan meydana gelen çift jetlerin oluşum tesir kesiti, jet çiftininin değişmez kütlesi ve jet rapiditesine göre ölçülmüştür. 36 pb^{-1}'lık toplam luminositeye denk gelen veri 2010 yılında CMS detektörü ile alınmıştır. Ölçüm, jet çifti değişmez kütlesinde 0.2 TeV'den 3.5 TeV'e, jet rapiditelerinde ise $|y|$=2.5'a kadar olan değerleri kapsamaktadır. Sonuç olarak ölçüm ve kuantum kromodinamik öngörülerin tutarlı olduğu gözlenmiştir.

TABLE OF CONTENTS

LIST OF FIGURES

LIST OF TABLES

LIST OF ACRONYMS/ABBREVIATIONS

APD	Avalanche PhotoDiode
ATLAS	A Toroidal LHC ApparatuS
CERN	(Conseil Européen pour la Recherche Nucléaire)
CMS	Compact Muon Solenoid
CP Violation	Charge-Parity Violation
CSC	Cathode Strip Chambers
CTEQ	Co-ordinated Theoretical-Experimental project on QCD
DAQ	Data AcQusition
DBS	Dataset Bookkeeping System
DIS	Deep Inelastic Scattering
DTC	Drift Tube Chamber
ECAL	Electromagnetic CALorimeter
HB	Hadronic Barrel
HCAL	Hadronic CALorimeter
HE	Hadronic Endcap
HF	Hadronic Forward
HLT	High Level Trigger
HO	Hadronic Outer
HSM	Standard Model Higgs boson
IC	Iterative Cone
IRC	InfraRed and Collinear
JES	Jet Energy Scale
LEP	Large Electron Positron Collider
LHC	Large Hadron Collider
LO	Leading Order
LSP	Lightest Supersymmetric Particle
MC	Monte Carlo
MET	Missing Transverse Energy
MPI	Multiple Parton Interaction

NLO	Next-to-Leading Order
NLO	Next-to-Next-to-Leading Order
PDF	Parton Distribution Function
pQCD	perturbative Quantum Chromodynamics
QCD	Quantum ChromoDynamics
QED	Quantum ElectroDynamics
RF	Radio Frequency
RPC	Resistive Plate Chambers
SM	Standard Model
SUSY	SUperSYmmetry
TEC	Tracker Endcap Discs
TIB	Tracker Inner Barrel
TID	Tracker Inner Discs
TOB	Tracker Outer Barrel
VPT	Vacuum PhotoTriode

1. INTRODUCTION

Particle physics is the discipline which seeks the ultimate answers of these two joint questions:

- What are the most fundamental constituents of matter?
- How do these constituents interact with each other?

In ancient Greek, Democritus of Abdera stated that everything is composed of "*atomos*" which means "uncuttable" in old Greek. Nevertheless, after Democritus' bright idea, it had been almost 2000 years for humankind to reveal all matter is a composition of generic and fundamental constituents. In 1932, there were four known particles, three of which constitute an atom. However, it did not take so much for this list to grow. Today, our knowledge about fundamental particles and their interactions is far beyond 1930s'. Needless to say, this does not mean that a complete and consistent theory which answers all questions is accomplished. There are many open questions to be answered and many theories to be confirmed. The acknowledged method for giving satisfactory answers and for performing reliable tests in high energy particle physics is to collide particles and observe the outcome.

Apart from the questions to be answered, the main goal of this thesis is to give a detailed description of an analysis performed in Compact Muon Solenoid (CMS) which is one of the four experiments of the Large Hadron Collider (LHC) physics program at CERN (*Conseil Européen pour la Recherche Nucléaire*). In this particular analysis, the predictions of the Quantum Chromodynamics (QCD); theory about the fundamental constituents of nuclei (partons and gluon), were tested.

In QCD, outgoing scattered partons from the parton-parton scattering manifest themselves as hadronic jets. Hence, events with two high transverse momentum jets (dijets) arise in proton-proton collisions. The invariant mass M_{JJ}^2 of the two jets can be given in terms of proton momentum fractions $x_{1,2}$ carried by the scattering partons

as follows;

$$M_{JJ}^2 = x_1 \cdot x_2 \cdot s \tag{1.1}$$

where $\sqrt{s}$ is the center-of-mass energy of the colliding protons. The dijet cross section as a function of M_{JJ}^2 can be precisely calculated in perturbative QCD and it also allows sensitive searches for physics beyond the Standard Model, such as dijet resonances or contact interactions. The measured cross-section challenges the QCD predictions at a new collision energy and in an unexplored kinematic regime, beyond the reach of previous collider measurements [1, 3]. So far, dedicated searches for dijet resonances and contact interactions with the CMS detector have been reported in several articles [4, 6]. In this thesis, the measurement of the double-differential inclusive dijet production cross section is described as a function of the dijet invariant mass and jet rapidity at $\sqrt{s} = 7$ TeV. The work explained in this dissertation was published [7] and presented at the several conferences [8, 9].

In the subsequent chapter, the standard model of the particle physics and the theory of the fundamental constituents of nuclei, Quantum Chromodynamics, will be described. In the third chapter, the specifications of the accelerator machine LHC and the detector CMS will be explained. The goal of the fourth chapter is to give a description of both Monte Carlo programs used in this analysis, and the reconstruction algorithms of the jet objects which are sprays of particles coming from a single parton will be discussed. The remaining chapters are dedicated to explain the work carried out to perform analysis and the results obtained, respectively.

2. THEORY

2.1. Standard Model

The ultimate objective of the particle physics is to give a prescription of all the phenomena related to the fundamental particles. The so called *Standard Model of the Particle Physics* (SM) is the most extensive theory of particle properties and particle interactions.

SM consists of quarks, leptons and force carrying bosons. For each quark and lepton, there is a corresponding antiparticle. According to the SM, all phenomena of particles can be explained by these fundamental particles along with the appropriate quantum field theory. There are three types of interactions in SM. In fact, two of them are two different aspects of a single type of interaction. The electromagnetic interaction between two charged particles is explained by photon exchange. However, the electromagnetic theory which uses electric and magnetic fields is just an effective theory of infinitely many photon exchanging charged particles. The weak force or weak interaction is propagated by $W^{\pm}$ and Z^0 bosons. In 1970's, a unified description of the electromagnetic and the weak interaction was given by Abdus Salam, Sheldon Glashow and Steven Weinberg. The other interaction which is known to be the force holding the nucleus together is the strong interaction mediated by the gluons. Hence the Standard Model consists of two parts; the electroweak and strong interactions. A visual summary of SM and the type of interactions are shown in Figure 2.1.

2.2. Quantum Chromodynamics

Quantum Chromodynamics (QCD) is the non-Abelian Yang-Mills theory of quarks and gluons. In quantum field theory, all the story begins with the necessity of the gauge invariance, especially the local gauge invariance. It was first proposed in 1964 by Oscar W. Greenberg that quarks, if they exist and constitutes the proton, should have an additional quantum property to rescue the Pauli exclusion principle. This property,

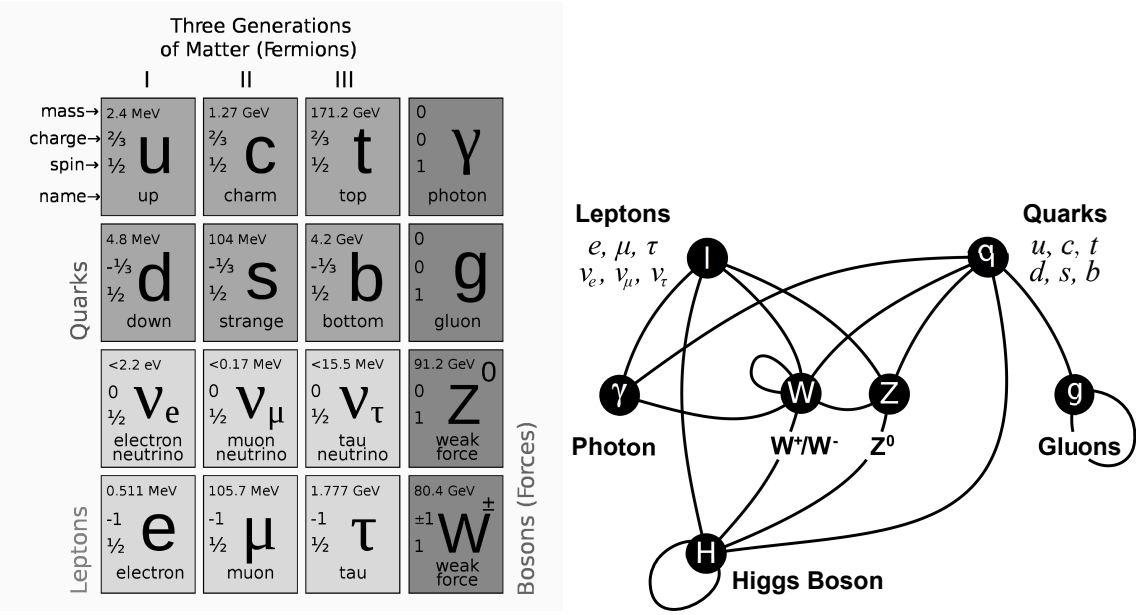

Figure 2.1. The Standard Model of elementary particles, with the gauge bosons in the rightmost column (left). Interactions between fundamental particles (right).

then, was named with colors (red, green, blue) referring to the three different quantum states of a given quark. It is like the electric charge where it is a single property which is represented by positive or negative values. The three colors are just names, and they have nothing to do with the colors we see in our daily lives. They are just labels to differentiate the three different quantum states of a given quark.

If quarks are fermionic particles with spin 1/2, they must obey the Dirac equation. However, a quark field which can be described as a Dirac spinor comes with three color states. Thus, we can write the quark field ψ as a three component column vector.

$$\vec{\psi} = \begin{pmatrix} \psi_1 \\ \psi_2 \\ \psi_3 \end{pmatrix} \tag{2.1}$$

where each element is a 4-component spinor.

Then, the Lagrangian density can be written as;

$$\boldsymbol{\mathcal{L}} = \overline{\psi}\left[i\hbar c\boldsymbol{\partial_\mu} - \boldsymbol{M}c^2\right]\psi \tag{2.2}$$

where

$$\overline{\psi} = \left(\psi_1^\dagger\gamma^0,\ \psi_2^\dagger\gamma^0,\ \psi_3^\dagger\gamma^0\right) \tag{2.3}$$

$$\boldsymbol{\partial_\mu} = \begin{pmatrix} \gamma^\mu\partial_\mu & 0 & 0 \\ 0 & \gamma^\mu\partial_\mu & 0 \\ 0 & 0 & \gamma^\mu\partial_\mu \end{pmatrix} \tag{2.4}$$

$$\boldsymbol{M} = \begin{pmatrix} m & 0 & 0 \\ 0 & m & 0 \\ 0 & 0 & m \end{pmatrix} \tag{2.5}$$

assuming the three different color states of a given quark have the same mass.

Now, the argument is that the Lagrangian density for the quark field must be invariant under a unitary transformation.

$$\psi\,' = \boldsymbol{U}\psi \tag{2.6}$$

where $\boldsymbol{U}$ is a 3×3 matrix in color case. A unitary operator (a 3 by 3 matrix in this case) can be expressed as;

$$\boldsymbol{U} = e^{i\boldsymbol{H}} \tag{2.7}$$

where $\boldsymbol{H}$ is a 3×3 Hermitian matrix. Moreover, any Hermitian matrix can be written

as a linear combination of nine 3×3 matrices;

$$\boldsymbol{H} = a_0\boldsymbol{I} + \vec{a}\cdot\vec{\boldsymbol{\lambda}} \tag{2.8}$$

Here, $\vec{a}\cdot\vec{\boldsymbol{\lambda}}$ is a shorthand notation for $\sum_{i=1}^{8} a_i\lambda_i$, where λ_i represents the so called Gell-Mann matrices which is a representation of the infinitesimal generators of the SU(3) group. They obey the following commutation relation;

$$[\lambda_i, \lambda_j] = 2if^{ijk}\lambda_k \tag{2.9}$$

where f^{ijk} are the structure constants of the SU(3) group, and antisymmetric in indices with the following non-vanishing values;

$$f^{123} = 1, \quad f^{147} = f^{165} = f^{246} = f^{257} = f^{345} = f^{376} = \frac{1}{2}, \quad f^{458} = f^{678} = \frac{\sqrt{3}}{2} \tag{2.10}$$

Thus, the unitary transformation of the field boils down to a phase transformation of the following form;

$$\psi\,' = e^{ia_0}\cdot e^{i\vec{a}\cdot\vec{\boldsymbol{\lambda}}}\psi \tag{2.11}$$

However, it can easily be argued that the phase transformation may change from one observer to another in the spirit of relativity. In fact, there is no reason not to make the components of the $\vec{a}$ space-time dependent. Hence Equation 2.11 can be written in a more general form;

$$\psi\,' = e^{ia_0(x^\mu)}\cdot e^{-iq\ \vec{a}(x^\mu)\cdot\vec{\boldsymbol{\lambda}}/\hbar c}\psi \tag{2.12}$$

Where the factor $-q/\hbar c$ is introduced for future convenience. The first part is just the 3×3 matrix representation of the U(1) group, and we know that all the electromagnetic theory for a Dirac particle can be generated from this symmetry by requiring a local gauge invariance. The second part of the transformation, $e^{-iq\ \vec{a}(x^\mu)\cdot\vec{\boldsymbol{\lambda}}/\hbar c}$, is the

non-Abelian part of the theory because of the non-commuting λ matrices. Again, it should be required that the SU(3) transformation, $\boldsymbol{S} = e^{-iq\ \vec{a}(x^\mu)\cdot\vec{\boldsymbol{\lambda}}/\hbar c}$, must leave the Lagrangian density invariant.

$$\psi\,' = \boldsymbol{S}\psi$$
$$\overline{\psi}\,' = \overline{\psi}\boldsymbol{S}^{-1}$$

Therefore, the transformed Lagrangian density becomes;

$$\boldsymbol{\mathcal{L}}\,' = \overline{\psi}\boldsymbol{S}^{-1}\left[i\hbar c\gamma^\mu\boldsymbol{\partial_\mu} - \boldsymbol{M}c^2\right]\boldsymbol{S}\psi \tag{2.13}$$
$$= \overline{\psi}\boldsymbol{S}^{-1}\left[i\hbar c\gamma^\mu(\boldsymbol{S}(\boldsymbol{\partial_\mu}\psi) + (\boldsymbol{\partial_\mu}\boldsymbol{S})\psi) - \boldsymbol{M}c^2\boldsymbol{S}\psi\right] \tag{2.14}$$

As it can easily be seen, $\partial_\mu(\boldsymbol{S}\psi) \neq \boldsymbol{S}(\partial_\mu\psi)$, hence, there is an extra term coming from the derivative of $\boldsymbol{S}$. By looking at the structure of the equation 2.14, the covariant derivative can be introduced as follows;

$$D_\mu = \partial_\mu + i\frac{q}{\hbar c}\vec{\lambda}\cdot A_\mu \tag{2.15}$$

The A_μ part changes with the SU(3) transformation such that the covariant derivative satisfies the identity;

$$D_\mu{}'(\boldsymbol{S}\psi) = \boldsymbol{S}(D_\mu\psi) \tag{2.16}$$

The prime symbol on D_μ denotes the transformation; $A_\mu \rightarrow A_\mu{}'$. However, the transformation of A_μ is not trivial, nevertheless, it can be deduced from the identity 2.16 as follows;

$$\vec{\lambda}\cdot A_\mu{}' = \boldsymbol{S}(\vec{\lambda}\cdot A_\mu)\boldsymbol{S}^{-1} + i(\frac{q}{\hbar c})(\partial_\mu\boldsymbol{S})\boldsymbol{S}^{-1} \tag{2.17}$$

In order to bring $\boldsymbol{S}$ and $\boldsymbol{S}^{-1}$ terms together, the commutator $[\boldsymbol{S}, \vec{\lambda}\cdot A_\mu]$ should be

evaluated. For the simplicity, an expansion of $\boldsymbol{S}$ for small values of $\vec{a}(x^\mu)$ will suffice.

$$\boldsymbol{S} \cong 1 - \frac{iq}{\hbar c}\vec{\lambda}\cdot\vec{a}(x^\mu), \qquad \boldsymbol{S}^{-1} \cong 1 + \frac{iq}{\hbar c}\vec{\lambda}\cdot\vec{a}(x^\mu), \qquad \partial_\mu \boldsymbol{S} \cong -\frac{iq}{\hbar c}\vec{\lambda}\cdot(\partial_\mu\vec{a}(x^\mu)) \quad (2.18)$$

With this approximation, Equation 2.17 becomes;

$$\vec{\lambda}\cdot A_\mu{}' \cong \vec{\lambda}\cdot A_\mu - \frac{iq}{\hbar c}[\vec{\lambda}\cdot\vec{a}(x^\mu), \vec{\lambda}\cdot A_\mu] + \vec{\lambda}\cdot(\partial_\mu\vec{a}(x^\mu)) \quad (2.19)$$

By using the commutation relation of the λ matrices (Equation 2.9), $[\vec{\lambda}\cdot\vec{a}(x^\mu), \vec{\lambda}\cdot A_\mu]$ term can be found as;

$$[\vec{\lambda}\cdot\vec{a}(x^\mu), \vec{\lambda}\cdot A_\mu] = 2i\vec{\lambda}(\vec{a}(x^\mu)\times A_\mu) \quad (2.20)$$

Therefore, the transformation of the vector field A_μ is given as;

$$A_\mu{}' \cong A_\mu + \frac{2q}{\hbar c}(\vec{a}(x^\mu)\times A_\mu) + \partial_\mu\vec{a}(x^\mu) \quad (2.21)$$

where $(\vec{a}(x^\mu)\times A_\mu)_i = \sum_{j,k}^{8} i f_{ijk}\vec{a}_j(x^\mu)(A_\mu)_k$.

The new modified Lagrangian;

$$\boldsymbol{\mathcal{L}} = \left[i\hbar c\overline{\psi}\gamma^\mu\boldsymbol{\partial_\mu}\psi - \boldsymbol{M}c^2\overline{\psi}\psi\right] - \left(q\overline{\psi}\gamma^\mu\lambda\psi\right)\cdot\boldsymbol{A_\mu} \quad (2.22)$$

which is invariant under SU(3) gauge transformation. The cost of such a gauge invariance requirement is to introduce the gauge fields ($\boldsymbol{A_\mu}$) that correspond to the gluons in physics point of view. Now, the free gluon Lagrangian density must be added to the Lagrangian density for completeness. The free gluon Lagrangian is given as follows;

$$\boldsymbol{\mathcal{L}}_{gluons} = -\frac{1}{16\pi}\boldsymbol{F_{\mu\nu}F^{\mu\nu}} \quad (2.23)$$

where $\boldsymbol{F^{\mu\nu}}$ is given as;

$$\boldsymbol{F^{\mu\nu}} = \partial^{\mu}\boldsymbol{A^{\nu}} - \partial^{\nu}\boldsymbol{A^{\mu}} + \frac{2q}{\hbar c}(\boldsymbol{A^{\mu}} \times \boldsymbol{A^{\nu}}) \tag{2.24}$$

with the cross product defined as in Equation 2.21. In order to define the gluon propagator, the choice of gauge must be fixed. This gauge fixing procedure pronounces itself as two terms in the Lagrangian density. One is the so called "*gauge fixing*" term, and the other is the "*Fadeev-Popov ghosts*" term. The gauge fixing term is given as a class of gauges named "$\boldsymbol{R_{\xi}}$ *gauges*" which is the generalization of the Lorenz gauge, and it is expressed as;

$$\boldsymbol{\mathcal{L}}_{gauge-fixing} = -\frac{1}{2\xi}(\partial_{\mu}\boldsymbol{A^{\mu}})^2 \tag{2.25}$$

In a non-abelian theory, there is also need for the ghost field Lagrangian density in the form of;

$$\boldsymbol{\mathcal{L}}_{ghost} = -\eta^{a\dagger}\partial_{\mu}\boldsymbol{D}^{ab}_{\mu}\eta^{b} \tag{2.26}$$

where η^{a} is a complex scalar field.

Altogether, the full QCD Lagrangian density is given as the sum of classical and the gauge-fixing part with the ghost field terms.

$$\boldsymbol{\mathcal{L}}_{QCD} = \boldsymbol{\mathcal{L}}_{classical} + \boldsymbol{\mathcal{L}}_{gauge-fixing} + \boldsymbol{\mathcal{L}}_{ghost} \tag{2.27}$$

Then, the appropriate Feynman rules for QCD can be derived from this Lagrangian density [10].

2.2.1. The Running Coupling Constant

For fundamental particles, the cross section of a specified process is given by

$$\sigma = \int \frac{1}{flux} \, |\mathcal{M}^2| \, d\Phi \tag{2.28}$$

where, σ is the cross section, *flux* is the incoming particle flux, $\mathcal{M}$ is the matrix element for a given process calculated from the Feynman diagrams and $d\Phi$ is the phase space volume for the process. For example, in an electromagnetic interaction, a factor of $\alpha = 1/137$ (coupling constant) is being introduced for each vertex in the relevant Feynman diagram while calculating the matrix element $\mathcal{M}$. This means that higher order diagrams with more vertices contribute less and less to the cross section. However, in QCD, the coupling constant, from the force between two protons, has been experimentally found out to be greater than one which has catastrophic consequences. If the coupling constant is greater than one, the more complicated Feynman diagrams with more vertices contribute more and more to the cross section which is the physical observable.

In QED, a diagram which includes a loop diagram,

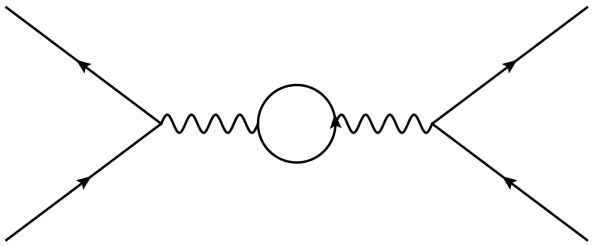

Figure 2.2. Electron-positron bubble diagram which creates a vacuum polarization in QED.

makes the effective charge of the electron ($e = \sqrt{4\pi\alpha}$);

$$\alpha(|q^2|) = \alpha(0)\{1 + \frac{\alpha(0)}{3\pi} \ln(|q^2|/(mc)^2)\} \tag{2.29}$$

Hence, higher order corrections coming from bubble-chain diagrams can be explicitly written as;

$$\alpha(|q^2|) = \alpha(0)\left(1+\frac{\alpha(0)}{3\pi}\ln(|q^2|/(mc)^2+\frac{\alpha^2(0)}{(3\pi)^2}\ln^2(|q^2|/(mc)^2+\ldots\right) \quad (2.30)$$

$$= \frac{\alpha(0)}{1-(\alpha(0)/3\pi)\ln(|q^2|/(mc)^2)} \quad (2.31)$$

In QCD case, there are also gluon-gluon couplings which lead to the gluon bubbles.

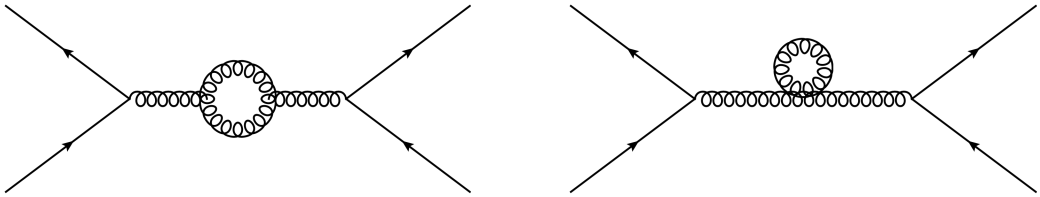

Figure 2.3. Gluon-gluon bubble diagram in QCD.

If the renormalization equations are solved in the *leading order* (LO), it can be found that the strong coupling depends on the momentum transfer as follows;

$$\alpha_s(|q^2|) = \frac{\alpha_s(\mu^2)}{1+\alpha_s(\mu^2)\ b\ \ln(|q^2|/\mu^2)} \quad (2.32)$$

where b is $(11n_c-2n_f)/12\pi$, n_c is the number of colors, n_f is the number of quark flavors.

As opposed to QED case, the gluon bubble contribution creates an anti-screening effect since the b term in Equation 2.32 is positive with $n_c = n_f = 3$ in the Standard Model. Also, there is a new parameter μ in the equation. In QED, it is natural to use the coupling strength for the fully screened charge where $q^2 = 0$. This is the charge we have already known from Coulomb and Milikan. In QCD, it is not possible to start from $q^2 = 0$ since it is where α_s is large. Therefore, a point where α_s is small enough

to perform perturbative expansion should be chosen. Given that μ^2 is large enough to satisfy $\alpha(\mu^2) < 1$, it does not matter which μ value is used in Equation 2.32 (See Appendix A). Hence, it is appropriate to define a new parameter Λ to write Equation 2.32 in terms of a single parameter.

If the new parameter Λ is defined as follows;

$$\ln \Lambda^2 = \ln \mu^2 - 12\pi / \left[(11n_c - 2n_f)\alpha_s(\mu^2)\right] \tag{2.33}$$

Equation 2.32 becomes

$$\alpha_s(|q^2|) = \frac{12\pi}{(11n_c - 2n_f)\ln(|q^2|/\Lambda^2)} \tag{2.34}$$

Equation 2.34 shows the q^2 dependence of α_s. For large values of q^2, α_s gets smaller which means that the "strong" force becomes relatively weak at short distances. This is the essence of the *asymptotic freedom*. If q^2 decreases, the α_s value increases. A small q^2 means that the interaction occurred over a relatively large distance. Thus, the force between two colored particles becomes much stronger. This effect is known as *color confinement* and it is the reason for the colored particles not to be able to be observed individually above a distance of $1/\Lambda_{QCD}$.

2.2.2. Structure of the Proton and Parton Distribution Functions

In the simplistic approach, protons are made of two up quarks and a down quark. Partons carry a certain fraction of the momentum of the proton, characterized by parton distribution functions (PDFs). However, the first measurements of PDFs revealed that the total momentum of the three quarks ("valence quarks") is only about 35% of the momentum of the proton. It was understood that the remaining fraction of the total momentum comes from gluons (50%), while 15% of the momentum comes from the "sea quarks". These are pairs of quarks and antiquarks, that can pop in and out of the vacuum because of the interactions between two gluons. Figure 2.5 shows a

cartoon of the proton structure, as much as it is currently understood.

Each of these partons inside the proton carries a fraction of total momentum given by the PDF. PDF is defined as the probability density for finding a particle within a longitudinal momentum fraction interval at a momentum transfer of Q^2. The function $f_i(x_i)$ is the probability for a parton to carry a fraction of the hadron between x_i and $x_i + \delta x_i$.

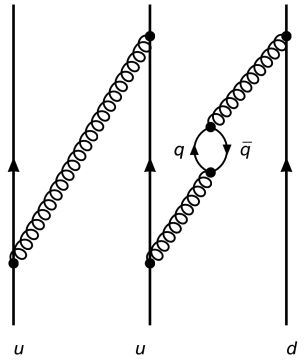

Figure 2.4. An illustration of the inner structure of the proton. At any given time, there might be one or several quark anti-quark pairs inside the proton.

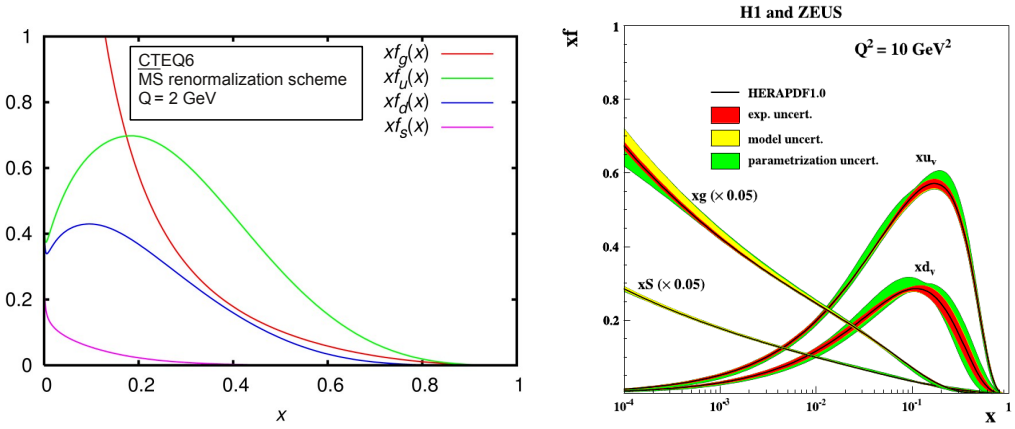

Figure 2.5. The CTEQ6 parton distribution functions in the $\overline{MS}$ renormalization scheme and Q = 2 GeV for gluons (red), up (green), down (blue), and strange (violet) quarks (left). The parton distribution functions from the HERAPDF1.0 at $Q^2 = 10$ GeV^2 (right).

2.2.3. Parton Parton Scattering and the Two-Jet Production in Hadron-Hadron Collisions

When two hadrons collide inelastically, the actual interaction occurs in terms of a momentum transfer between two constituents of the colliding hadrons. In LHC, two protons collide so harshly that the partons inside the protons go into a *deep inelastic scattering* (DIS) (Figure 2.6). The differential cross section for the collision of two hadrons, P_1 and P_2, to give particles c and d is given by

$$d\sigma(P_1P_2 \to cd) = \int_0^1 dx_1 dx_2 \sum_{q_i,q_j} f_i(x_1,\mu_F^2) f_j(x_2,\mu_F^2) d\hat{\sigma}_{(q_iq_j\to cd)}(Q^2,\mu_F^2) \qquad (2.35)$$

where the momenta of the partons which are strongly interacted are $p_i^\mu = x_1 P_1$ and $p_i^\mu = x_1 P_1$, x_1 and x_2 are fractions of hadron momentum carried by interacting partons. The function $f_i(x,\mu_F^2)$ is the quark gluon parton PDFs are defined at a factorization scale of μ_F which is typically at the order of Q - a hard scale characteristic of the parton scattering. $d\hat{\sigma}(q_iq_j \to cd)$ is the short-distance (partonic) differential cross section for the scattering of partons of type i and j. The outgoing partons, c and d are observed as

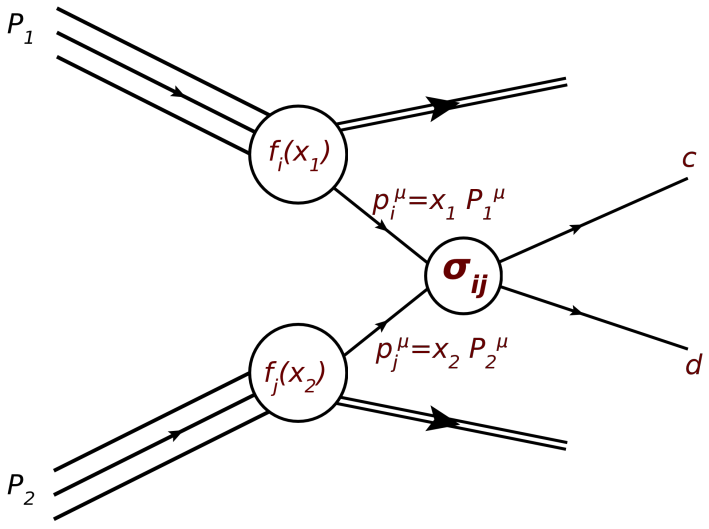

Figure 2.6. A schematic diagram of hadron-hadron collision which shows the hard subprocess of internal partons for the production of final states c and d.

jets since they eventually turn into a spray of color singlet particles, namely hadrons. From the conservation of momentum, the momenta of outgoing partons will be the same

in magnitude but opposite in direction. For 2→2 parton scattering (a(p_1^μ)+b(p_2^μ)→ c(p_3^μ)+d(p_4^μ)), the differential cross section is given by [18]

$$\frac{E_3 E_4 d^6\hat{\sigma}}{d^3p_3 d^3p_4} = \frac{1}{2\hat{s}} \frac{1}{16\pi^2} \overline{\sum} |\mathcal{M}|^2 \ \delta^4(p_1 + p_2 - p_3 - p_4) \tag{2.36}$$

where $\overline{\sum}$ denotes the averaged sum over the initial and the final state spins and colors. All the leading-order parton-parton contributions can be derived from the diagrams shown in the Figure 2.7 by including all the crossing symmetries of the given diagrams. The expressions for the total scattering amplitude $\overline{\sum}|\mathcal{M}|^2$ is given in Table 2.1, where $\hat{s} = (p_1^\mu + p_1^\mu)^2$, $\hat{u} = (p_1^\mu - p_3^\mu)^2$ and $\hat{t} = (p_2^\mu - p_3^\mu)^2$.

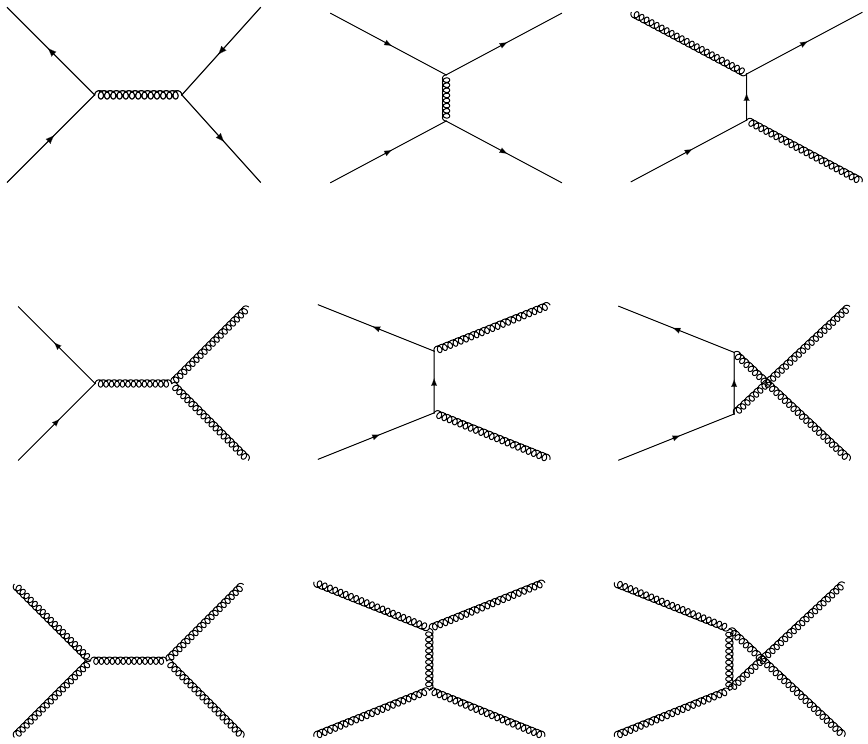

Figure 2.7. Feynman diagrams which contribute to parton-parton scattering.

Then, the two-jet inclusive cross section can be written as a convolution of the PDFs with the Equation 2.35

$$\frac{d^3\sigma}{dy_3 dy_4 dp_T^2} = \frac{1}{16\pi s^2} \sum_{i,j,k,l=q,\bar{q},g} \frac{f_i(x_1,\mu^2)}{x_1} \frac{f_i(x_2,\mu^2)}{x_2} \times \overline{\sum} |\mathcal{M}(ij \to kl)|^2 \frac{1}{1+\delta_{kl}} \quad (2.37)$$

where y_3 and y_4 represents the rapidities of the outgoing partons in the laboratory frame. The momentum fractions x_1, x_2 are determined by using the conservation of momentum

$$x_1 = \frac{1}{2} x_T (e^{y_3} + e^{y_4}), \qquad \frac{1}{2} x_T (e^{-y_3} + e^{-y_4}) \quad (2.38)$$

where $x_T = 2p_T/\sqrt{s}$.

Table 2.1. The differential cross sections for the various constituent quark-quark, quark-gluon, and gluon-gluon subprocesses [19].

Process	$\overline{\sum}\|\mathcal{M}\|^2/g^4$
$qq \to qq$	$\frac{4}{9}\frac{\hat{s}^2+\hat{u}^2}{\hat{t}^2}$
$qq' \to qq'$	$\frac{4}{9}\left(\frac{\hat{s}^2+\hat{u}^2}{\hat{t}^2}+\frac{\hat{s}^2+\hat{t}^2}{\hat{u}^2}\right)-\frac{8}{27}\frac{\hat{s}^2}{\hat{u}\hat{t}}$
$q\bar{q}' \to q\bar{q}'$	$\frac{4}{9}\frac{\hat{s}^2+\hat{u}^2}{\hat{t}^2}$
$q\bar{q} \to q\bar{q}$	$\frac{4}{9}\left(\frac{\hat{s}^2+\hat{u}^2}{\hat{t}^2}+\frac{\hat{u}^2+\hat{t}^2}{\hat{s}^2}\right)-\frac{8}{27}\frac{\hat{u}^2}{\hat{s}\hat{t}}$
$qq' \to q'\bar{q}'$	$\frac{4}{9}\frac{\hat{t}^2+\hat{u}^2}{\hat{s}^2}$
$qg \to qg$	$-\frac{4}{9}\frac{\hat{s}^2+\hat{u}^2}{\hat{s}\hat{u}}+\frac{\hat{s}^2+\hat{u}^2}{\hat{t}^2}$
$gg \to gg$	$\frac{2}{9}\left(3-\frac{\hat{t}\hat{u}}{\hat{s}^2}-\frac{\hat{s}\hat{u}}{\hat{t}^2}-\frac{\hat{s}\hat{t}}{\hat{u}^2}\right)$
$q\bar{q} \to gg$	$\frac{32}{27}\frac{\hat{t}^2+\hat{u}^2}{\hat{t}\hat{u}}-\frac{8}{3}\frac{\hat{t}^2+\hat{u}^2}{\hat{s}^2}$
$gg \to q\bar{q}$	$\frac{1}{6}\frac{\hat{t}^2+\hat{u}^2}{\hat{t}\hat{u}}-\frac{8}{3}\frac{\hat{t}^2+\hat{u}^2}{\hat{s}^2}$

2.2.4. Relativistic Kinematics of The Dijet System

Now, it is convenient to consider the kinematics of the two resultant jets in detail. Since the momentum fractions of the two incoming partons are not the same, the center of mass frame of the parton-parton system is boosted along the z-axis in laboratory frame. The rapidity, $y = \frac{1}{2} ln \left(\frac{E + p_z}{E - p_z} \right)$, transforms under boosts along z-axis as follows;

$$E \rightarrow \gamma(E + \beta p_z) \tag{2.39}$$

$$p_z \rightarrow \gamma(p_z + \beta E) \tag{2.40}$$

$$y \rightarrow \frac{1}{2} ln \left(\frac{\gamma(E + \beta p_z) + \gamma(p_z + \beta E)}{\gamma(E + \beta p_z) - \gamma(p_z + \beta E)} \right) \tag{2.41}$$

$$= \frac{1}{2} ln \left(\frac{E(\beta + 1) + p_z(\beta + 1)}{E(1 - \beta) + p_z(1 - \beta)} \right) \tag{2.42}$$

$$= \frac{1}{2} ln \left(\frac{E + p_z}{E - p_z} \cdot \frac{1 + \beta}{1 - \beta} \right) \tag{2.43}$$

$$= \frac{1}{2} ln \left(\frac{E + p_z}{E - p_z} \right) + \frac{1}{2} ln \left(\frac{1 + \beta}{1 - \beta} \right) \tag{2.44}$$

$$= y + y_{boost} \tag{2.45}$$

It means that the rapidity is additive under Lorentz transformations. Given that the rapidities of two jets are back-to-back in the center of mass frame of the two-jet system, they are given in the laboratory frame as follows

$$y_3^{lab} = y_3^{CM} + y_{boost} \tag{2.46}$$

$$y_4^{lab} = -y_3^{CM} + y_{boost} \tag{2.47}$$

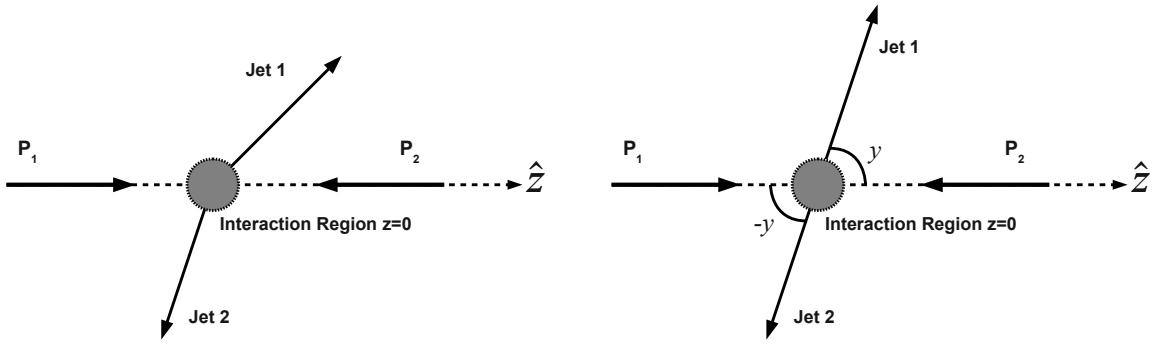

Figure 2.8. An illustration of the two jet $\hat{z} - y$ plane geometry in the laboratory frame (left) and in the parton-parton center of mass frame (right).

From Equations 2.45 and 2.46, the rapidities in the center of mass frame can be extracted by the rapidities in the laboratory frame.

$$y_3^{CM} = \frac{y_3^{lab} - y_4^{lab}}{2} \tag{2.48}$$

$$y_4^{CM} = -y_3^{CM} = \frac{y_4^{lab} - y_3^{lab}}{2} \tag{2.49}$$

$$y_{boost} = \frac{y_3^{lab} + y_4^{lab}}{2} \tag{2.50}$$

For a massless parton ($\beta = 1$) the rapidity in the center of mass frame is given by

$$y^* = \frac{1}{2} \ln \left(\frac{1 + cos\theta^*}{1 - cos\theta^*} \right) \tag{2.51}$$

This leads to

$$\cos \theta^* = \tanh(y^*) \tag{2.52}$$

where θ^* is the scattering angle from the collision axis of two partons in the center of mass frame. The invariant mass of the system is derived by starting from the basic

relativistic kinematics

$$
\begin{aligned}
M_{jj}^2 &= (p_1^\mu + p_2^\mu)^2 = (p_1^0 + p_2^0)^2 - (\vec{\boldsymbol{p_1}} + \vec{\boldsymbol{p_2}})^2 && (2.53)\\
&= E_1^2 + E_2^2 + 2E_1E_2 - |\vec{\boldsymbol{p_1}}|^2 - |\vec{\boldsymbol{p_1}}|^2 - 2\vec{\boldsymbol{p_1}} \cdot \vec{\boldsymbol{p_2}} && (2.54)\\
\vec{\boldsymbol{p_1}} \cdot \vec{\boldsymbol{p_2}} &= p_{1x}p_{2x} + p_{1y}p_{2y} + p_{1z}p_{2z} && (2.55)\\
p_{ix} &= p_{Ti}\cos\phi_1 && (2.56)\\
p_{iy} &= p_{Ti}\sin\phi_1 && (2.57)\\
\frac{p_{iz}}{E_i} &= \beta_i\cos\theta_i = E\tanh y_i && (2.58)\\
p_{Ti} &= \beta_{Ti}E_{Ti} && (2.59)
\end{aligned}
$$

where $i = 1, 2$

$$
\begin{aligned}
{E_{Ti}}^2 &= E_i^2 - p_{iz}^2 = E_i^2 - E_i^2\tanh^2 y_i = E_i^2(1 - \tanh^2 y_i) && (2.60)\\
\Rightarrow E_i &= E_{Ti}\cosh y_i && (2.61)
\end{aligned}
$$

so the scalar product of $\vec{\boldsymbol{p_1}} \cdot \vec{\boldsymbol{p_2}}$ becomes

$$
\begin{aligned}
\vec{\boldsymbol{p_1}} \cdot \vec{\boldsymbol{p_2}} &= (\frac{\beta_{T1}\beta_{T2}E_1E_2}{\cosh y_1 \cosh y_2})(\cos\phi_1\cos\phi_2 + \sin\phi_1\sin\phi_2) && (2.62)\\
&+ E_1E_2\tanh y_1\tanh y_2 \\
&= \frac{E_{T1}E_{T2}}{\cosh y_1\cosh y_2}(\beta_{T1}\beta_{T2}\cos\Delta\phi + \sinh y_1\sinh y_2) && (2.63)
\end{aligned}
$$

Thus

$$
M_{jj}^2 = m_1^2 + m_2^2 + 2E_{T1}E_{T2}(\cosh\Delta y - \beta_{T1}\beta_{T2}\cos\Delta\phi) \quad (2.64)
$$

in the limit where $\beta_{T1} = \beta_{T2} \approx 1$ it becomes

$$
M_{jj}^2 = 2p_{T1}p_{T2}(\cosh\Delta y - \cos\Delta\phi) \quad (2.65)
$$

It is worth noting that even the outgoing jets are almost massless, the polar and azimuthal separation between them govern the invariant mass of the dijet system.

2.3. Non-Perturbative Corrections

Since the NLO pQCD calculations provide predictions at the *parton level*, whereas the experimental data are corrected to the *particle level*, the non-perturbative effects must be taken into account when a comparison between the data and the theoretical predictions is desired. In this study, two Monte Carlo event generators, PYTHIA 6.4 [11] (both D6T and Z2 tunes) and Herwig++ [12] which have different hadronization and multiple parton interactions (MPI) models are employed in order to extract the non-perturbative corrections to the NLO calculation.

With the very steep falling nature of the dijet mass spectrum, it is very important to have enough number of events to describe the spectrum correctly. Current event generator programs, by default, produce events due to their cross section weights which can be interpreted as the probability of producing an event from the generator point of view. Hence, it is practically impossible to populate the entire phase space since the cross section values for the dijet mass spectrum lies between 10^{10} pb to 10^{-11} pb in the order of magnitude. However, there is an appropriate technique of constructing these steeply falling spectra which is called as $\hat{p}_T$ slicing. In this technique, only a certain region of the phase space is taken into account during the calculation of the matrix element. Thus, generator program allows the transverse momentum exchange between two hardly interacted partons to be in a given range namely $\hat{p}_T$ bins.

For the derivation of non-perturbative corrections, it is necessary to have two different datasets where the hadronic and the partonic final states are kept, respectively. This can be achieved by setting the parameters `MSTP(81)=0` and `MSTJ(1)=0`[1] where the first one switches off MPI and the latter switches off hadronization. It should be noted that these effects cannot be disentangled since the multi-parton interactions may directly feed the hadronization process. In this study, 20 $\hat{p}_T$ bins are used to construct the dijet mass spectrum (Table 2.2) for both cases. At the end the ratio of the two different mass spectra is fit to a parametrized function of the dijet mass which is considered as the non-perturbative correction to the NLO calculation. The ratio is

[1]for PYTHIA 6.4 Z2 tune the MSTP(81) parameter should be set to 20 instead of 0.

Table 2.2. Number of events used for each $\hat{p}_T$ slice and corresponding cross sections which is necessary to construct a correct dijet mass spectrum.

$\hat{p_T}$ bin (GeV)	Number of Events	Cross Sections (pb)
0-15	30M	4.844e+10
15-20	30M	5.794e+8
20-30	30M	2.361e+8
30-50	30M	5.311e+7
50-80	15M	6.358e+6
80-120	10M	7.849e+5
120-170	10M	1.151e+5
170-230	10M	2.014e+4
230-300	10M	4.094e+3
300-380	10M	9.346e+2
380-470	10M	2.338e+2
470-600	10M	7.021e+1
600-800	10M	1.557e+1
800-1000	10M	1.843e+0
1000-1400	10M	3.318e-1
1400-1800	10M	1.086e-2
1800-2200	10M	3.499e-4
2200-2600	10M	7.549e-6
2600-3000	10M	6.465e-8
3000-3500	10M	6.295e-11

formally expressed as below:

$$C_i = \frac{N_i^{MPI+Had}}{N_i^{No\ MPI+No\ Had}} \tag{2.66}$$

where C_i is the non-perturbative correction factor for the bin i, $N_i^{MPI+Had}$ is the number of events obtained for the bin i at the hadron level and $N_i^{No\ MPI+No\ Had}$ is the number of events obtained for the same bin at the parton level. Finally, the weighted mean of the corrections extracted from PYTHIA 6.4 (both D6T and Z2 tunes) and Herwig++ is used as the overall correction factors, and the half of the difference from the unity is set as the systematic uncertainty. The overall correction factors are fit to

a parametrized function of the dijet mass as follows:

$$f(m) = A + \frac{B}{m^C} \tag{2.67}$$

Table 2.3 summarizes the fit values for the non-perturbative correction for all $|y|_{max}$ bins, while Figure 2.9 shows the NP corrections from each MC sample, the average fit and the assigned systematic uncertainty.

Table 2.3. Parameters of the overall correction for each y_{Max} bin.

y_{Max} bin	A	B	C
$0 < y_{Max} < 0.5$	1.01	0.03	1.40
$0.5 < y_{Max} < 1.0$	1.01	0.03	1.35
$1.0 < y_{Max} < 1.5$	1.02	0.04	1.54
$1.5 < y_{Max} < 2.0$	1.00	0.10	1.11
$2.0 < y_{Max} < 2.5$	1.04	0.12	1.54

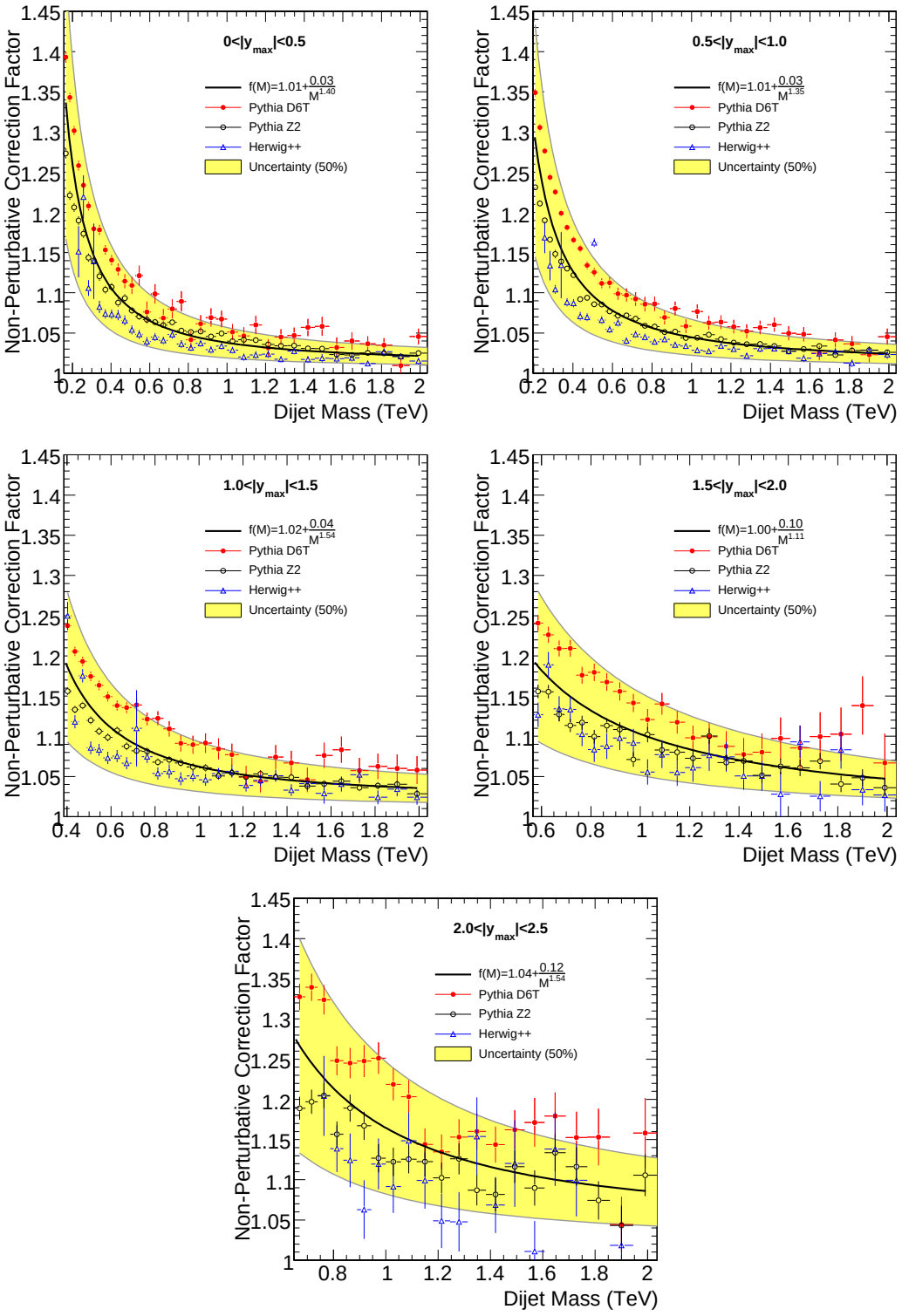

Figure 2.9. Non-Perturbative Corrections extracted from PYTHIA 6.4 (both for D6T and Z2 tunes) and HERWIG++ for each $|y|_{max}$ interval. The band represents the assigned systematic uncertainty.

3. EXPERIMENTAL APPARATUS

3.1. CERN Large Hadron Collider

The *Large Hadron Collider* LHC [14] is a proton-proton collider ring which was built by the European Laboratory for Particle Physics (*Organisation Europenne pour la Recherche Nuclaire*). The collider is 27 km long ring accelerator constructed inside the old Large Electron Positron Collider (LEP) tunnel located about 100 meter underground at the French-Swiss border near Geneva. The design of LHC aims to collide protons with an energy of 7 TeV for each which corresponds to a center of mass energy of $\sqrt{s}$=14 TeV. The main goal of LHC programme is to investigate the electroweak symmetry breaking that is explained by the Higgs mechanism for the time being. Although the current explanation of electroweak symmetry breaking is under investigation at LHC, there are also studies on alternatives to Higgs mechanism associated with more symmetries, new forces, new particles or even new phenomena which probably have not been proposed yet. Moreover, it is hoped that puzzling questions of the standard model and the modern cosmology such as about the dark matter, charge-parity (CP) violation, matter-antimatter imbalance of the universe and possible existence of extra dimensions would be answered. The LHC is noted not only for $\sqrt{s}$=14 TeV center of mass energy of proton-proton collisions but also for its design luminosity of $\mathcal{L}$=10^{34} cm^{-2}s^{-1}. Before reaching its maximum capacity, it will be operated at a lower luminosity of about $\mathcal{L}$=2×10^{33} cm^{-2}s^{-1}.

The collider consists of two rings where two counter-rotating proton bunches travel. Superconducting RF cavities are responsible to accelerate these rotating proton bunches and to keep the protons together in the bunch. There are eight RF cavities for each beam that give 2 MV at 400 MHz. In each turn a single proton gains 0.5 MeV of energy through these eight RF cavities. There are 2808 bunches in one beam each spaced 25 ns apart. In each bunch, there are approximately 1.15×10^{11} protons. Although 25 ns spacing means a frequency of 40 MHz, the large gaps in between beams lower the bunch crossing frequency down to ∼30 MHz (Figure 3.2).

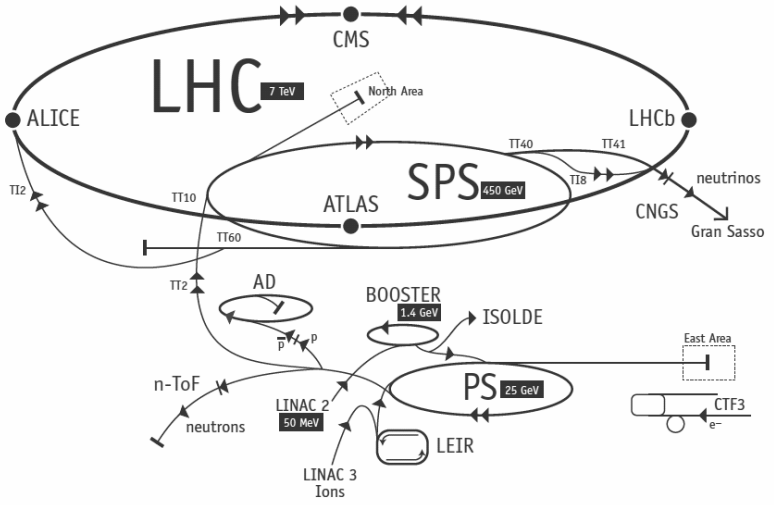

Figure 3.1. General view of the Large Hadron Collider.

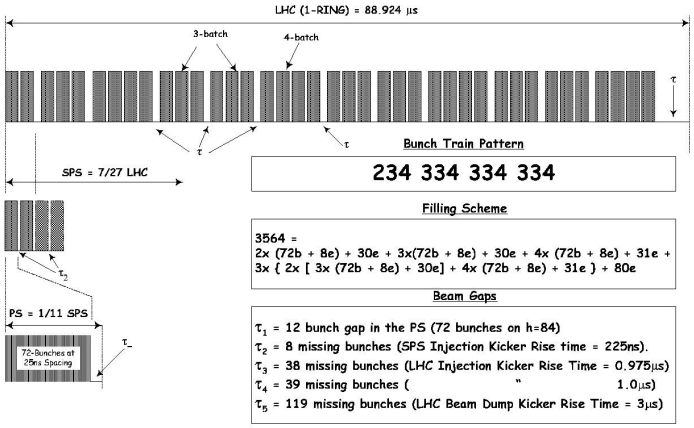

Figure 3.2. The bunch structure of the LHC beam. Notice the large gap at the end.

3.2. Compact Muon Solenoid

The Compact Muon Solenoid (CMS) [15, 13] is one of the two general purpose detectors[2] in the Large Hadron Collider experiment which will study a variety of physics phenomena at the Tera electron Volt (TeV) energy scale. Its surface complex is located in Cessy, France and its experimental cavern is directly under that at the point 5 of the LHC (Figure 3.1).

3.2.1. Physics Goals of the CMS

The primary objective of the CMS is to search for the proposed signature of the Higgs boson which is predicted by the Standard Model of particle physics and is believed to be responsible for the electroweak symmetry breaking. In early seventies, Gerard 't Hooft showed that the gauge theories are automatically renormalizable. After A. Salam and S. Weinberg revised the electroweak theory of S. Glashow in the light of local gauge invariance, it was shown that the gauge bosons should be massless, which was revealed by UA1 and UA2 collaborations in 1983 that it is not the case. The solution was found by adding an extra field which keeps the local gauge invariance of the Lagrangian of the system while giving mass to the gauge boson by a mechanism called "Higgs Mechanism". It suggests that picking a particular ground state of the system may not conserve the symmetries of the Lagrangian. Then, if the Lagrangian is rewritten in terms of the picked ground states, there remains a massive scalar particle (Higgs particle) and a massive gauge field (Higgs field). From Figure 3.3 (right-side plot) it can be observed that the Higgs boson has many decay channels with branching ratios depending on the Higgs boson mass. It can be seen that the decays of the Standard Model Higgs boson into a pair of photons (HSM$\rightarrow \gamma\gamma$) is significant if the Higgs boson mass is below 150 GeV/c^2. Although the dominant decay mode of the Higgs is $b\bar{b}$ in this mass range, the $\gamma\gamma$ decay mode can be well identified experimentally [16].

Beyond the Standard Model, SUperSYmmetry (SUSY) [17] is considered to be a

[2]The other is ATLAS.

good candidate for solving the problem of the potentially diverging mass of the Higgs boson, the so-called 'hierarchy problem'. Supersymmetry offers that, for each boson, there is a corresponding fermion with exactly the same quantum numbers. The useful point of such a fantastic claim is that the extra loop correction due to the supersymmetric partner coming in with a minus sign cancels the quadratic divergences. Another strong motivation of supersymmetry is that the difference between M_{SM} and M_{SUSY} should be in the order of the mass of the Higgs boson, and this is why SUSY particles are expected to be discovered at TeV colliders. Moreover, requiring the conservation of R-parity prevents the so-called Lightest Supersymmetric Particle (LSP) to decay further, offering a candidate for the dark matter problem in the universe.

Besides that, all predictions of Standard Model will be tested at the kinematic regime due to the high center of mass energy of proton-proton collisions at the LHC. One of its prediction about the parton - parton scattering cross section as a function of the invariant mass of the scattered parton-parton system is the main discussion of this thesis.

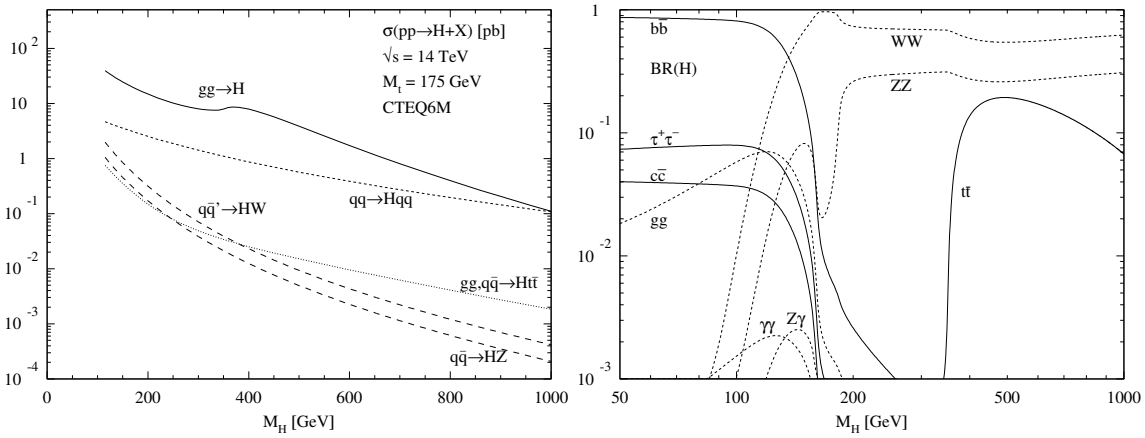

Figure 3.3. Higgs production cross sections at the LHC for the various production mechanisms as a function of the Higgs mass (left). Branching ratios of the dominant decay modes of the SM Higgs particle (right)

3.3. CMS Design and Construction

CMS takes the name from its compactness[3] with respect to its sister ATLAS and the capability of measuring the momentum of high energy muons accurately thanks to solenoid type magnet that can reach to a maximum field strength of 4 Tesla. CMS has a diameter of 15m and a length of 28.7m, small compared to ATLAS (25m diameter and 44m length). However, CMS weighs 14000 tonnes which is about two times heavier than ATLAS. The detector was designed as concentric layers of sub-detectors; the silicon tracker, electromagnetic calorimeter, hadronic calorimeter and the muon system at the outermost part (Figure 3.4).

The coordinate convention of the CMS detector is as follows; the interaction point is accepted as the origin, with the x-axis pointing radially inward toward the center of the LHC and y-axis pointing vertically upwards. z-axis points along the beam line in the direction of the Jura Mountains from LHC Point 5. The azimuthal angle ϕ is measured from the x-axis in the $x - y$ plane. The polar angle θ is measured from the z-axis. The pseudorapidity (η), which is commonly used in particle physics, is defined as;

$$\eta = -ln\left[tan\left(\frac{\theta}{2}\right)\right] \tag{3.1}$$

[3]The solenoid of CMS encloses all the calorimetric systems.

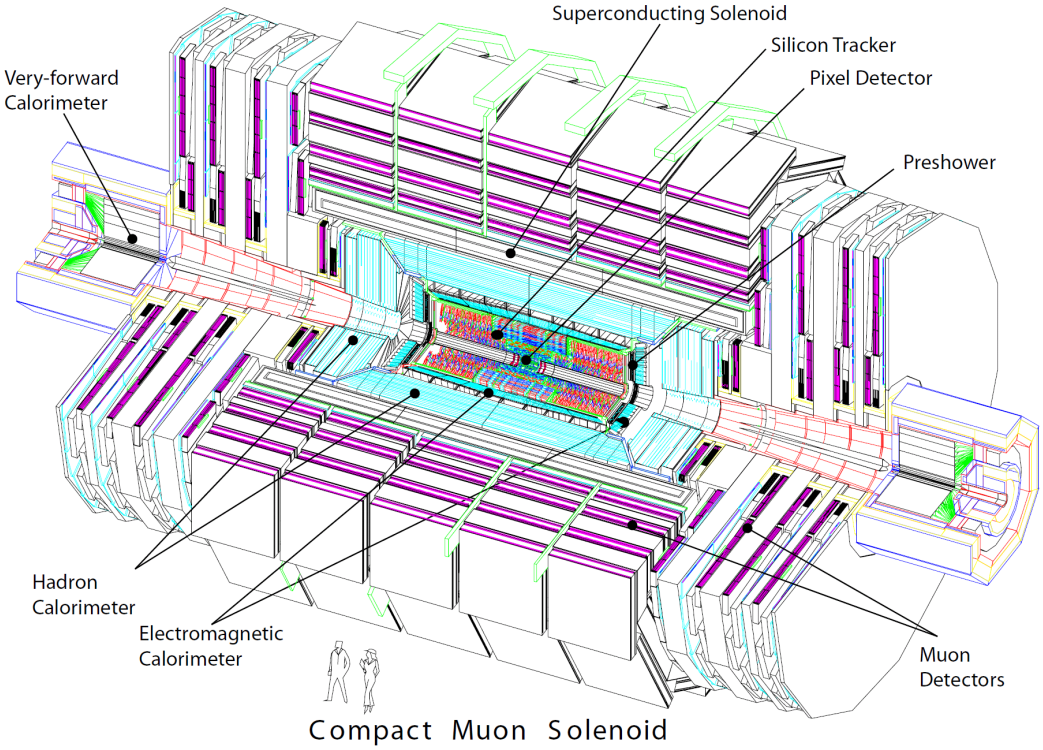

Figure 3.4. An exploded view of the CMS detector [15].

3.3.1. Magnet System

The muon detection requirements drive the specifications and field configuration of the CMS magnet. High magnetic field is needed to make accurate momentum measurements of the TeV scale muons. CMS employs a large superconducting solenoid type magnet that can reach a magnetic field of about 4 T. The dimensions of magnet are 6 m in diameter and 12.5 m in length, and it weighs 12000 tonnes (Figure 3.5). The stored energy in the magnet is 2.6 GJ at full current. The flux is returned via a 10 000-t yoke integrated to the muon system. Three layers of iron return yokes are interlaced with the muon detectors to host and return the magnetic flux. Moreover, the return yokes are responsible for filtering. They absorb hadrons and let only muons and weakly interacting particles to pass through.

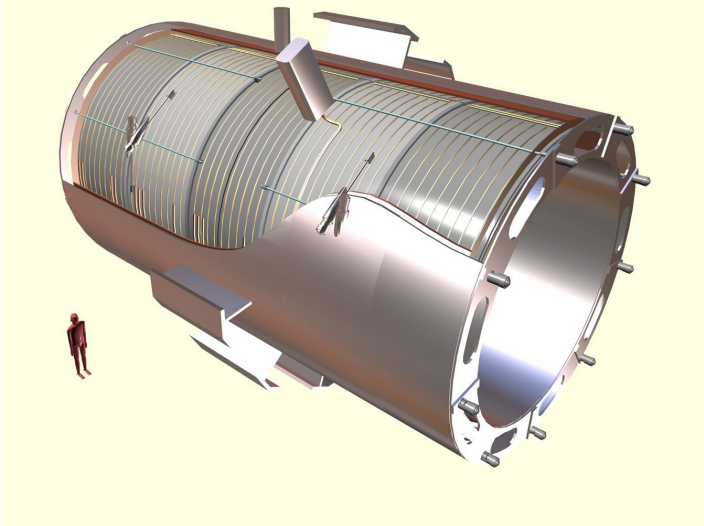

Figure 3.5. Artistic view of the 5 modules composing the cold mass inside the cryostat, with details of the supporting system (vertical, radial and longitudinal tie rods) [13].

3.3.2. Central Tracking System

The silicon tracker is the most inner part of the CMS detector which is responsible for extracting the trajectories of charged particles and measuring their momenta. High particle flux expected from proton-proton collisions brings the necessity of constructing a fast and radiation hard tracker system. The system is based on a silicon technology

which endures the violent radiation for several years and its design is totally driven by requirements of the LHC physics programme. The most critical specifications are: precise reconstruction of charged particle trajectories above 1 GeV/c and good secondary vertex resolution for heavy flavor identification. Mainly, the tracker consists of two parts; the inner tracker is a silicon pixel detector with a total surface of 1 m^2 and 66 million pixels, a silicon strip sensors in the outer region covering a total area of 200 m^2 surrounds the inner tracker (Figure 3.6). The dimensions of the tracker are 5.8 m in length and 2.5 m in diameter. Thus, the acceptance is up to $|\eta|$ <2.5. The homogeneous magnetic field of nominal 4 T is present for the whole volume of tracker.

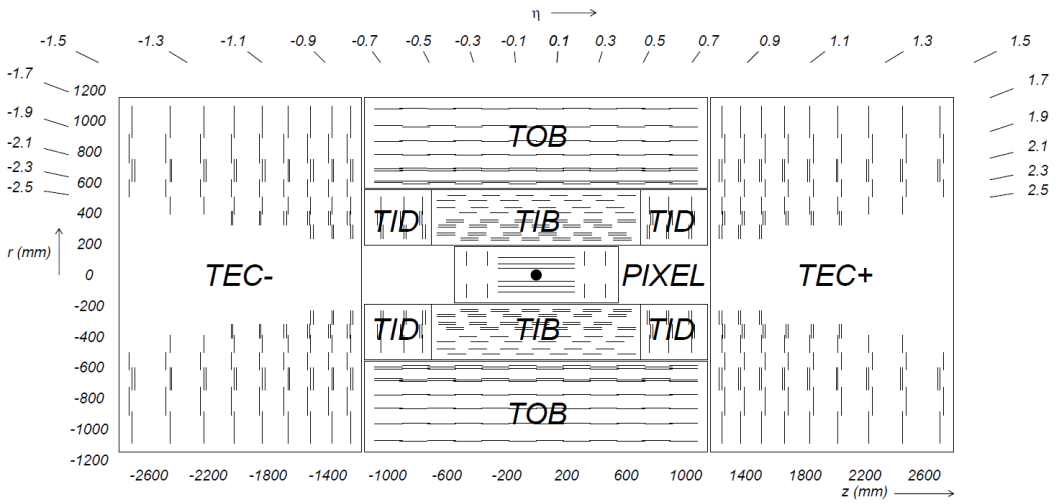

Figure 3.6. Schematic cross section through the CMS tracker. Each line represents a detector module. Double lines indicate back-to-back modules which deliver stereo hits [13].

Three pixel layers are positioned at a radial distance of 4.4, 7.3 and 10.2 cm from the beam axis (Figure 3.7, top). On each side of the barrel two discs complement the tracker at z = ±32.5 and z = ±46.5 cm. The size of each pixel is 100×150 μm^2 and there is a total number of 65 million pixels. The silicon strip tracker encircles the pixel tracker (Figure 3.7, bottom). The inner and outer part is different. The inner barrel (TIB) consists of four layers ranging from 20 to 55 cm and covering $|z| < 65$ cm. Three tracker inner discs (TID) are positioned at each end in the region of $65 < |z| < 110$ cm. The inner strip tracker performs four spatial point measurements for each trajectory. The resolution for a single point measurement is 23 to 34 μm. The inner part is beset

by the tracker outer barrel (TOB) comprising 6 layers, which extends from 55 to 116 cm in radius and ±118 cm in z. The barrel part performs 6 measurements with a single point resolution in between 35 and 53 μm. The outermost part of the tracker is accomplished by 9 endcap discs (TEC) on each side ranging from 124 cm$< |z| <$ 282 cm and 22.5 cm $<$ r $<$ 113.5 cm. The endcaps can perform up to 9 measurements in total.

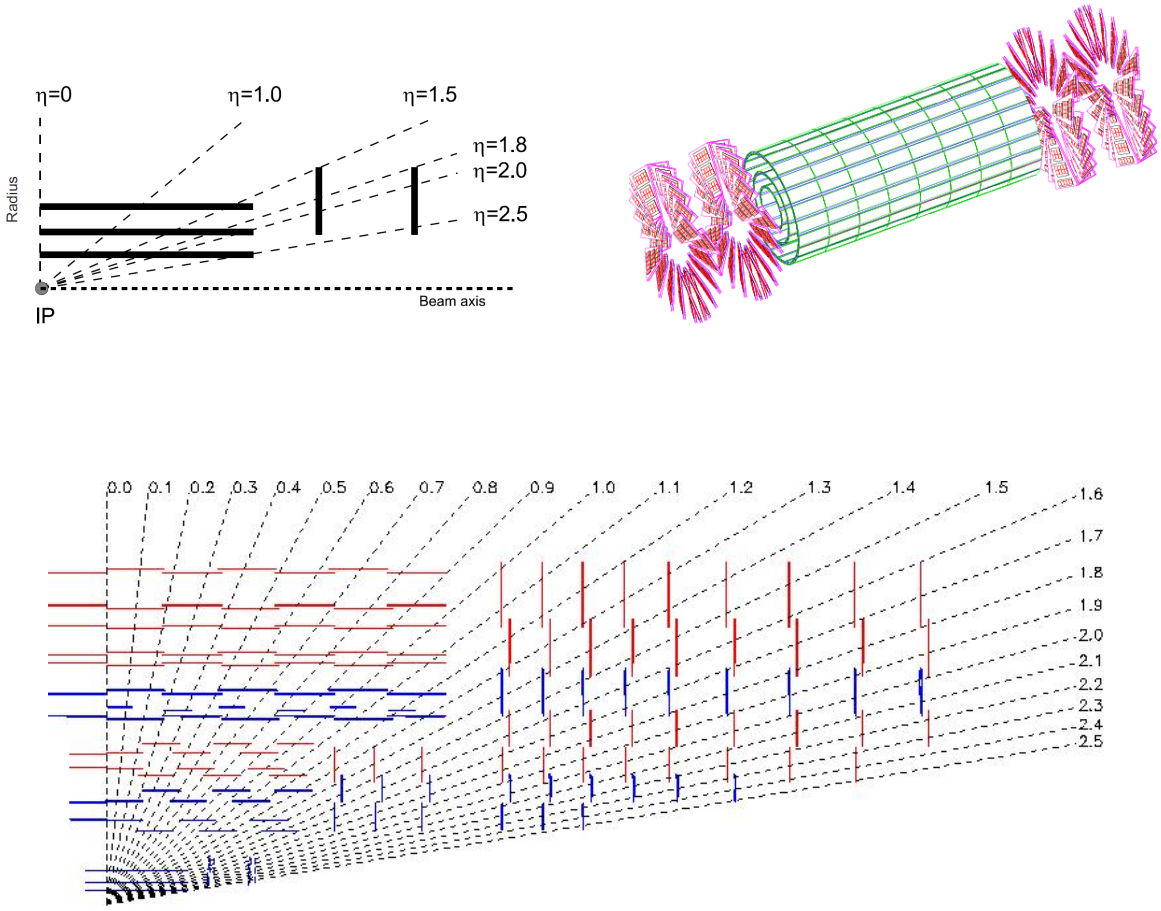

Figure 3.7. Geometrical layout of the pixel detector(top) and schematic layout of the silicon microstrip detector (bottom).

3.3.3. Electromagnetic Calorimeter

The electromagnetic calorimeter (ECAL) is the sub-detector of CMS which measures the energy of electrons and photons produced in the proton-proton collisions. The main design motivation is to perform a good reconstruction of di-photon decays of postulated Higgs boson if it is below 150 GeV. The CMS electromagnetic calorimeter

is made of 61200 lead tungstate ($PbWO_4$) crystals in the barrel part and 7324 crystals in each of the two endcaps. $PbWO_4$ crystals have a density of 8.28 g/cm^3, radiation length of 0.89 cm and a Molière radius of 2.2 cm. These properties of $PbWO_4$ crystals allow a fine granularity and compactness. A preshower detector is placed in front of the endcap crystals. Avalanche photodiodes (APDs) are used as photodetectors in the barrel part and vacuum phototriodes (VPTs) in the endcaps. The barrel region covers a pseudorapidity interval of $|\eta| < 1.48$ and it is segmented 360 - fold in ϕ and 2 $\times$ 85 - fold in η. In total, there are 61200 crystals installed in the ECAL barrel (EB). The front face of the crystals has a cross section of 26 $\times$ 26 mm^2 (0.0174 $\times$ 0.0174 in $\Delta\eta \times \Delta\phi$) and a length of 230 mm (25.8 X_0). Crystals front faces are located at a radial distance of 1.29 m from the beam axis. The single crystals in ECAL barrel are grouped into supermodules containing 17 crystals each. The ECAL endcaps (EE) cover the rapidity range from 1.48 to 3.00, and supermodules are formed out of 25 crystals. The face cross section here is 28.62 $\times$ 28.62 mm^2. Their length is 220 mm (24.7 X_0). The endcaps are installed with a preshower detector to identify neutral pions (π^0), which range from η=1.65 to η=2.60. The total thickness of the preshower detector is 20 cm ($3X_0$). The expected energy resolution, for both EB and EE, is given according to formula;

$$\left(\frac{\sigma_E}{E}\right)^2 = \left(\frac{S}{\sqrt{E}}\right)^2 + \left(\frac{N}{E}\right)^2 + C^2 \tag{3.2}$$

There are several reasons which affect the resolution. The stochastic term (S) depends on the event-to-event fluctuations, photo-statistics, and other fluctuations in the energy deposited in the preshower absorber. The constant term (C) comes from the light collection non-uniformity, errors on the inter-calibration among the modules, and the energy leakage from the back of the crystal. The noise term (N) accounts for the electronic, digitization, and pileup noise.

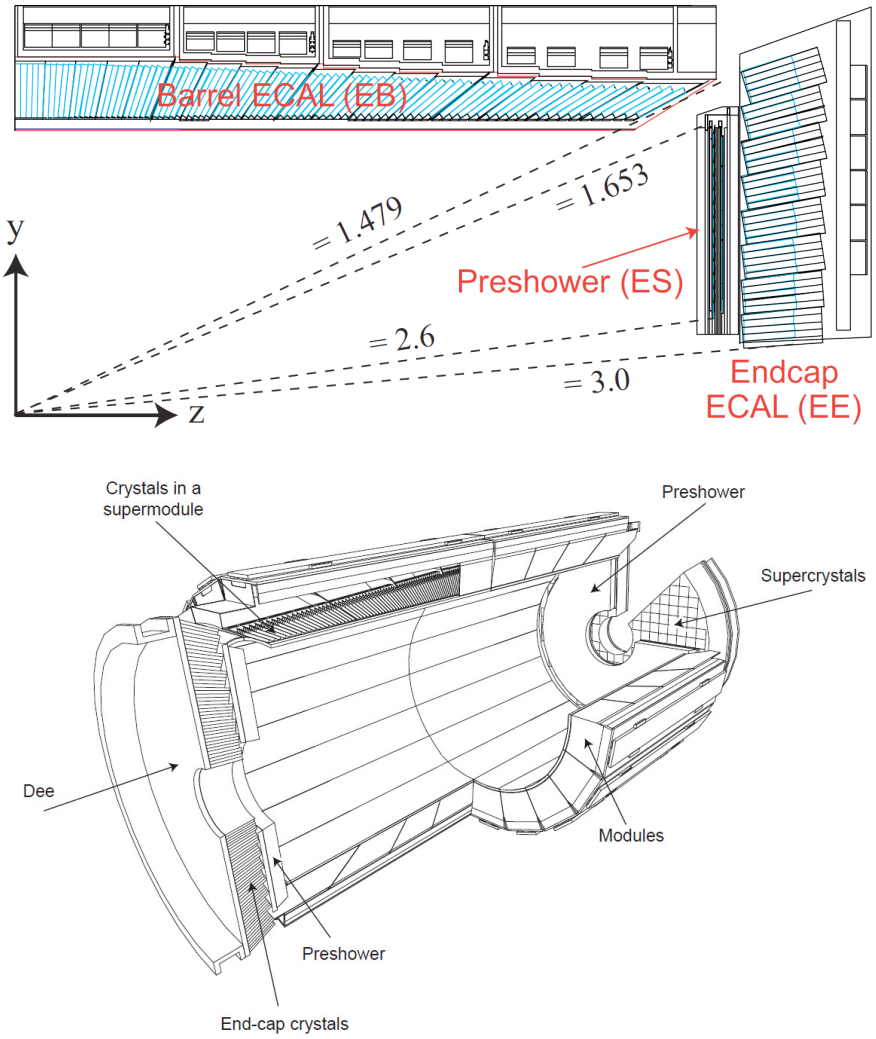

Figure 3.8. Geometric view of one quarter of the ECAL (top). Layout of the CMS electromagnetic calorimeter presenting the arrangement of crystal modules, supermodules, endcaps and the preshower in front (bottom) [13].

3.3.4. Hadronic Calorimeter (HCAL)

Since LHC is a hadron - hadron collider, the major fraction of the produced particles are hadrons. The hadronic calorimeter (HCAL) is the part of the CMS calorimeter system that is responsible for measuring the hadronic particle energies and the determination of missing transverse energy. The calorimeter ranges from 1.77 m to 2.95 m in radial dimension and is divided into four parts: barrel (HB), endcap (HE), outer barrel (HO), and hadronic forward (HF) calorimeter. Figure 3.9 gives a schematic overview on the HCAL sub-detector. It reaches from the outer surface of the ECAL at 1.77 m to the inner surface of the magnet at 2.95 m radially. The hadron barrel part of the HCAL covers a region of $|\eta| < 1.4$ and consists of 2304 towers, resulting in a segmentation of $\Delta\eta \times \Delta\phi = 0.087 \times 0.087$. Each tower is made up of alternating layers of non-magnetic brass absorber and plastic scintillator material. The reason for the absorber material to be non-magnetic is that it must not affect the magnetic field. The two hadron endcaps cover a region of $1.3 < |\eta| < 3.0$. They are positioned in the end parts of the CMS detector and thus are allowed to contain magnetic material. Here iron is used as the absorber material. The granularity begins from $\Delta\eta \times \Delta\phi = 0.087 \times 0.087$ at $|\eta| < 1.6$ up to $\Delta\eta \times \Delta\phi = 0.17 \times 0.17$ at $1.6 < |\eta| < 3.0$.

An additional calorimeter, the outer barrel, is needed to be placed outside of the magnet to absorb escaping hadron showers from particles with transverse energies above 500 GeV. Without the outer barrel, these particles would cause a large missing transverse energy which is not convenient for many physics analysis purposes. The granularity and η range of outer barrel is the same as the hadron barrel. The forward region of $3.0 < |\eta| < 5.0$ is covered by the steel/quartz fiber hadron forward calorimeter. The whole coverage of the HCAL is almost hermetic; $0 < \phi < 2\pi$ in azimuth and $0 < |\eta| < 5.0$ in pseudorapidity.

In order to reconstruct jets from measured energies of hadrons, there exists different algorithms (See Section 4.4). One of these adds the E_T of crystals close in $\eta - \phi$ to the crystal with the highest energy deposit and creates a proto-jet. This recombining procedure is repeated taking the proto-jet as the jet axis until the parameters of the

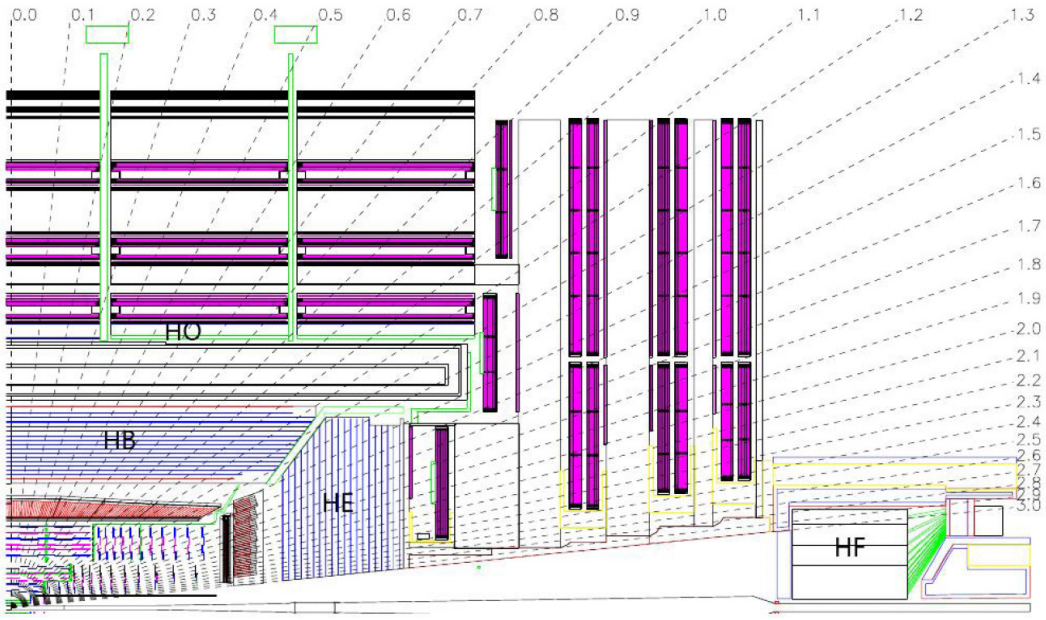

Figure 3.9. Longitudinal view of one quarter of the detector in the $r\eta$ - plane, showing the positions of the HCAL parts: hadron barrel (HB), hadron outer (HO), hadron endcap (HE) and hadron forward (HF) [13].

proto-jet is stabilized.

In the head on collision of protons, the initial total transverse momentum and energy are zero. From the conservation of energy and momentum, the sum of these should stay as zero after the collision. If this sum differs after the collision, this is a clear indication that some particles have not been detected by the detector. Each cell in the calorimeter produces a four-vector, with an energy equal to the measured energy in the cell (massless), a direction pointing from the vertex to the center of the cell. The nonzero total transverse momentum is considered as the momentum imbalance arisen because of the non - detected particles. Thus, the vector of total transverse momentum, with the minus sign, is called as *missing transverse energy* (MET).

$$\vec{E}_{T,miss} = -\sum_{i} \vec{E}_T^{\,i} \tag{3.3}$$

where $\vec{E}_{T,miss}$ is the four vector of MET and $\vec{E}_T^{\,i}$ are the four vectors of the calorimeter cells.

The overall energy resolution (combined with ECAL) is given as;

$$\left(\frac{\sigma_E}{E}\right)^2 = \left(\frac{120\%}{\sqrt{E}}\right)^2 + (6.9\%)^2 \tag{3.4}$$

Both granularity and energy resolution of the HCAL are worse than ECAL. Therefore the overall precision of the calorimeter output is determined by the HCAL.

3.3.5. Muon Chamber

If the Higgs boson mass is above 115 GeV/c^2, the $H \to ZZ \to 4\mu$ and $H \to WW \to 2\mu$ decay channels become dominant (Figure 3.3). Hence, a clear muon identification plays a crucial role in a prospective discovery of the Higgs boson. The muon system of the CMS detector is a tracking device in the outermost region. Only muons and non-interacting particles such as neutrinos can achieve pass through all the calorimetric systems without leaving a large fraction of their energy. An important task of the muon system is to provide a fast recognition and an efficient reconstruction of the muons. Three different type of gaseous detectors are used to construct a complete muon system. In the barrel region ($|\eta| < 1.2$) drift tube chambers (DTCs) are mounted. There are four layers of muon chambers positioned in the return yoke, and cathode strip chambers (CSC) are located in the endcap ($0.9 < |\eta| < 2.4$) (Figure 3.10). In order to improve muon trigger system and for a good measurement of the bunch crossing time, resistive plate chambers (RPC) are mounted in the barrel and endcap region ($|\eta| < 1.6$). They provide a fast response, which is much shorter than the bunch crossing time, but with coarser spatial resolution. In total, muons are measured up to four times. Once in the inner tracking system and three times in the muon system.

3.3.6. Trigger and Data Acquisition System

At the design luminosity of 10^{34} cm^{-2}s^{-1}, each bunch, traveling oppositely inside the beam pipes, encounters the other 40 million times per second and they passes through each other. In other words, the bunch crossing frequency is 40 MHz. The average proton-proton collision per each bunch crossing is approximately 20. This cor-

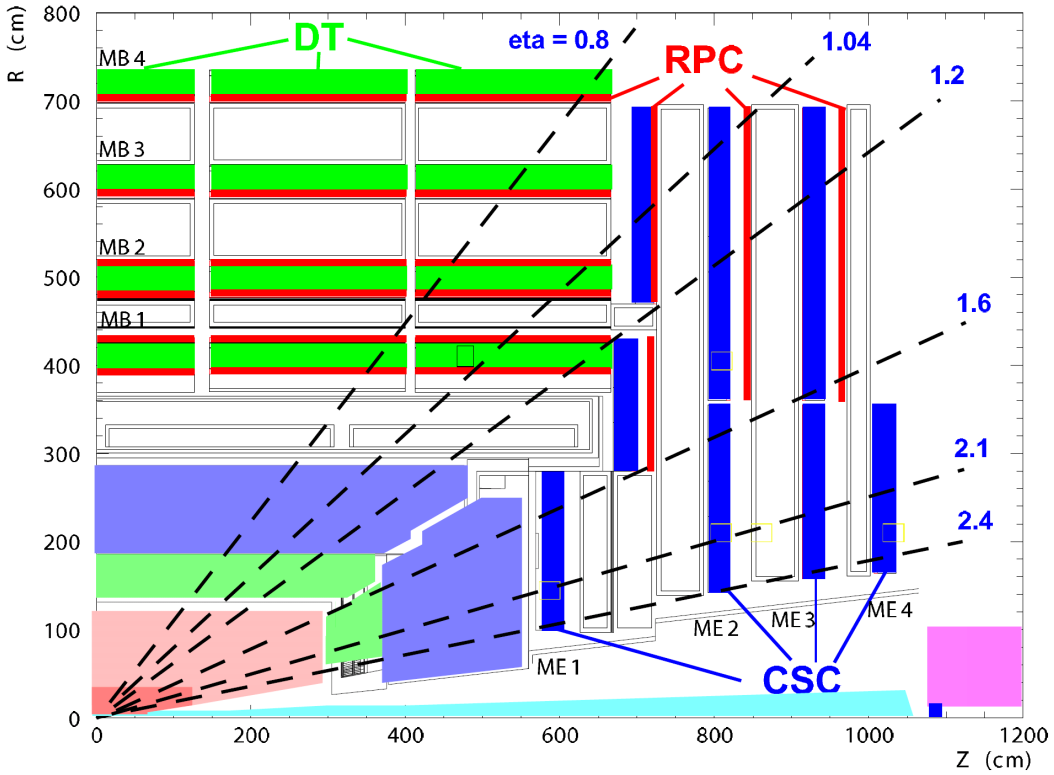

Figure 3.10. A longitudinal view of the muon system indicating the location of the three detector types contributing to the muon spectrometer [13].

responds to a data rate of 1.2 Tbyte/s, which is practically impossible to store in any tape or disk. Thus, the data are reduced first by the level-one trigger (L1 Trigger). L1 trigger system is implemented as a programmable hardware system that uses information from the muon chambers and calorimeters for selecting event signatures which are specified by physics interests. However, there exists a very limited time for L1 trigger to make a decision which means a rough form of the raw data from the calorimeters and muon system should be used. The L1 trigger system is located 90 m outside the detector which causes a latency of 3.2 μs between the bunch crossing and the L1 accept signal. The signal information accumulated in that time interval is buffered. The L1 trigger system reduces the event rate of 40 MHz down to 100 kHz to be passed to the High Level Trigger (HLT) system. HLT system is a software system that uses the detector signals that pass the L1 trigger. It can run on high resolution data with complex reconstruction algorithms. The HLT decisions are based on the output signals from all sub-detectors. After the HLT decisions, the event rate decreases down to 100

Hz for mass storage which corresponds to a data rate of 150 Mbyte/s.

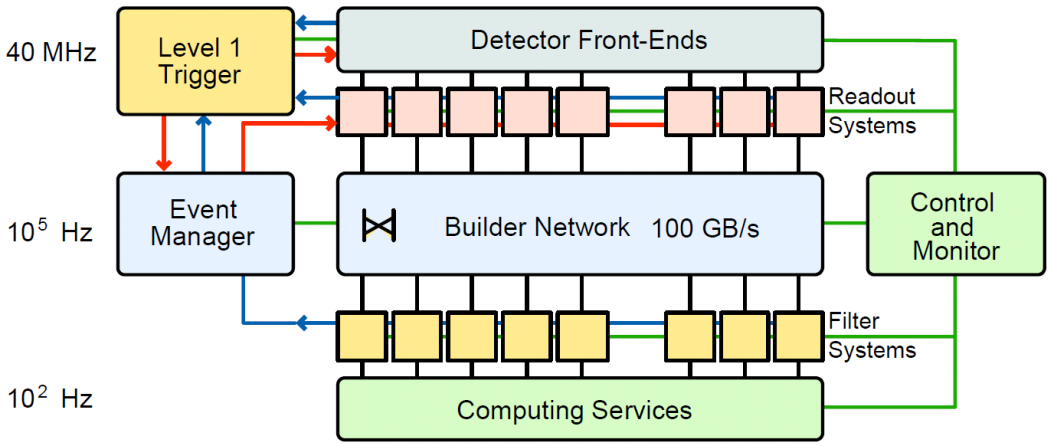

Figure 3.11. Architecture of the CMS Data Acqusition (DAQ) system.

4. EVENT GENERATION, DETECTOR SIMULATION AND JET RECONSTRUCTION

Monte Carlo event generators are computer programs calculating particle physics processes numerically. There are two main reasons to use Monte Carlo techniques in high energy particle physics. Firstly, cross section values must be calculated for complex regions of the phase space in order to compare the experimental results with the theoretical expectations, yet it is practically impossible to perform these calculations analytically. Secondly, it is always needed to have realistic event simulations in order to have a foresight for both designing the experimental device and analyzing its data. As discussed in the Section 2.2, QCD gives different descriptions for different scales of the momentum transfer Q. First, a set of primary partons are produced by the hard subprocess that can be explained by a fixed-order (LO or NLO or even NNLO) matrix element, then a parton shower evolves these primary partons while the scale decreases down to a cut-off scale $Q_0 \approx 1GeV$. Finally, the resultant partons of the shower arrange themselves as color singlet (color neutral) hadrons. At this final step, the scale is too low, which means the strong coupling constant α_s is large, and this hadronization process is non-perturbative. Hard matrix elements (ME) are computed to a particular order in perturbation theory while the parton evolution process governed by the DGLAP (Dokshitzer-Gribov-Lipatov-Altarelli-Parisi) equations is done via the parton shower (PS) approach. Experimentally determined parton distribution functions are taken as input for the parton evolution. MPI and hadronization, the non-perturbative parts which are beyond our means of calculation, are evaluated by using dedicated phenomenological models. In an abstract sense, the whole process can be written as

$$(\text{Hard subprocess} \oplus \text{MPI}) \otimes \text{Parton Shower} \otimes \text{Hadronization}$$

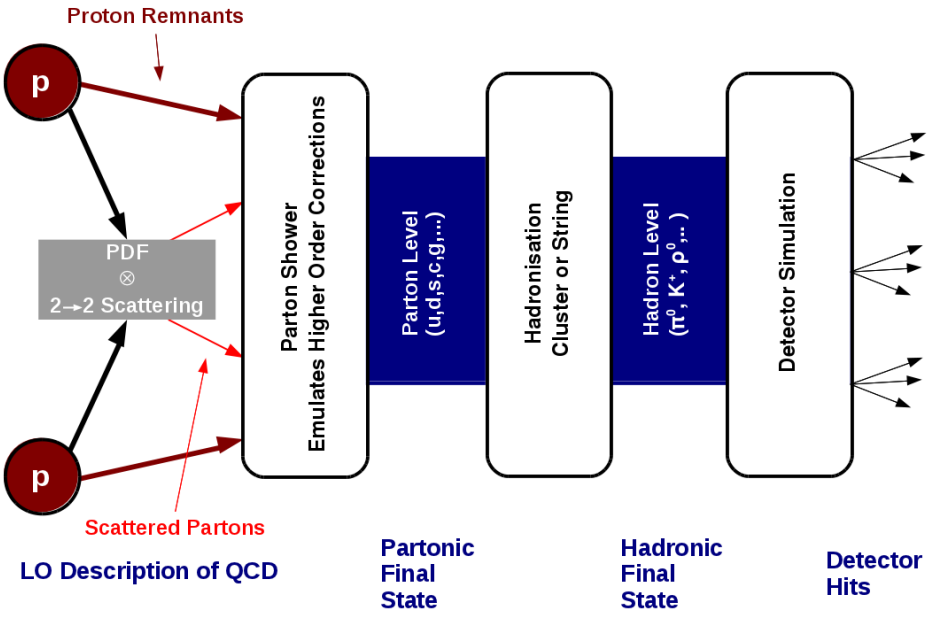

Figure 4.1. The basic steps in the generation of a simulated event.

Monte Carlo generators compute single collisions (events), by this providing the opportunity not only to calculate inclusive quantities such as cross sections, but also to check different observables on an event-by-event basis.

4.1. PYTHIA

PYTHIA is a general-purpose leading-order MC event generator. It has been used extensively at LEP, HERA and the Tevatron for e^+e^-, ep and $p\bar{p}$ physics. It contains an extensive subprocess library covering Standard Model physics with SUSY, Technicolor and many other exotic processes. The Lund string model [20] is used to describe the hadronization process. This model is based on a picture where quarks and antiquarks are linearly confined, located at the ends of a string, and gluons are energy and momentum carrying kinks on this string. The production of a quark-antiquark pair in electron-positron annihilation can be given as a trivial example. At the annihilation point, the quark and antiquark move apart from each other, with half of the total energy for each in the center-of-mass frame. As the gluon string is stretched between them, its potential energy increases. At some critical point, when the potential energy reaches at the order of hadron masses, the strings are energetically more likely to be

broken through the creation of a new quark-antiquark pair. The new antiquark at the end of the string segment which is connected to the original quark and the new quark which is connected to the antiquark. Successive sequence of stretching and breaking continues until all the energy is converted into quark-antiquark pairs connected by short string segments, which can be considered as "hadrons".

The generation of the underlying event is a complicated process. Different phenomenological models describing underlying event exist, with various degrees of complexities. Hence, there are different "tunes" of Pythia. In CMS, two Pythia tunes are studued and used to generate MC samples: the Z2 [21] tune which seems to be in a better agreement with collected data and the D6T [22] tune is used as complementary for "systematics"" studies.

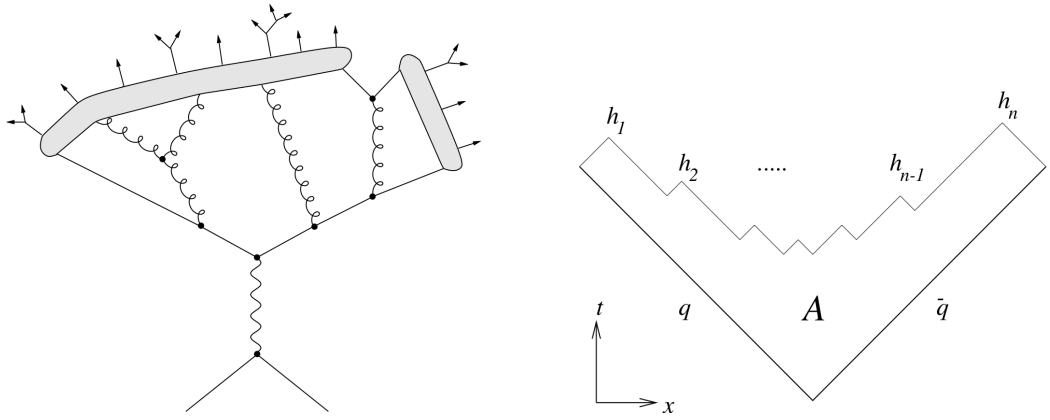

Figure 4.2. Schematic representation of the string model (left). Space-time picture of string hadronization (right).

4.2. Herwig++

Herwig++ is a C++ version of the Herwig (Hadron Emission Reactions With Interfering Gluons) [23] event generator, whose earlier versions were programmed in Fortran. It includes some improvements compared to Herwig6 such as the covariant formulation of the parton shower and mass-dependent splitting functions. Herwig also uses leading order calculations with different parton shower and hadronization models than Pythia uses. It has its own tunes and an implementation of a parton shower which uses a cluster hadronization model. That implementation of the different parton

shower model gives the possibility of extracting uncertainties by comparing Pythia and Herwig outputs. The cluster hadronization model is based on the pre-confinement property of QCD. It has been shown that at evolution scales, much less than the hard subprocess scale, $q \ll Q$, the partons in a shower form color singlet groups with an invariant mass distribution. Nevertheless, invariant mass distribution of the formed group is independent of the scale of the hard subprocess; it depends only on q and Λ_{QCD}. Then, these clusters at the hadronization scale Q_0 can be identified as proto-hadrons which are candidates to decay into observed hadrons.

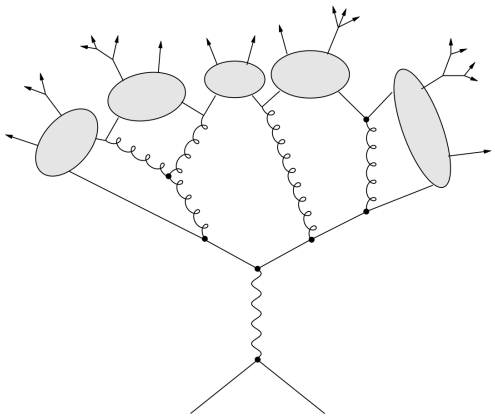

Figure 4.3. Cluster Hadronization Model.

4.3. Detector Simulation

A realistic simulation of the CMS detector is based on the GEANT4 [26] toolkit. It relies on a detailed description of the sub-detector volumes and materials, and the necessary information about the "sensitive detector". It takes generated particles as input, passes them through the simulated geometry, and models physics processes that accompany particle passage through matter. Results of each particle's interactions with matter are recorded in the form of simulated hits. Energy loss by a given particle inside "sensitive volume of one of the sub-detectors, recorded with several other characteristics of the interaction is an example of a simulated hit. Generated particles are called as "primary", and the particles originating from GEANT4-modeled interactions of a primary particle with matter are called as "secondary". These simulated hits are then used as input to emulators which mimic the response of the detector readout and trigger

electronics and digitize this information by also considering noise and other factors.

4.4. Jet Reconstruction

4.4.1. Jet Reconstruction Algorithms

As it was discussed in Chapter 2, scattered partons from the hard subprocess eventually turn into a spray of hadrons due to color confinement. This spray of particles can be identified as jet objects in the detector through the application of a set of mathematical rules by taking detector entries as inputs. A jet is reconstructed by using energy depositions in calorimeter towers and track momentum information of charged particles, and by clustering this information in an appropriate way to assign a four vector to the jet object. Since a jet algorithm is a complicated combinatoric process and highly definition dependent, theorists and experimenters decide on the features of a good jet reconstruction algorithm that should satisfy the following [27] ;

- A jet algorithm should be simple to implement in an experimental analysis;
- A jet algorithm should be simple to implement in the theoretical calculation;
- A jet algorithm should be defined at any order of perturbation theory;
- A jet algorithm should yield finite cross sections at any order of perturbation theory;
- A jet algorithm should yield a cross section that is relatively insensitive to hadronization.

Infrared and collinear (IRC) safety is a fundamental requirement for jet algorithms. Infrared safety means that adding a soft gluon should not change the results of the jet clustering. Collinear safety is splitting one parton into two partons should not change the results of the jet clustering. The configurations of the infrared and collinear safety are shown separately in Figure 4.4. Several algorithms have been developed during the past years, and three of them are officially chosen by the CMS collaboration: Iterative Cone, k_T and anti-k_T.

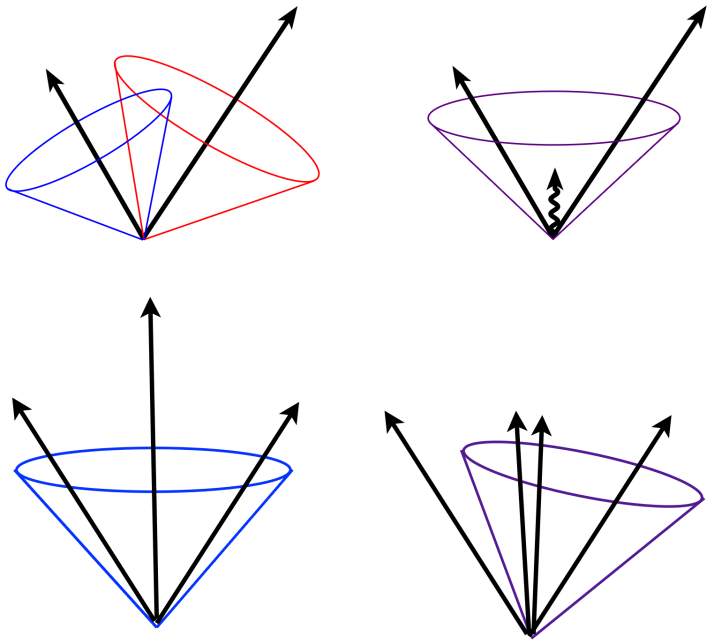

Figure 4.4. Illustration of the infrared sensitivity of a cursory designed jet algorithm (top). Illustration of the product of a collinear unsafe jet algorithm. A collinear splitting changes the number of jets (bottom).

4.4.2. Iterative Cone Algorithm

Although it lacks collinear and infrared safety, Iterative Cone (IC) algorithm is still present in the CMS official reconstruction scheme for the practical purposes of high level trigger system. It is fast and it has a local behavior, so it makes IC algorithm suitable to use in high level triggers. In order to reconstruct IC jets, an iterative procedure is followed. The particle in the event with the biggest transverse energy is taken as seed, and a cone with a radius $R = \sqrt{\delta\eta^2 + \delta\phi^2}$ is built around it. All the objects contained in that cone are merged into a proto-jet, whose direction and transverse energy of which are given as

$$E_T = \sum iE_T^i; \quad \eta = \frac{1}{E_T}\sum iE_T^i \cdot \eta_i; \quad \phi = \frac{1}{E_T}\sum iE_T^i \cdot \phi_i \tag{4.1}$$

After this determination, first proto-jet is used as the seed of the second iteration. This iterative procedure continues until the desired minimum difference between the seed

and the resultant proto-jet is achieved. Finally, the last proto-jet is declared as "the jet object".

4.4.3. Generalised k_T Algorithm

The k_T, anti-k_T and Cambridge-Aachen algorithms can be given in a single type, the generalized k_T algorithm.The generalized k_T algorithm represents a whole family of infrared- and collinear-safe algorithms depending on a continuous parameter, denoted as p. The k_T algorithm is based on a pair-wise recombination and it combines two particles (or calorimeter towers) if their relative transverse momentum is less than a given threshold. The distance d_{ij} between the particle (or calorimeter tower) i and j, and the distance d_{iB} between the particle i and beam (B) are defined as

$$d_{ij} = min(k_{ti}^{2p}, k_{tj}^{2p})\Delta R_{ij}^2/R^2; \quad d_{iB} = k_{Ti}^2; \quad \Delta R_{ij}^2 = (y_i - y_j)^2 + (\phi_i - \phi_j)^2 \tag{4.2}$$

where k_T is the momentum of the particle and p values of $-1, 0, 1$ represent anti-k_T, Cambridge-Aachen and k_T respectively. The k_T algorithm with $p = 1$ means that soft particles are clustered initially [28]. If $p = -1$, anti-$_T$ algorithm is obtained and hard particles are clustered initially rather than soft particles [29]. If p =0, an energy dependent clustering algorithm which is called as Cambridge/Aachen (CA) algorithm is obtained [30]. The behaviors of different jet algorithms are illustrated in Figure 4.5. As it can be seen in Figure 4.5, the anti-kT jet algorithm gives the best shape of jets. In this thesis, jets are reconstructed using anti-k_T algorithm with cone size parameter R=0.7.

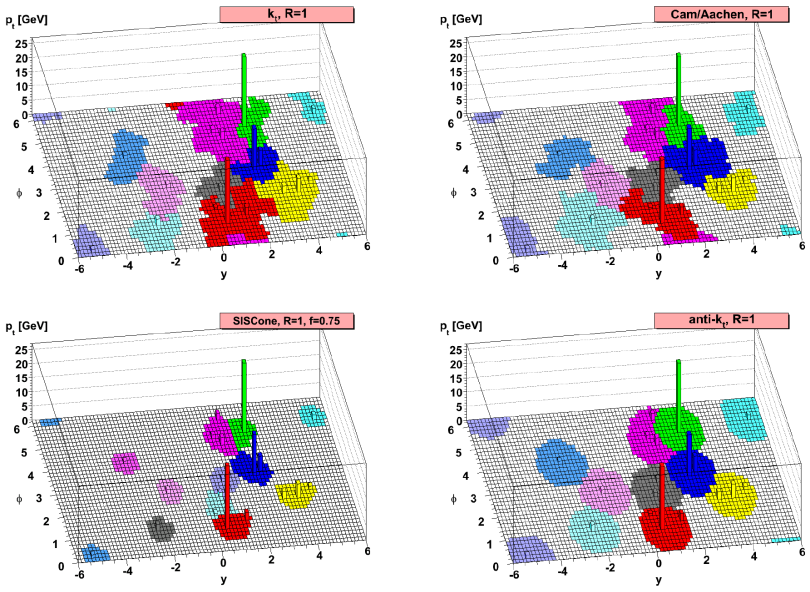

Figure 4.5. Illustration of different jet algorithms in parton level [29].

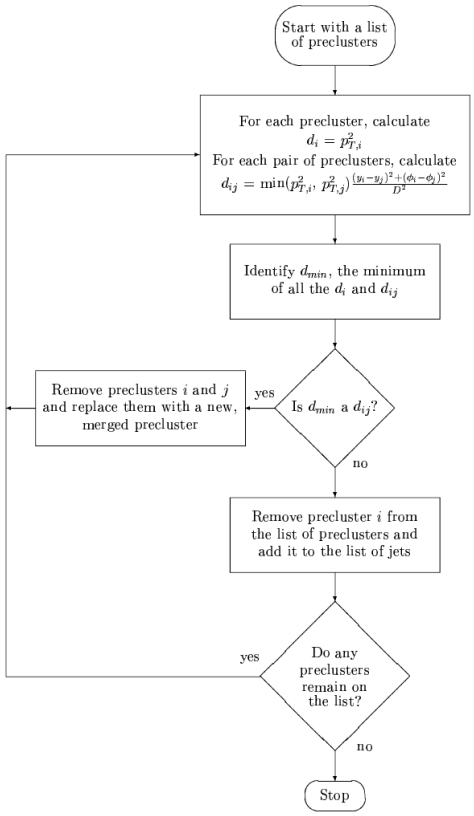

Figure 4.6. A flow chart for the k_T algorithm.

4.4.4. NLOJet++ and fastNLO

NLOJET++ [31] is a QCD event generator for hadron-hadron collisions, developed by Zoltàn Nagy, which can calculate one-, two-, and three-jet observables at next-to-leading order. In case of the three-jet or inclusive jet cross section, it extremely reduces the renormalization and factorization scale dependence with respect to a leading order calculation. A slightly modified Catani-Seymour [32] dipole formalism is used in the calculation to cancel infrared divergences which allows an extensive precision and flexibility during phase space generation. Nevertheless, production of individual events which are suitable for detector simulation cannot be produced by this program.

Since precise computations in NLO are very time consuming or equivalently CPU consuming, a more efficient set-up in the form of the fastNLO project [33] has been setup. It allows the fast re-derivation of the considered cross section for arbitrary input parton distribution functions and α_s values. This is done by separating the PDF dependency from the hard matrix element calculation. The fastNLO package is attached to NLOJET++, which performs the initial perturbative calculation in next-to-leading order.

5. ANALYSIS

This section is dedicated to describe the analysis in detail. Event and jet selections, trigger studies, spectrum construction and corrections for the smearing effect are discussed.

The differential cross section was calculated using equation 5.1

$$\frac{\mathrm{d}^2\sigma}{\mathrm{d}M_{JJ}\mathrm{d}|y|_{max}} = \frac{\mathcal{C}}{\epsilon \cdot \mathcal{L}_{\mathrm{equiv}}} \cdot \frac{N}{\Delta M_{JJ}\Delta|y|_{max}} \tag{5.1}$$

N is the number of dijet events, ΔM_{JJ} and $\Delta|y|_{max}$ are mass and rapidity bins respectively, $\mathcal{L}_{\mathrm{equiv}}$ is the equivalent luminosity for each dataset where the dijet event is coming from, ϵ is the efficiency factor for even selection (i.e., trigger and JetID), $\mathcal{C}$ is the correction factor for smearing effects due to the finite detector resolution. All these components will be discussed in the following sections.

5.1. Data Set, Event Selection and Jet Selection

5.1.1. Data Set

This analysis was performed with the 36 pb^{-1} of data collected by the CMS in 2010 Run with High Level Jet triggers. The data are reconstructed with CMSSW (CMS Software) which is the official software framework of the CMS experiment. Good runs and good luminosity sections of them are declared by the data validation group at CMS was. The main concern of this official declaration is data taking condition of the detector with all its components. There are namely three primary data sets used in this analysis and their names and Dataset Bookkeeping System (DBS) identifications are listed in Table 5.1.

Table 5.1. Primary Data sets used in the analysis .

ERA	Primary Dataset	DBS Name
2010A	JetMETTau	/JetMETTau/Run2010A-Nov4ReReco_v1/RECO
2010A	JetMET	/JetMET/Run2010A-Nov4ReReco_v1/RECO
2010B	Jet	/Jet/Run2010B-Nov4ReReco_v1/RECO

5.1.2. Event and Jet Selection

In order to calculate the invariant dijet mass and to construct the spectrum, each event in the data set must satisfy a certain set of selection criteria. First of all, an event should be triggered by one of these HLT Jet triggers; HLT_Jet_30U, HLT_Jet_50U, HLT_Jet_70U, HLT_Jet_140U. A brief definition of these triggers is given in Table 5.2. Each event should have at least two jets satisfying 0 $<|y|_{max} <$ 2.5 condition where $|y|_{max}$ is defined as:

$$|y|_{max} = max(|y_1|, |y_2|) \tag{5.2}$$

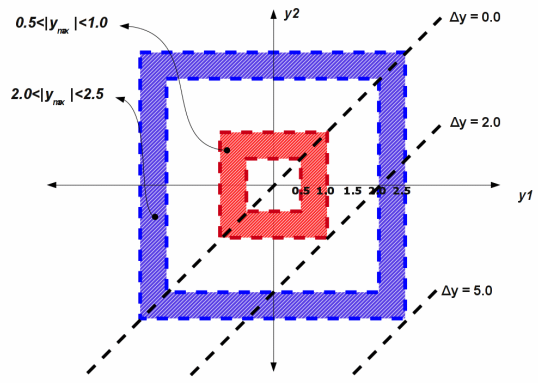

Figure 5.1. $|y|_{max}$ bins in y_1,y_2 phase space.

Events are further required to have at least one well reconstructed primary vertex (PV) with |z(PV)| <24 cm and at least four tracks associated with the primary vertex fit ($n_{dof} \geq 5$) where z=0 represents the central point of the detector. These PV selection criteria ensure that the event in interest is originated in the region of interaction. Additionally events with at least two reconstructed particle flow jets (PF Jets) with p_T >30 GeV (corrected) and both satisfying the loose PF JetID criteria are selected. PF JetID criteria are a set of criteria developed at CMS to reject most of the fake jets arising due to the calorimeter or readout noise or both [34]. There are two types of PF JetID criteria called *"loose PF JetID"* and *"tight PF JetID"* and the loose one which requires at least two particles in a jet, one of which is a charged hadron, is used in this analysis. If any of the leading jet fails to satisfy loose PF JetID requirments, the event is not considered in the analysis.

Table 5.2. L1 and High Level Jet Triggers.

Trigger Path	L1 seeds	Requirement
HLT_Jet30U	L1_SingleJet20U	requiring $\geq$ 1 jet at HLT with $p_T > 30$ GeV
HLT_Jet30U_v3	L1_SingleJet20U	requiring $\geq$ 1 jet at HLT with $p_T > 30$ GeV
HLT_Jet50U	L1_SingleJet30U	requiring $\geq$ 1 jet at HLT with $p_T > 50$ GeV
HLT_Jet50U_v3	L1_SingleJet30U	requiring $\geq$ 1 jet at HLT with $p_T > 50$ GeV
HLT_Jet70U	L1_SingleJet30U	requiring $\geq$ 1 jet at HLT with $p_T > 70$ GeV
HLT_Jet70U_v2	L1_SingleJet40U	requiring $\geq$ 1 jet at HLT with $p_T > 70$ GeV
HLT_Jet70U_v3	L1_SingleJet40U	requiring $\geq$ 1 jet at HLT with $p_T > 70$ GeV
HLT_Jet100U	L1_SingleJet30U	requiring $\geq$ 1 jet at HLT with $p_T > 100$ GeV
HLT_Jet100U_v2	L1_SingleJet60U	requiring $\geq$ 1 jet at HLT with $p_T > 100$ GeV
HLT_Jet100U_v3	L1_SingleJet60U	requiring $\geq$ 1 jet at HLT with $p_T > 100$ GeV
HLT_Jet140U_v1	L1_SingleJet60U	requiring $\geq$ 1 jet at HLT with $p_T > 140$ GeV
HLT_Jet140U_v3	L1_SingleJet60U	requiring $\geq$ 1 jet at HLT with $p_T > 140$ GeV

5.2. Trigger Studies

As it was discussed in Section 5.1.2, events triggered with the HLT jet triggers are used in this analysis. Each of these triggers has different Level-1 seeds and different p_T thresholds. With the increasing instantaneous luminosity of proton proton collisions at LHC the number of hard scattering events has increased. As a result, the number of events that satisfy the requirements of HLT Jet triggers has increased. In order to keep the data writing rate in an acceptable value, the triggers with lower thresholds has been pre-scaled. Furthermore, each of them has been introduced to DAQ system at different periods of the 2010 Run. Thus, each data sample with one of these triggers has different effective luminosity (Table 5.3). It is an important task to determine

Table 5.3. High Level Triggers used in the analysis accompanied by the effective luminosity, and the effective trigger prescales.

Sample	HLT Paths (OR)	Eff. Luminosity pb^{-1}	Eff. Prescale
Jet30U	HLT_Jet30U, HLT_Jet30U_v3	0.4	111
Jet50U	HLT_Jet50U, HLT_Jet50U_v3	3.2	10.9
Jet70U	HLT_Jet70U, HLT_Jet70U_v2, HLT_Jet70U_v3	8.6	4.1
Jet100U	HLT_Jet100U, HLT_Jet100U_v2, HLT_Jet100U_v3	19.0	1.9
Jet140U	HLT_Jet100U, HLT_Jet140U_v1, HLT_Jet140U_v3	35.3	1

the lower limits of parameter in interest for each of the data samples where the sample efficiency is 99%. In this case the lower limits of the invariant dijet mass for all samples in each $|y|_{max}$ bin are determined. This is done by extracting the turn-on curve of every HLT jet trigger with respect to one step lower threshold trigger. The turn-on curves are constructed according the formula below;

$$\epsilon_A = \frac{N_{TriggerA}}{N_{TriggerB}} \cdot \frac{\mathcal{L}_A}{\mathcal{L}_B} \tag{5.3}$$

where ϵ_A is the efficiency of the higher threshold sample and $\mathcal{L}_{A,B}$ are the effective luminosities of two samples. After constructing the turn-on curve, it was parametrized by performing a fit to a sigmoid type of function in order to estimate the 99% efficient

mass point more precisely.

In this study, an adjusted form of the error function was used to perform this fit.

$$\epsilon_A(m_{jj}) = \frac{1}{2}[Erf(\alpha m_{jj} - \beta) + 1] \tag{5.4}$$

Here m_{jj} is the invariant mass of the dijet system, α and β are the free parameters of the fit, and Erf is the well know error function. In Figure 5.2 the turn-on curves for HLT_Jet_70U in all $|y|_{max}$ bin are given. All other plots of different samples can be found in Appendix A. Also the 99% efficiency mass points for all samples and rapidity bins are summarized on Table 5.4

Table 5.4. Trigger efficiency turn-on masses for all jet samples and rapidity regions.

Sample	[0.0-0.5]	[0.5-1.0]	[1.0-1.5]	[1.5-2.0]	[2.0-2.5]
Jet30U	156 GeV	197 GeV	386 GeV	565 GeV	649 GeV
Jet50U	220 GeV	296 GeV	489 GeV	693 GeV	890 GeV
Jet70U	270 GeV	386 GeV	649 GeV	890 GeV	1246 GeV
Jet100U	386 GeV	489 GeV	838 GeV	1058 GeV	1687 GeV
Jet140U	489 GeV	649 GeV	1058 GeV	1607 GeV	2231 GeV

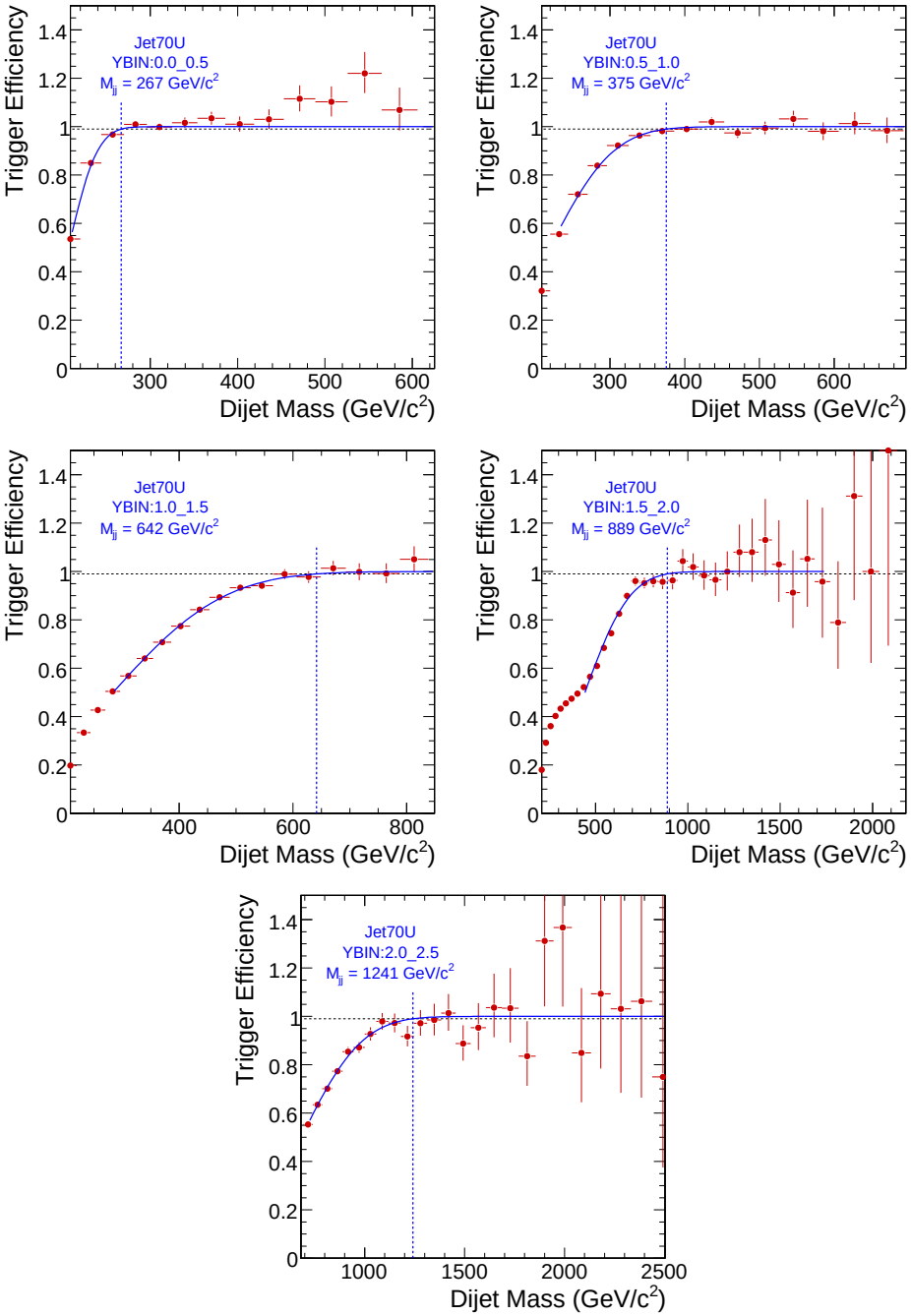

Figure 5.2. Relative trigger efficiencies as a function of dijet mass for the five different $|y|_{max}$ bins and for the HLT_Jet70U trigger. The 99% efficiency point is determined by performing a fit with an error function.

After determination of the 99% efficiency point from the fit, the starting value of the next dijet mass bin is considered as the lower limit for the group obtained from that sample. It should be noted that all these turn-on curves are relative to the lower threshold trigger of the same kind, and they are adequate to construct a smooth and continuous spectrum. However, for an absolute efficiency, it should be checked with an orthogonal trigger. Such a measurement is shown in Figure 5.3 and it is found to be 100% efficient.

In Tables 5.5 to 5.9 number of events that have survived after each cut (event cut flow) is shown in all $|y|_{max}$ bins.

Table 5.5. Event cut flow for the Jet30U sample.

Cut	[0.0-0.5]	[0.5-1.0]	[1.0-1.5]	[1.5-2.0]	[2.0-2.5]
$\|y\|_{max}$	107989	351063	506990	623448	769297
p_T	107795	345634	485850	579603	687070
Trigger efficiency cut	22290	38568	6728	3564	5903
JetID	22282	38558	6722	3563	5901

Table 5.6. Event cut flow for the Jet50U sample.

Cut	[0.0-0.5]	[0.5-1.0]	[1.0-1.5]	[1.5-2.0]	[2.0-2.5]
$\|y\|_{max}$	119591	461123	766864	949419	1082527
p_T	119591	461123	766570	946585	1073452
Trigger efficiency cut	52729	66816	22539	12798	11319
JetID	52704	66791	22505	12796	11315

Table 5.7. Event cut flow for the Jet70U sample.

Cut	[0.0-0.5]	[0.5-1.0]	[1.0-1.5]	[1.5-2.0]	[2.0-2.5]
$\|y\|_{max}$	177399	565583	775226	875831	900091
p_T	177398	565576	775176	875581	899180
Trigger efficiency cut	58564	53252	14799	9019	4326
JetID	58528	53230	14752	9017	4325

Table 5.8. Event cut flow for the Jet100U sample.

Cut	[0.0-0.5]	[0.5-1.0]	[1.0-1.5]	[1.5-2.0]	[2.0-2.5]
$\|y\|_{max}$	79057	275526	402864	442696	399093
p_T	79057	275525	402847	442676	399062
Trigger efficiency cut	26823	39238	8799	7820	1263
JetID	26804	39210	8743	7816	1261

Table 5.9. Event cut flow for the Jet140U sample.

Cut	[0.0-0.5]	[0.5-1.0]	[1.0-1.5]	[1.5-2.0]	[2.0-2.5]
$\|y\|_{max}$	66032	212202	297779	318654	265268
p_T	66032	212199	297767	318631	265250
Trigger efficiency cut	16781	18257	4437	1171	251
JetID	16765	18239	4385	1170	251

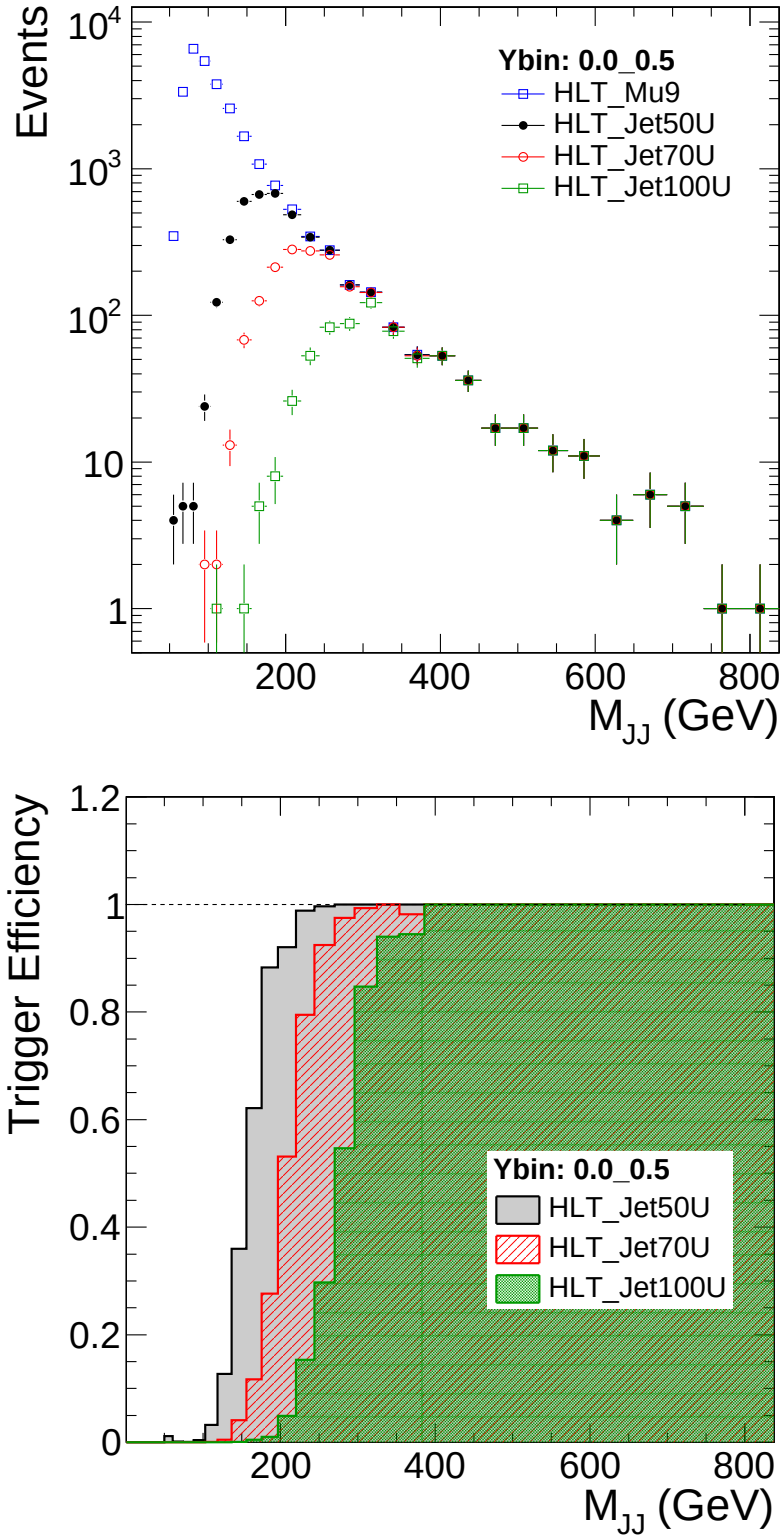

Figure 5.3. Trigger efficiencies measured with respect to the HLT_Mu9 trigger.

5.3. Data Quality

5.3.1. Data and Monte Carlo Simulation Comparisons

In order to examine and study the quality of our data and robustness of the event and jet selection, comparisons of event related and jet related variables with their Monte Carlo simulated predictions are performed. A lack of quality might be originated from the beam and detector related noise, detector pathologies, catastrophic reconstruction failures etc. As it was pointed before, two categories of distributions are examined; event related variables and jet related variables. The examined event related variables are;

- The ratio of the missing transverse energy in the event to the total transverse energy, $E_T^{miss}/\sum E_T$
- The azimuthal angle between the two leading jets, $\Delta\phi = \phi_1 - \phi_2$
- The polar angle between the colliding partons and the scattered partons at the center-of-mass frame, $cos(\theta^*) = tanh(y_1 - y_2)$

The first variable $E_T^{miss}/\sum E_T$ is sensitive to the detector originated noise which would end up with a significant energy imbalance in the event. Therefore, in the presence of noise, higher values of this variable is expected to be populated in the distribution. The second variable, $\Delta\phi = \phi_1 - \phi_2$, is sensitive to both a general noise in the detector and a particular noise which could mimic a jet. In that case this value is expected to be away from the $\Delta\phi = \pi$ expectation. The third variable, $cos(\theta^*)$, is also sensitive to a general noise in the detector and it shows the deviation from the expected value which might indicate a pathology in the data sample. In Figures 5.4-5.6 the comparisons between the data and simulated events for the Jet70U sample in five $|y|_{max}$ bins are shown. The rest of the plots can be found in Appendix B. All distributions for the data are in agreement with the simulated ones and no significant deviations from the expectations are observed.

Secondly, the following jet properties are examined;

- The charged hadron fraction, representing mostly the $\pi^{\pm}$ jet content
- The neutral hadron fraction, representing mostly the n jet content
- The neutral electromagnetic fraction, representing mostly the π^0 and the photons

If there were noise in the hadronic calorimeter (HCAL), we would observe an excess of events in the neutral hadron fraction distribution of the data with respect to simulated events (MC). Similarly, if there were noise in the electromagnetic calorimeter, we would observe an excess of events in the neutral electromagnetic fraction distribution of the data with respect to simulated events (MC). In Figures 5.7-5.9 the distributions of these jet variables are shown for Jet70U sample and all the rest of the plots for different samples can be found in Appendix C. In general, a very good agreement between the data and the simulated events is observed. Moreover, comparisons of jet kinematic quantities (p_T , η, ϕ) between the data and the MC events were studied, and they are shown in Figures 5.10-5.12 for Jet70U sample in all five $|y|_{max}$ bins. Again, a good agreement between the data and the simulated events is observed except for the ϕ distributions. This significant difference which pronounce itself as an asymmetry is due to the HCAL mis-calibration. A bias in the calibration scheme tends to over-calibrate jets in the $(-\pi, 0)$ azimuthal range. Jets in this region are more likely to be the first leading one in p_T and whenever a jet, originally the second leading one, is promoted to the first leading one by the mis-calibration, the actual first leading one becomes the second one automatically on the other side. As a result, the asymmetry arise in the ϕ distributions of the jets. This property has an effect on jet resolution making it worse in the data than it is expected from the MC study and dealt with as a systematic uncertainty.

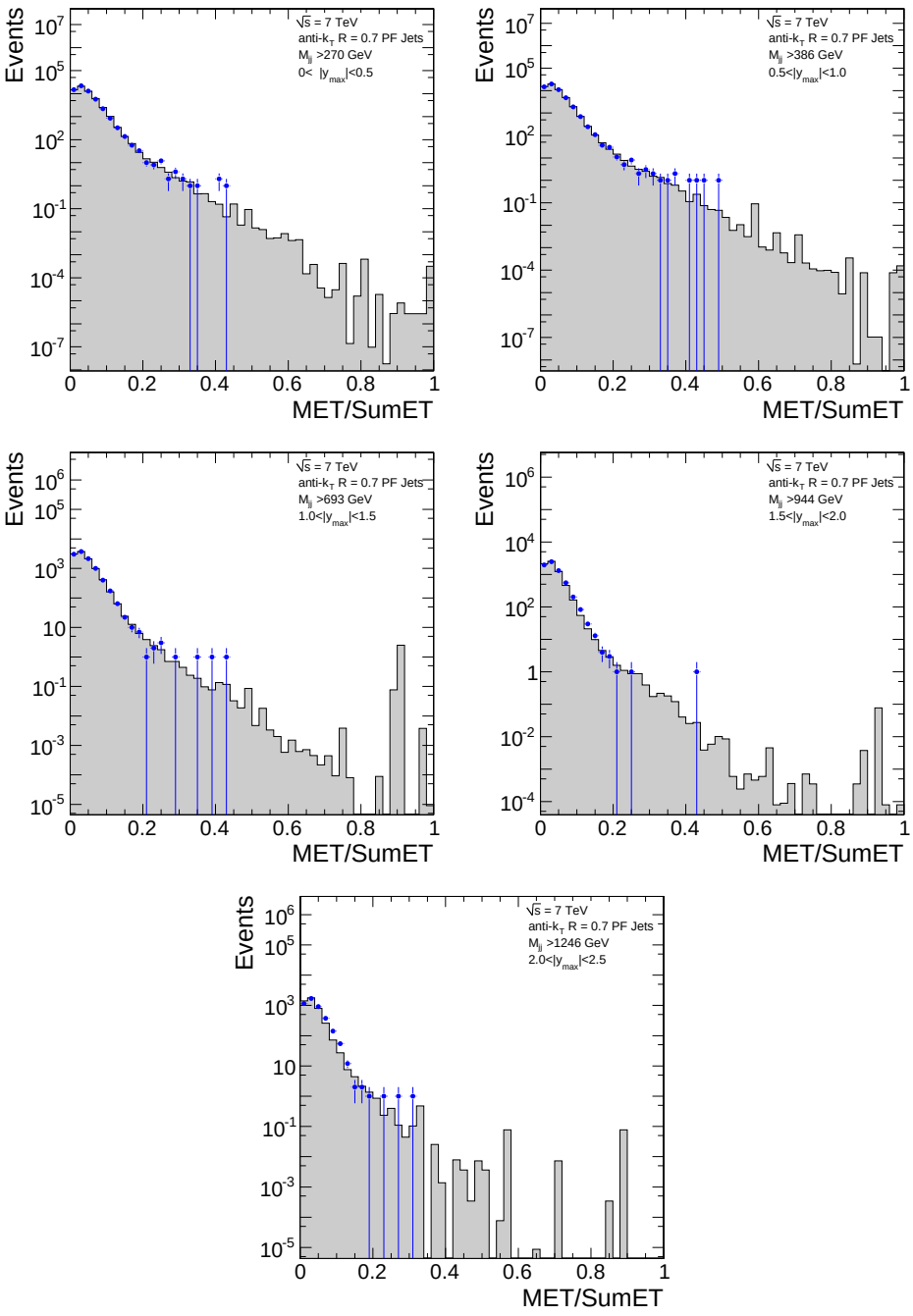

Figure 5.4. Ratio of the transverse missing energy to the total transverse energy of the event for the five different $|y|_{max}$ bins and for the Jet70U sample. The plots for data (points) and simulated (dashed histogram) events are compared.

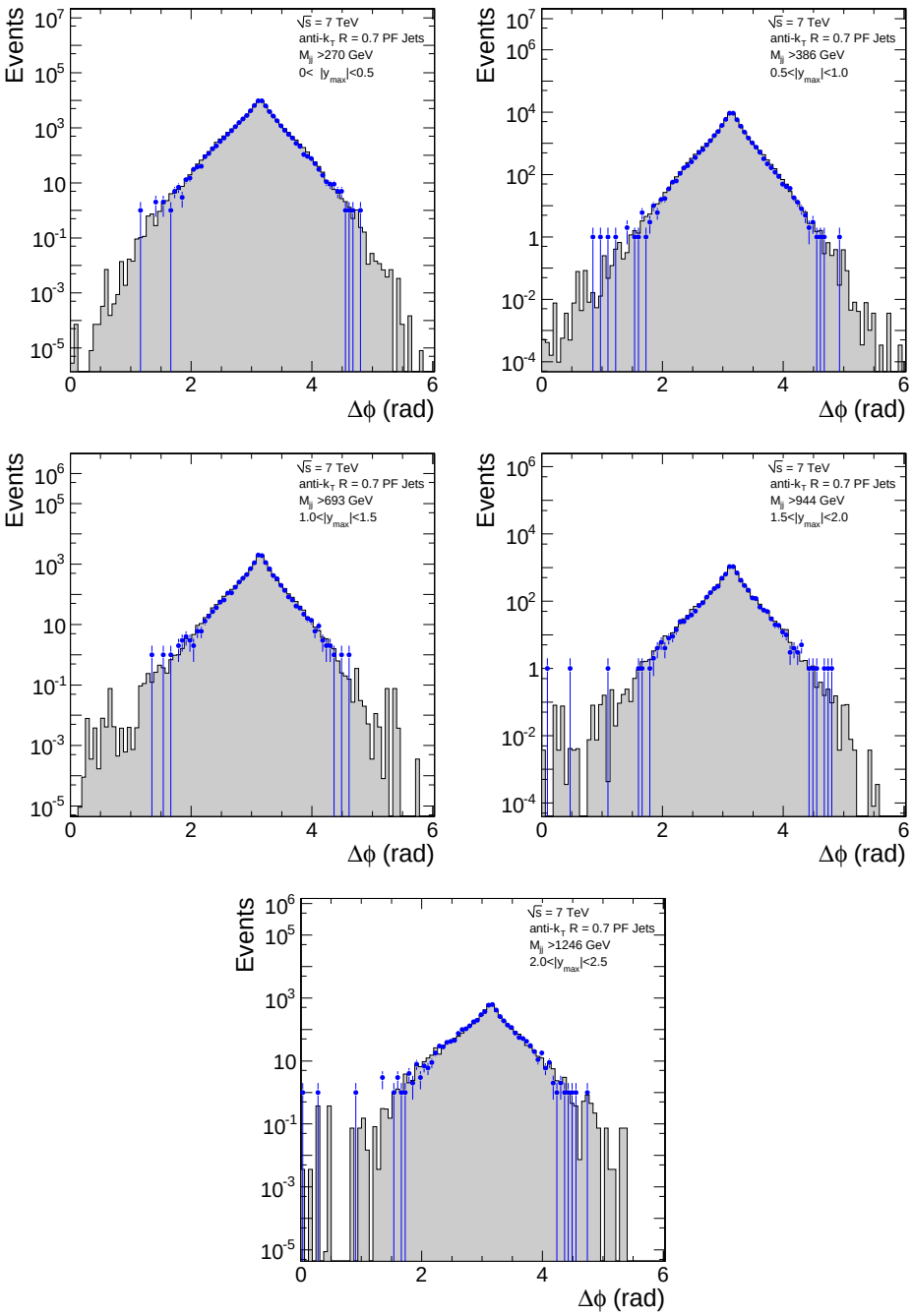

Figure 5.5. The angle between the two leading jets, $\Delta\phi$ for the five different $|y|_{max}$ bins and for the Jet70U sample. The plots for data (points) and simulated (dashed histogram) events are compared.

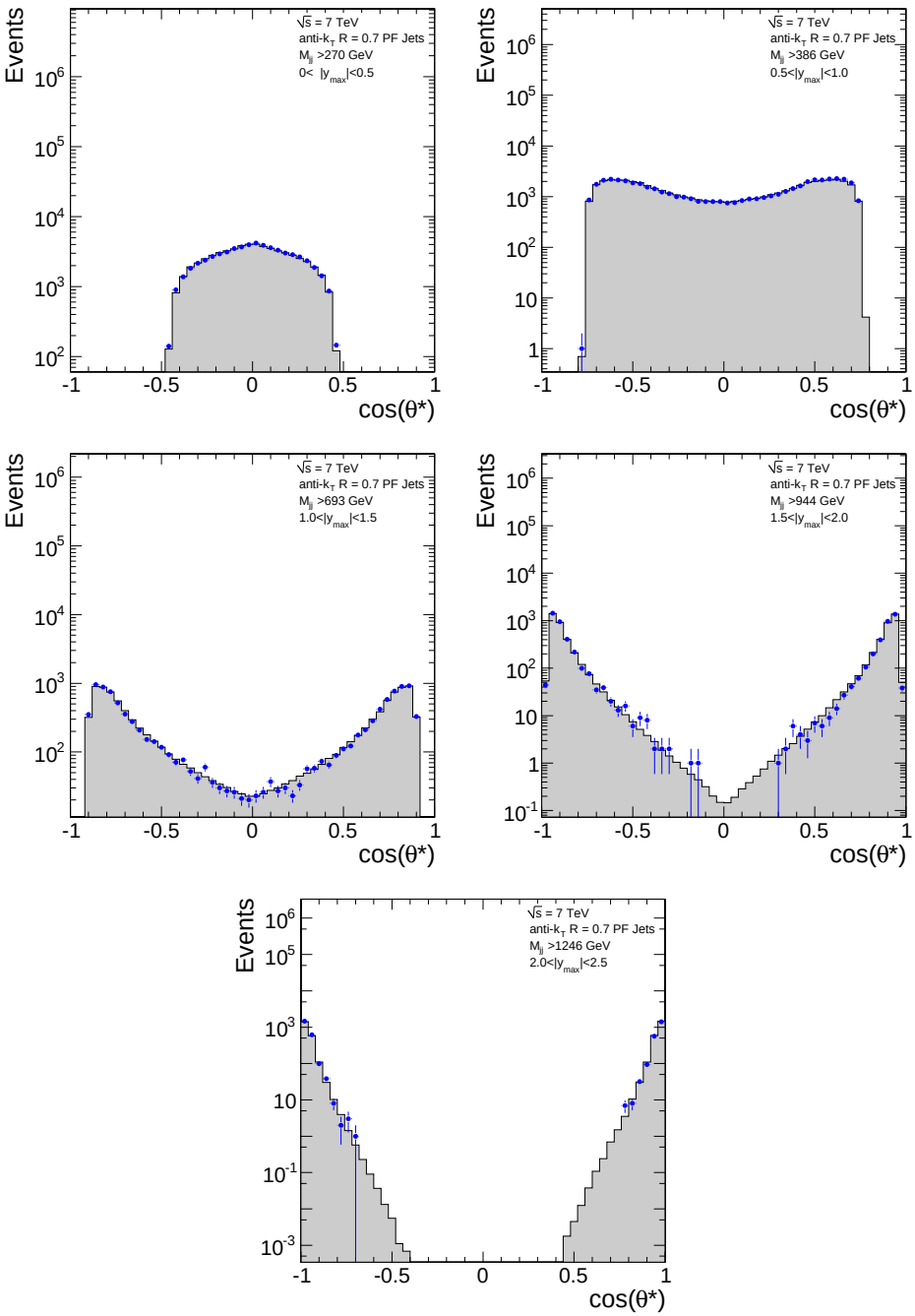

Figure 5.6. The angle between beam axis and the dijet system at the center-of-mass frames, $cos(\theta^*)$, for the five different $|y|_{max}$ bins and for the Jet70U sample. The plots for data (points) and simulated (dashed histogram) events are compared.

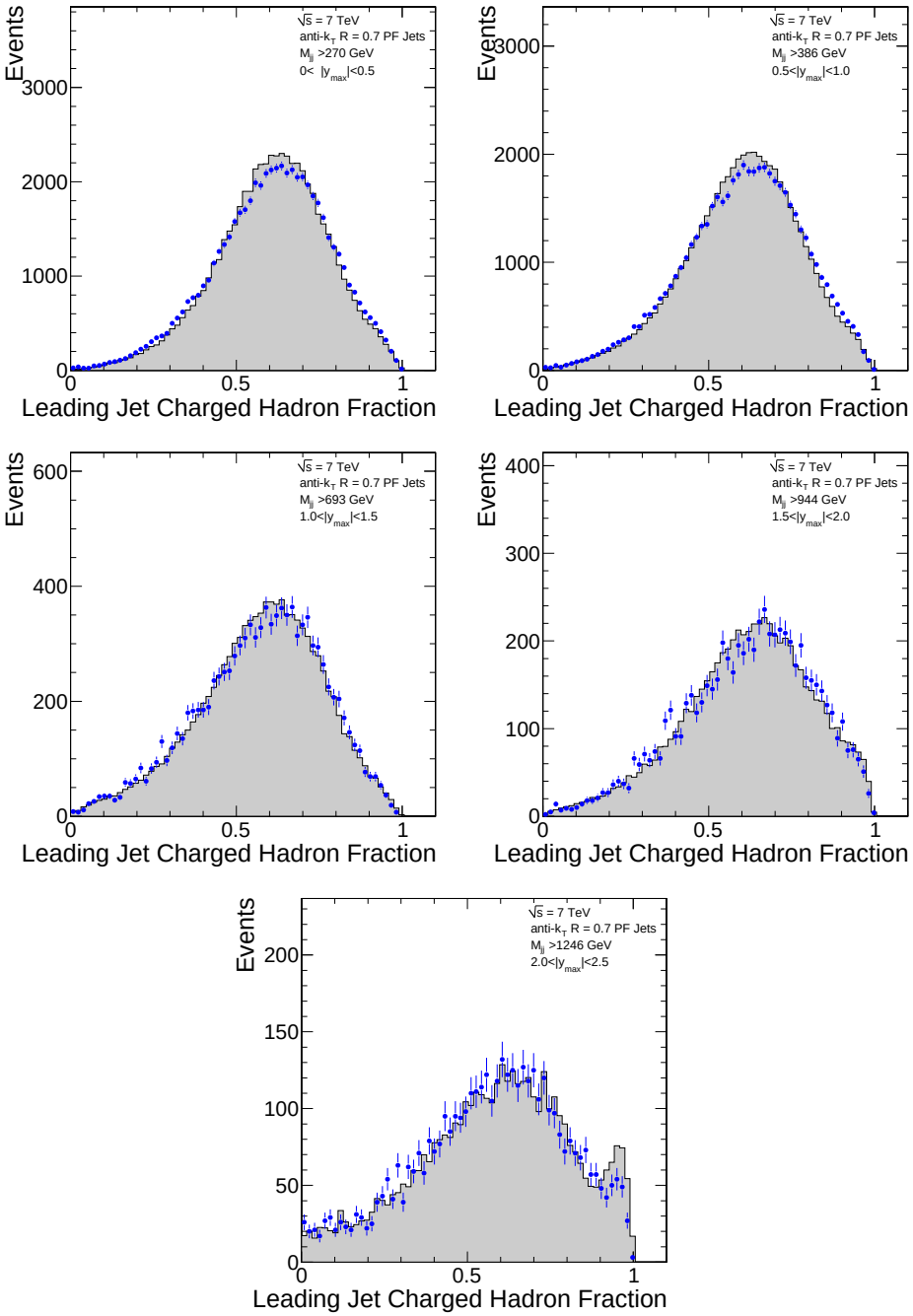

Figure 5.7. The charged hadron fraction of the leading jet for the five different $|y|_{max}$ bins and for the Jet70U sample. The plots for data (points) and simulated (dashed histogram) events are compared.

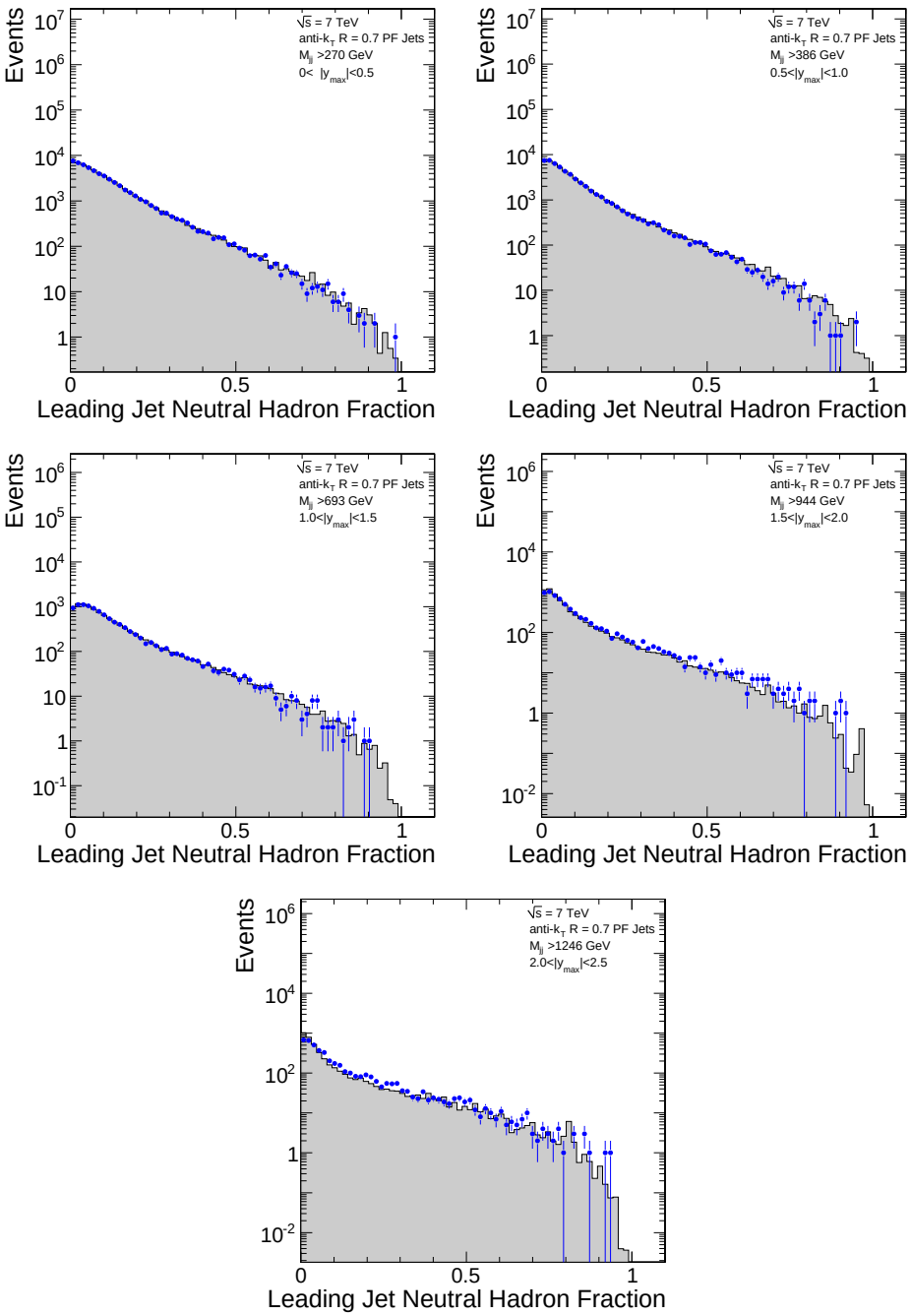

Figure 5.8. The neutral hadron fraction of the leading jet for the five different $|y|_{max}$ bins and for the Jet70U sample. The plots for data (points) and simulated (dashed histogram) events are compared.

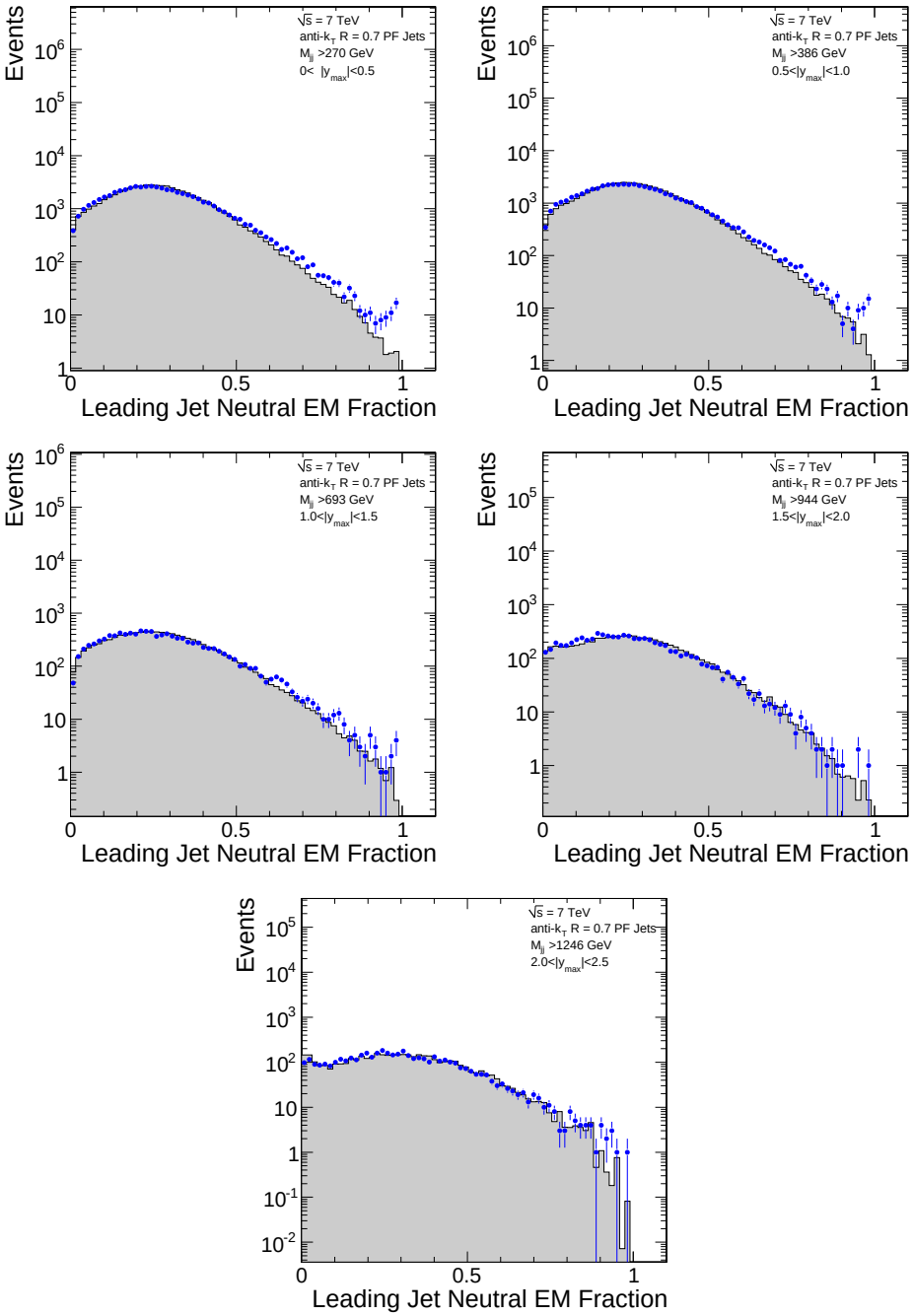

Figure 5.9. The neutral electromagnetic fraction of the leading jet for the five different $|y|_{max}$ bins and for the HLT_Jet70U sample. The plots for data (points) and simulated (dashed histogram) events are compared.

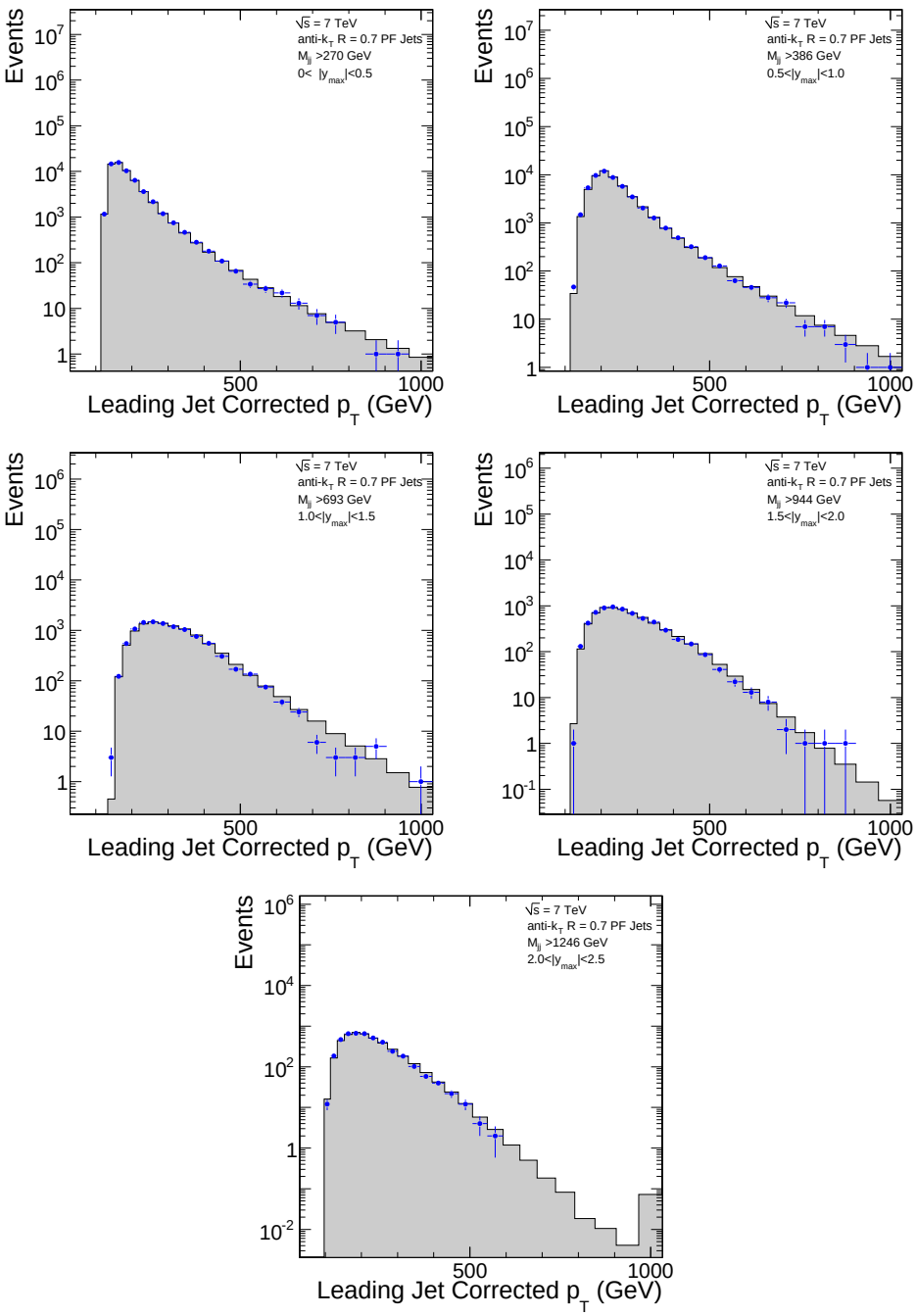

Figure 5.10. The p_T of the leading jet for the five different $|y|_{max}$ bins and for the Jet70U sample. The plots for data (points) and simulated (dashed histogram) events are compared.

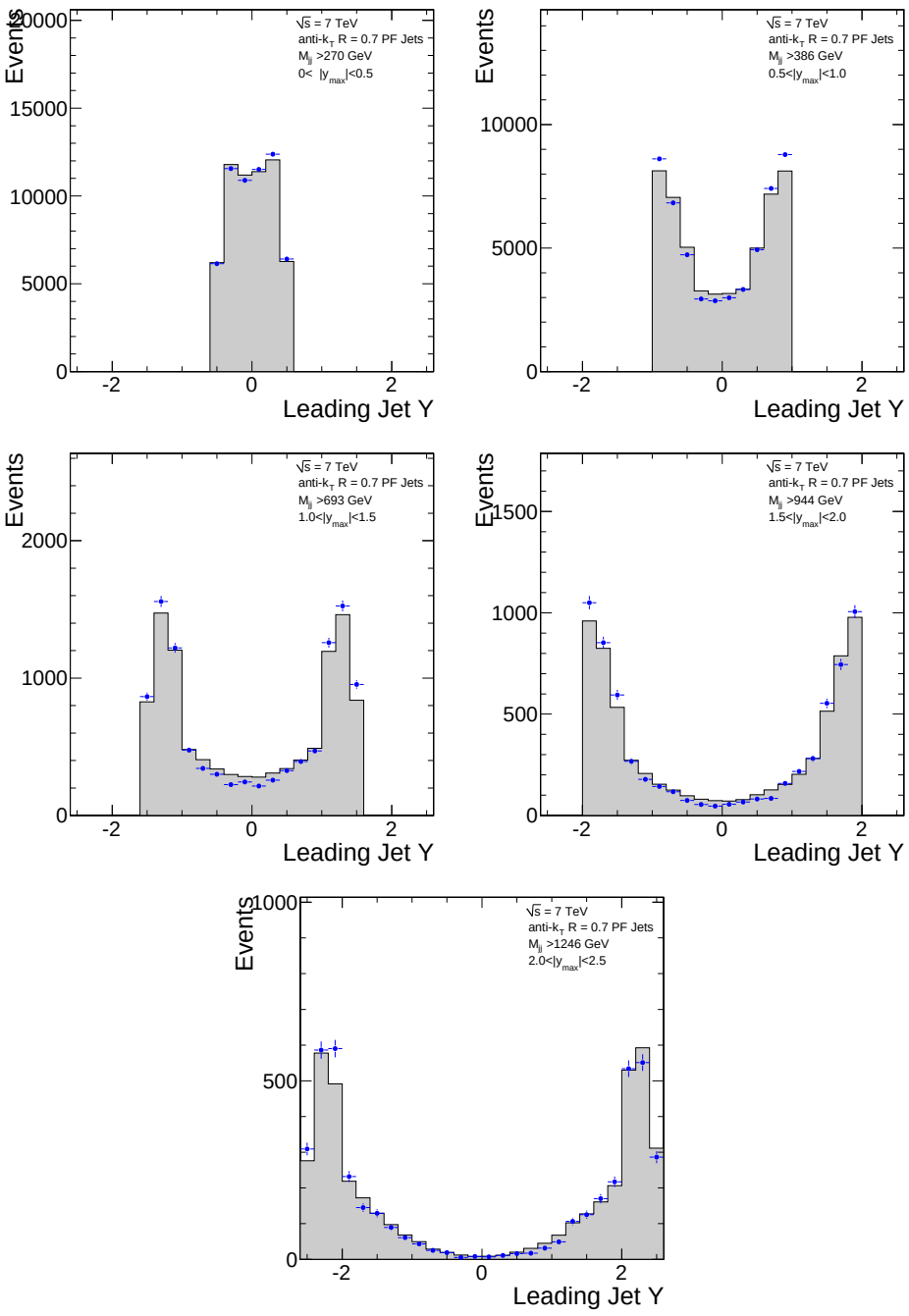

Figure 5.11. The η of the leading jet for the five different $|y|_{max}$ bins and for the Jet70U sample. The plots for data (points) and simulated (dashed histogram) events are compared.

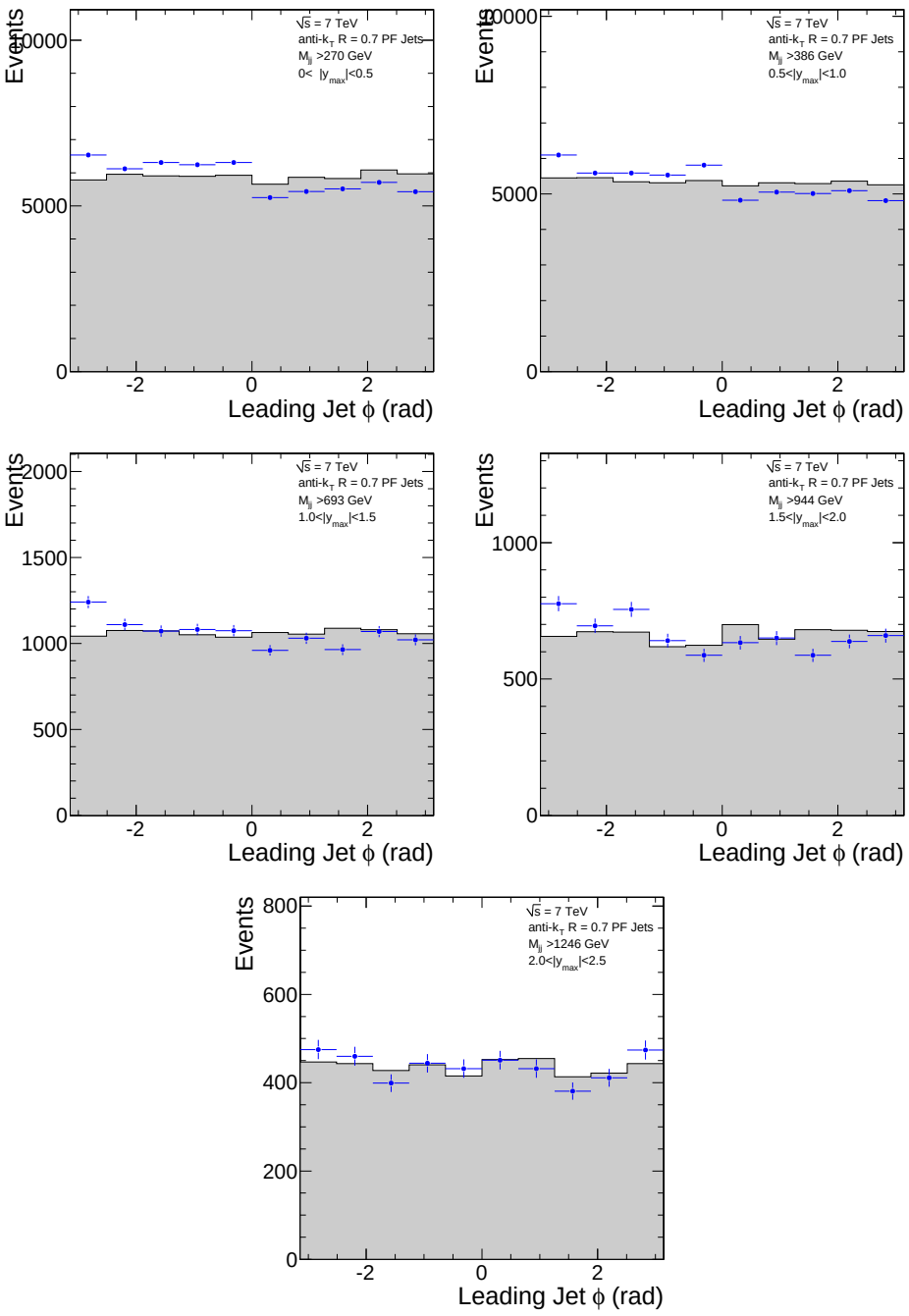

Figure 5.12. The ϕ of the leading jet for the five different $|y|_{max}$ bins and for the Jet70U sample. The plots for data (points) and simulated (dashed histogram) events are compared.

5.3.2. Stability Over the Run Period

All the checks presented in the previous section indicate that there are no significant pathologies in the data or an abnormal effect which is not modeled in the simulation. However, the time evolution of these basic data quantities should be checked in order to ensure that the quality of the recorded and selected data is stable during the run period. For that, all of the quantities introduced in the previous section have been examined as a function of the run number which is a time stamp in a sense.

In Figure 5.13 the leading and second jet p_T for the Jet70U sample as a function of time (ordered run numbers and shown starting from 0 regardless of the actual run number for each plot) were shown for the runs with an integrated luminosity greater than 9 pb^{-1}, and then are fitted with a first degree polynomial The fit is consistent with the constant term and the slope is not statistically significant for all different $|y|_{max}$ bins which is an indication of a stable behavior. A stable behavior as a function of run number is again observed when examining the jet particle content plots, shown in Figures 5.14-5.16. As it was observed for the jet p_T, the fit is consistent with the constant term and the slope is not statistically significant for all different $|y|_{max}$ bins which is an indication of a stable behavior. The plots for the rest of the samples are shown in Appendix D.

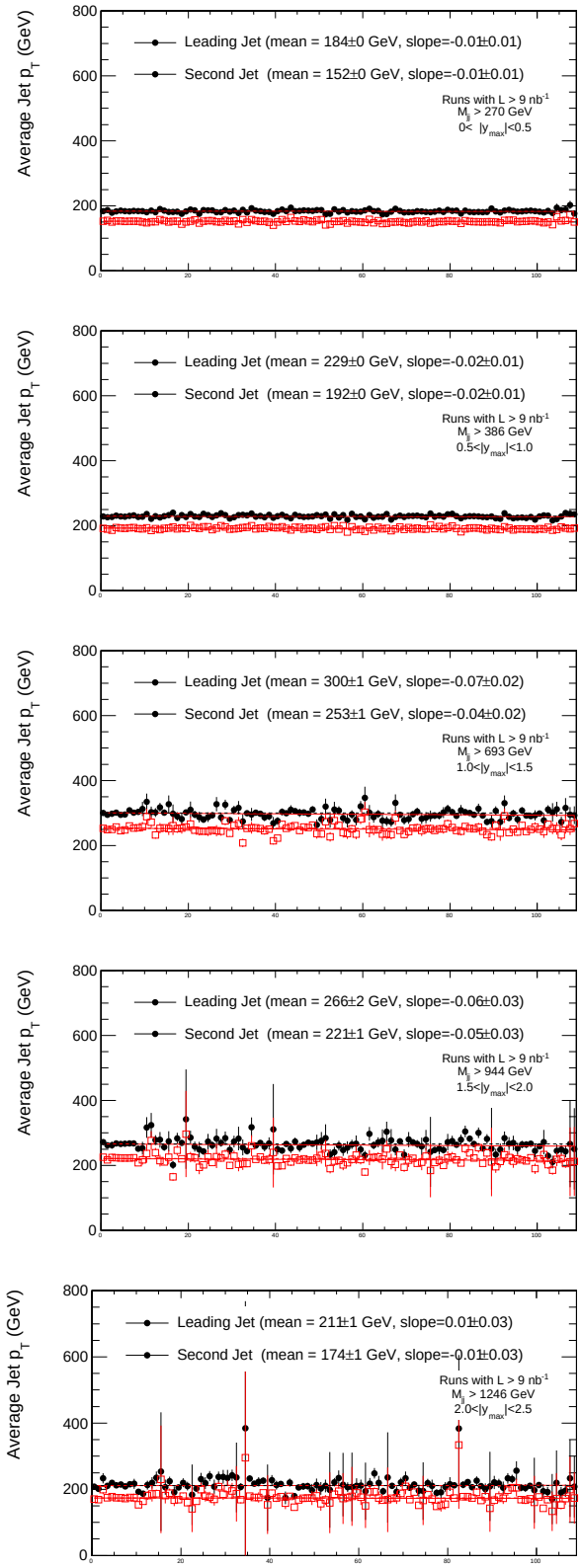

Figure 5.13. The p_T of the leading and second jet for the five different $|y|_{max}$ bins and for the Jet70U sample as a function of time (run number), fitted with a first degree polynomial.

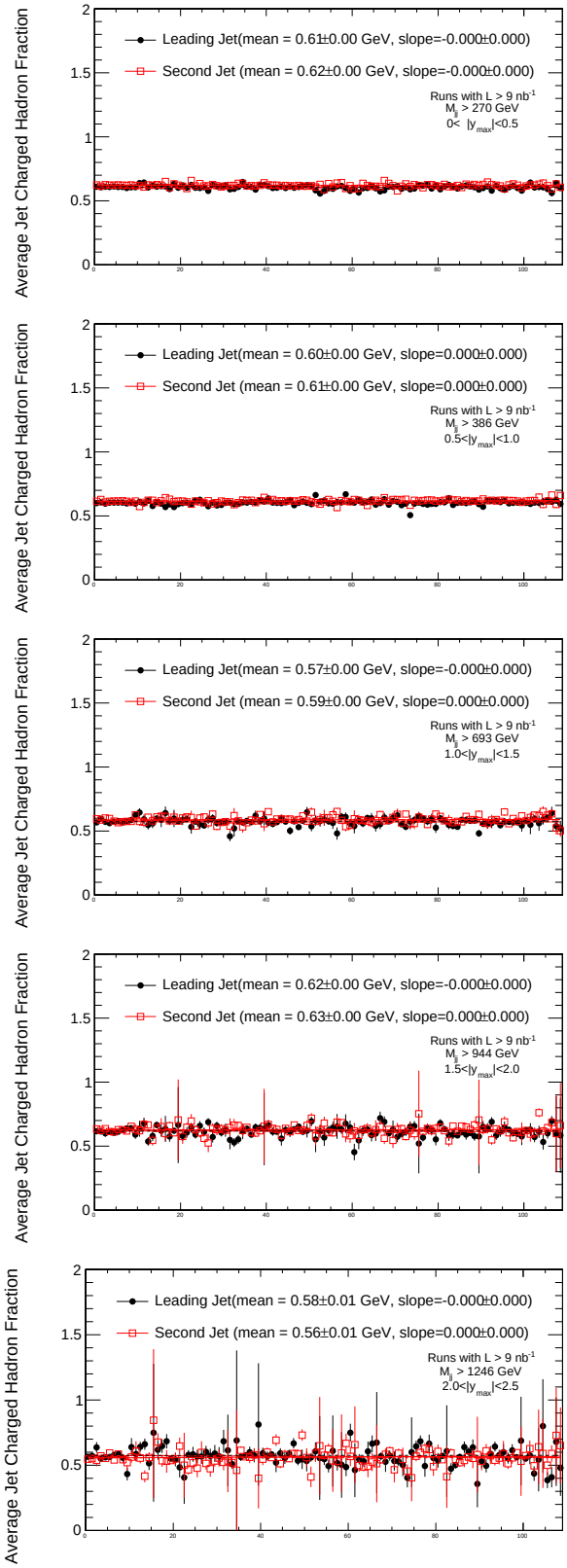

Figure 5.14. The charged hadron fraction of the leading and second jet for the five different $|y|_{max}$ bins and for the Jet70U sample as a function of time (run number), fitted with a first degree polynomial.

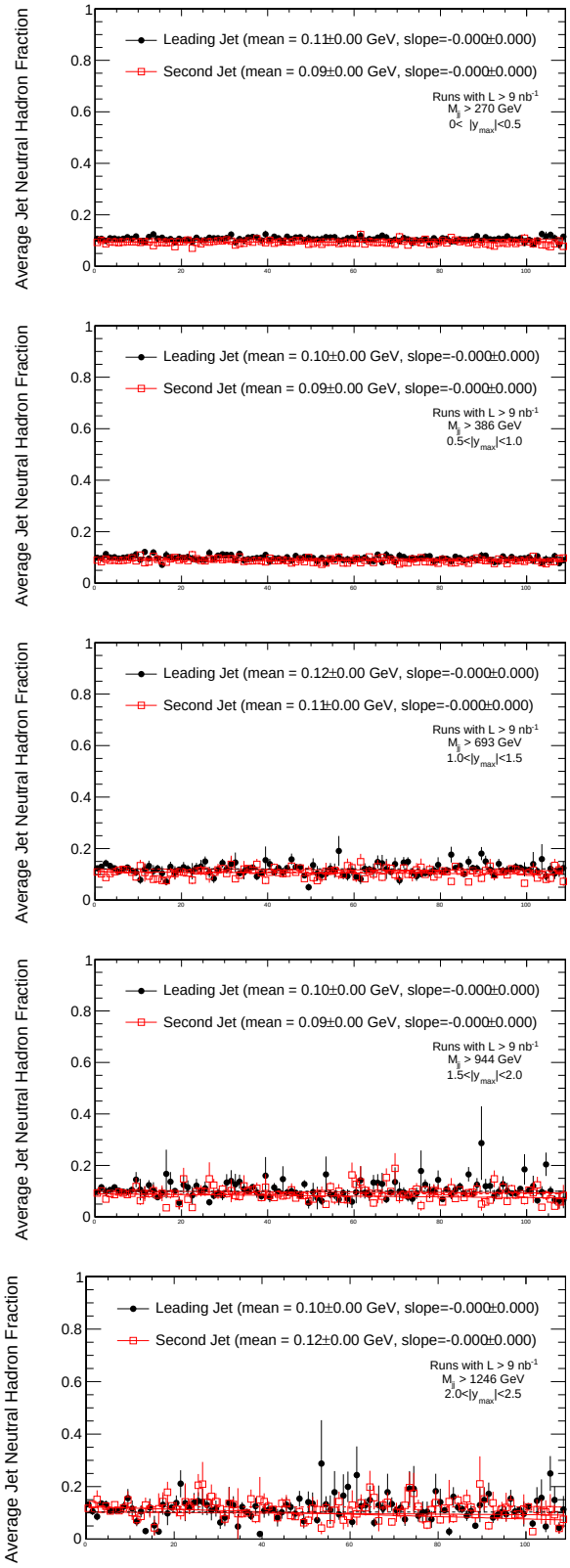

Figure 5.15. The neutral hadron fraction of the leading and second jet for the five different $|y|_{max}$ bins and for the Jet70U sample as a function of time (run number), fitted with a first degree polynomial.

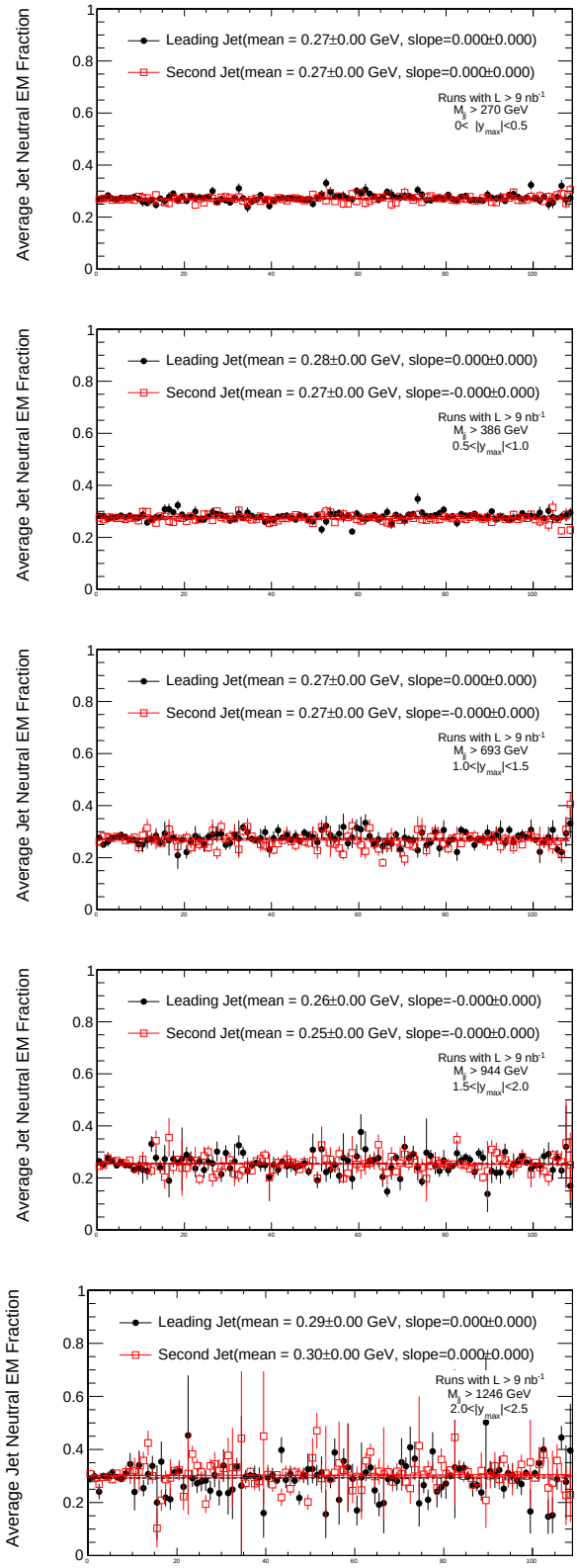

Figure 5.16. The neutral electromagnetic fraction of the leading and second jet for the five different $|y|_{max}$ bins and for the Jet70U sample as a function of time (run number), fitted with a first degree polynomial.

5.4. Jet Energy Corrections

A jet that is reconstructed and measured by the detector signals (reconstructed jet) has the energy usually different than that of the corresponding particle jet (generated jet). The generated jet is obtained from the Monte Carlo simulation by clustering - using the same jet reconstruction algorithm - the stable colorless particles arising at the end of the hadronization process which presumably occurs after the hard interaction. The reason for this energy to be different in the reconstructed jet than the generated jet is the non-uniform and non-linear response of the CMS calorimeters. Moreover, electronic noise and multiple proton-proton interactions in the same bunch crossing (pile-up events) can cause this extra amount of energy. The goal of the jet energy calibration is to find the relation between the energy measured in the detector jet and that of the corresponding particle jet. After finding the relation, a correction factor can be applied to each component of the jet momentum four-vector as a multiplicative factor $C(p_T^{raw}, \eta)$ [35] (the index μ represents the components of four-vector).

$$P_\mu^{corrected} = C(p_T^{raw}, \eta) \cdot P_\mu^{raw} \tag{5.5}$$

In order to achieve this correction, CMS had adopted a successive factorized approach [36]. The order of the sequence is as follows ;

1. *Offset*: Correction for pile-up, electronic noise, and jet energy lost by thresholds.
2. *Relative(η)*: Correction for variations in jet response with pseudo-rapidity relative to a control region.
3. *Absolute (p_T)*: Correction to particle level versus jet p_T in the control region.
4. *EMF*: Correction for variations in jet response with electromagnetic energy fraction.
5. *Flavor*: Correction to particle level for different types of jet (light quark, c, b, gluon)
6. *Underlying Event*: Luminosity independent underlying event energy in jet removed.
7. *Parton*: Correction to parton level.

Figure 5.17. Schematic picture of a factorized multi-level jet correction, in which corrections to the reconstructed jet are applied in sequence to obtain the final calibrated jet. Required correction levels are shown in solid boxes and optional correction levels are shown in dashed boxes.

5.4.1. Offset Corrections

The first step of factorized correction sequence starts with the offset correction which aims to estimate and subtract the extra amount of energy from the jet. This extra unwanted energy has presumably nothing to do with high-p_T scattering of partons. It includes contributions from the detector noise and from the multiple proton interactions (pile-up) in the same bunch crossing. For studying the noise, events are first collected with Zero Bias trigger (a random trigger with no conditions) and events with Minimum Bias trigger (a trigger requiring coincident hits in the Beam Scintillating Counters) are discarded. Since the Minimum Bias trigger is a sign of proton-proton interaction at a given bunch crossing, the remaining sample after the removal can be considered as a pure noise sample. In order to account for one additional event, Minimum Bias triggered events from the early runs are selected. In the early runs, the average number of proton-proton interaction per event is less than one, hence, a sample with Minimum Bias triggered events from the early runs can be taken as noise+one event sample. Figure 5.18 shows the $E_{offset}(\eta)$ and $p_{Toffset}(\eta)$ distributions for noise and noise+one pile-up samples. The contribution from the noise is less than 250 MeV and from the noise+one pile-up is less than 400 GeV in p_T. It increases up to 7 GeV in energy in the very forward region.

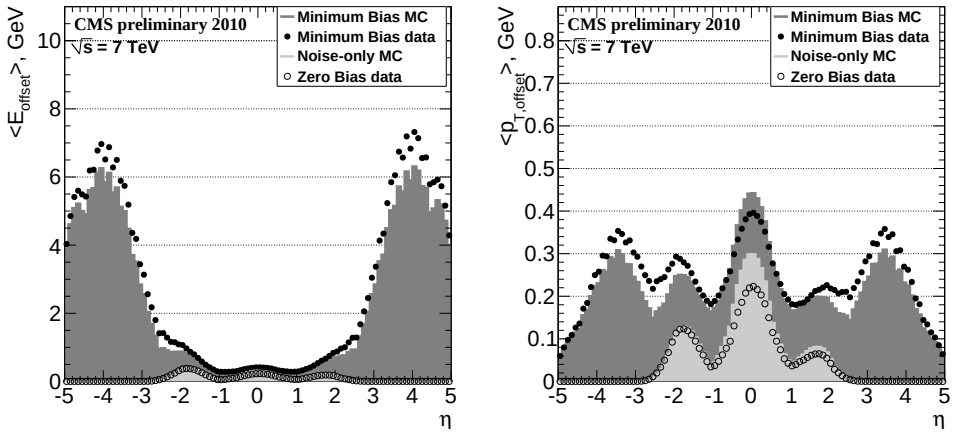

Figure 5.18. Offset contribution from the noise only and noise+one pile-up as function of η in energy (left) and transverse momentum (right) [37].

5.4.2. Relative Corrections: η Dependence

For a given true p_T of the jet, the CMS detector's response changes as a function of η. The relative correction aims to make this dependence flat in η and it should be applied after the offset correction. The derivation of the relative energy corrections employs the dijet p_T balance technique which is first used at SPPS [38], and later improved in the Tevatron experiments [39, 40]. The idea is to use p_T balance in back-to-back dijet events with one barrel jet in the central control region of the calorimeter, $|\eta| < 1.3$, and the other probe jet at arbitrary η. The $|\eta| < 1.3$ region is chosen as reference since the detector response to jets is uniform in this region [**?**]. The two leading jets must be separated by $\Delta\phi > 2.7$ and no additional third jet in the event with $p_T^{3^{rd}jet}/p_T^{dijet}$ >0.2 is allowed to increase the fraction of 2→2 processes in the sample, where $p_T^{dijet} = (p_T^{probe} + p_T^{barrel})/2$ is an average uncorrected p_T of two leading jets. The quality of the dijet balance is given by:

$$B = \frac{p_T^{probe} - p_T^{barrel}}{p_T^{dijet}} \tag{5.6}$$

The relative response in terms of the expectation value of B distribution, <B>, in a given η^{probe} and p_T^{dijet} bin is defined as below [41].

$$R(\eta^{probe}, p_T^{dijet}) = \frac{2+ < B >}{2- < B >} \tag{5.7}$$

The relative jet response as a function of η obtained from the data and the Monte Carlo prediction are shown in Figure 5.19 for different p_T^{dijet} ranges.

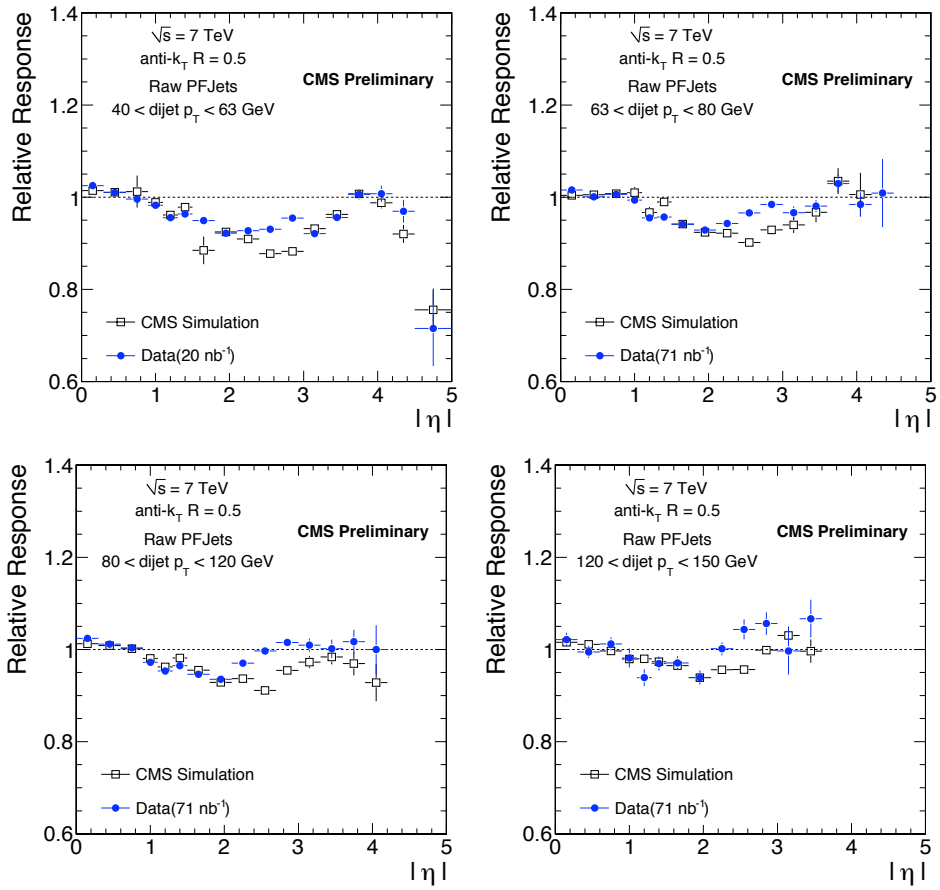

Figure 5.19. Relative jet response for PF jets as a function of η, for various p_T^{dijet} bins [37].

5.4.3. Absolute Corrections: p_T Dependence

Removal of the noise and pileup contributions and then making the response flat in η allows us to apply an absolute calibration in p_T by using the γ+jet events. There

are two methods for absolute calibration; p_T balancing method and the Missing E_T Projection Fraction (MPF) method [37]. The latter is the main method in CMS. In MPF method, the primary assumption is that the γ+ jet events have no real missing E_T. Therefore, there is a perfect balance between the photon and the hadronic recoil in transverse plane.

$$\vec{p}_T^{\,\gamma} + \vec{p}_T^{\,recoil} = 0 \tag{5.8}$$

In fact, this is the ideal case for the balance. In real life, the detector response should be taken into account, and the balance is usually satisfied by introducing a quantity called missing transverse energy ($\vec{E}_T^{\,missing}$). Thus, the Equation 5.8 can be rewritten for reconstructed events as;

$$R_\gamma \cdot \vec{p}_T^{\,\gamma} + R_{recoil} \cdot \vec{p}_T^{\,recoil} = -\vec{E}_T^{\,missing} \tag{5.9}$$

where R_γ and R_{recoil} are the detector responses to the photon and the hadronic recoil. The good calibration of photons enhances us to take R_γ=1, then solving above equations gives;

$$R_{MPF} \equiv \frac{R_{recoil}}{R_\gamma} = 1 + \frac{\vec{p}_T^{\,\gamma} \cdot \vec{E}_T^{\,missing}}{(p_T^\gamma)^2} = R_{recoil} \tag{5.10}$$

Figure 5.20 shows the $< p_T/p_\gamma >$ response of and MPF response as a function of photon p_T .

5.5. Corrections for the Smearing Effects

Due to the finite resolution of the detector, the measured spectrum, which is called *"at the detector level"*, is a smeared form of the actual distribution which is *"at the particle level"*. The smearing effect is considerable because of the very steep nature of the dijet mass spectrum. Each mass bin in the spectrum is contaminated by events that have migrated from neighboring bins and the original residents of the bin have a

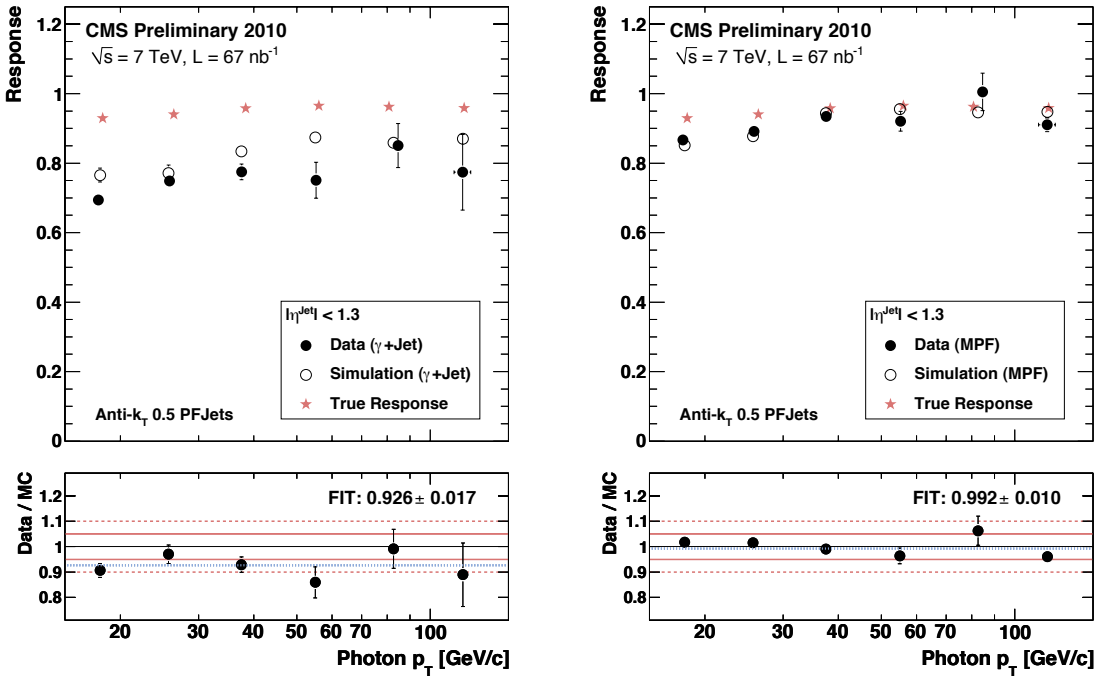

Figure 5.20. Response of $< p_T/p_\gamma >$ (left) and MPF response (right) as a function of photon p_T from data and simulation [37].

finite probability to migrate to the other bins depending on the detector resolution for the mass value at that bin. Since the event population of a bin with lower dijet mass value is far greater than the event population of a bin with higher dijet mass value, it is more likely for a bin with higher mass value to have a higher fraction of immigrant events. As a result of this fact, the measured spectrum is steeper than in the case that the resolution would be perfect. In Figure 5.21 a cartoon illustration of the smearing effect for a falling spectrum is shown.

The measured cross section can be modeled as the convolution of the particle level spectrum with the detector resolution:

$$F(m^{reco}) = \int_0^\infty f(m^{gen}) R(m^{reco}, m^{gen}) dm^{gen} \tag{5.11}$$

where m^{reco} and m^{gen} represent the measured mass value and the mass value at the particle level respectively.

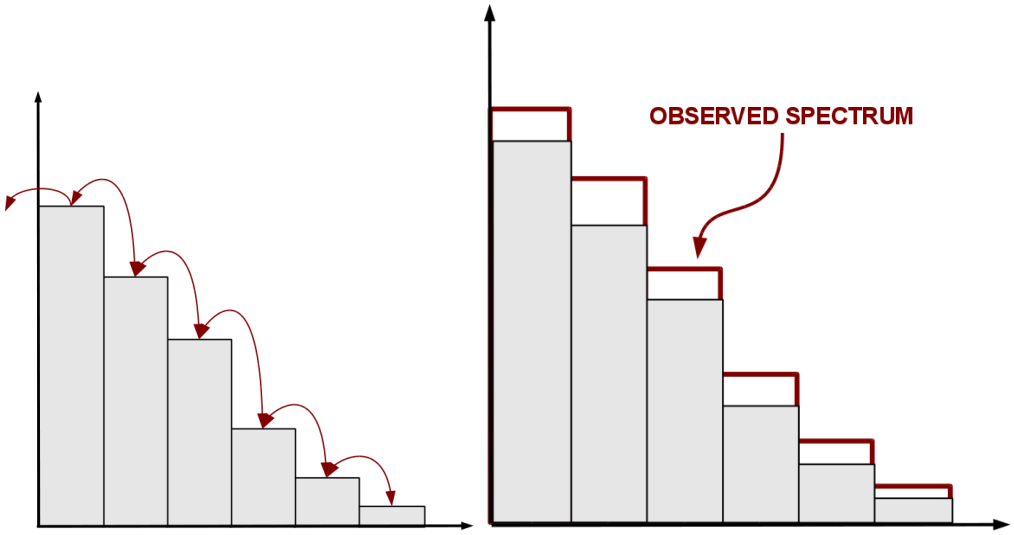

Figure 5.21. A cartoon illustration of smearing effects for a steeply falling distribution.

In order to estimate the size of the smearing effect, a technique called *"forward smearing"* is adopted. In this technique, dijet mass values at the particle level are generated randomly according to the spectrum predicted by PYTHIA6 then smeared with the response function which effectively simulates the detector effects on the generated value. The dijet mass resolution is modeled by a Gaussian function centered at the generated mass:

$$R(m^{reco}, m^{gen}) = \frac{1}{\sqrt{2\pi}\sigma(m^{gen})} \exp\left[-\frac{1}{2}\frac{m^2_{gen}}{\sigma^2(m^{gen})}\right] \tag{5.12}$$

The σ of the Gaussian is determined from the relative resolution parametrization. The details of the determination of resolution parameters will be discussed in the next section. Finally, the observed ("smeared") and the true ("generated") spectra are compared bin-to-bin in terms of the ratio of the bin contents, namely; $N_{true}/N_{observed}$. In Figure 5.22 the correction factors for unsmearing effect are shown for all five $|\mathrm{y}|_{max}$ bins and it can be observed that the ratio is close to the unity in all rapidity bins. The shape of the curves is closely related to the mass dependence of the resolution and the spectrum slope. At lower dijet mass values the resolution is relatively worse than it is at higher mass values and the effect of smearing is larger. At higher mass values, even if the resolution improves, the spectrum becomes steeper which leads again to

a larger smearing effect. Since the effect of smearing is small it allows us to attempt an average unfolding using the ratio $N_{True}/N_{Observed}$ as a multiplicative correction factor (bin-by-bin correction). It is understood that the more advanced and statistically sound treatments of the unfolding problem yield the correct statistical uncertainties, which are underestimated in the simple approach described here. However, the size of the effect is so small that the effect on the statistical uncertainty is negligible compared to the other systematic uncertainties of the measurement.

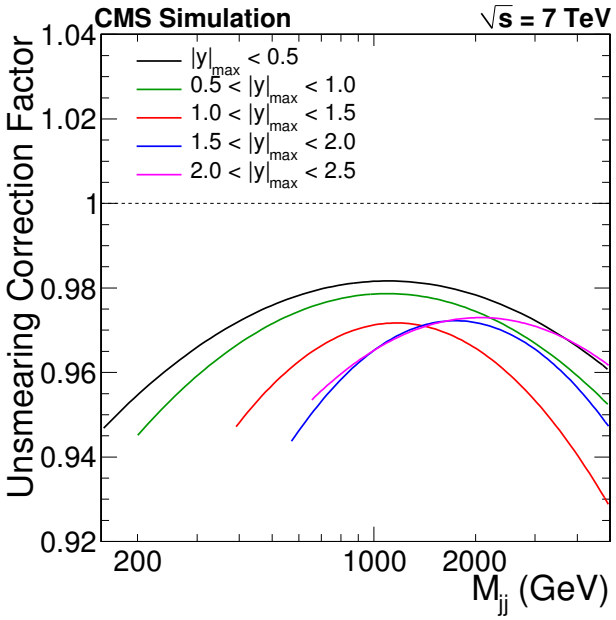

Figure 5.22. Unsmearing correction factors as a function of the dijet mass, in the various $|y|_{max}$ bins.

5.6. Dijet Mass Resolution

The dijet mass resolution is studied by using the full Monte Carlo simulation. The full Monte Carlo simulation means that the proton-proton collisions are simulated starting from the collision itself to the signals in the detector. These signals are reconstructed according to the reconstruction scheme. In simulated events, identical kinematic selection is applied to generated and reconstructed jets, and then the mass of two generated jets (m^{gen}) are compared to the mass of two reconstructed jets (m^{reco}). The quantity m^{reco}/m^{gen} (mass response) is recorded, in the bins of the generated dijet mass (Figure 5.23, left-side plot). The resulting distribution is projected onto the y-axis for a certain range of m^{gen} value then each projection is fitted with a Gaussian in the range of $\pm 1.5 \cdot RMS$ around the mean value. The extracted $\sigma\left(\frac{m^{reco}}{m^{gen}}\right)$ represents the relative mass resolution. At the end, the relative mass resolution as a function of m^{gen} is parametrized with a smooth continuous function of the following form:

$$\frac{\sigma(M^{gen})}{M^{gen}} = A + \frac{B}{(M^{gen})^{C}} \tag{5.13}$$

Figure 5.24 shows the quantity $\langle M/M^{gen} \rangle$ as a function of M^{gen} demonstrating that the reconstructed dijet mass agrees with the generated mass within 3%. Figure 5.25 shows the relative dijet mass resolution as a function of M^{gen}, fitted with the continuous function described above.

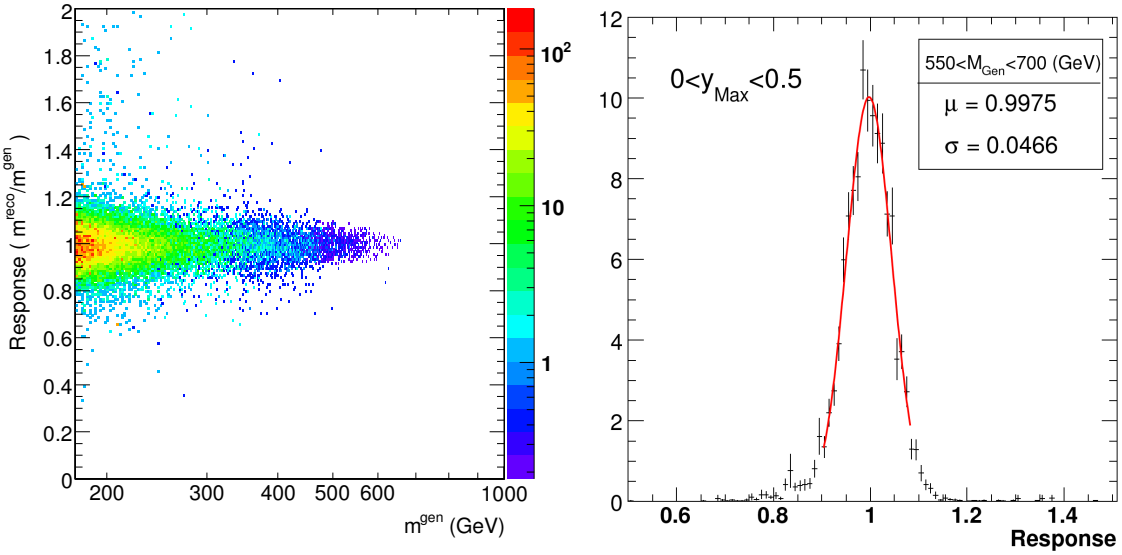

Figure 5.23. The response of the detector as a function of the generated mass in $0 < |y|_{max} < 0.5$ (left). The distribution of the ratio of the reconstructed dijet mass over the generated mass in $0 < |y|_{max} < 0.5$ bin, for 550 GeV$< M_{Gen} <$ 700 GeV (right).

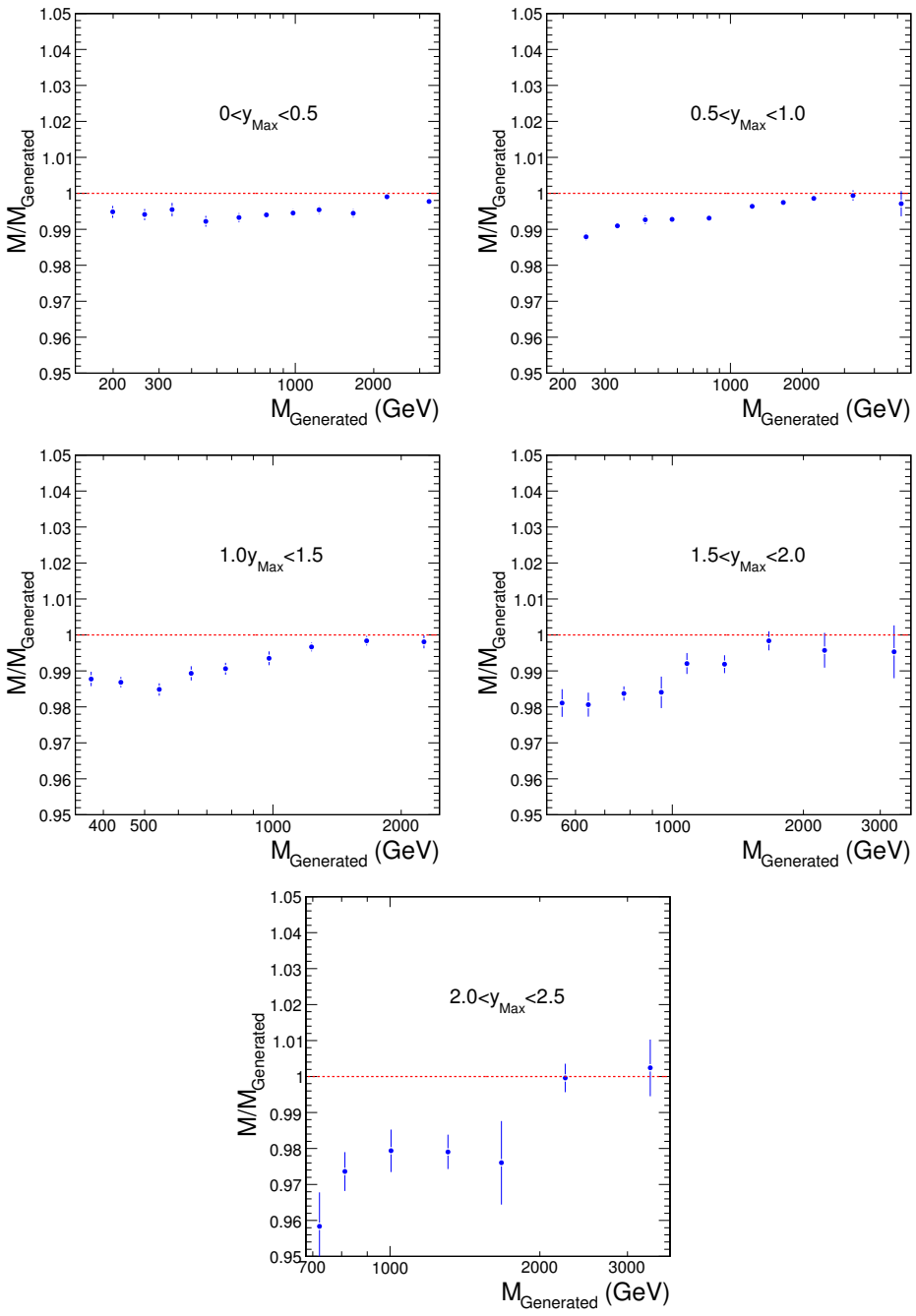

Figure 5.24. Average ratio of the reconstructed dijet mass over the generated mass in all $|y|_{max}$ bins.

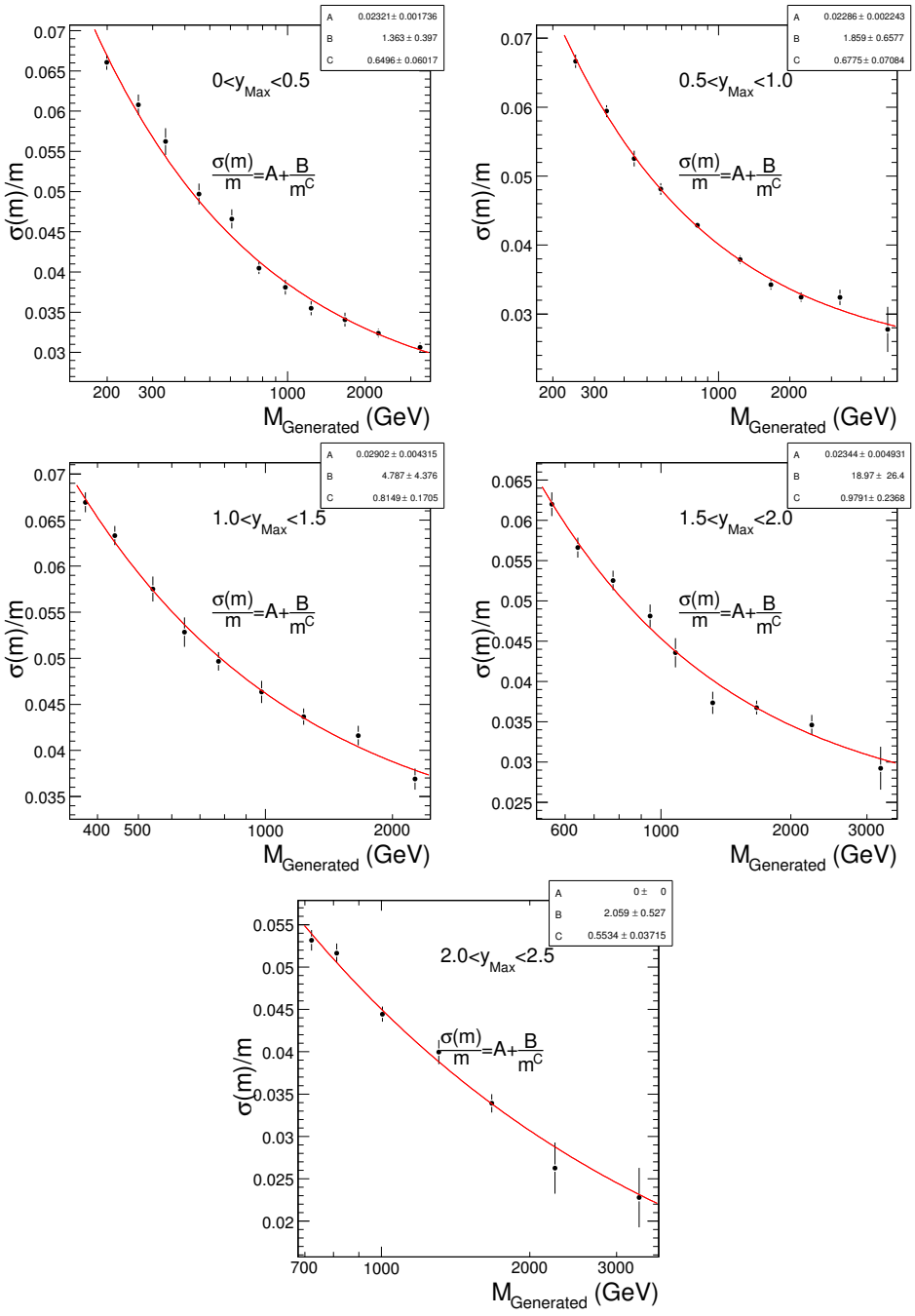

Figure 5.25. Relative dijet mass resolution, as a function of the generated mass in all $|y|_{max}$ bins.

5.7. Construction of the Dijet Mass Spectrum

Finally, the spectrum of the dijet invariant mass in each rapidity bin is constructed by all data samples by combining them according to the trigger efficiencies. In order to use the maximum available number of events, each mass bin is populated by one and only one sample which is at least 99% efficient and has the highest effective luminosity. The size of the dijet mass bins is approximately equal or larger than the width of the mass resolution at the bin center. Figure 5.26 shows how the data samples from different triggers are combined. At the end, the prescaled samples are scaled up by a number so that they match the rate of the un-prescaled sample. The resulting dijet mass spectra can be shown in Figure 5.27.

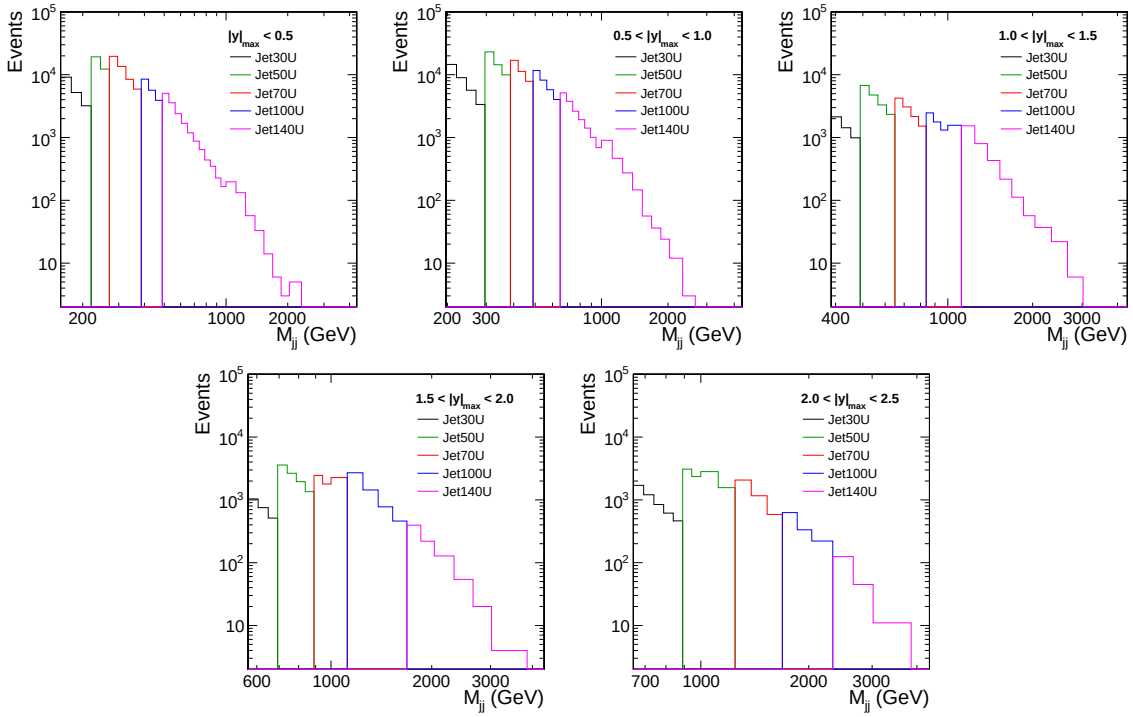

Figure 5.26. Event yield of the different samples. In each mass bin, only the contributing sample is shown.

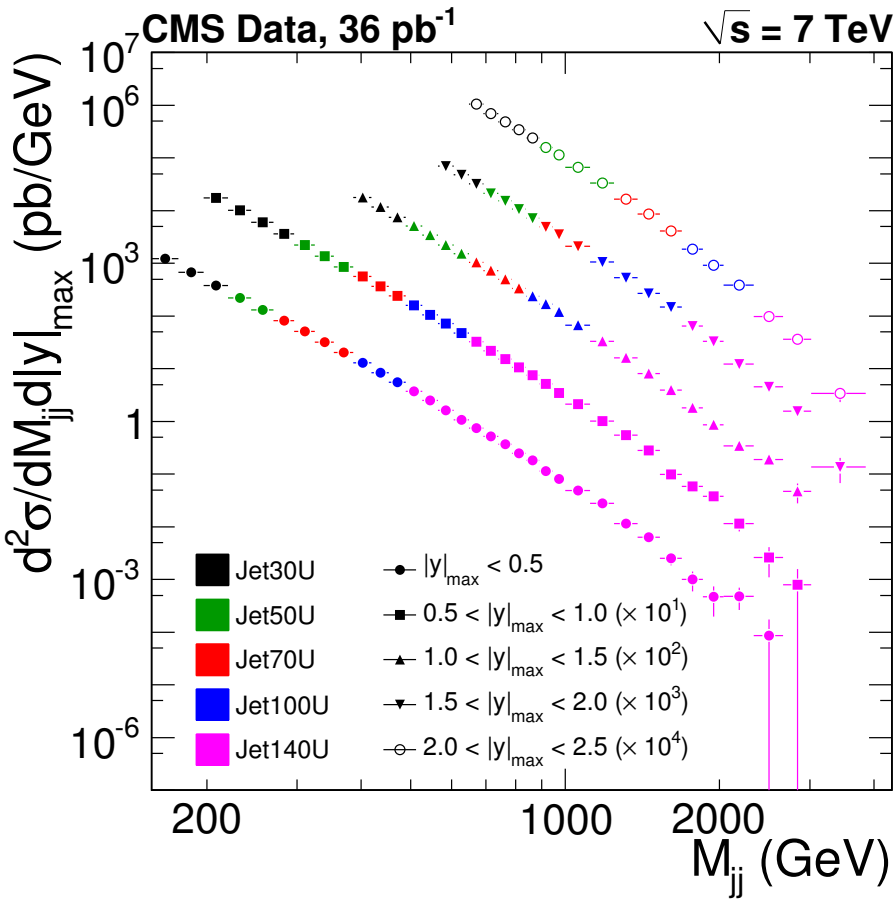

Figure 5.27. Dijet mass spectrum formed by the combination of the different samples. Each rapidity bin is further scaled by the number given in parentheses.

6. SYSTEMATIC UNCERTAINTIES

6.1. Experimental Uncertainties

The experimental uncertainties are the uncertainties related with every step of the measurement process starting from the reconstruction to the spectrum construction. There are three main sources of experimental uncertainties; Jet Energy Scale uncertainty (JES Uncertainty), luminosity uncertainty and the uncertainty on the unsmearing corrections. The total experimental uncertainty is obtained by quadratic sum of these three independent uncertainties:

$$\sigma^2_{Experimental} = \sigma^2_{JES} + \sigma^2_{luminosity} + \sigma^2_{unsmearing} \tag{6.1}$$

Figure 6.1 shows all the independent experimental uncertainties and the total experimental uncertainty in all $|y|_{max}$ bins. The typical range is between $\sim 15\%$ at low mass values and $\sim 60\%$ at high mass values, approximately the same in all rapidity bins. All individual components will be discussed below.

6.1.1. Jet Energy Scale (JES) Uncertainty

The JES uncertainty is the most dominant uncertainty source in all of three components of the experimental uncertainty. Due to the very steep fall of the dijet mass spectrum, a small uncertainty on the mass scale is translated into the cross section by a multiple of ∼5-7. The dijet mass spectrum can be described by a continuous function of the following form:

$$f(m) = A \cdot \left(m/\sqrt{s}\right)^{-a} \cdot \left(1 - m/\sqrt{s}\right)^{b} \tag{6.2}$$

In Equation 6.2, a change of variable $m/\sqrt{s} = x$ yields the Equation 6.3.

$$\tilde{f}(x) = A \cdot x^{-a} \cdot (1-x)^{b} \tag{6.3}$$

Then the relative uncertainty can be calculated by a differentiation with respect to x

$$\frac{\delta(\tilde{f}(x))}{\tilde{f}(x)} = \left[-a - b \cdot x \cdot (1-x)^{-1}\right] \frac{\delta x}{x} \tag{6.4}$$

Since the change of variable $m/\sqrt{s} = x$ is only a proportion, the relative uncertainty of mass scale $\delta m/m$ is equal to the $\delta x/x$. Hence, it can easily be seen that the relative uncertainty on the mass scale is pronounced in the cross section by a factor of $\pm\left[a + b \cdot x \cdot (1-x)^{-1}\right]$. However, this is a back of the envelope calculation, and a more rigorous study is needed to estimate the effect of JES uncertainty. On the other side, the JES uncertainty is given in terms of the p_T and the η of a given jet. The uncertainty on the JES cannot be analytically mapped to the mass scale since the mass of the dijet system also depends on the polar and the azimuthal separation of jets. In other words, there might be many pairs of jets with different p_T and η which give the same dijet mass value. Therefore, all jets in the selected events are systematically shifted by the respective uncertainty, and then a new value for the dijet mass is calculated. The average shift at each mass value is then fitted with a continuous function (Figure 6.2, right-side plot). It is important to note that for the increasing $|\mathrm{y}|_{max}$, the uncertainty at a given mass value decreases. For a given dijet mass, two leading jets in a higher rapidity bin are more likely to have smaller p_T values which are accompanied by smaller uncertainties. Figure 6.2 (right) shows the uncertainty induced on the cross section, due to the dijet mass scale uncertainty. This is calculated by the formula below:

$$\delta_{\pm} = \frac{\int_{m_1'}^{m_2'} f(m)\, dm}{\int_{m_1}^{m_2} f(m)\, dm} - 1 \tag{6.5}$$

where $\delta_{\pm}$ is the fractional change of the cross section, $m_{1,2}$ are the bin boundaries, $m'_{1,2} = m_{1,2} \cdot [1 \pm a_{JES}(m_{1,2})]$ are the shifted mass boundaries due to the relative mass scale change $a_{JES}(m)$ and $f(m)$ is a continuous fit on the measured spectrum. The resulting cross section uncertainty is asymmetric and almost fully correlated between the mass bins, ranging from 10% at M_{JJ}=200 GeV/c^2 to 60% at M_{JJ} =3 TeV/c^2.

6.1.2. Luminosity Uncertainty

The luminosity uncertainty is estimated to be 4% [42] and directly transferred to the cross section measurement. It is also correlated 100% across the mass bins.

6.1.3. Unsmearing Uncertainty

There are two sources of the uncertainty on the correction factors for smearing effects. As discussed in Section 5.5, the unsmearing corrections are derived by taking inputs from a toy Monte Carlo model of the dijet mass spectrum followed by a forward smearing due to the detector resolution for the dijet mass variable. In this technique, the slope of the spectrum and the resolution parameters depend on the pure Monte Carlo study. As a result, they may be slightly different than they are in reality. A reasonable approach to estimate the uncertainty on the unsmearing correction factors is by varying the spectrum slope and the resolution parameters. The spectrum slope is varied by 5% and this is conservatively based on the comparison of the data and the theory. The analytical method to achieve the slope variation is just by varying the exponents in Equation 6.2 by exactly the same amount with the amount desired for the slope variation. The derivative of the Equation 6.2 is

$$\frac{\mathrm{d}f(m)}{\mathrm{d}m} = A \cdot \left(m/\sqrt{s}\right)^{-a} \cdot \left(1 - m/\sqrt{s}\right)^{b} \cdot \left[-a(\frac{m}{\sqrt{s}})^{-1} - b(1 - \frac{m}{\sqrt{s}})^{-1}\right] \tag{6.6}$$

which is equivalent to the;

$$\frac{\mathrm{d}f(m)/\mathrm{d}m}{f(m)} = \left[-a(\frac{m}{\sqrt{s}})^{-1} - b(1 - \frac{m}{\sqrt{s}})^{-1}\right] \tag{6.7}$$

If both exponents a and b are scaled by 1.05 (5%), then the Equation 6.7 becomes;

$$\frac{\mathrm{d}\tilde{f}(m)/\mathrm{d}m}{\tilde{f}(m)} = -1.05 \left[a(\frac{m}{\sqrt{s}})^{-1} + b(1 - \frac{m}{\sqrt{s}})^{-1}\right] \tag{6.8}$$

where $\tilde{f}(m)$ is the new function with scaled exponents. As it can easily be seen, the functional property of the Equation 6.2 allows us to vary the spectrum slope analytically (Figure 6.3). The resolution is varied by 10% where this number is motivated by the observed difference between data and simulation in the jet energy resolution [43]. Figure 6.4 shows the response of the unsmearing correction to the variations described above. Overall, the unsmearing uncertainty is in the order of 2-3%, fully correlated across the mass bins.

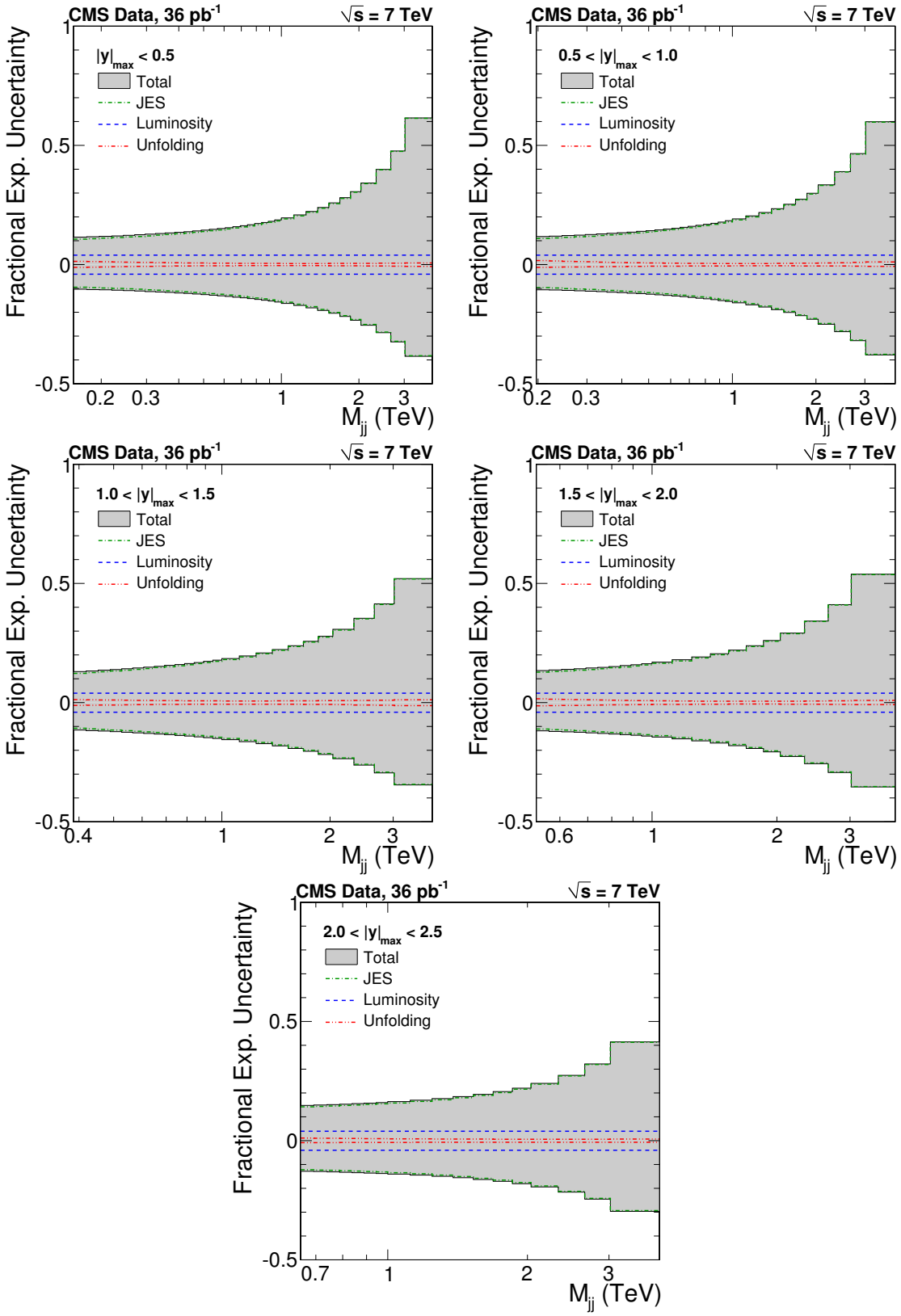

Figure 6.1. Summary of the experimental systematic uncertainties: jet energy scale (green dashdotted line), luminosity (blue dashed line), unsmearing (red dash-double dotted line) and their sum in quadrature (filled).

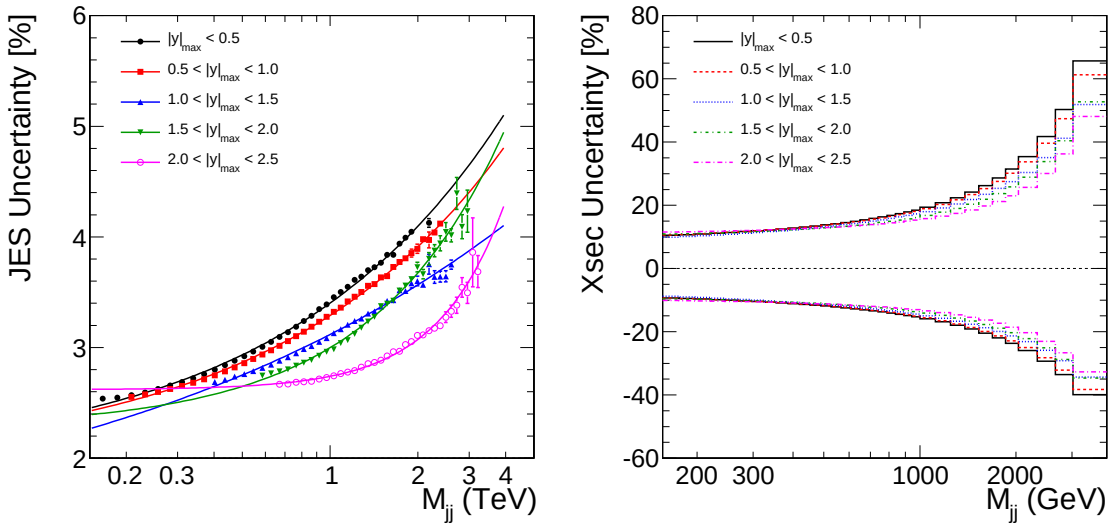

Figure 6.2. Left: Average dijet mass scale uncertainty in all $|y|_{max}$ bins. Right: Cross section uncertainty due to the mass scale uncertainty.

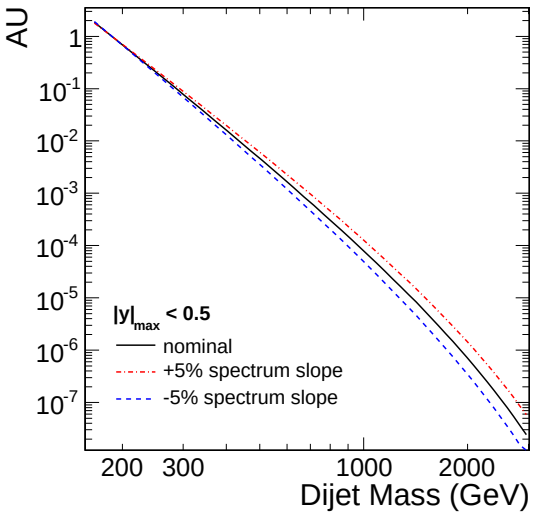

Figure 6.3. Simulated dijet mass spectrum (continuous line) in the rapidity bin $|y|_{max} < 0.5$ which is used for the evaluation of the smearing effect. The dashed and the dashed-dotted lines correspond to softer and harder spectra respectively, systematically shifted by changing the slope by 5%.

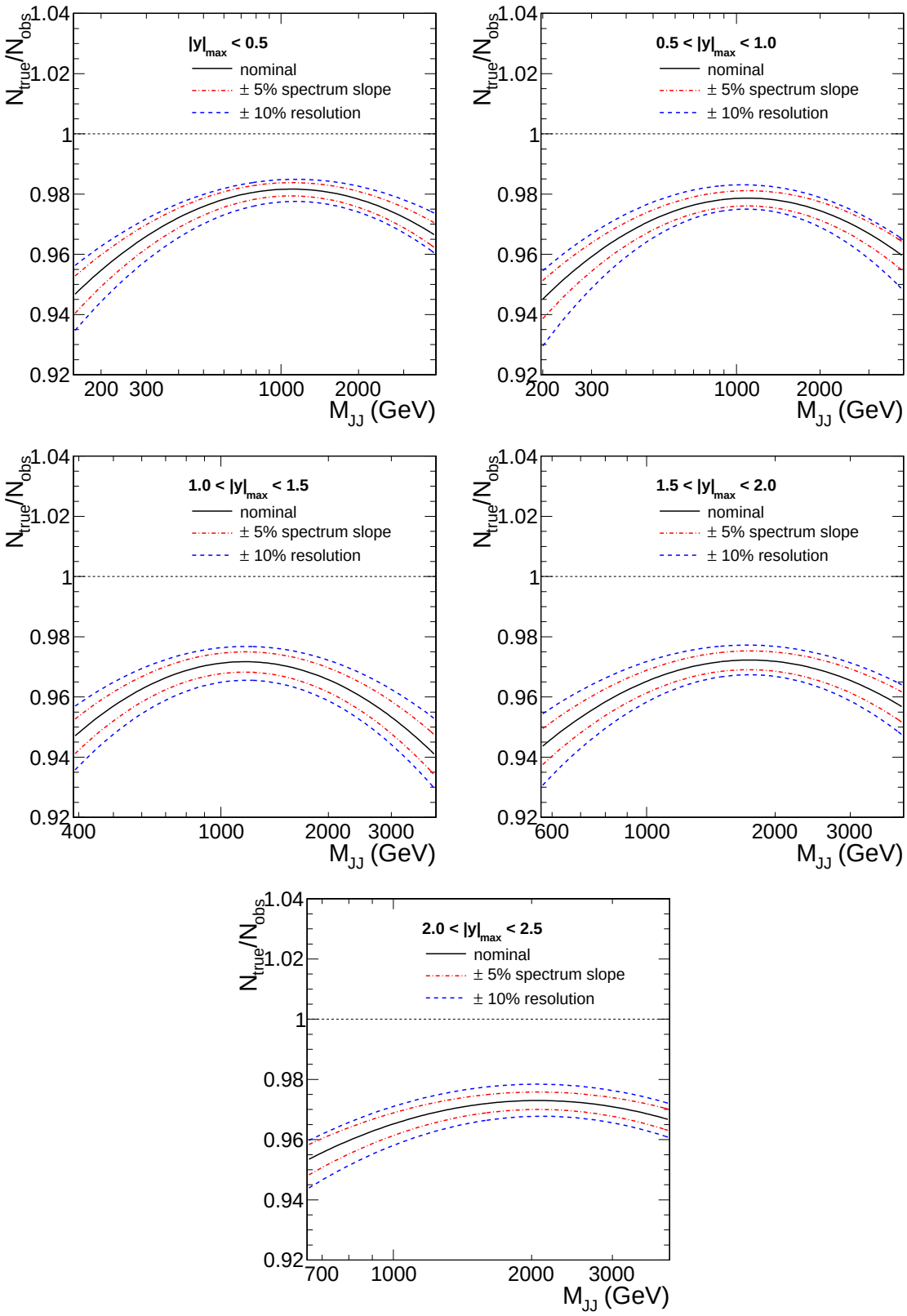

Figure 6.4. Unsmearing correction in the various rapidity bins. The uncertainty of the correction factor on the dijet mass resolution and the simulated spectrum are also shown.

6.2. Theoretical Uncertainties

The theoretical uncertainties are introduced due to the PDF dependence, the renormalization and factorization scale choice and by the non-perturbative corrections. The PDF uncertainty is estimated according to the PDF4LHC [44] prescription through the variation of the CT10, MSTW2008NLO and NNPDF2.0 PDF sets (see Figure 6.5). The renormalization and factorization scale uncertainty is estimated as the maximal deviation of the six point variation (μ_F/p_T^{ave}, μ_R/p_T^{ave})=(1/2, 1/2), (2, 2), (1, 1/2), (1, 2), (1/2, 1), (2, 1). Finally, the non-perturbative correction uncertainty is estimated as half of the NP correction deviation from unity (see Figure 2.9). Overall, the PDF uncertainty dominates at high mass values, while the non-perturbative correction uncertainty is dominant at low masses. Figure 6.6 shows the theoretical uncertainty decomposition in all rapidity bins.

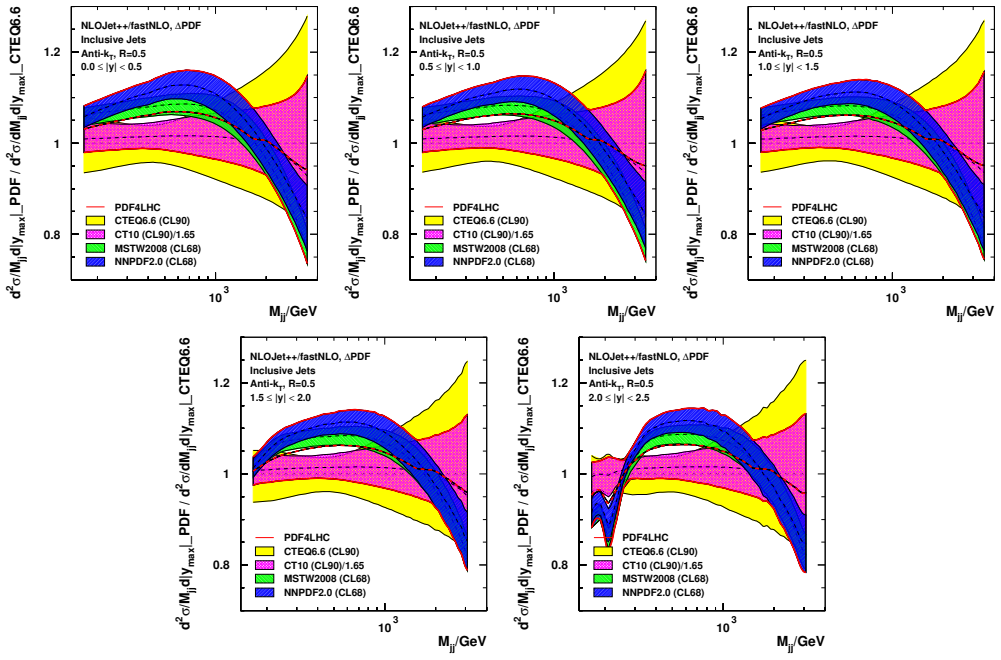

Figure 6.5. PDF Uncertainties according to PDF4LHC prescription. CT10, MSTW2008NLO, NNPDF2.0. are used to perform NLO calculations and the ratio between each of these three and CTEQ6.6 are used to set the PDF uncertainty.

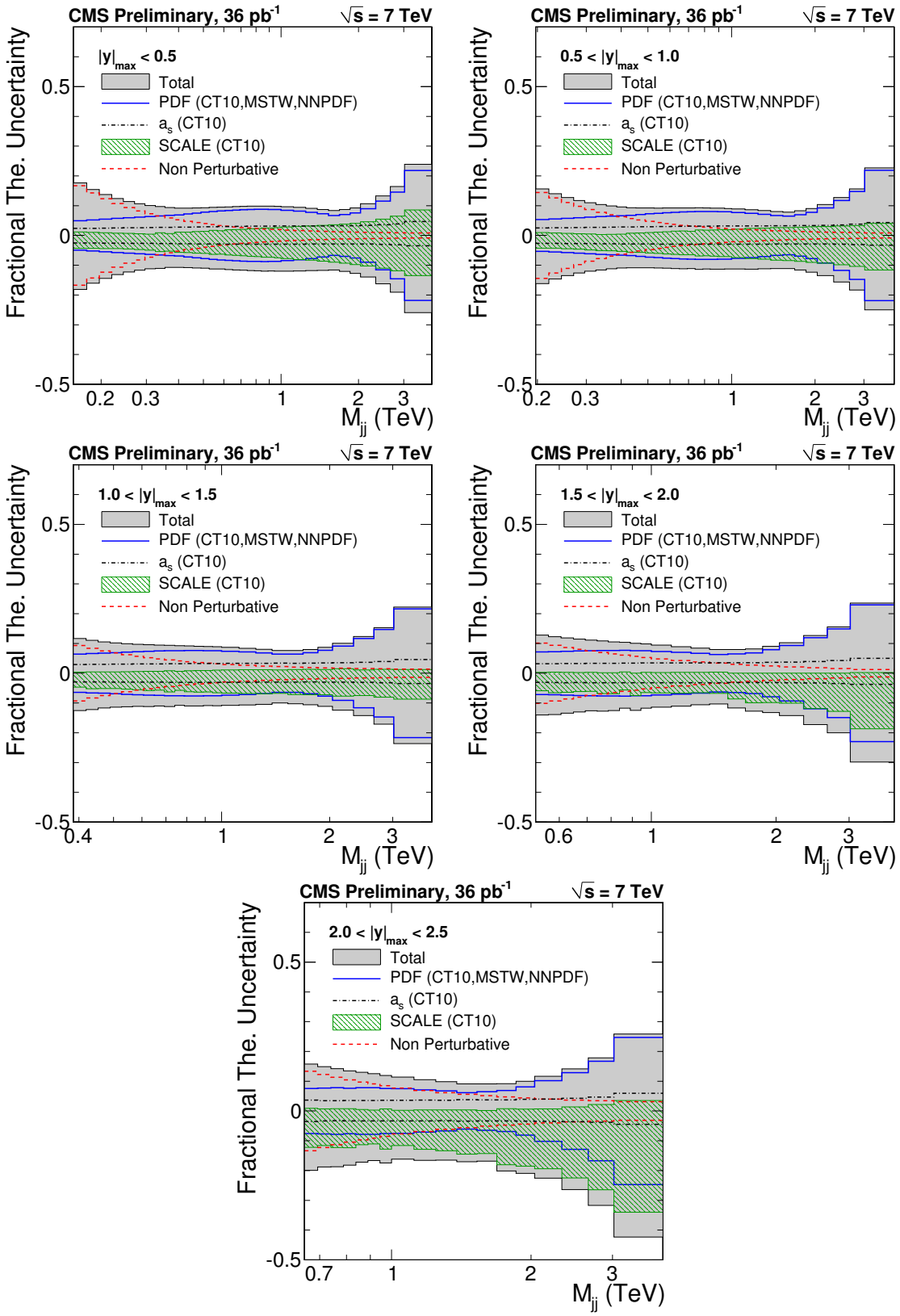

Figure 6.6. Summary of the theoretical systematic uncertainties: PDF (blue dashed-dotted line), scale variations (red dashed line), non-perturbative correction (green dashed-double dotted line) and the sum in quadrature (filled).

7. RESULTS AND CONCLUSIONS

7.1. Results

In this last chapter, the measured dijet mass cross-section is compared to the theory predictions at the particle level. The double differential cross-section in logarithmic scale is shown in Figure 7.1 with statistical uncertainties only. The different $|y|_{max}$ bins are scaled for a better visualization. It is observed that the dijet mass spectrum falls steeply and smoothly by many orders of magnitude, in agreement with the theory predictions, and the measurement covers the range from 0.2 TeV to 3.5 TeV. The exact mass ranges and the cross-section values are given in Tables 7.1-7.5. The central values quoted in the tables for each bin are the mass value m_0 which satisfies the equation

$$f(m_0)(m_2 - m_1) = \int_{m_1}^{2} f(m)dm \tag{7.1}$$

where m_1, m_2 are the bin boundaries and $f(m)$ is the continuous t of the cross section. The choice of the central value is adopted from the approach described in [45].

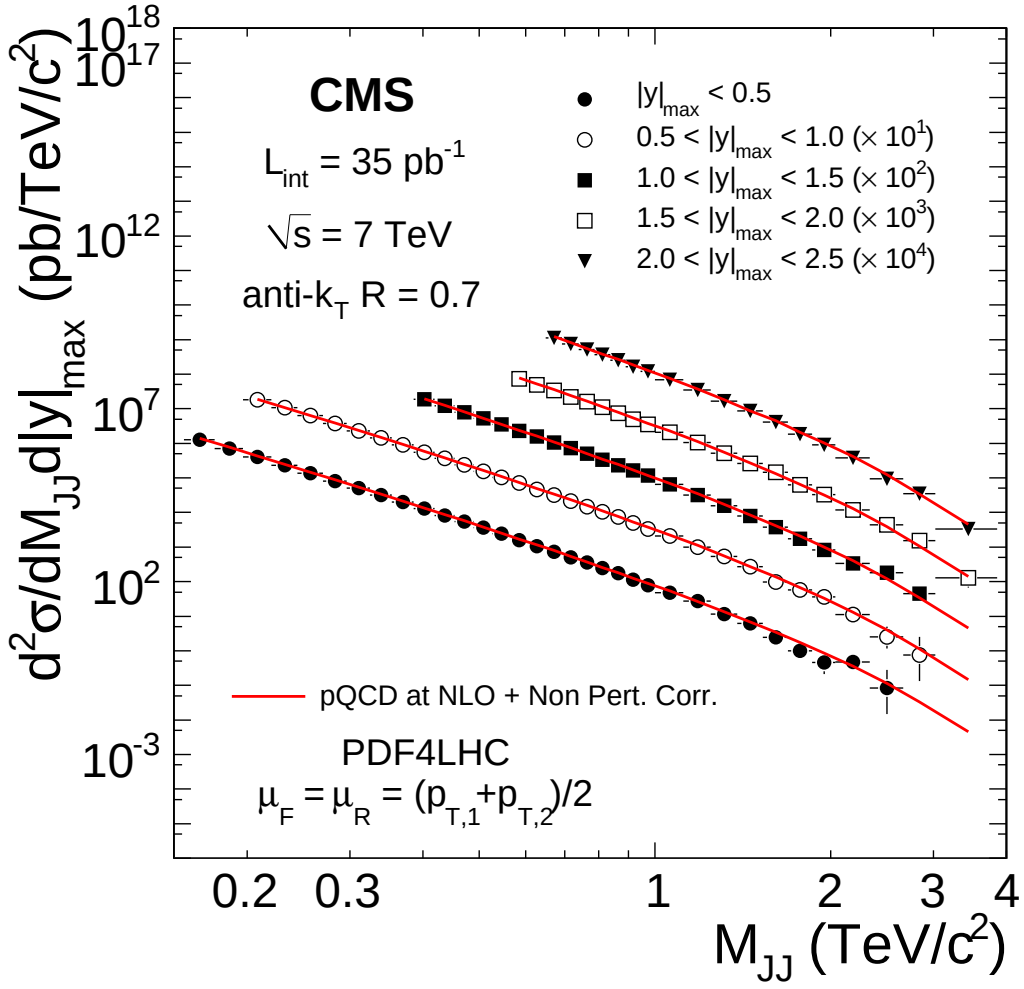

Figure 7.1. Measured double-differential dijet production cross sections (points scaled by the factors shown in the figure) as a function of the dijet invariant mass in bins of the variable $|y|_{max}$, compared to the theoretical predictions (curves). The horizontal error bars represent the bin widths, while the vertical error bars represent the statistical uncertainties of the data [7].

Table 7.1. Double-differential dijet mass cross section in the rapidity range $|y|_{\max} < 0.5$. The reference mass is the point at which the cross section is drawn in Figures 7.1 and 7.2 and is calculated as described in the text. The experimental systematic uncertainties of the individual dijet-mass bins are almost 100% correlated [7].

Mass Range (TeV)	Reference Mass (TeV)	Measured Cross Section (pb/TeV)	Statistical Uncertainty %	Systematic Uncertainty %
[0.156, 0.176]	0.165	1.32×10^6	−1.1, +1.1	−10, +11
[0.176, 0.197]	0.186	7.26×10^5	−1.4, +1.4	−10, +12
[0.197, 0.220]	0.208	4.12×10^5	−1.8, +1.8	−11, +12
[0.220, 0.244]	0.231	2.35×10^5	−0.7, +0.7	−11, +12
[0.244, 0.270]	0.256	1.39×10^5	−0.9, +0.9	−11, +12
[0.270, 0.296]	0.282	8.18×10^4	−0.7, +0.7	−11, +13
[0.296, 0.325]	0.310	5.08×10^4	−0.9, +0.9	−11, +13
[0.325, 0.354]	0.339	3.18×10^4	−1.1, +1.1	−11, +13
[0.354, 0.386]	0.369	2.04×10^4	−1.3, +1.3	−12, +13
[0.386, 0.419]	0.402	1.28×10^4	−1.1, +1.1	−12, +14
[0.419, 0.453]	0.435	8.22×10^3	−1.4, +1.4	−12, +14
[0.453, 0.489]	0.470	5.42×10^3	−1.6, +1.6	−12, +14
[0.489, 0.526]	0.507	3.65×10^3	−1.4, +1.5	−13, +14
[0.526, 0.565]	0.545	2.44×10^3	−1.7, +1.7	−13, +15
[0.565, 0.606]	0.585	1.58×10^3	−2.1, +2.1	−13, +15
[0.606, 0.649]	0.627	1.05×10^3	−2.5, +2.5	−13, +16
[0.649, 0.693]	0.670	7.35×10^2	−2.9, +3.0	−14, +16
[0.693, 0.740]	0.716	5.05×10^2	−3.4, +3.5	−14, +16
[0.740, 0.788]	0.763	3.62×10^2	−4.0, +4.2	−14, +17
[0.788, 0.838]	0.812	2.45×10^2	−4.8, +5.0	−15, +17
[0.838, 0.890]	0.863	1.77×10^2	−5.5, +5.8	−15, +18
[0.890, 0.944]	0.916	1.13×10^2	−6.8, +7.2	−15, +18
[0.944, 1.000]	0.971	7.94×10^1	−7.9, +8.5	−16, +19
[1.000, 1.118]	1.055	4.76×10^1	−7.0, +7.5	−16, +20
[1.118, 1.246]	1.178	2.72×10^1	−8.9, +9.8	−17, +21
[1.246, 1.383]	1.310	1.14×10^1	−13, +15	−18, +22
[1.383, 1.530]	1.452	6.24	−17, +21	−19, +24
[1.530, 1.687]	1.604	2.48	−26, +35	−20, +26
[1.687, 1.856]	1.766	9.85×10^{-1}	−40, +60	−22, +28
[1.856, 2.037]	1.941	4.59×10^{-1}	−54, +97	−23, +31
[2.037, 2.332]	2.170	4.69×10^{-1}	−43, +68	−25, +34
[2.332, 2.659]	2.479	8.45×10^{-2}	−83, +230	−29, +40

Table 7.2. Double-differential dijet mass cross section in the rapidity range $0.5 < |y|_{\max} < 1.0$. The reference mass is the point at which the cross section is drawn in Figures 7.1 and 7.2 and is calculated as described in the text. The experimental systematic uncertainties of the individual dijet-mass bins are almost 100% correlated [7].

Mass Range (TeV)	Reference Mass (TeV)	Measured Cross Section (pb/TeV)	Statistical Uncertainty %	Systematic Uncertainty %
[0.197, 0.220]	0.208	1.74×10^6	−0.8, +0.9	−11, +12
[0.220, 0.244]	0.231	1.02×10^6	−1.1, +1.1	−11, +12
[0.244, 0.270]	0.256	6.00×10^5	−1.4, +1.4	−11, +12
[0.270, 0.296]	0.282	3.64×10^5	−1.7, +1.8	−11, +12
[0.296, 0.325]	0.310	2.22×10^5	−0.7, +0.7	−11, +13
[0.325, 0.354]	0.339	1.38×10^5	−0.8, +0.9	−11, +13
[0.354, 0.386]	0.369	8.64×10^4	−1.0, +1.0	−12, +13
[0.386, 0.419]	0.402	5.42×10^4	−0.8, +0.8	−12, +13
[0.419, 0.453]	0.435	3.55×10^4	−1.0, +1.0	−12, +14
[0.453, 0.489]	0.470	2.34×10^4	−1.1, +1.2	−12, +14
[0.489, 0.526]	0.507	1.53×10^4	−0.9, +0.9	−12, +14
[0.526, 0.565]	0.545	1.01×10^4	−1.1, +1.1	−13, +15
[0.565, 0.606]	0.585	6.90×10^3	−1.3, +1.3	−13, +15
[0.606, 0.649]	0.627	4.60×10^3	−1.6, +1.6	−13, +15
[0.649, 0.693]	0.670	3.15×10^3	−1.4, +1.4	−13, +16
[0.693, 0.740]	0.716	2.14×10^3	−1.7, +1.7	−14, +16
[0.740, 0.788]	0.763	1.48×10^3	−2.0, +2.0	−14, +16
[0.788, 0.838]	0.812	1.04×10^3	−2.3, +2.4	−14, +17
[0.838, 0.890]	0.863	7.42×10^2	−2.7, +2.8	−15, +17
[0.890, 0.944]	0.916	5.01×10^2	−3.2, +3.3	−15, +18
[0.944, 1.000]	0.971	3.37×10^2	−3.8, +4.0	−15, +18
[1.000, 1.118]	1.055	2.08×10^2	−3.4, +3.5	−16, +19
[1.118, 1.246]	1.178	9.94×10^1	−4.7, +4.9	−17, +20
[1.246, 1.383]	1.310	5.38×10^1	−6.1, +6.5	−18, +22
[1.383, 1.530]	1.452	2.73×10^1	−8.3, +9.0	−19, +23
[1.530, 1.687]	1.604	9.70	−13, +15	−20, +25
[1.687, 1.856]	1.766	5.73	−17, +20	−21, +27
[1.856, 2.037]	1.941	3.66	−20, +25	−23, +30
[2.037, 2.332]	2.170	1.12	−28, +38	−25, +33
[2.332, 2.659]	2.479	2.52×10^{-1}	−54, +97	−28, +39
[2.659, 3.019]	2.819	7.62×10^{-2}	−83, +230	−32, +47

Table 7.3. Double-differential dijet mass cross section in the rapidity range $1.0 < |y|_{\max} < 1.5$. The reference mass is the point at which the cross section is drawn in Figures 7.1 and 7.2 and is calculated as described in the text. The experimental systematic uncertainties of the individual dijet-mass bins are almost 100% correlated [7].

Mass Range (TeV)	Reference Mass (TeV)	Measured Cross Section (pb/TeV)	Statistical Uncertainty %	Systematic Uncertainty %
[0.386, 0.419]	0.402	1.84×10^5	−2.2, +2.3	−12, +13
[0.419, 0.453]	0.435	1.21×10^5	−2.7, +2.8	−12, +13
[0.453, 0.489]	0.470	7.77×10^4	−3.3, +3.4	−12, +14
[0.489, 0.526]	0.507	5.26×10^4	−1.2, +1.2	−12, +14
[0.526, 0.565]	0.545	3.56×10^4	−1.5, +1.5	−12, +14
[0.565, 0.606]	0.585	2.31×10^4	−1.8, +1.8	−13, +15
[0.606, 0.649]	0.627	1.60×10^4	−2.1, +2.1	−13, +15
[0.649, 0.693]	0.670	1.04×10^4	−1.6, +1.6	−13, +15
[0.693, 0.740]	0.716	7.20×10^3	−1.8, +1.9	−13, +16
[0.740, 0.788]	0.763	4.98×10^3	−2.2, +2.2	−14, +16
[0.788, 0.838]	0.812	3.35×10^3	−2.6, +2.7	−14, +16
[0.838, 0.890]	0.863	2.34×10^3	−2.0, +2.1	−14, +17
[0.890, 0.944]	0.916	1.65×10^3	−2.4, +2.5	−15, +17
[0.944, 1.000]	0.971	1.18×10^3	−2.8, +2.9	−15, +18
[1.000, 1.118]	1.055	6.61×10^2	−2.6, +2.6	−16, +19
[1.118, 1.246]	1.178	3.22×10^2	−2.6, +2.7	−16, +20
[1.246, 1.383]	1.310	1.57×10^2	−3.6, +3.7	−17, +21
[1.383, 1.530]	1.452	7.86×10^1	−4.9, +5.1	−18, +22
[1.530, 1.687]	1.603	3.80×10^1	−6.8, +7.3	−19, +24
[1.687, 1.856]	1.766	1.75×10^1	−9.6, +11	−20, +26
[1.856, 2.037]	1.941	8.32	−13, +15	−22, +28
[2.037, 2.332]	2.170	3.33	−17, +20	−23, +31
[2.332, 2.659]	2.478	1.83	−21, +26	−26, +35
[2.659, 3.019]	2.819	4.51×10^{-1}	−40, +60	−29, +41

Table 7.4. Double-differential dijet mass cross section in the rapidity range $1.5 < |y|_{\max} < 2.0$. The reference mass is the point at which the cross section is drawn in Figures 7.1 and 7.2 and is calculated as described in the text. The experimental systematic uncertainties of the individual dijet-mass bins are almost 100% correlated [7].

Mass Range (TeV)	Reference Mass (TeV)	Measured Cross Section (pb/TeV)	Statistical Uncertainty %	Systematic Uncertainty %
[0.565, 0.606]	0.585	6.68×10^4	−3.1, +3.2	−12, +14
[0.606, 0.649]	0.627	4.52×10^4	−3.7, +3.9	−12, +14
[0.649, 0.693]	0.670	3.05×10^4	−4.5, +4.7	−12, +14
[0.693, 0.740]	0.716	2.02×10^4	−1.7, +1.7	−13, +15
[0.740, 0.788]	0.763	1.47×10^4	−2.0, +2.0	−13, +15
[0.788, 0.838]	0.812	1.04×10^4	−2.3, +2.4	−13, +15
[0.838, 0.890]	0.863	6.92×10^3	−2.8, +2.8	−13, +16
[0.890, 0.944]	0.916	4.77×10^3	−2.1, +2.1	−14, +16
[0.944, 1.000]	0.971	3.41×10^3	−2.4, +2.4	−14, +16
[1.000, 1.118]	1.055	2.04×10^3	−2.1, +2.2	−14, +17
[1.118, 1.246]	1.178	1.04×10^3	−2.0, +2.0	−15, +18
[1.246, 1.383]	1.310	5.20×10^2	−2.7, +2.7	−16, +19
[1.383, 1.530]	1.452	2.60×10^2	−3.6, +3.8	−17, +21
[1.530, 1.687]	1.604	1.45×10^2	−4.7, +5.0	−18, +22
[1.687, 1.856]	1.766	6.31×10^1	−5.1, +5.3	−19, +24
[1.856, 2.037]	1.941	3.24×10^1	−6.8, +7.3	−21, +26
[2.037, 2.332]	2.170	1.18×10^1	−8.9, +9.7	−23, +29
[2.332, 2.659]	2.479	4.37	−14, +16	−26, +34
[2.659, 3.019]	2.820	1.52	−22, +28	−29, +41
[3.019, 3.854]	3.344	1.31×10^{-1}	−48, +79	−35, +54

Table 7.5. Double-differential dijet mass cross section in the rapidity range $2.0 < |y|_{\max} < 2.5$. The reference mass is the point at which the cross section is drawn in Figures 7.1 and 7.2 and is calculated as described in the text. The experimental systematic uncertainties of the individual dijet-mass bins are almost 100% correlated [7].

Mass Range (TeV)	Reference Mass (TeV)	Measured Cross Section (pb/TeV)	Statistical Uncertainty %	Systematic Uncertainty %
[0.649, 0.693]	0.670	1.00×10^5	−2.5, +2.5	−13, +15
[0.693, 0.740]	0.716	6.70×10^4	−2.9, +3.0	−13, +15
[0.740, 0.788]	0.763	4.63×10^4	−3.5, +3.6	−13, +15
[0.788, 0.838]	0.812	3.29×10^4	−4.1, +4.2	−13, +15
[0.838, 0.890]	0.863	2.31×10^4	−4.8, +5.0	−13, +16
[0.890, 0.944]	0.916	1.52×10^4	−1.8, +1.9	−14, +16
[0.944, 1.000]	0.971	1.11×10^4	−2.1, +2.2	−14, +16
[1.000, 1.118]	1.055	6.41×10^3	−1.9, +1.9	−14, +16
[1.118, 1.246]	1.178	3.26×10^3	−2.6, +2.6	−14, +17
[1.246, 1.383]	1.310	1.59×10^3	−2.2, +2.3	−15, +18
[1.383, 1.530]	1.452	8.39×10^2	−3.0, +3.1	−16, +18
[1.530, 1.687]	1.604	4.01×10^2	−4.2, +4.4	−16, +19
[1.687, 1.856]	1.766	1.80×10^2	−4.1, +4.2	−17, +21
[1.856, 2.037]	1.941	8.96×10^1	−5.6, +5.9	−18, +22
[2.037, 2.332]	2.170	3.75×10^1	−6.8, +7.2	−19, +24
[2.332, 2.659]	2.479	9.44	−9.4, +10	−22, +27
[2.659, 3.019]	2.819	3.52	−15, +17	−25, +32
[3.019, 3.854]	3.338	3.29×10^{-1}	−31, +43	−30, +41

7.2. Data vs. Theory Comparison

In Figure 7.2 the ratio data/theory is shown superimposed with the experimental and theoretical uncertainties. Although the experimental uncertainties are comparable to the theoretical uncertainties, they are not small enough to constrain the parameters in the theory. Nevertheless, an excellent agreement is observed, indicating that the QCD predictions describe the parton-parton scattering accurately in this kinematic regime.

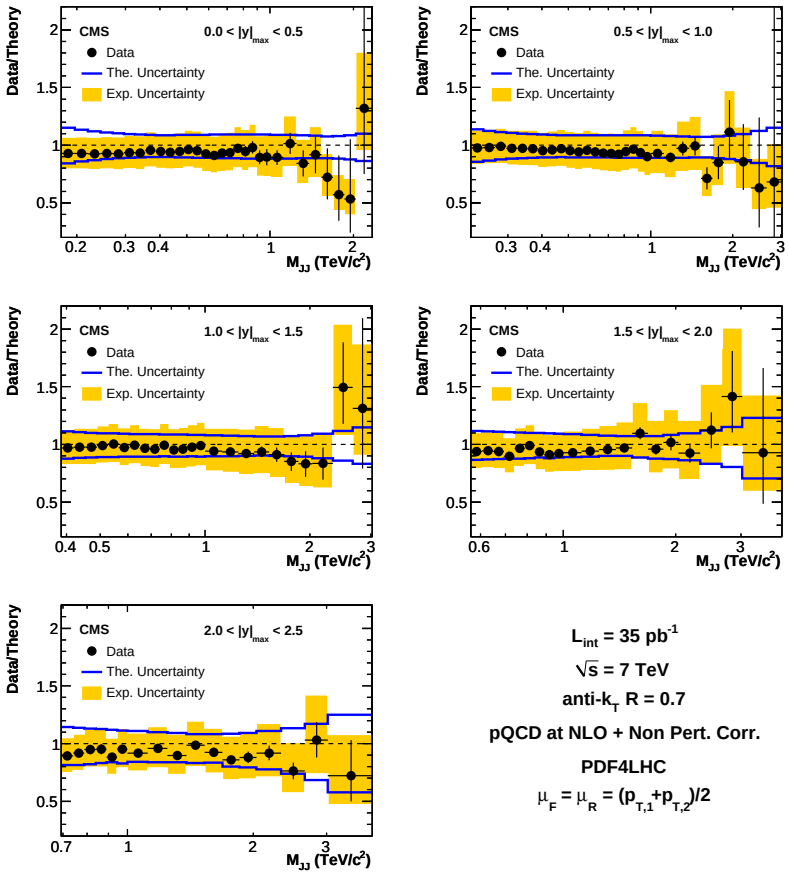

Figure 7.2. Ratio of the measured double differential dijet production cross-section over the theory prediction in the different rapidity bins. The solid band represents the experimental systematical uncertainty and is centered around the points. The error bars on the points represent the statistical uncertainty. The theoretical uncertainty is shown as lines centered around unity [7].

7.3. Conclusions

The double differential dijet mass cross section was presented in this dissertation and is the most extensive measurement with the farthest range in both rapidity and energy to date. Good agreement between data and perturbative QCD was observed in all five rapidity regions which confirms the Standard Model predictions. This measurement can then be used to reduce the uncertainties on the parton distribution functions. Such reduction will be useful for the future versions of Monte Carlo simulations and NLO calculation softwares. For most of the other analyses in particle physics, QCD events are often a major background, such as searches for the Higgs boson. Understanding the nature of the hard parton-parton scattering helps physicists to understand the background in their analyses.

APPENDIX A: Running Coupling Constant

In Section 2.2.1, it was mentioned that the value of μ in Equation 2.32 does not effect the result of the equation. It means that two different values of μ are simultaneously correct. In order to prove it let us start with the Equation 2.32.

$$\alpha_s(|q^2|) = \frac{\alpha_s(\mu^2)}{1 + \alpha_s(\mu^2)\ b\ \ln(|q^2|/\mu^2)} \tag{A.1}$$

$\alpha_s(\mu^2)$ term in the equation can be written as follows, referring to the original equation;

$$\alpha_s(\mu^2) = \frac{\alpha_s(\mu_0^2)}{1 + \alpha_s(\mu_0^2)\ b\ \ln(|q^2|/\mu_0^2)} \tag{A.2}$$

If we plug the equation above into Equation A.1, we have

$$\alpha_s(|q^2|) = \frac{\dfrac{\alpha_s(\mu_0^2)}{1 + \alpha_s(\mu_0^2)\ b\ \ln(|q^2|/\mu_0^2)}}{1 + \dfrac{\alpha_s(\mu_0^2)}{1 + \alpha_s(\mu_0^2)\ b\ \ln(|q^2|/\mu_0^2)}\ b\ \ln(|q^2|/\mu^2)} \tag{A.3}$$

$$= \frac{\alpha_s(\mu_0^2)}{1 + \alpha_s(\mu_0^2)\ b\ \ln(\mu_0/\mu^2) + \alpha_s(\mu_0^2)\ b\ \ln(|q^2|/\mu^2)} = \frac{\alpha_s(\mu_0^2)}{1 + \alpha_s(\mu_0^2)\ b\ \ln(|q^2|/\mu_0^2)} \tag{A.4}$$

APPENDIX B: Trigger Efficiencies

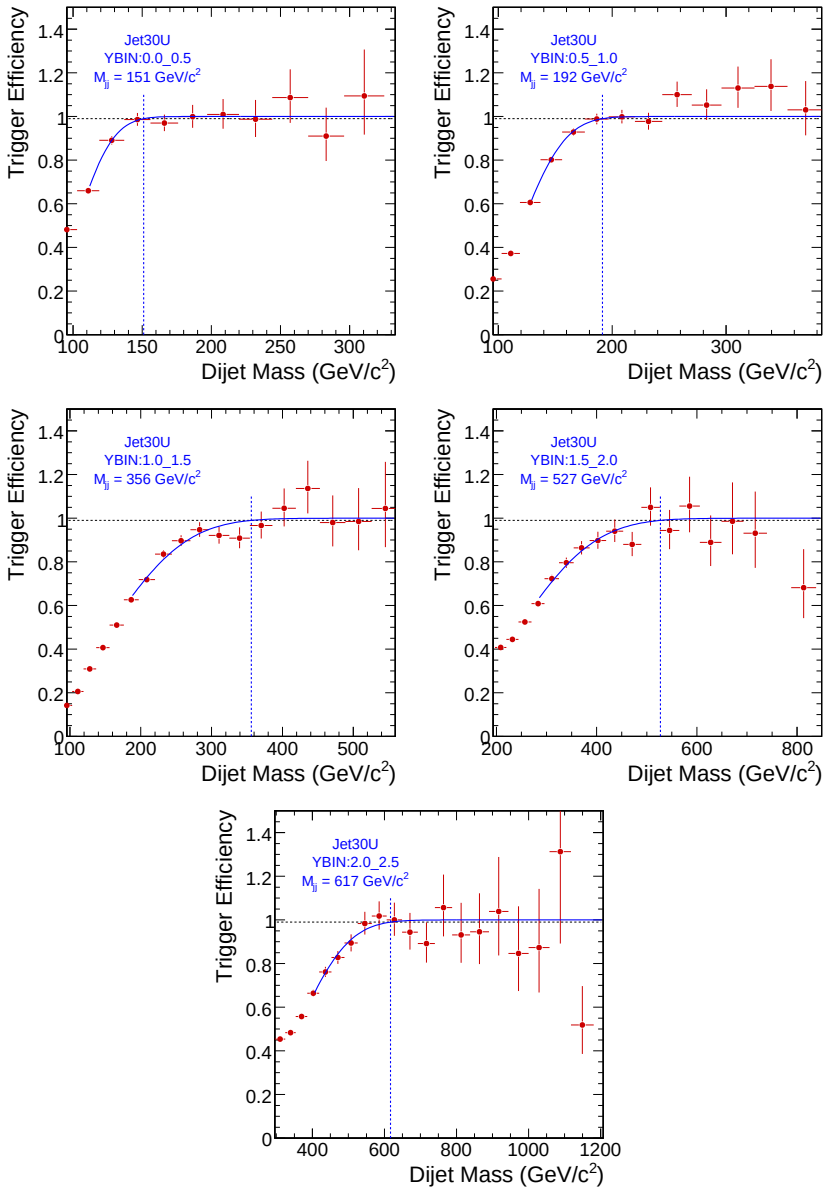

Figure B.1. Relative trigger efficiencies as a function of dijet mass for the five different $|y|_{max}$ bins and for the HLT_Jet30U trigger. The 100% efficiency point is determined by performing a fit with an error function.

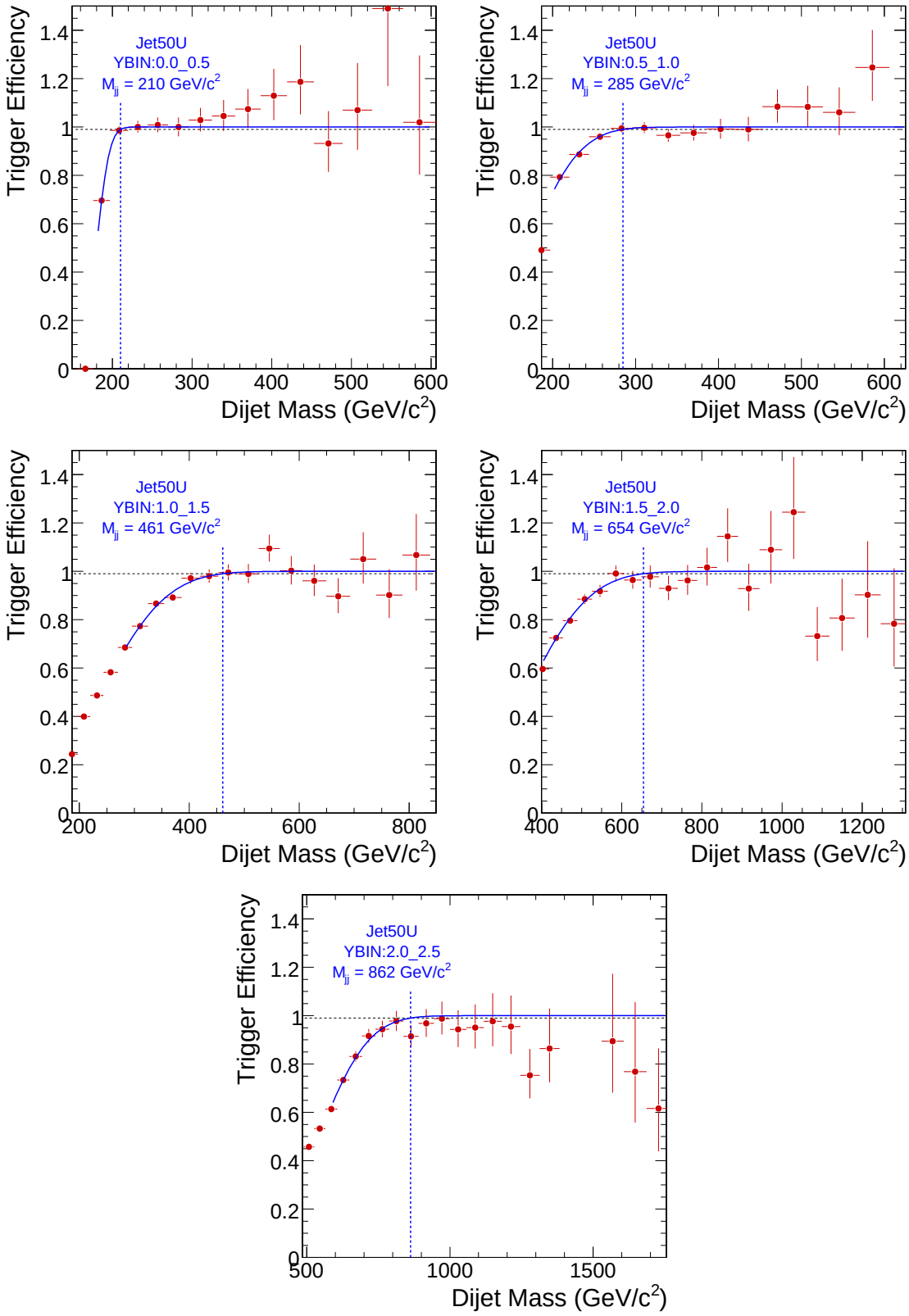

Figure B.2. Relative trigger efficiencies as a function of dijet mass for the five different $|y|_{max}$ bins and for the HLT_Jet50U trigger. The 100% efficiency point is determined by performing a fit with an error function.

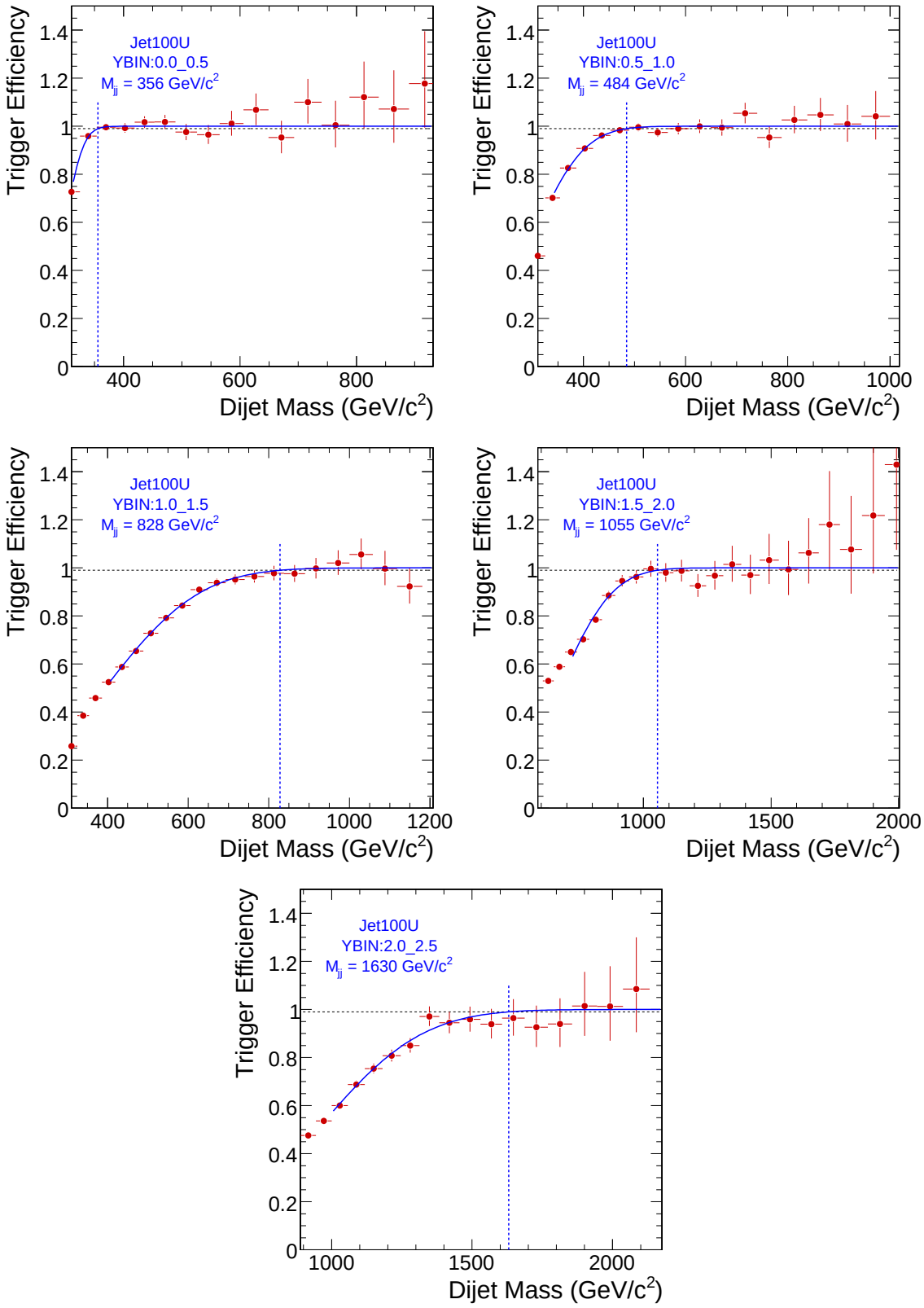

Figure B.3. Relative trigger efficiencies as a function of dijet mass for the five different $|y|_{max}$ bins and for the HLT_Jet100U trigger. The 100% efficiency point is determined by performing a fit with an error function.

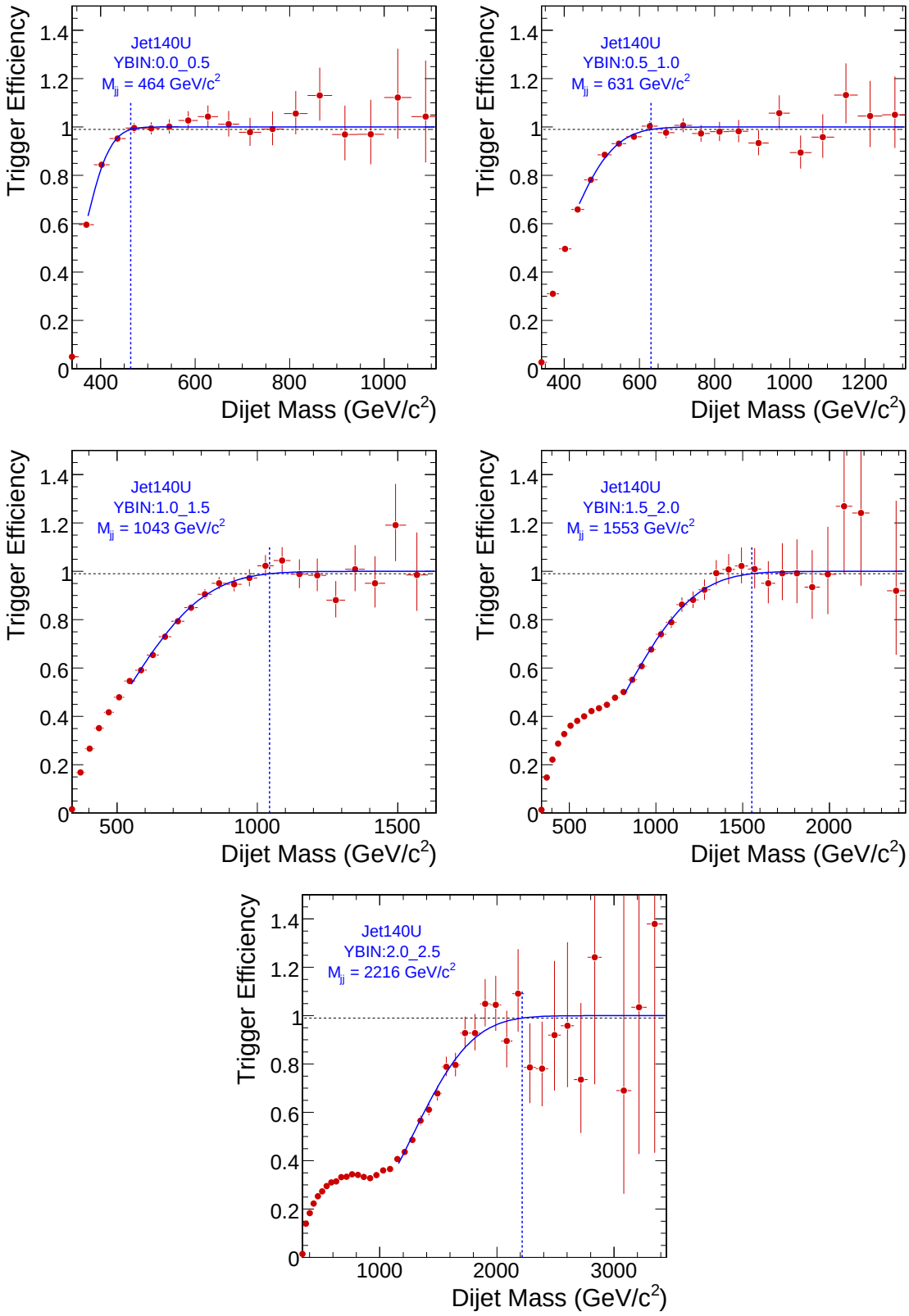

Figure B.4. Relative trigger efficiencies as a function of dijet mass for the five different $|y|_{max}$ bins and for the HLT_Jet140U trigger. The 100% efficiency point is determined by performing a fit with an error function.

B.1. Appendix C

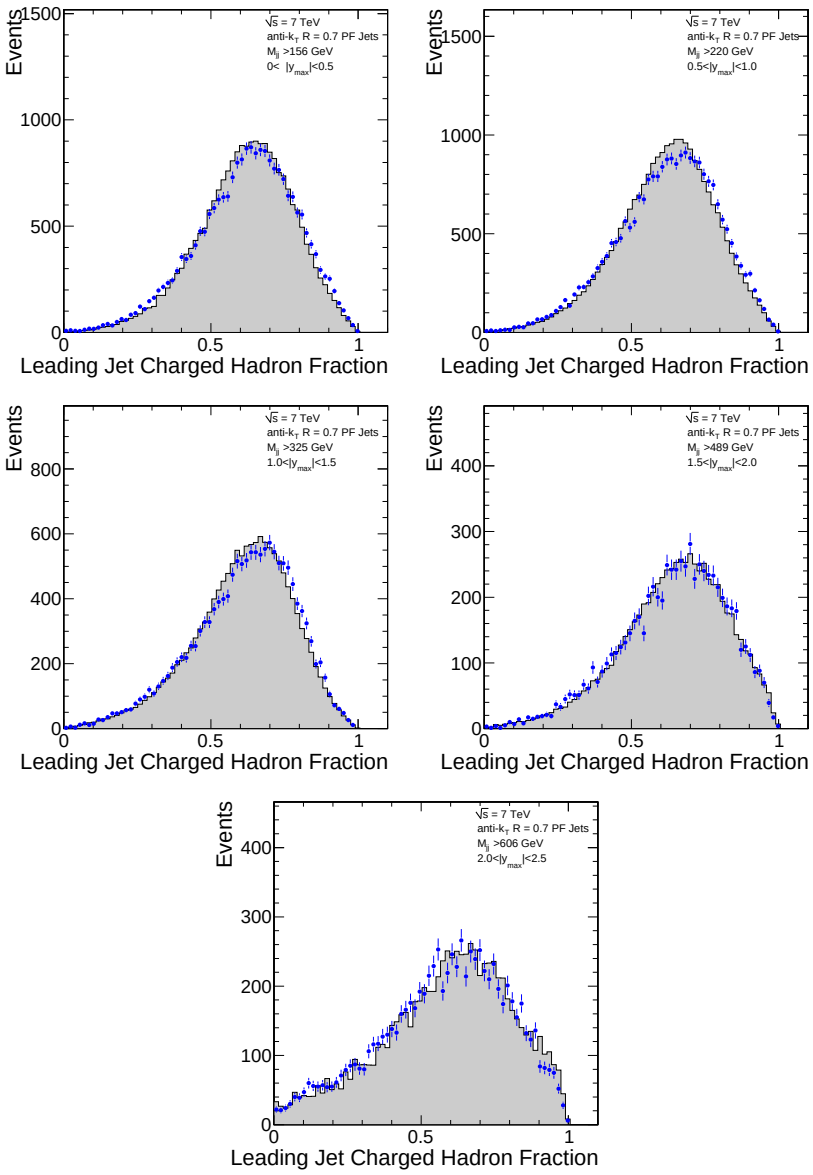

Figure B.5. The charged hadron fraction of the leading jet for the five different y_{max} bins and for the HLT_Jet30U trigger, for data (points) and simulated (dashed histogram) events.

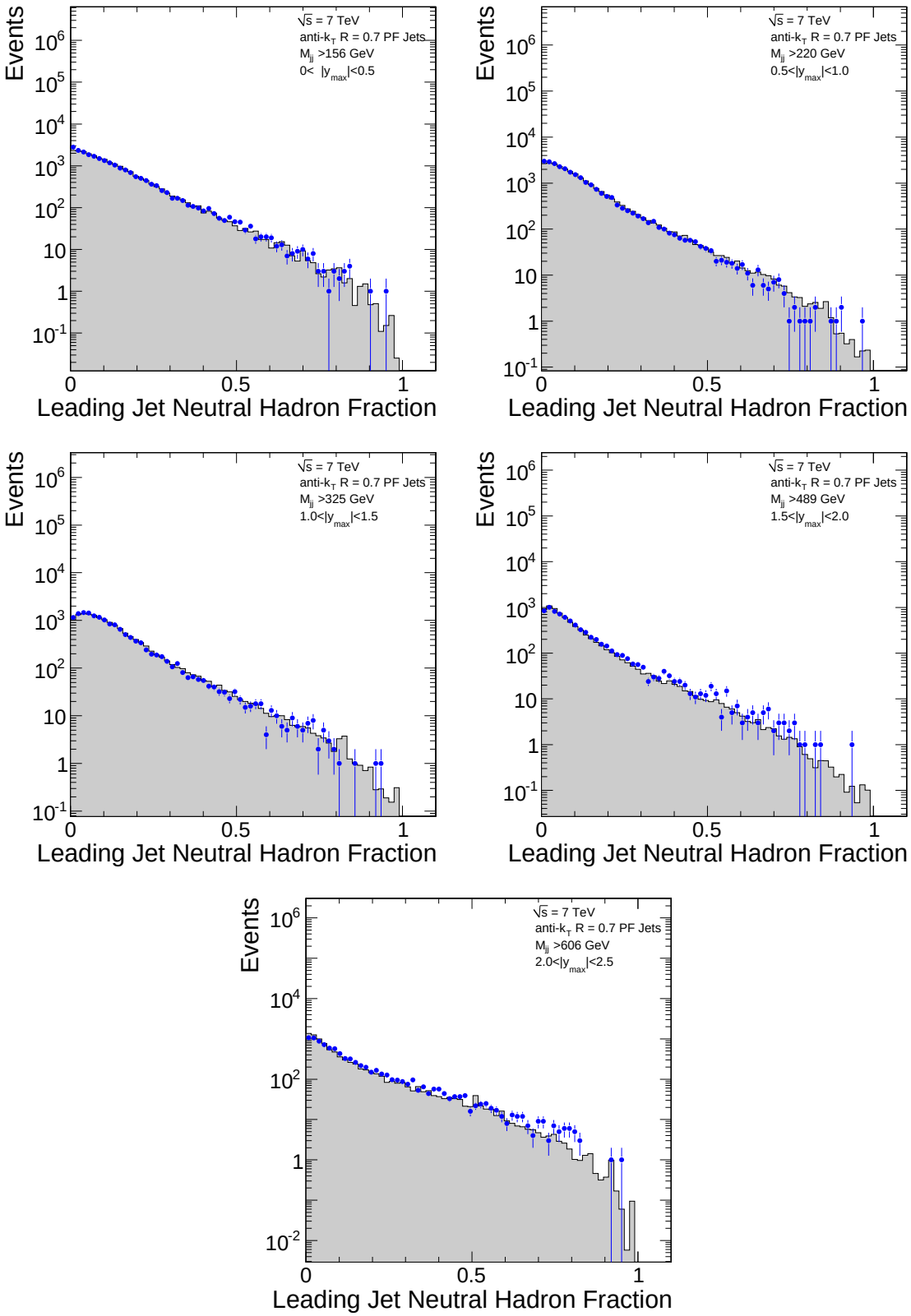

Figure B.6. The neutral hadron fraction of the leading jet for the five different y_{max} bins and for the HLT_Jet30U trigger, for data (points) and simulated (dashed histogram) events.

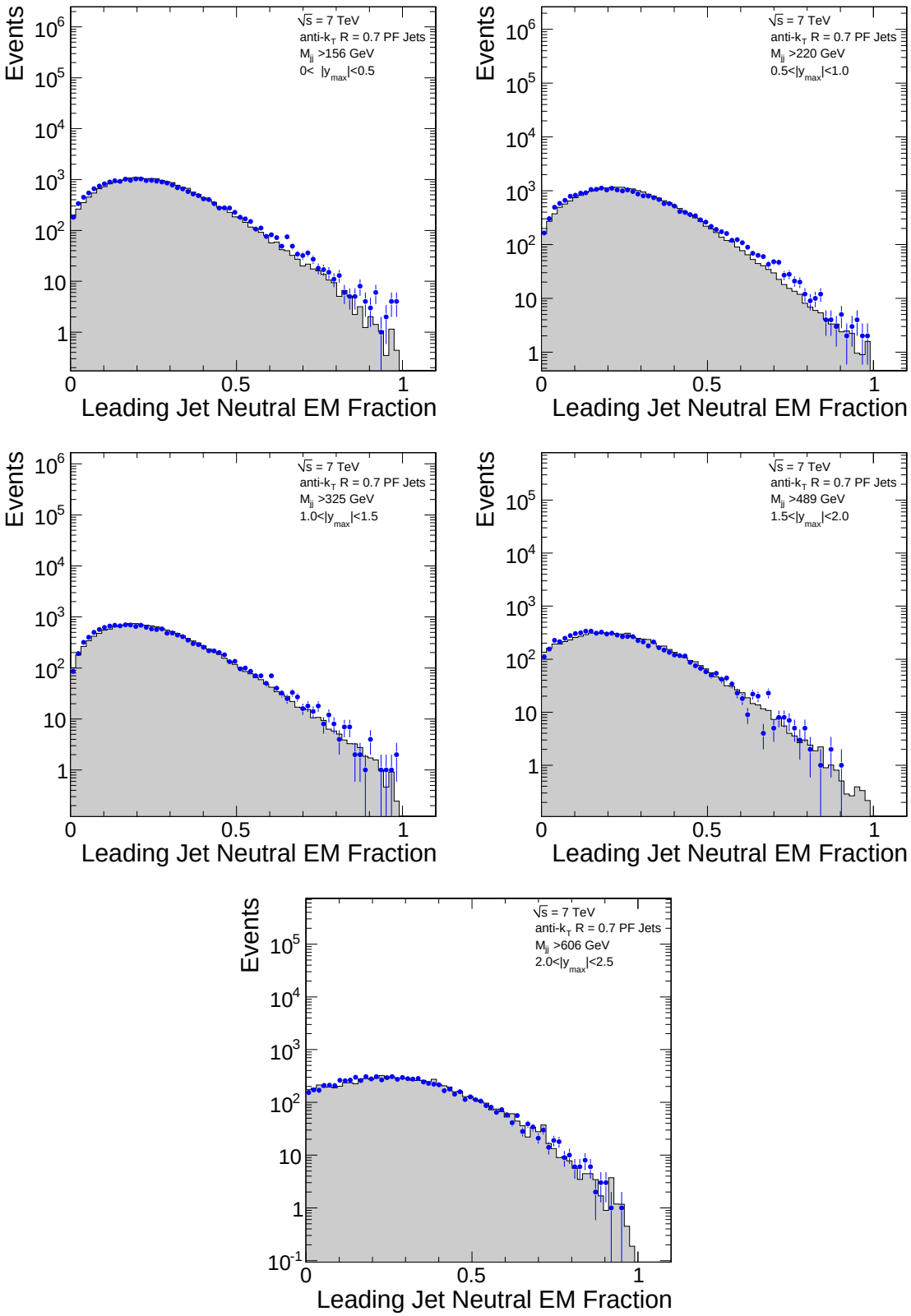

Figure B.7. The neutral electromagnetic fraction of the leading jet for the five different y_{max} bins and for the HLT_Jet30U trigger, for data (points) and simulated (dashed histogram) events.

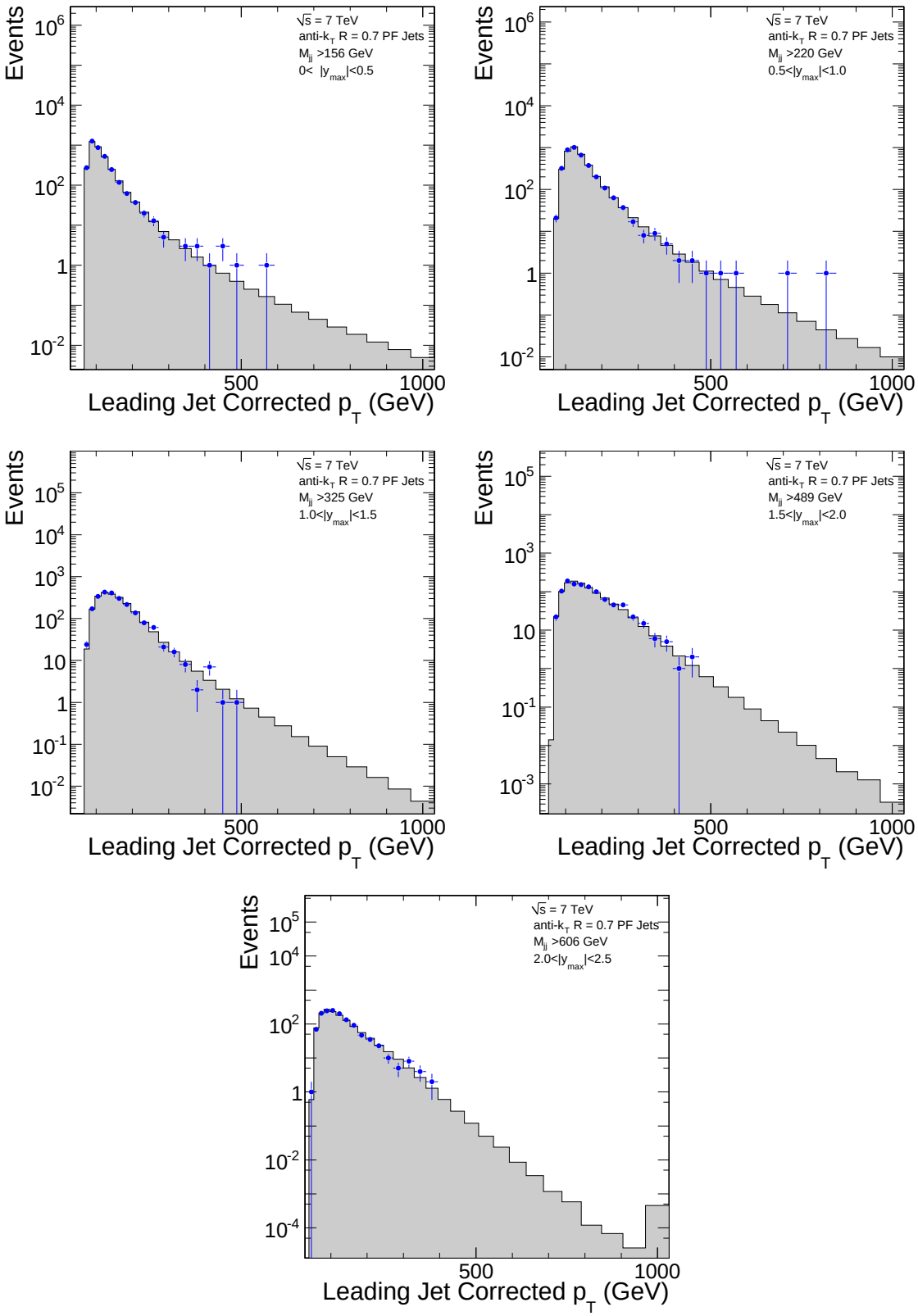

Figure B.8. The p_Tf of the leading jet for the five different y_{max} bins and for the HLT_Jet30U trigger, for data (points) and simulated (dashed histogram) events.

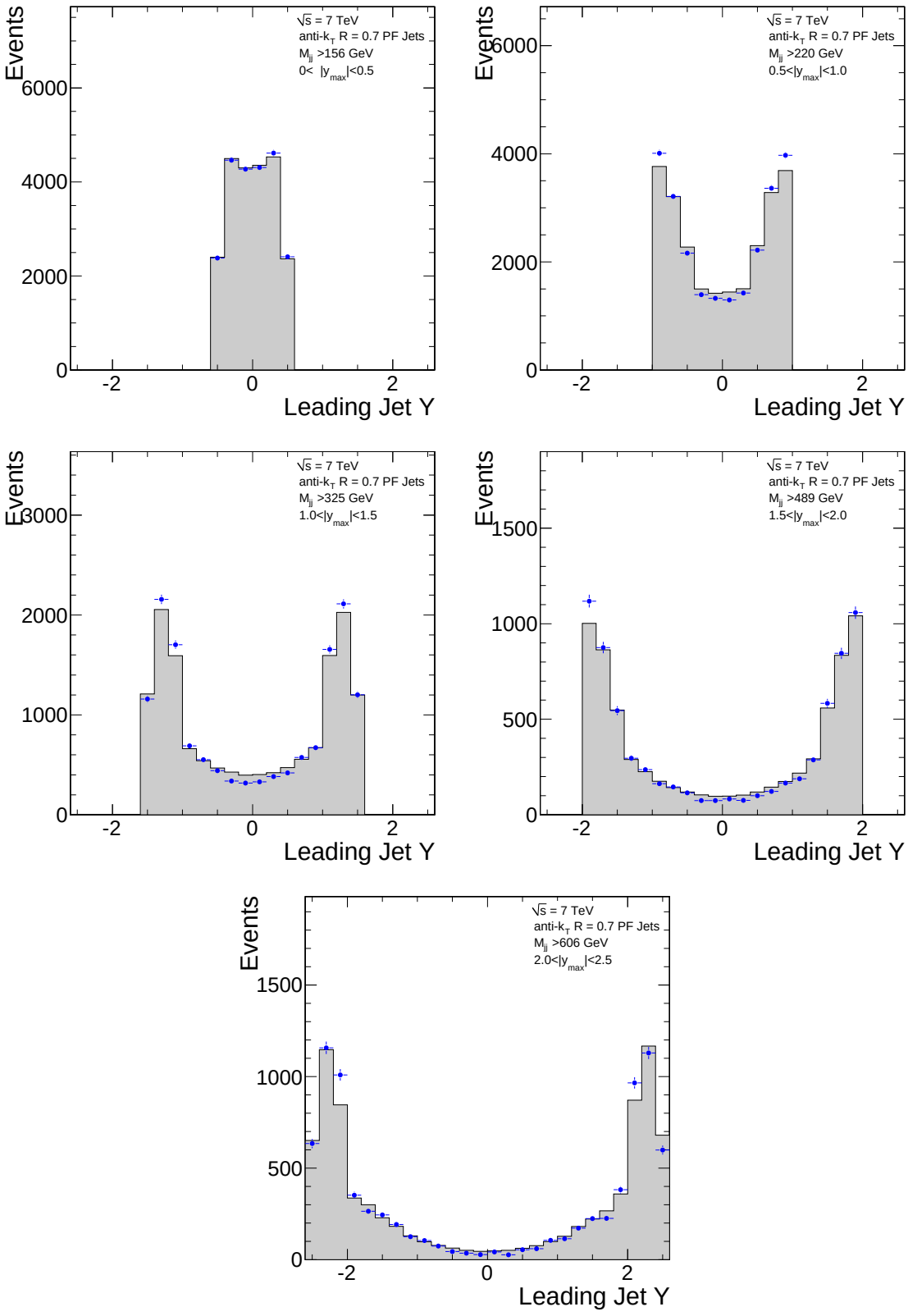

Figure B.9. The η of the leading jet for the five different y_{max} bins and for the HLT_Jet30U trigger, for data (points) and simulated (dashed histogram) events.

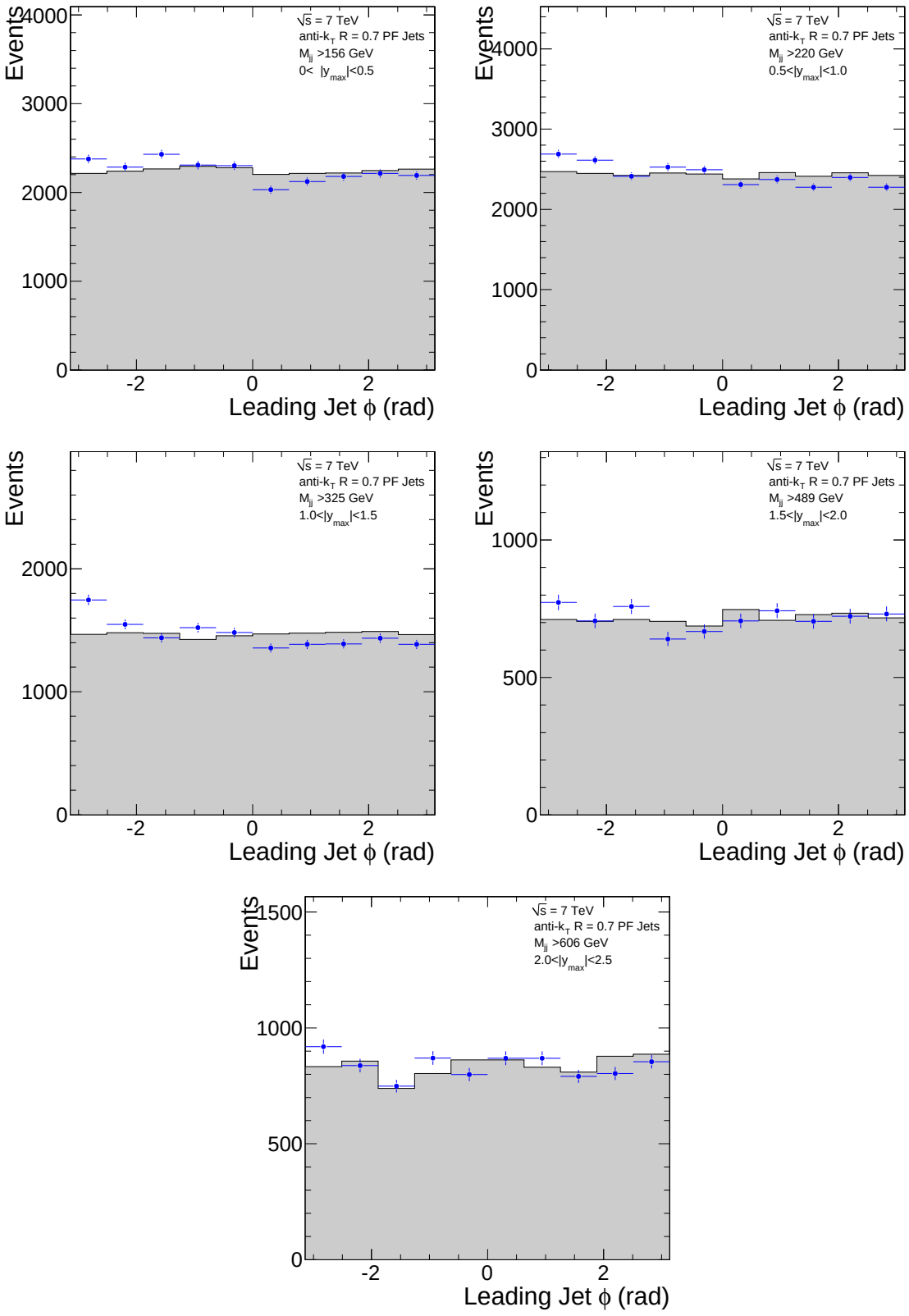

Figure B.10. The ϕ of the leading jet for the five different y_{max} bins and for the HLT_Jet30U trigger, for data (points) and simulated (dashed histogram) events.

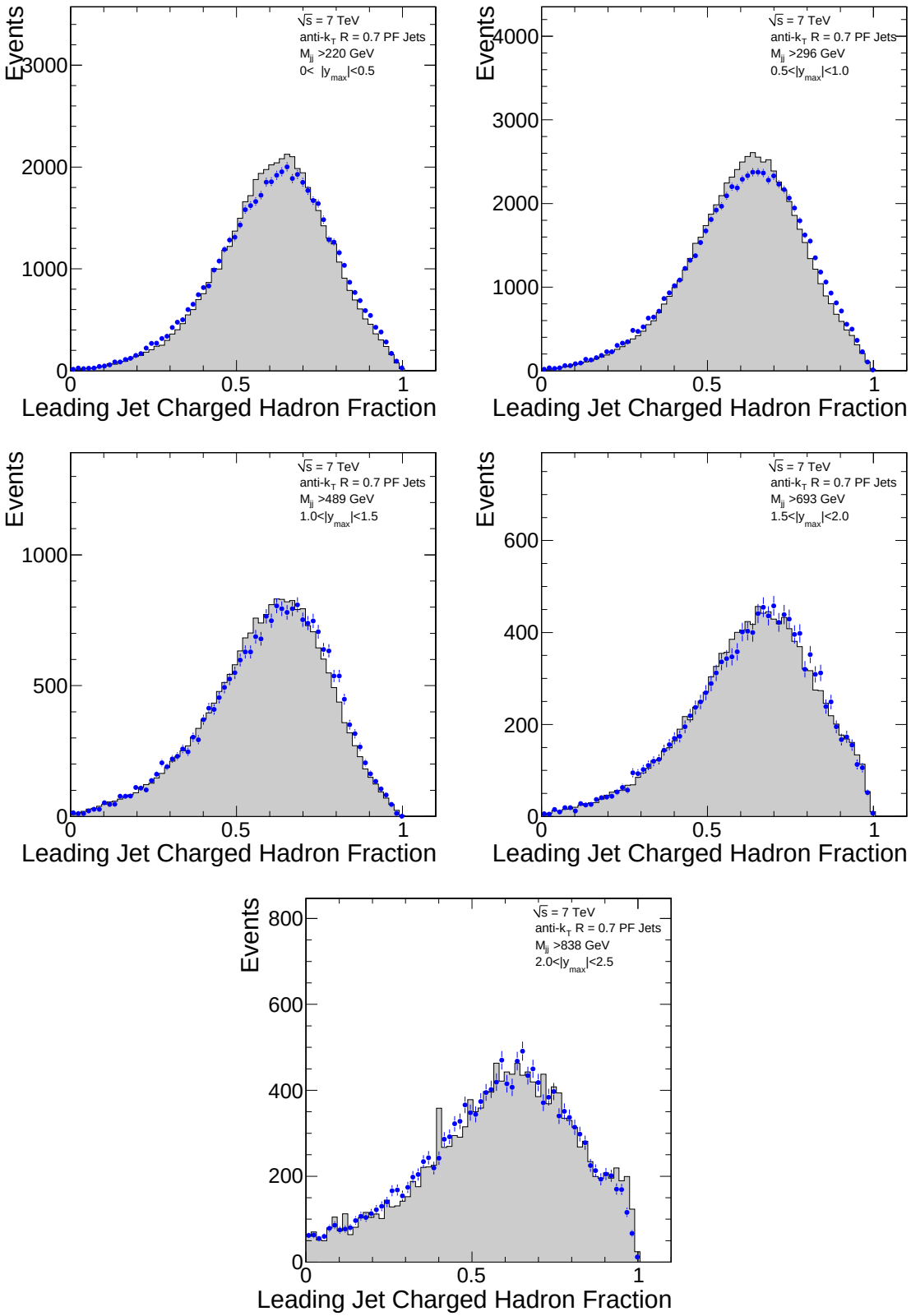

Figure B.11. The charged hadron fraction of the leading jet for the five different y_{max} bins and for the HLT_Jet50U trigger, for data (points) and simulated (dashed histogram) events.

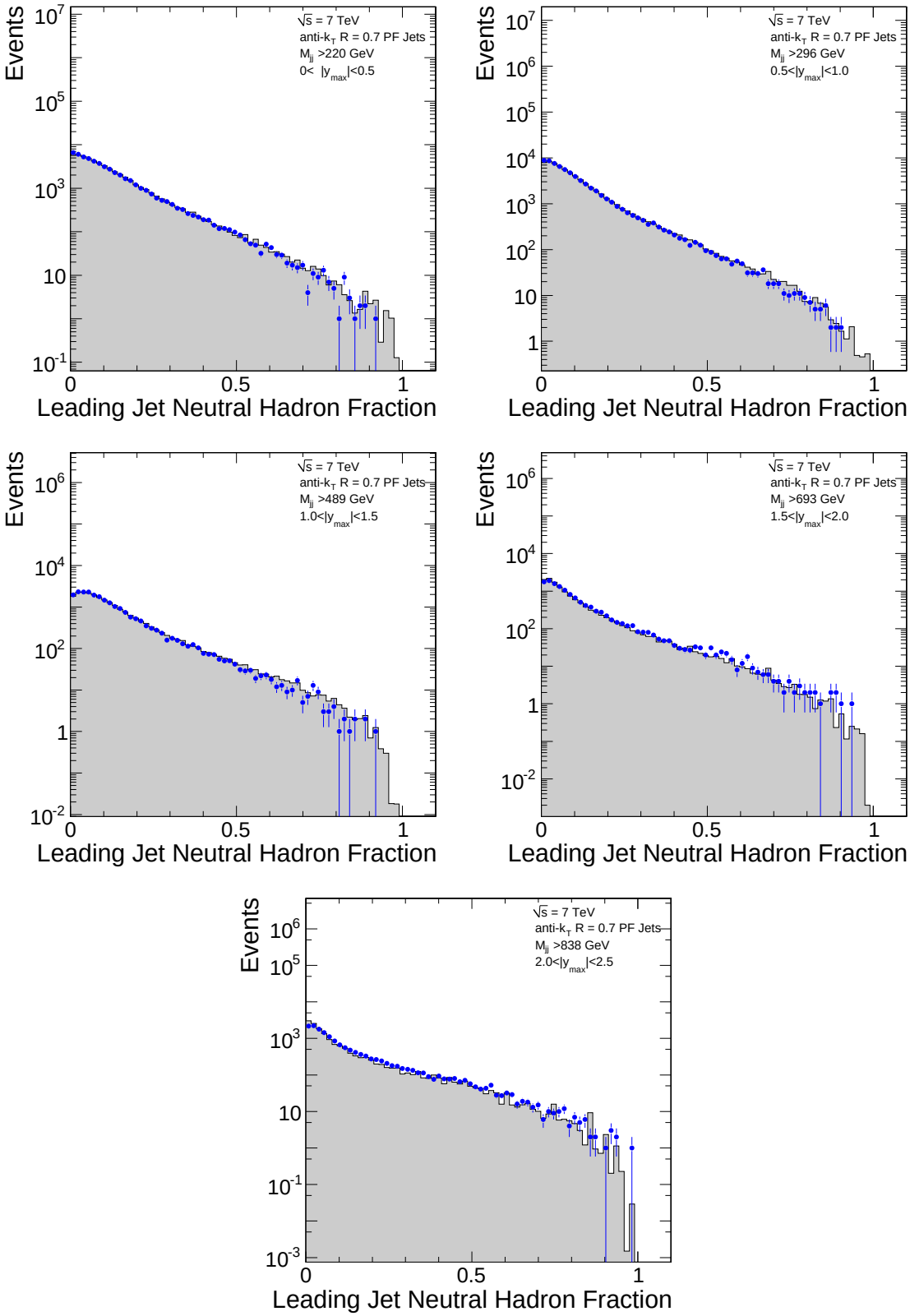

Figure B.12. The neutral hadron fraction of the leading jet for the five different y_{max} bins and for the HLT_Jet50U trigger, for data (points) and simulated (dashed histogram) events.

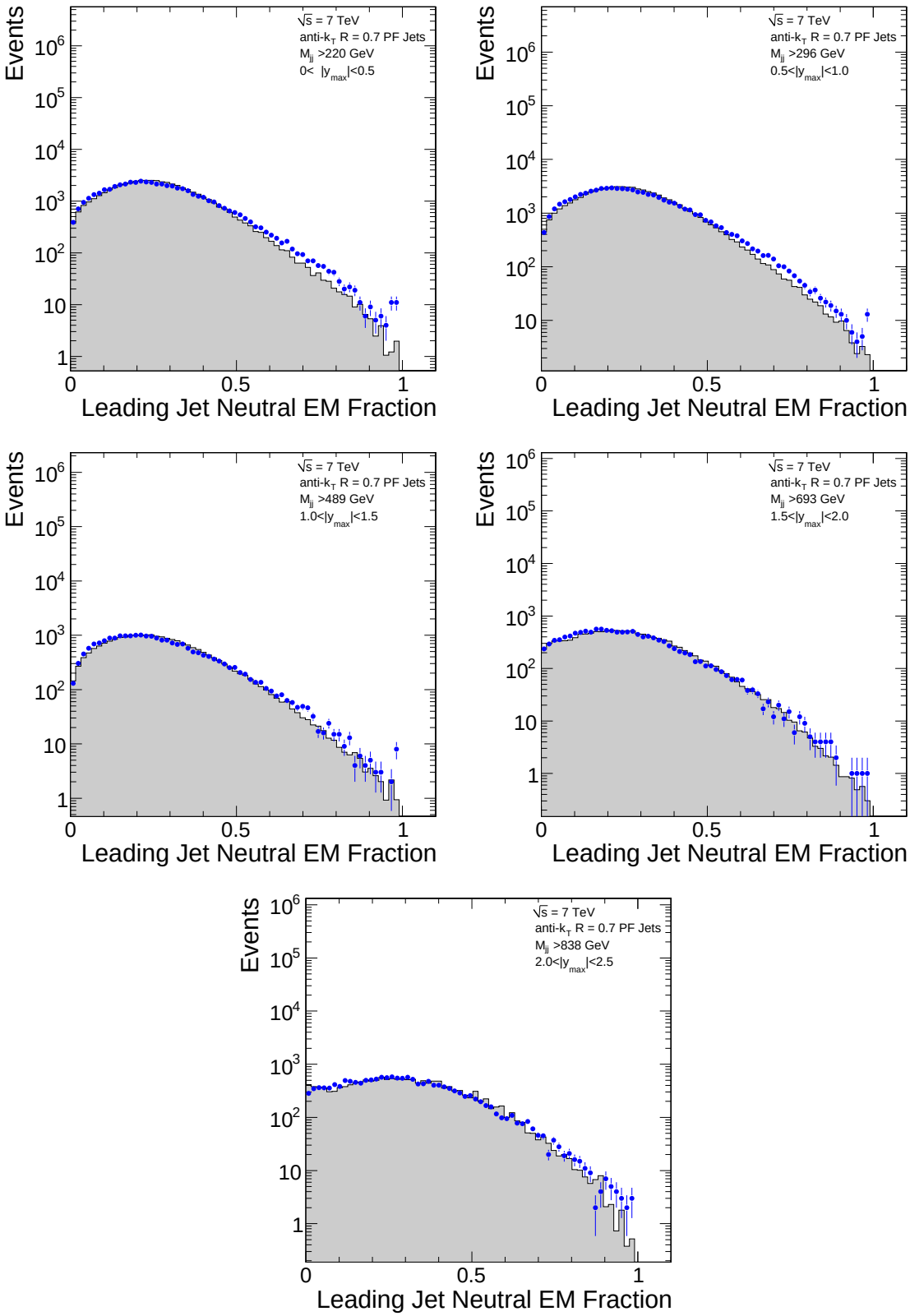

Figure B.13. The neutral electromagnetic fraction of the leading jet for the five different y_{max} bins and for the HLT_Jet50U trigger, for data (points) and simulated (dashed histogram) events.

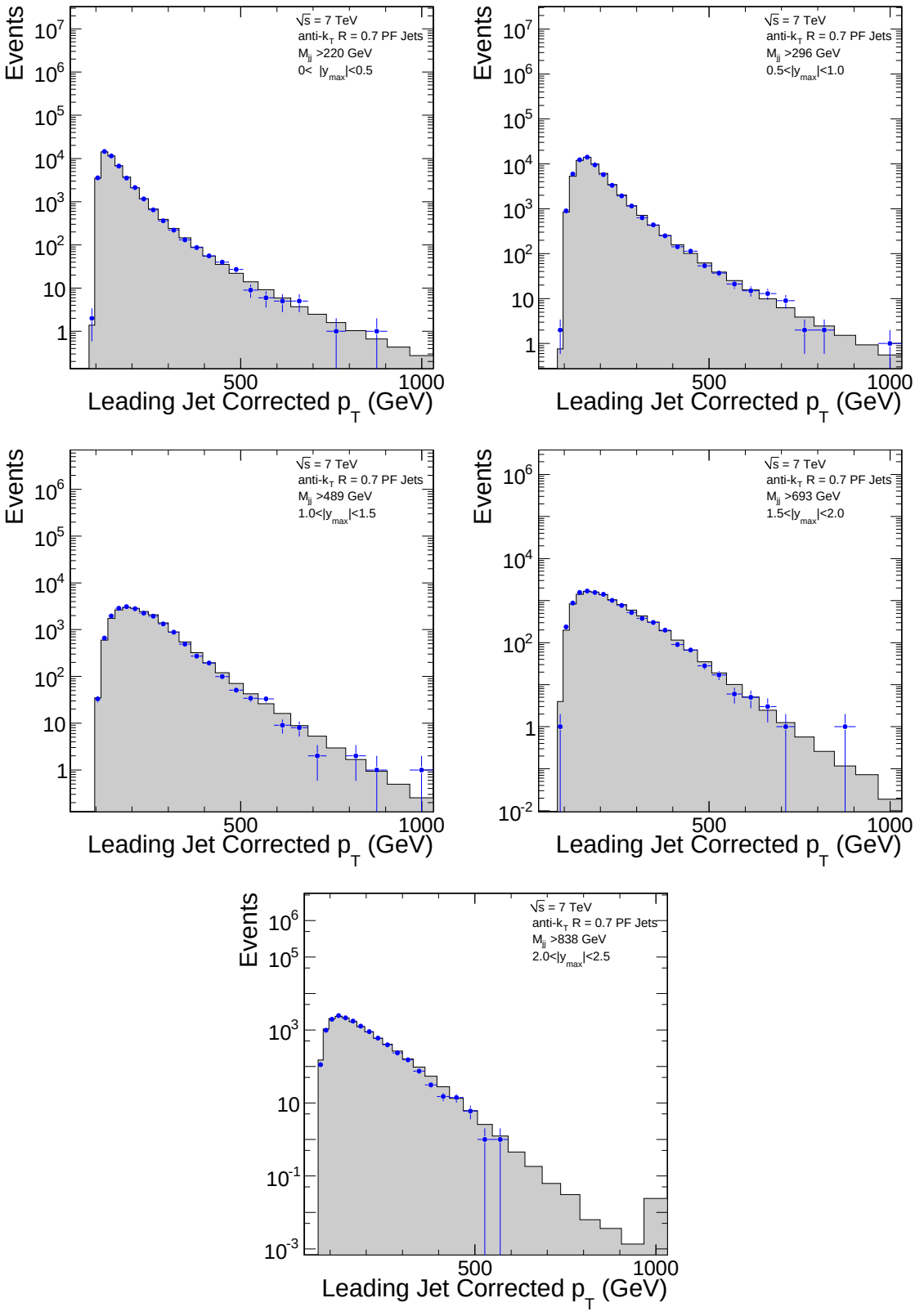

Figure B.14. The p_Tf of the leading jet for the five different y_{max} bins and for the HLT_Jet50U trigger, for data (points) and simulated (dashed histogram) events.

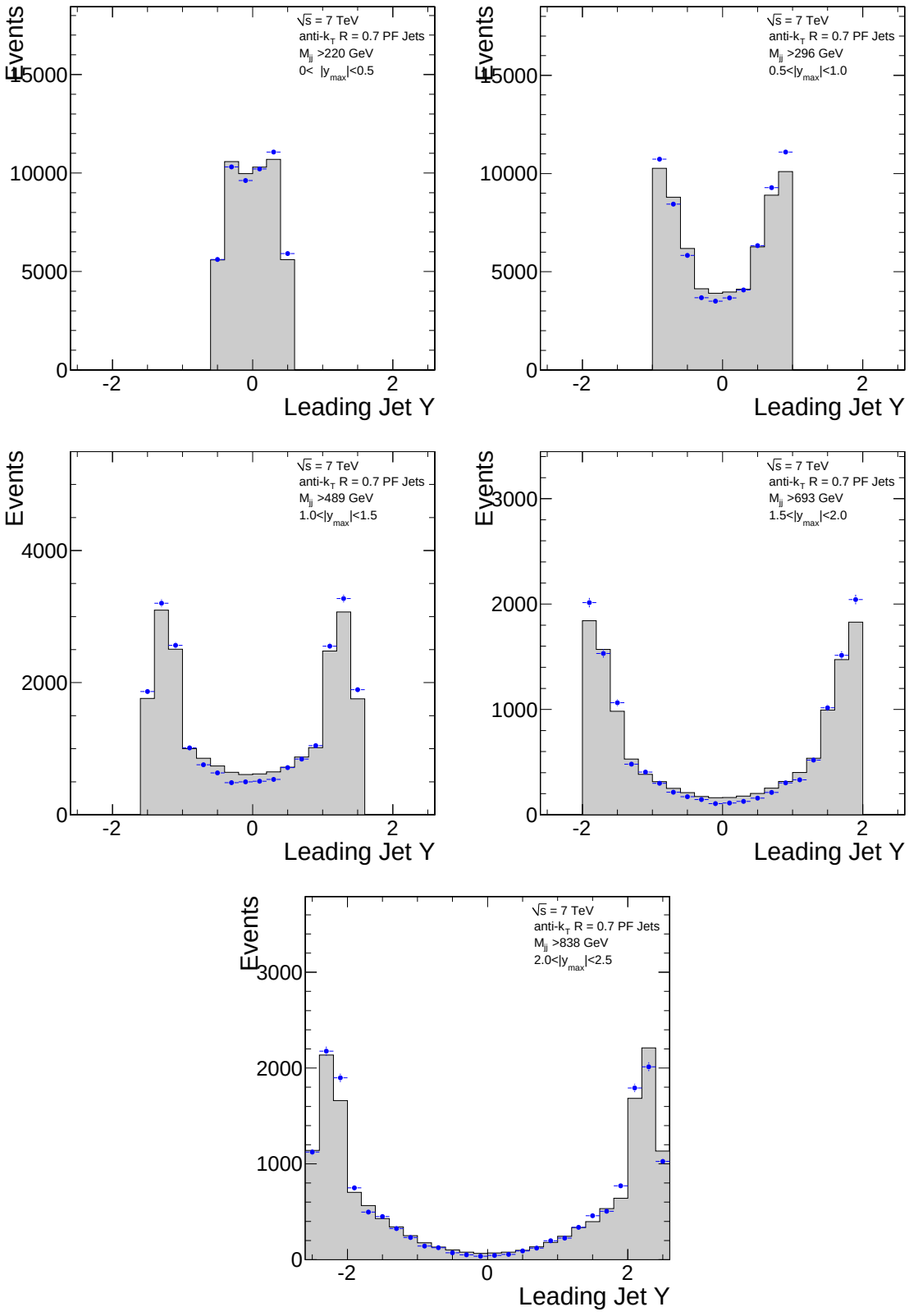

Figure B.15. The η of the leading jet for the five different y_{max} bins and for the HLT_Jet50U trigger, for data (points) and simulated (dashed histogram) events.

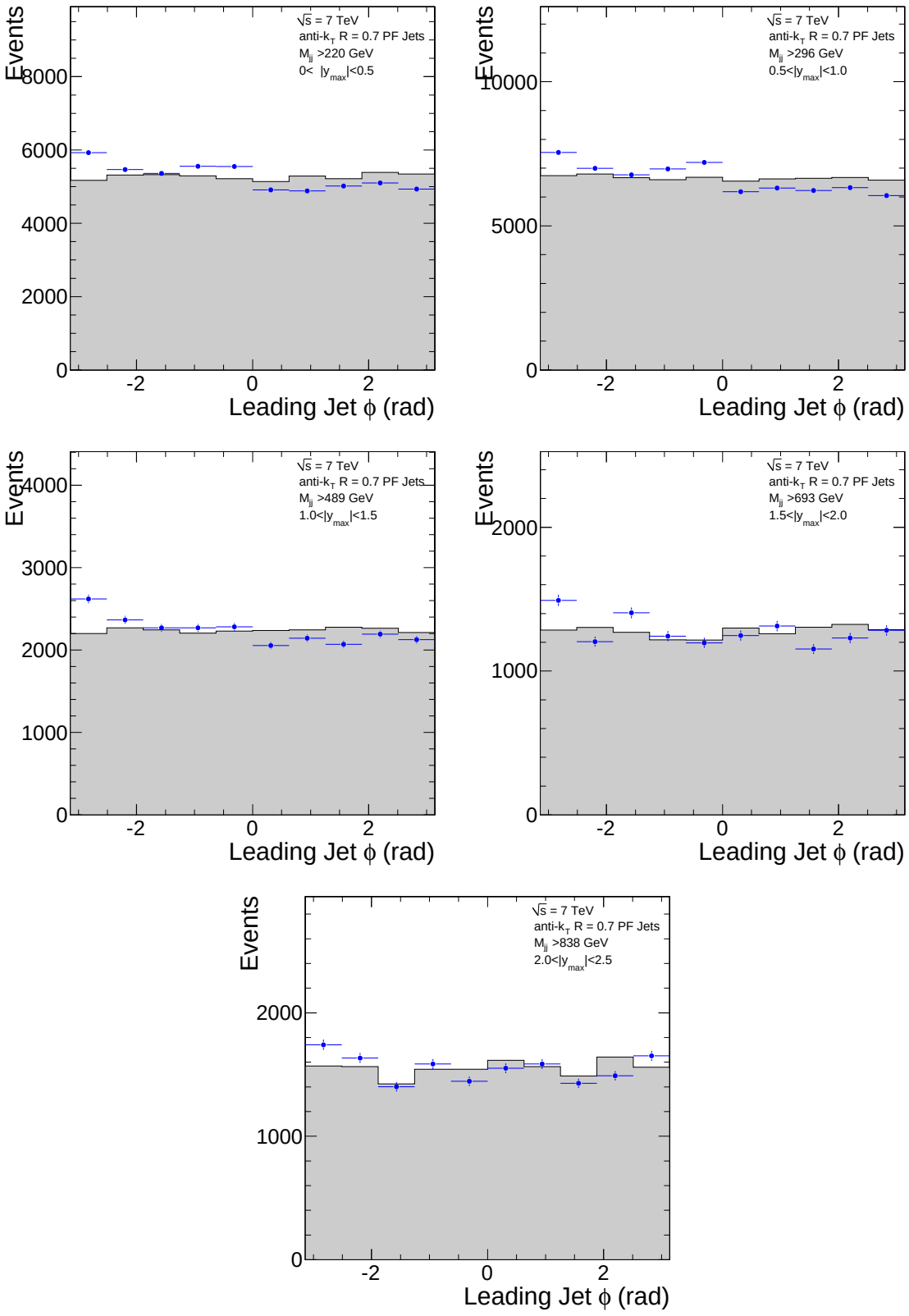

Figure B.16. The ϕ of the leading jet for the five different y_{max} bins and for the HLT_Jet50U trigger, for data (points) and simulated (dashed histogram) events.

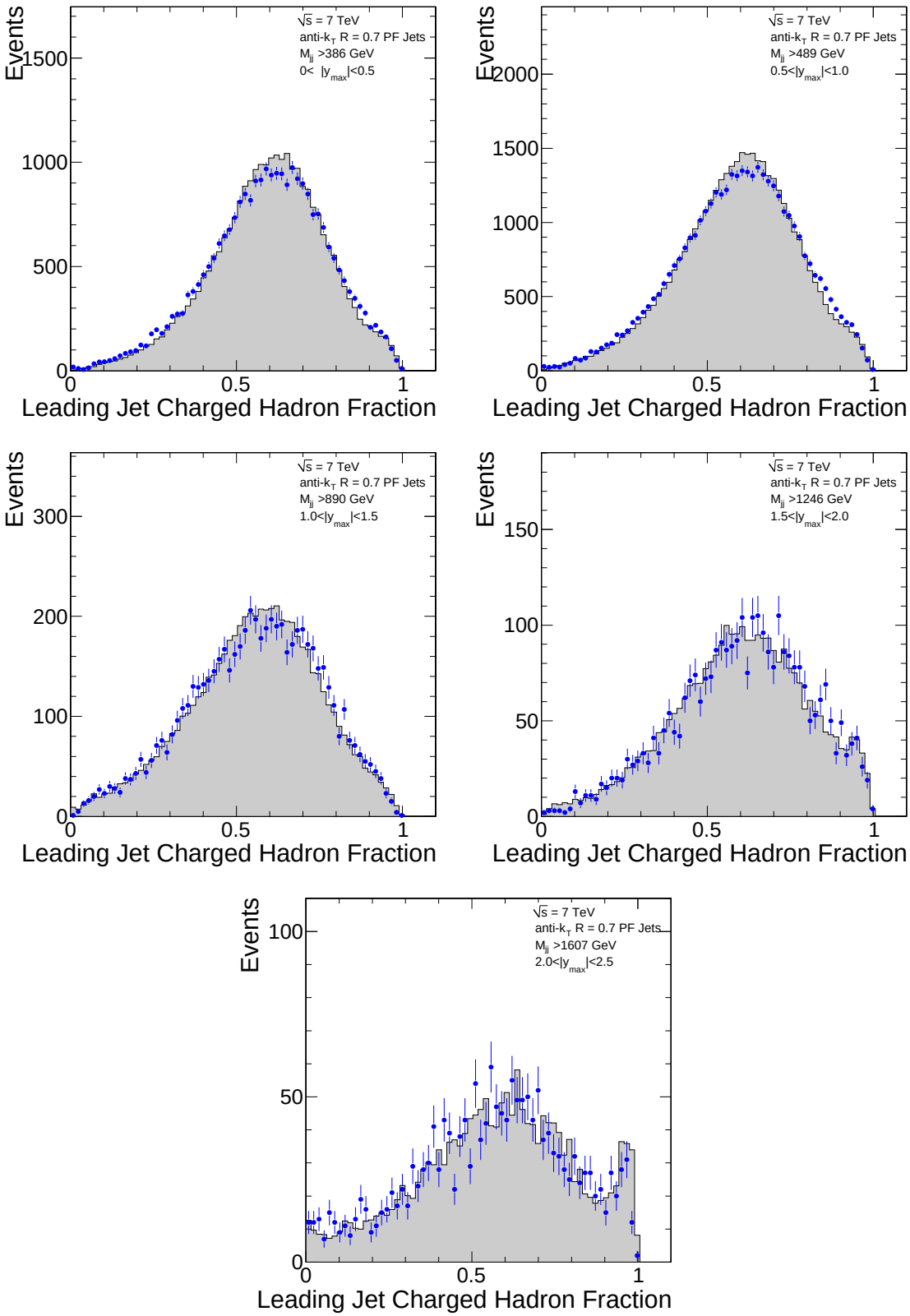

Figure B.17. The charged hadron fraction of the leading jet for the five different y_{max} bins and for the HLT_Jet100U trigger, for data (points) and simulated (dashed histogram) events.

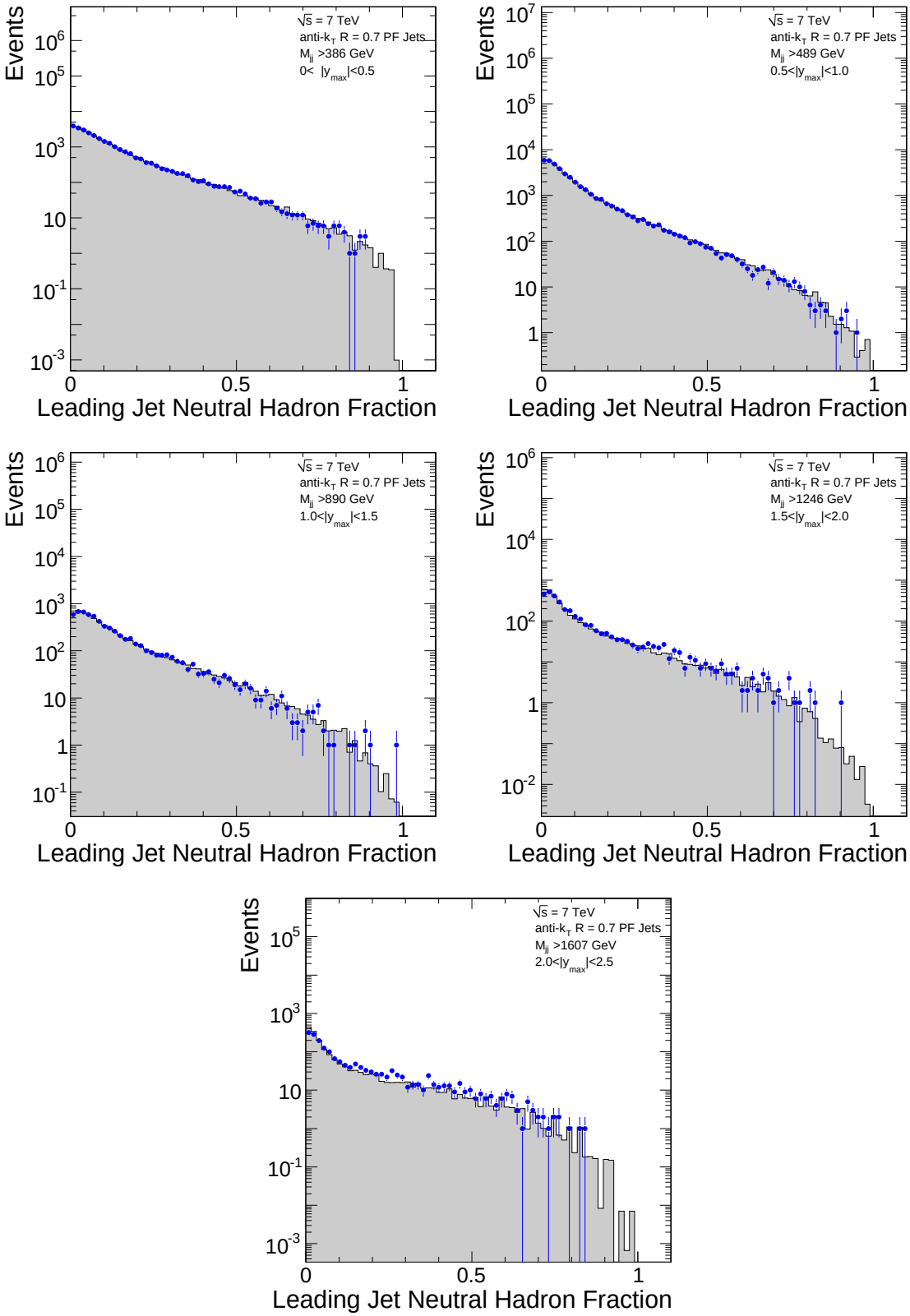

Figure B.18. The neutral hadron fraction of the leading jet for the five different y_{max} bins and for the HLT_Jet100U trigger, for data (points) and simulated (dashed histogram) events.

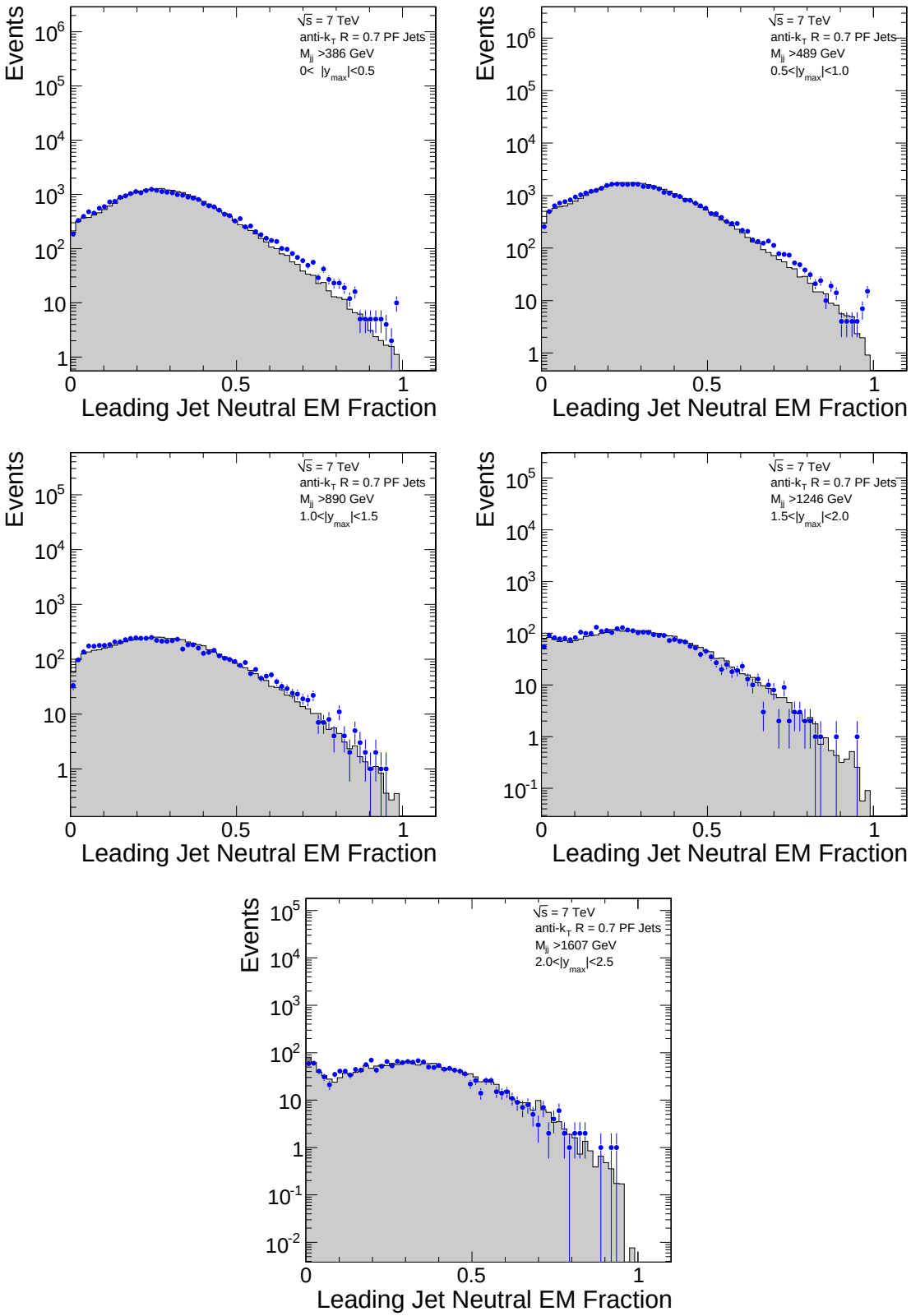

Figure B.19. The neutral electromagnetic fraction of the leading jet for the five different y_{max} bins and for the HLT_Jet100U trigger, for data (points) and simulated (dashed histogram) events.

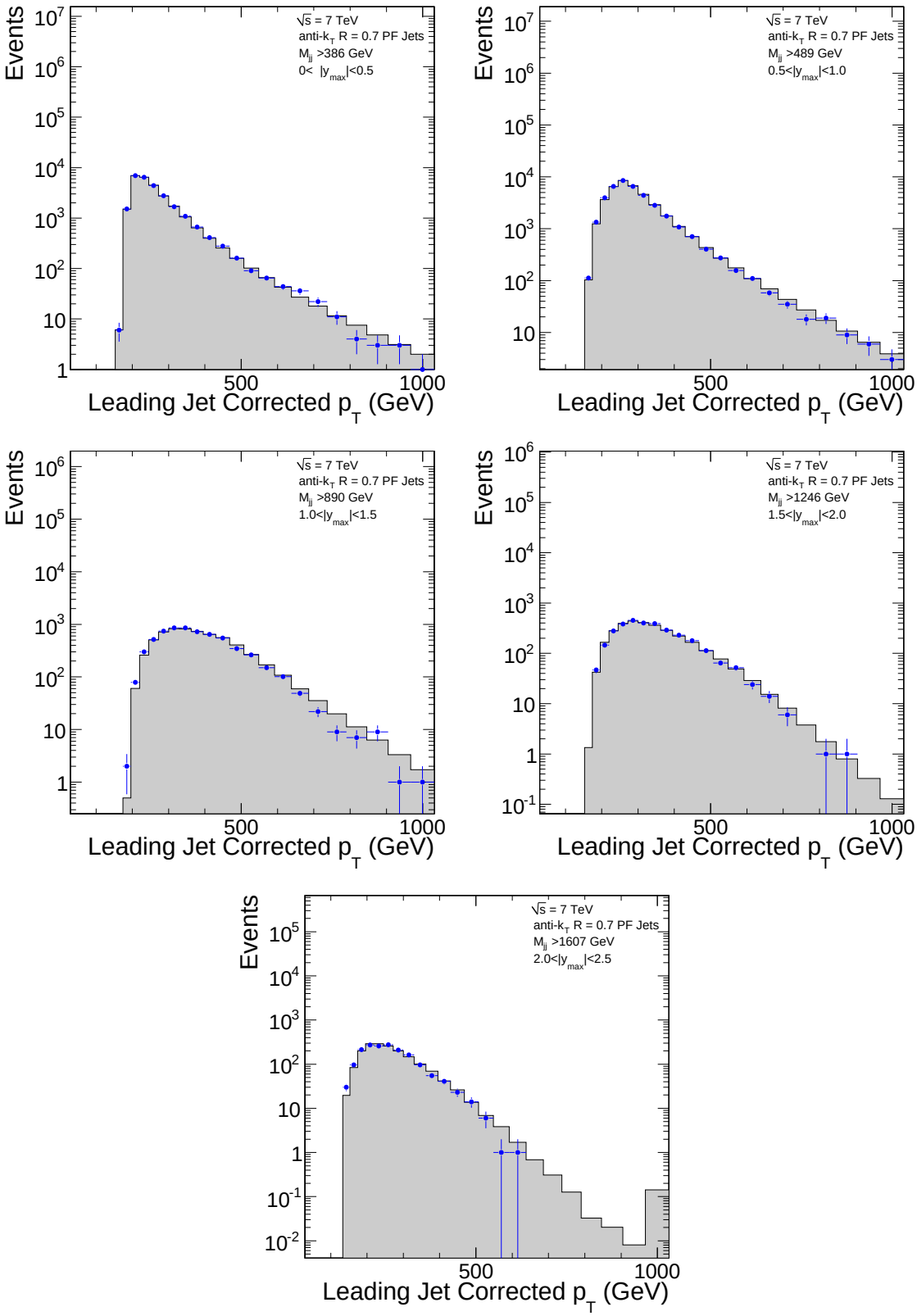

Figure B.20. The p_Tf of the leading jet for the five different y_{max} bins and for the HLT_Jet100U trigger, for data (points) and simulated (dashed histogram) events.

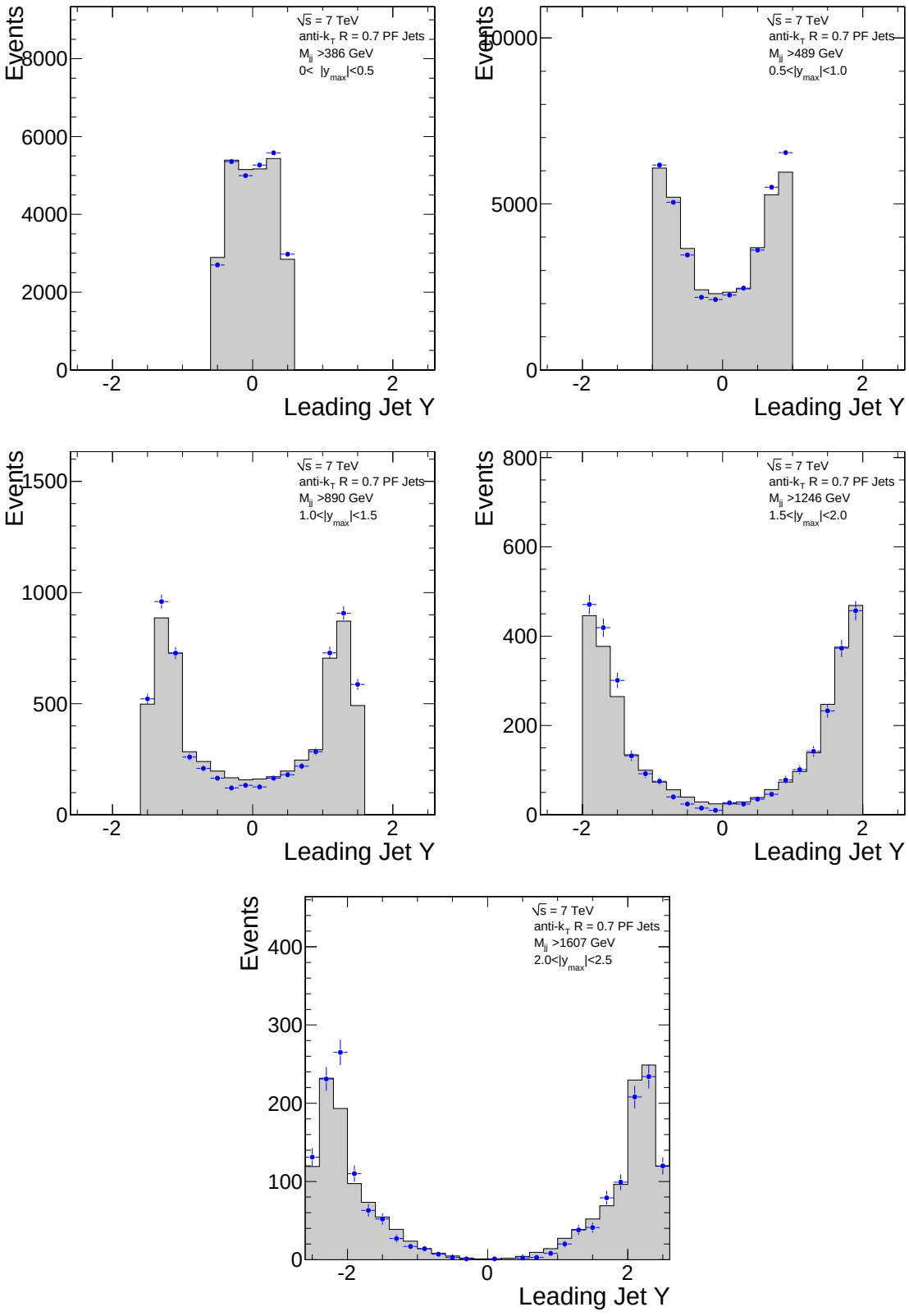

Figure B.21. The η of the leading jet for the five different y_{max} bins and for the HLT_Jet100U trigger, for data (points) and simulated (dashed histogram) events.

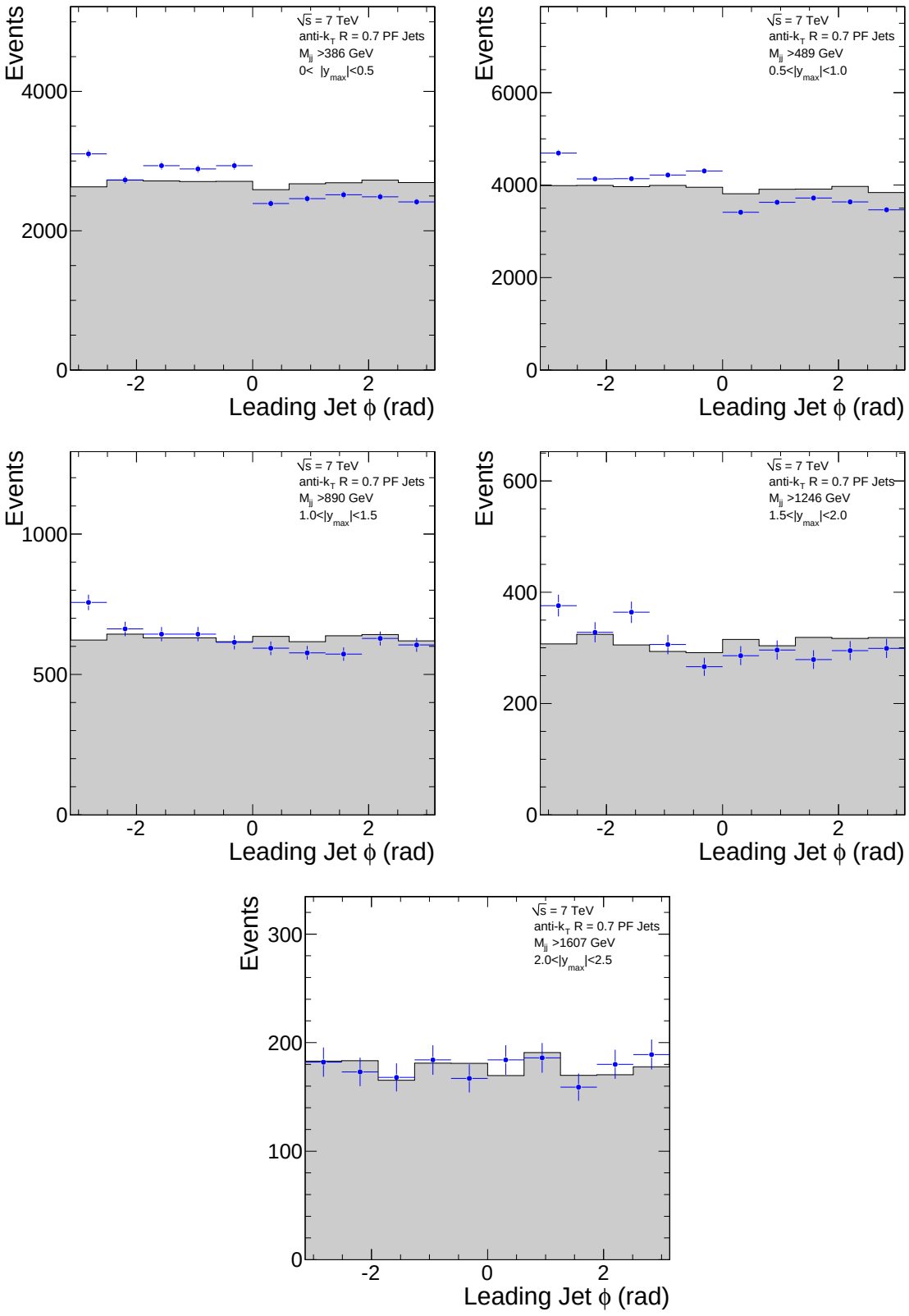

Figure B.22. The ϕ of the leading jet for the five different y_{max} bins and for the HLT_Jet100U trigger, for data (points) and simulated (dashed histogram) events.

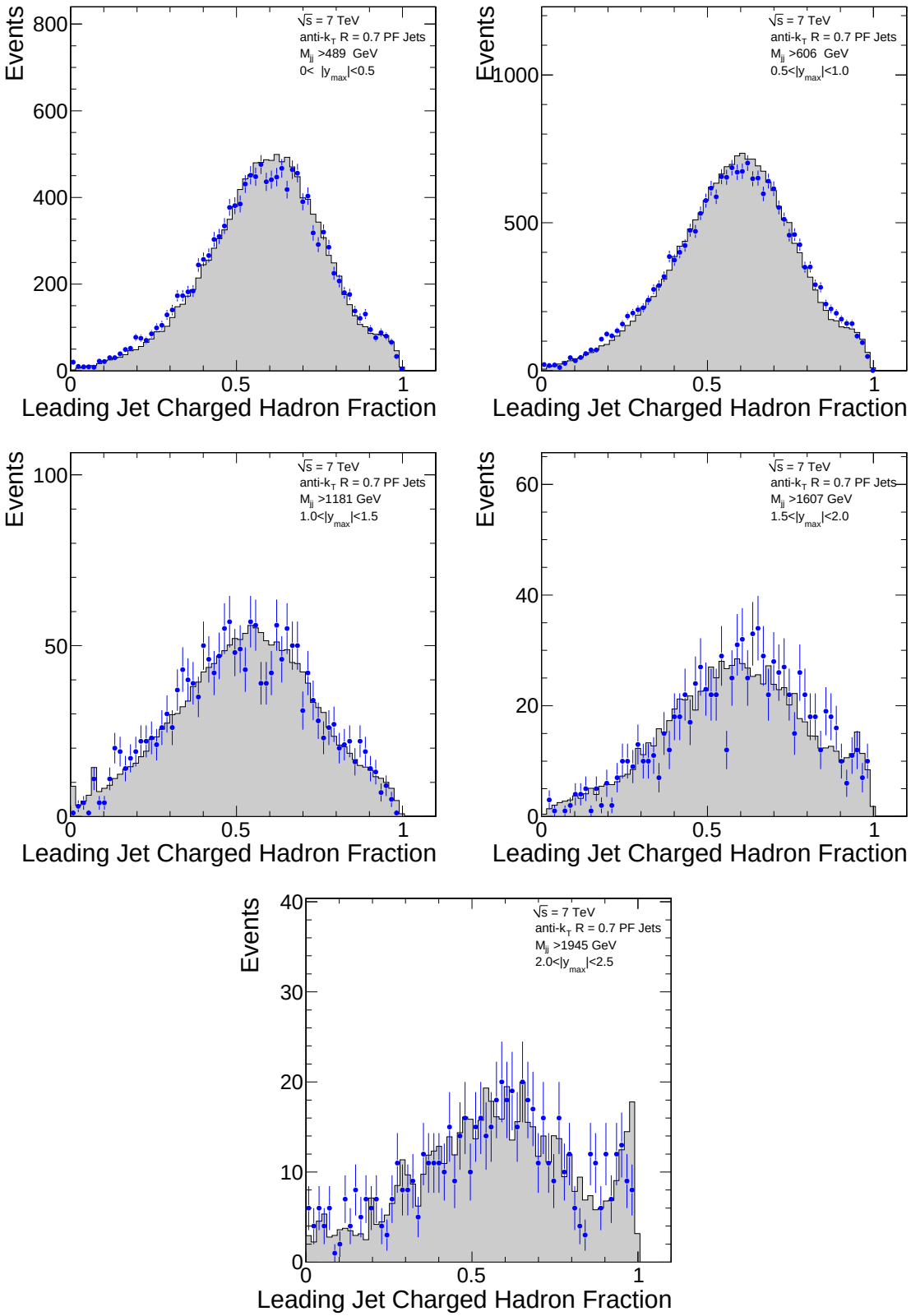

Figure B.23. The charged hadron fraction of the leading jet for the five different y_{max} bins and for the HLT_Jet140U trigger, for data (points) and simulated (dashed histogram) events.

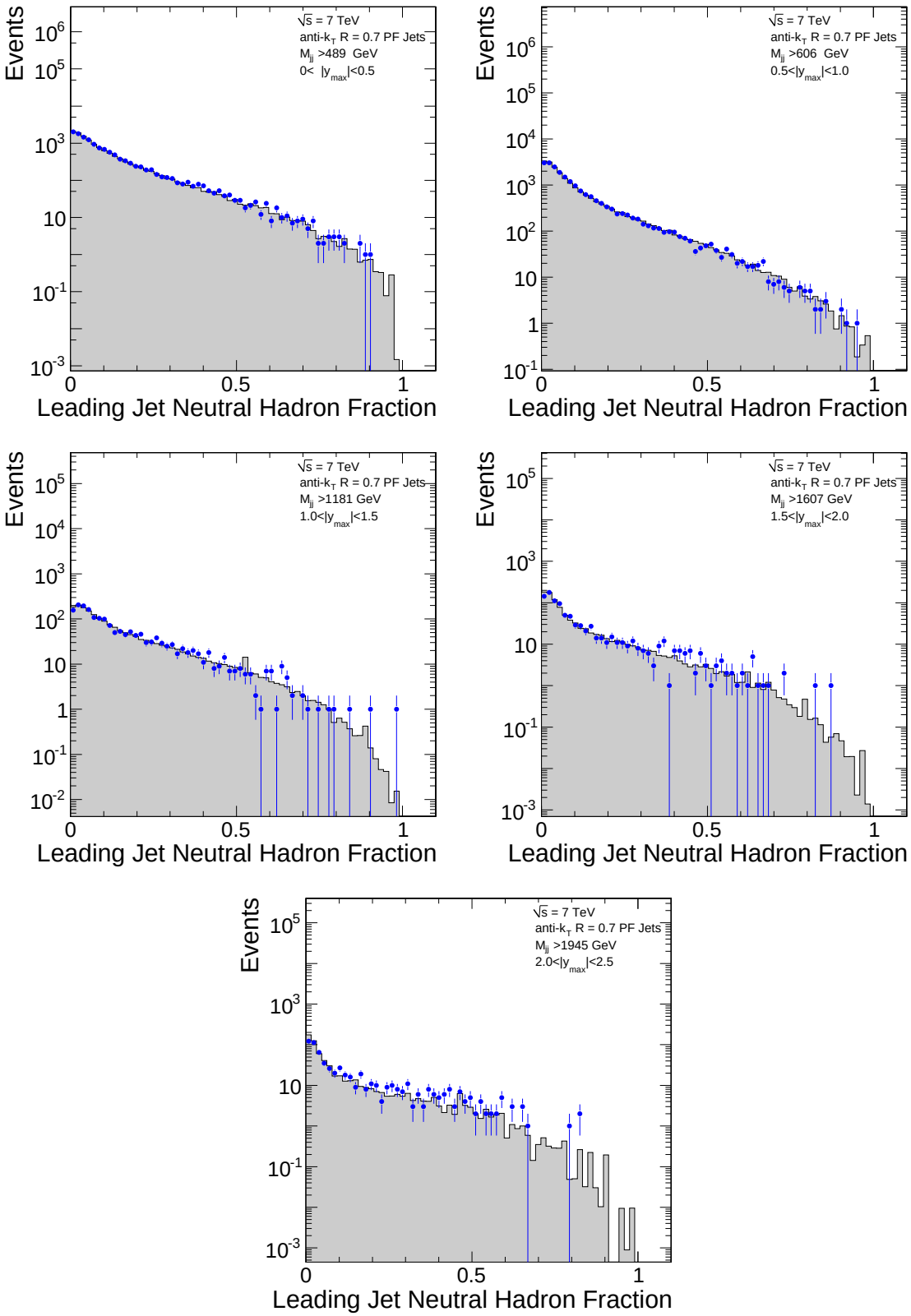

Figure B.24. The neutral hadron fraction of the leading jet for the five different y_{max} bins and for the HLT_Jet140U trigger, for data (points) and simulated (dashed histogram) events.

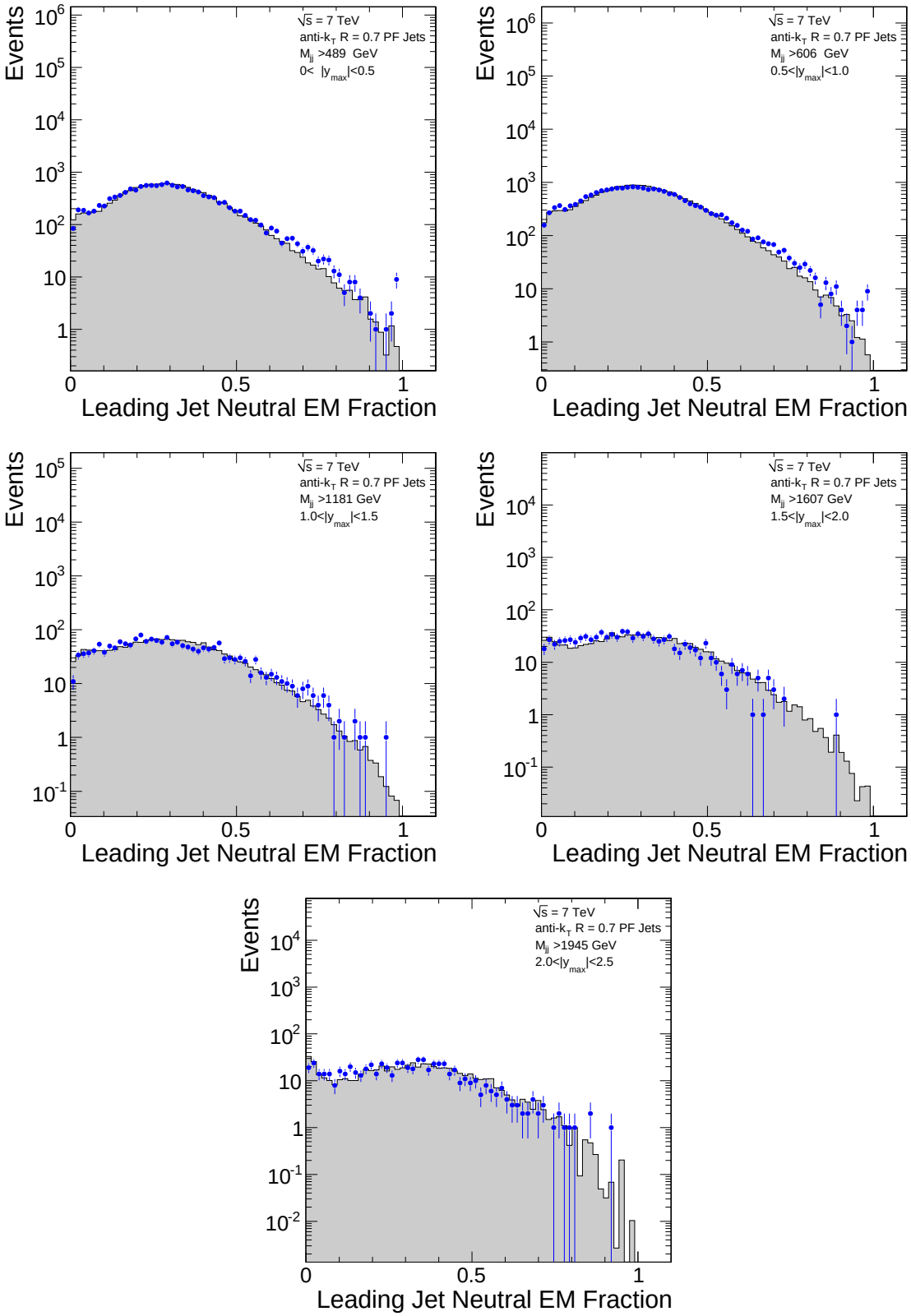

Figure B.25. The neutral electromagnetic fraction of the leading jet for the five different y_{max} bins and for the HLT_Jet140U trigger, for data (points) and simulated (dashed histogram) events.

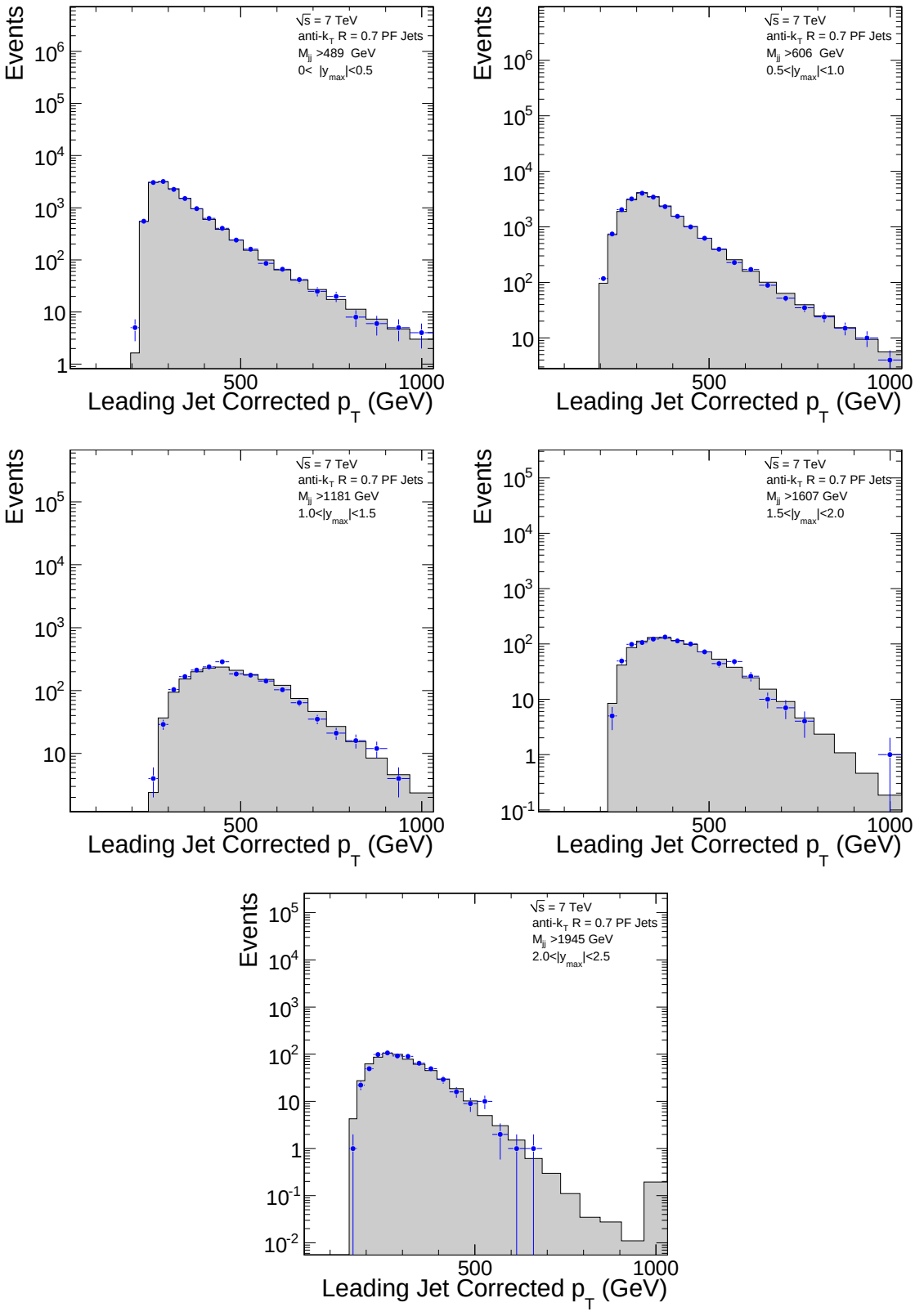

Figure B.26. The p_Tf of the leading jet for the five different y_{max} bins and for the HLT_Jet140U trigger, for data (points) and simulated (dashed histogram) events.

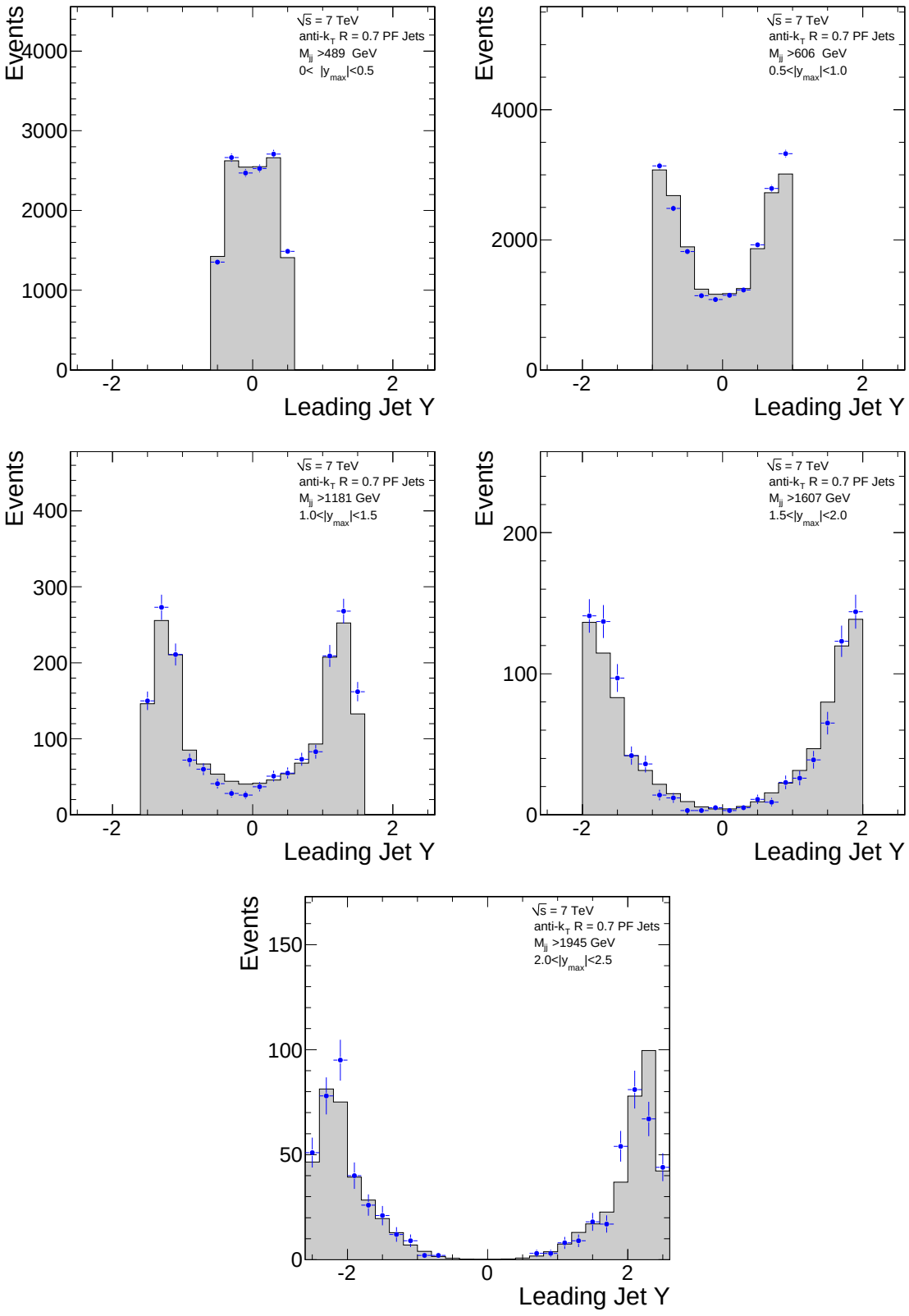

Figure B.27. The η of the leading jet for the five different y_{max} bins and for the HLT_Jet140U trigger, for data (points) and simulated (dashed histogram) events.

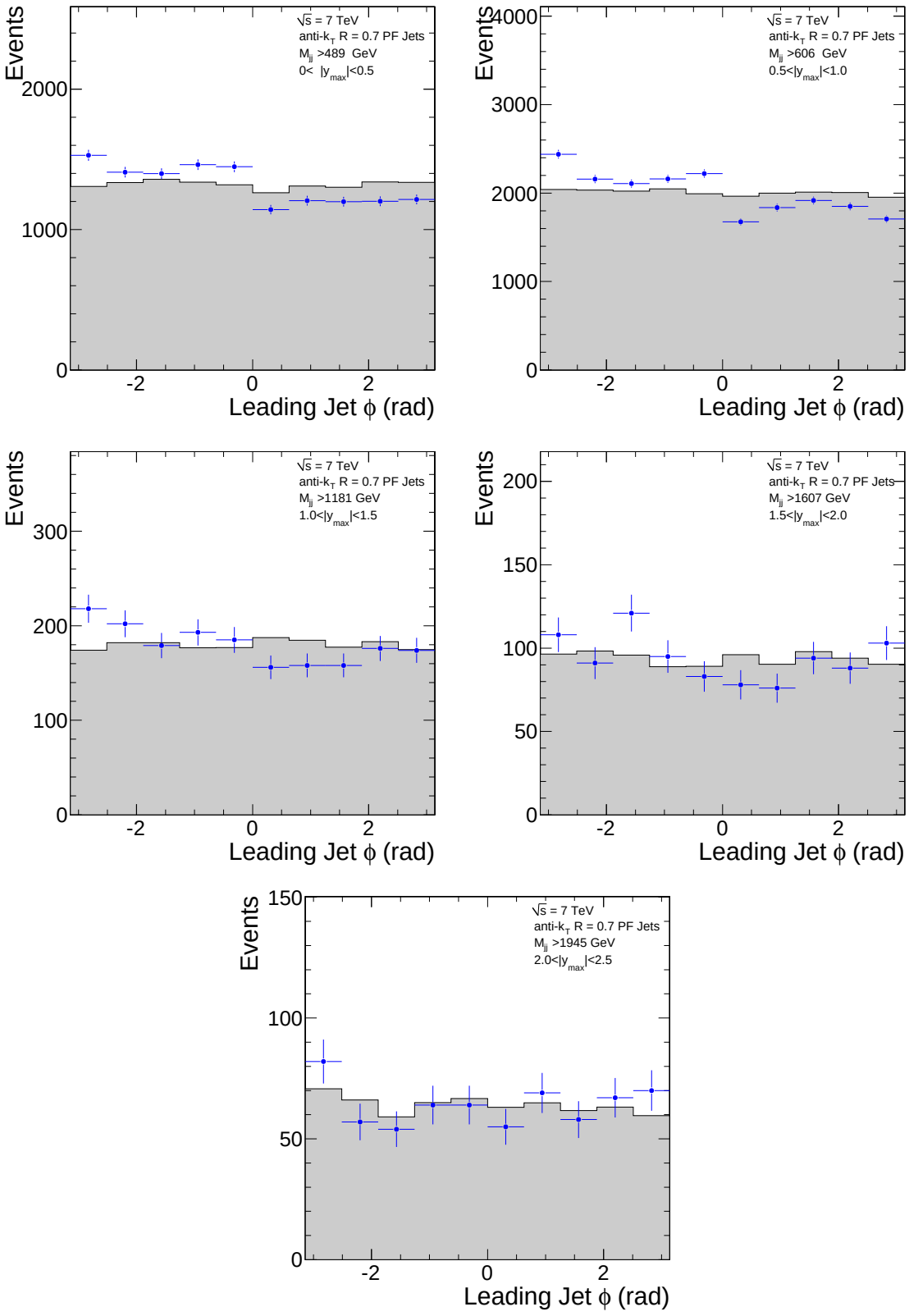

Figure B.28. The ϕ of the leading jet for the five different y_{max} bins and for the HLT_Jet140U trigger, for data (points) and simulated (dashed histogram) events.

B.2. Appendix D

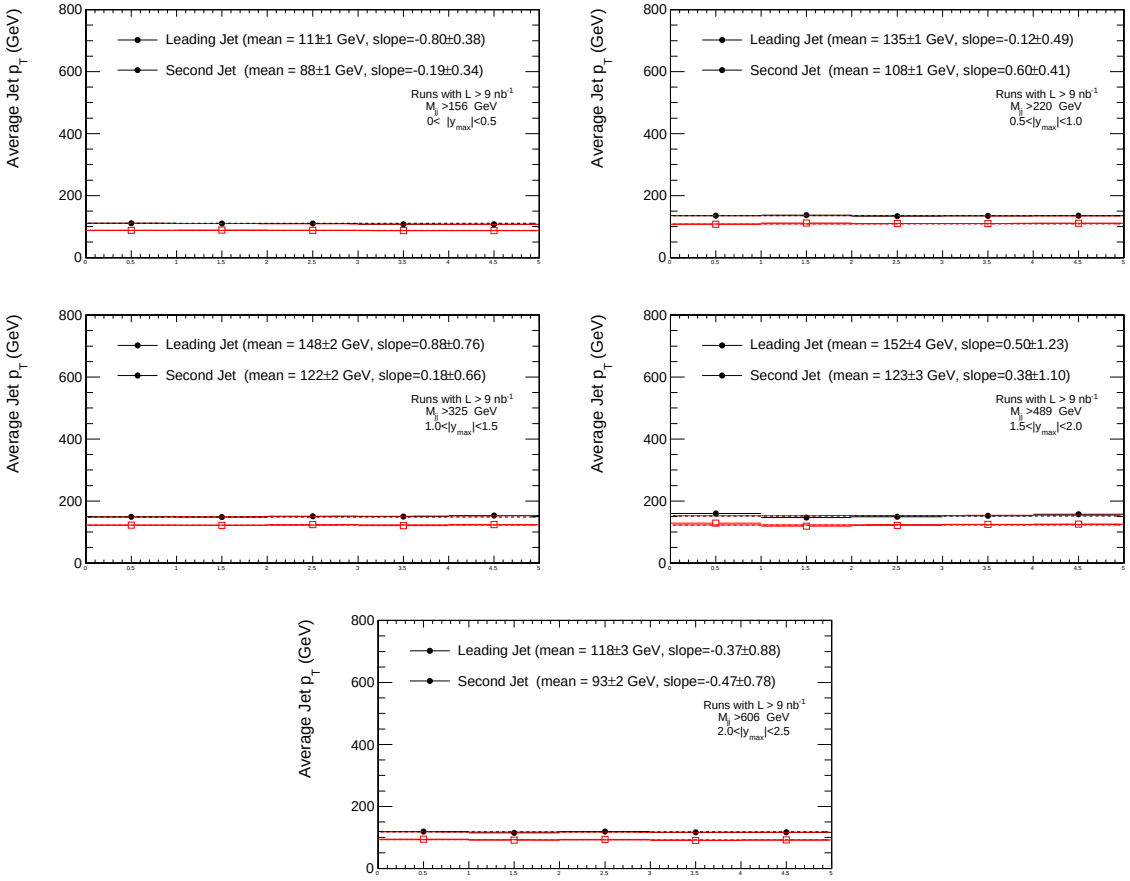

Figure B.29. The p_T of the leading and second jet for the five different y_{max} bins and for the HLT_Jet30U trigger as a function of time (run number), fitted with a first degree polynomial.

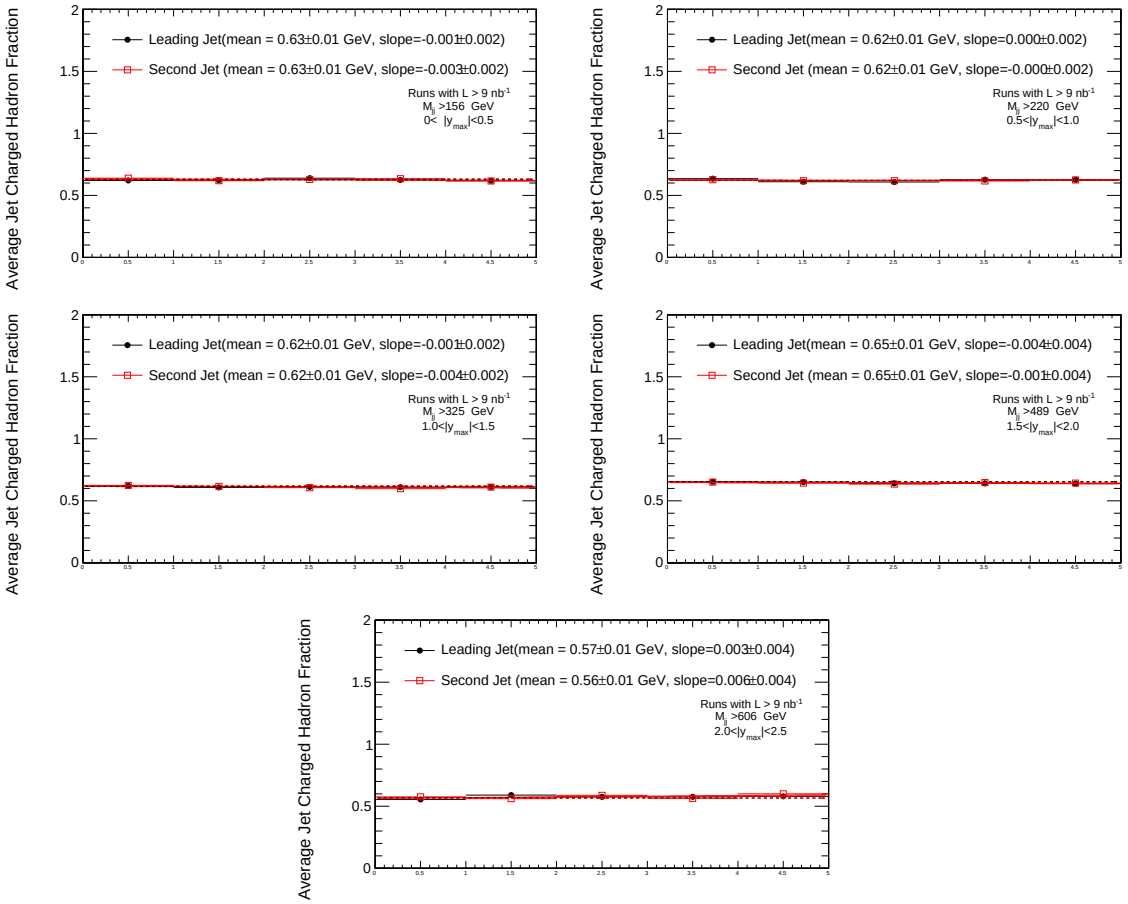

Figure B.30. The charged hadron fraction of the leading and second jet for the five different y_{max} bins and for the HLT_Jet30U trigger as a function of time (run number), fitted with a first degree polynomial.

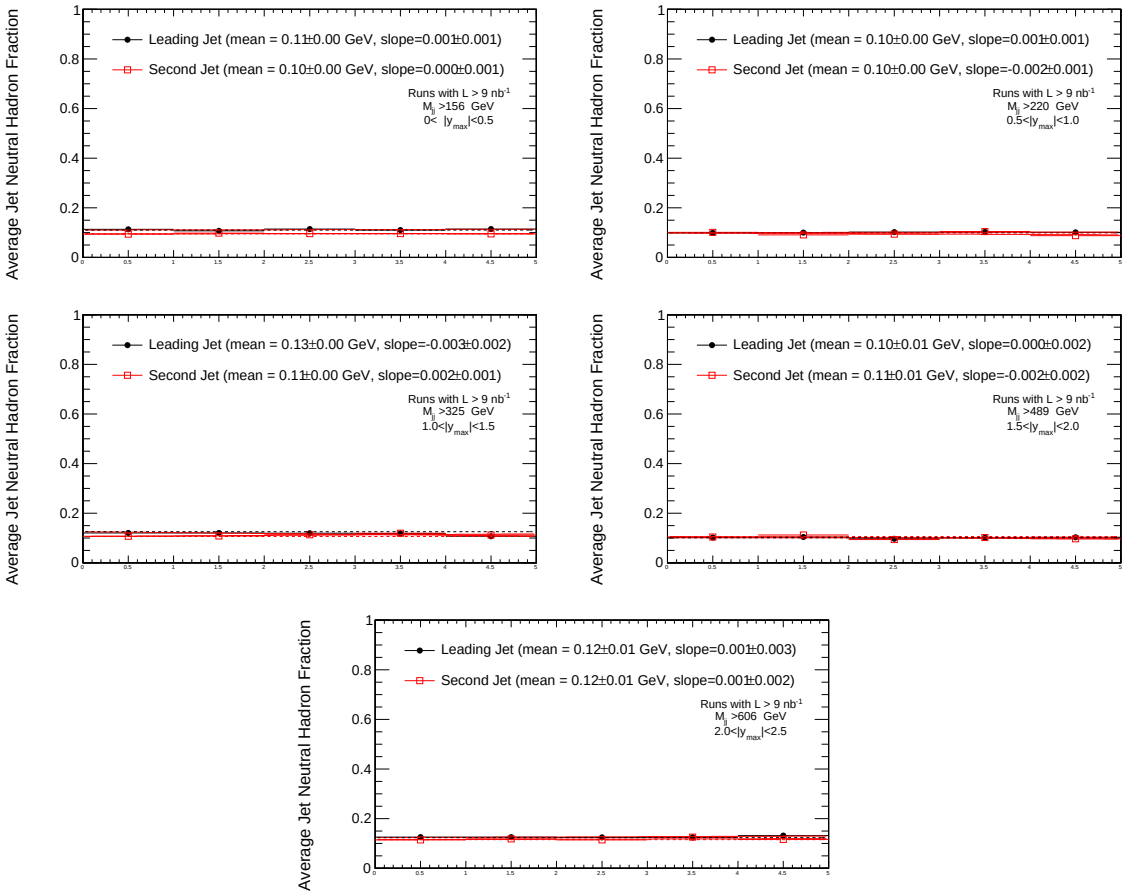

Figure B.31. The neutral hadron fraction of the leading and second jet for the five different y_{max} bins and for the HLT_Jet30U trigger as a function of time (run number), fitted with a first degree polynomial.

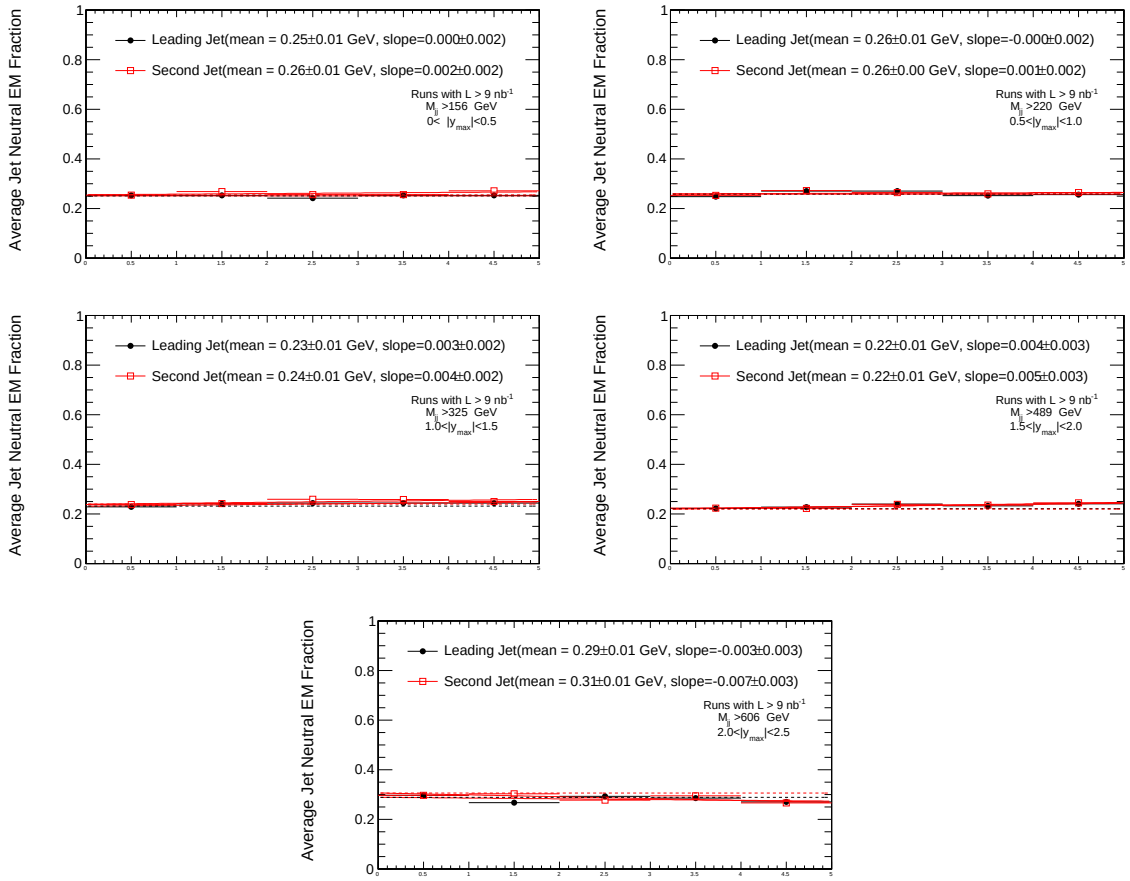

Figure B.32. The neutral electromagnetic fraction of the leading and second jet for the five different y_{max} bins and for the HLT_Jet30U trigger as a function of time (run number), fitted with a first degree polynomial.

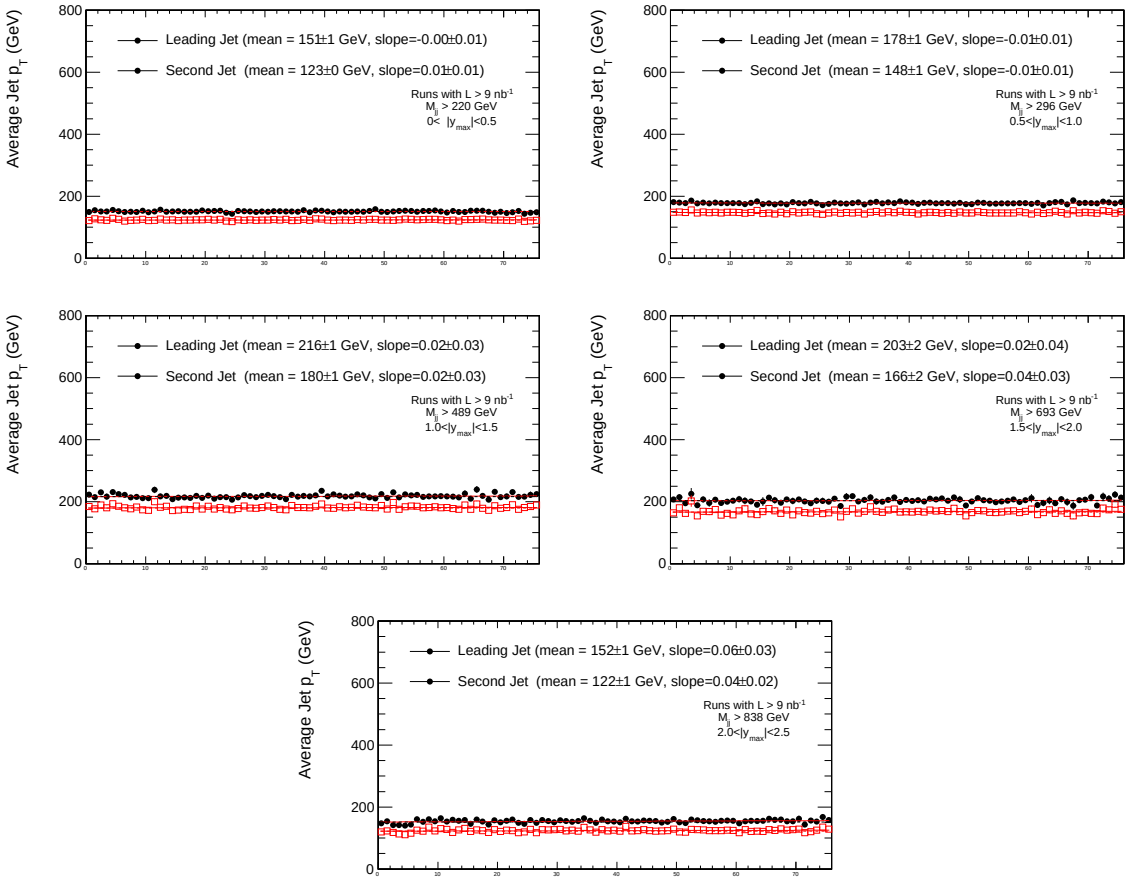

Figure B.33. The p_T of the leading and second jet for the five different y_{max} bins and for the HLT_Jet50U trigger as a function of time (run number), fitted with a first degree polynomial.

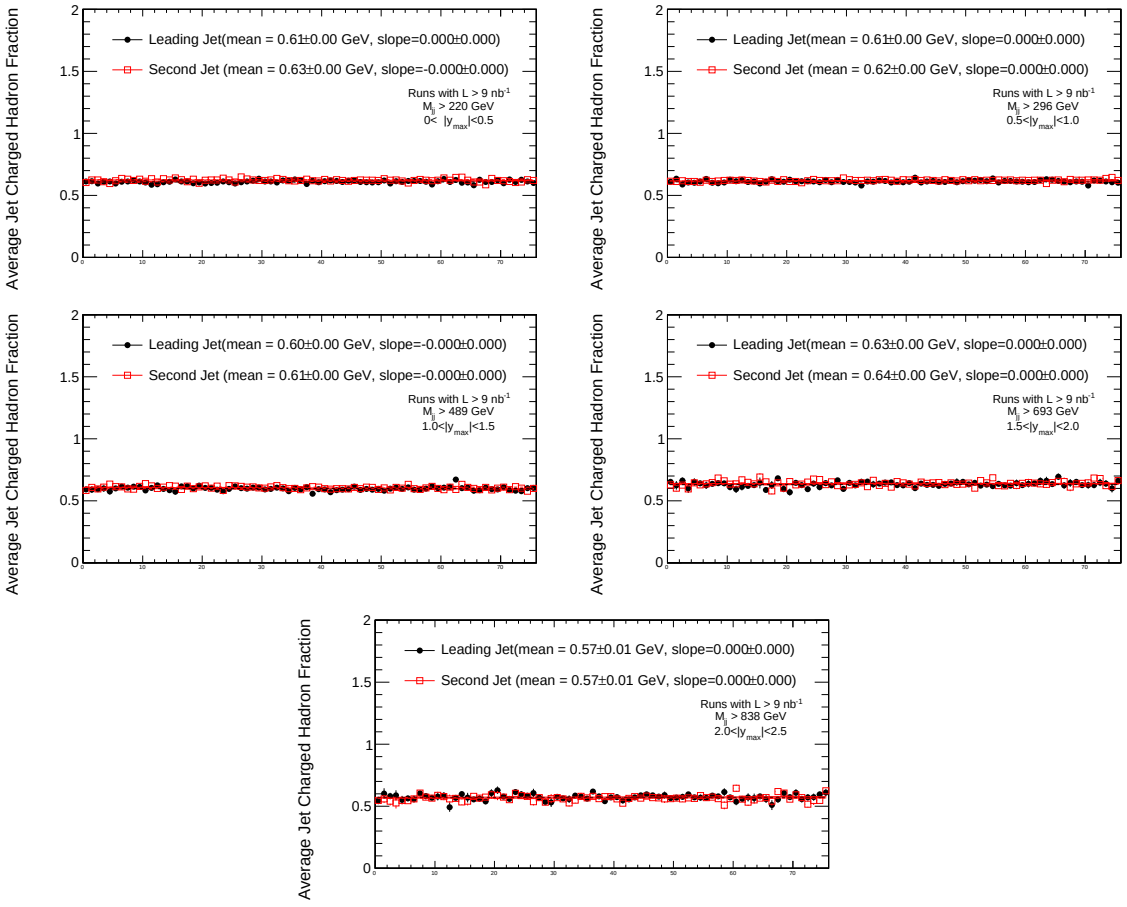

Figure B.34. The charged hadron fraction of the leading and second jet for the five different y_{max} bins and for the HLT_Jet50U trigger as a function of time (run number), fitted with a first degree polynomial.

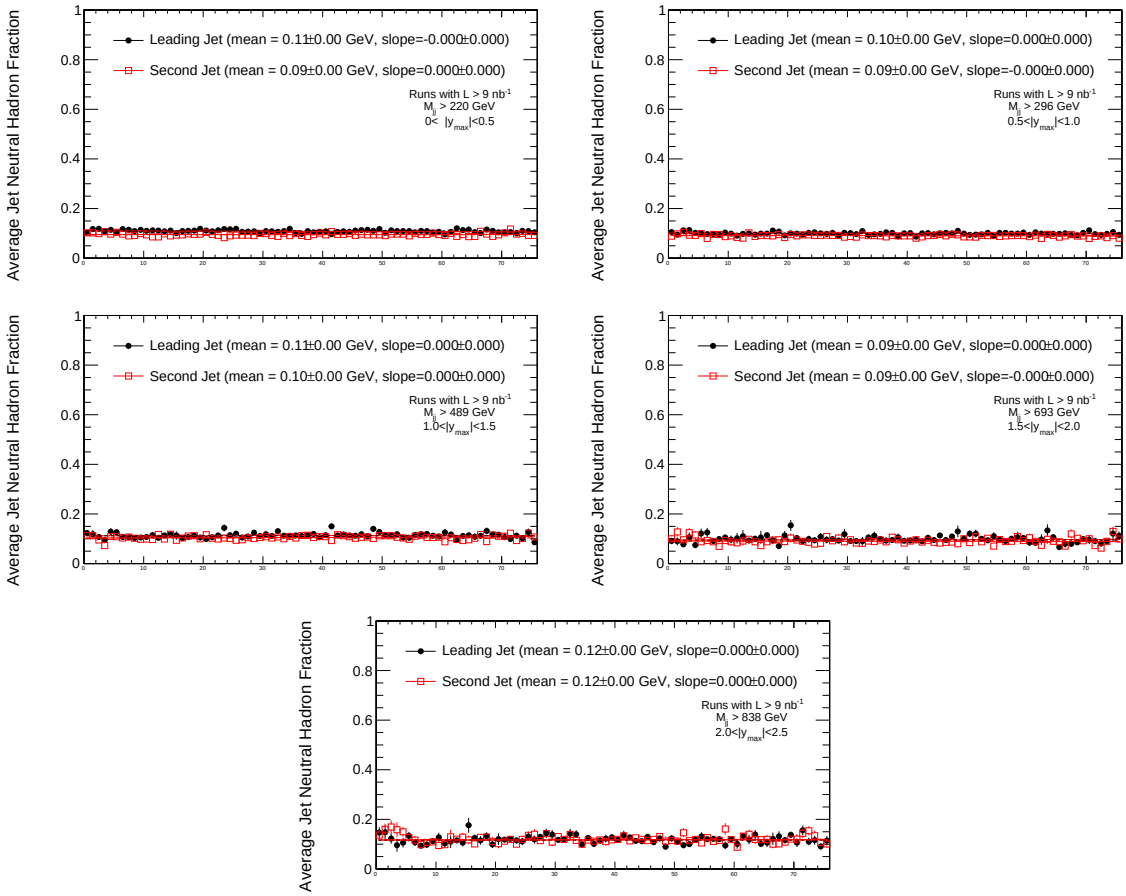

Figure B.35. The neutral hadron fraction of the leading and second jet for the five different y_{max} bins and for the HLT_Jet50U trigger as a function of time (run number), fitted with a first degree polynomial.

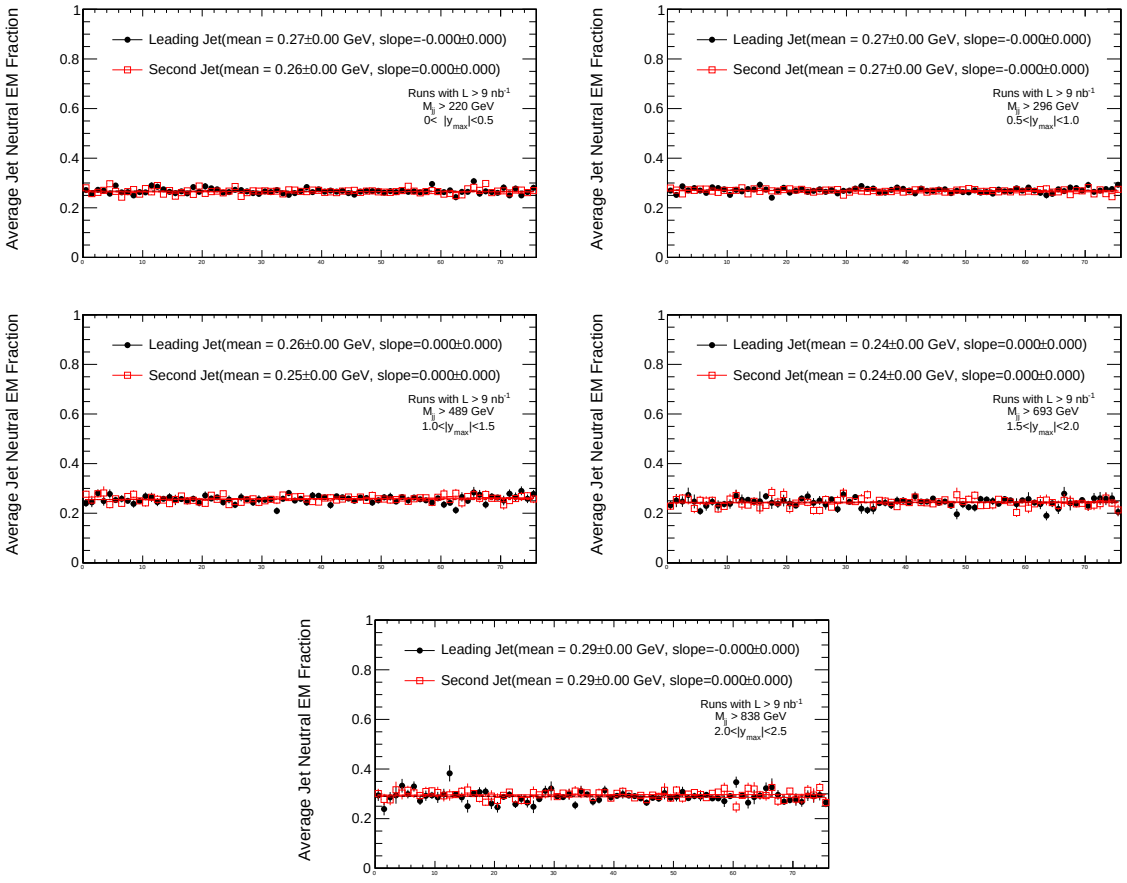

Figure B.36. The neutral electromagnetic fraction of the leading and second jet for the five different y_{max} bins and for the HLT_Jet50U trigger as a function of time (run number), fitted with a first degree polynomial.

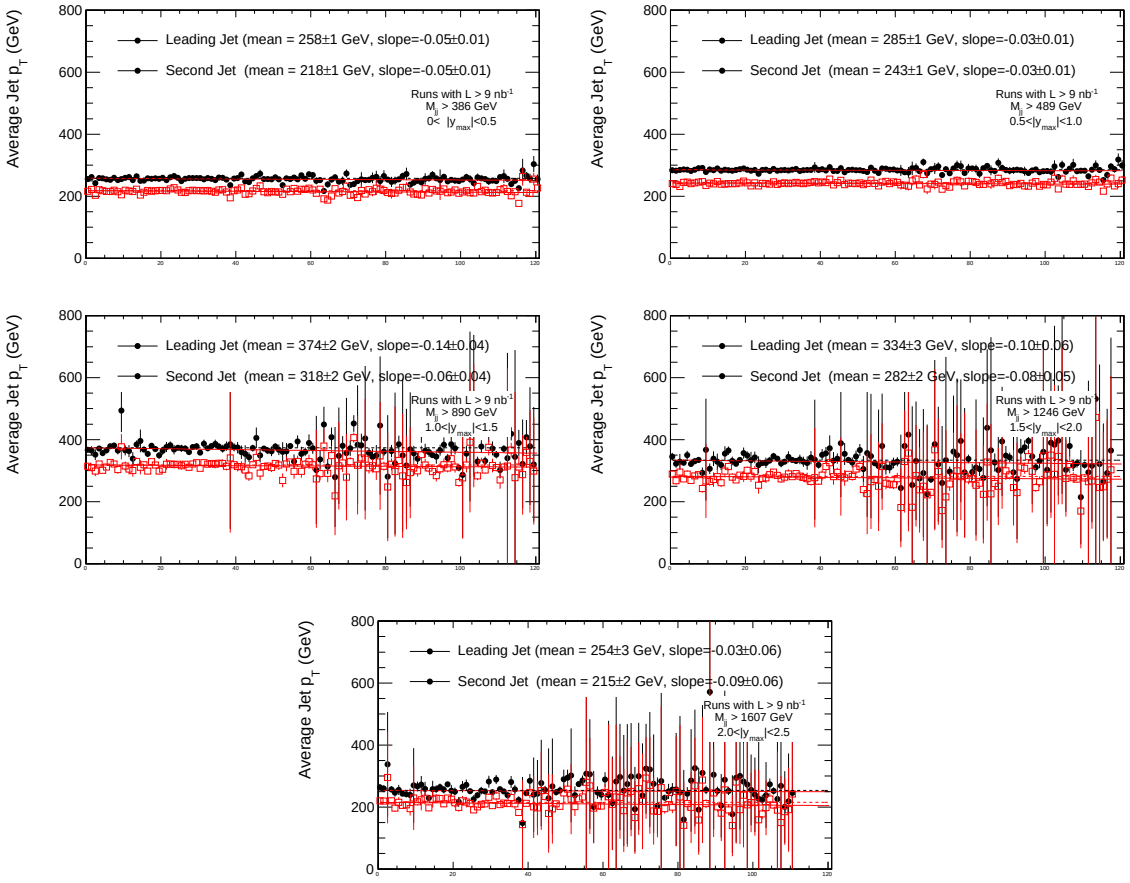

Figure B.37. The p_T of the leading and second jet for the five different y_{max} bins and for the HLT_Jet100U trigger as a function of time (run number), fitted with a first degree polynomial.

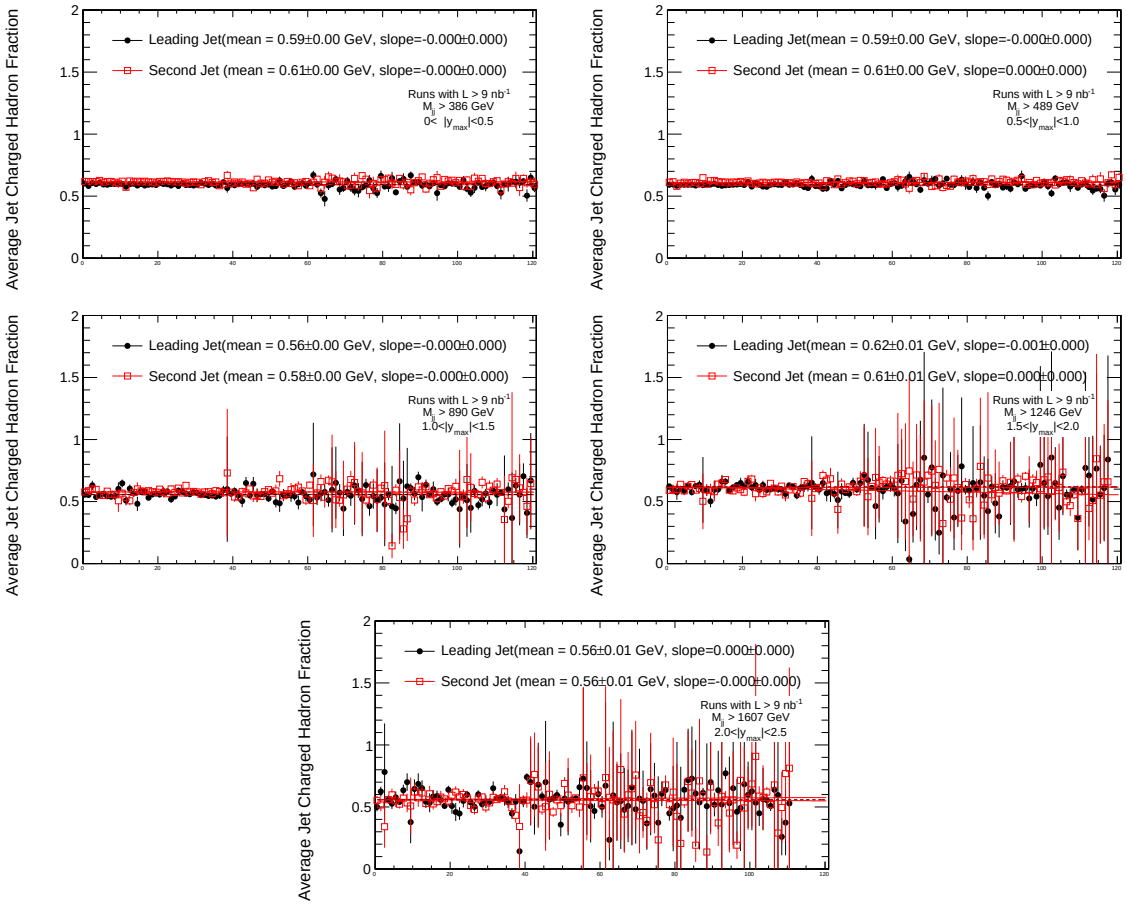

Figure B.38. The charged hadron fraction of the leading and second jet for the five different y_{max} bins and for the HLT_Jet100U trigger as a function of time (run number), fitted with a first degree polynomial.

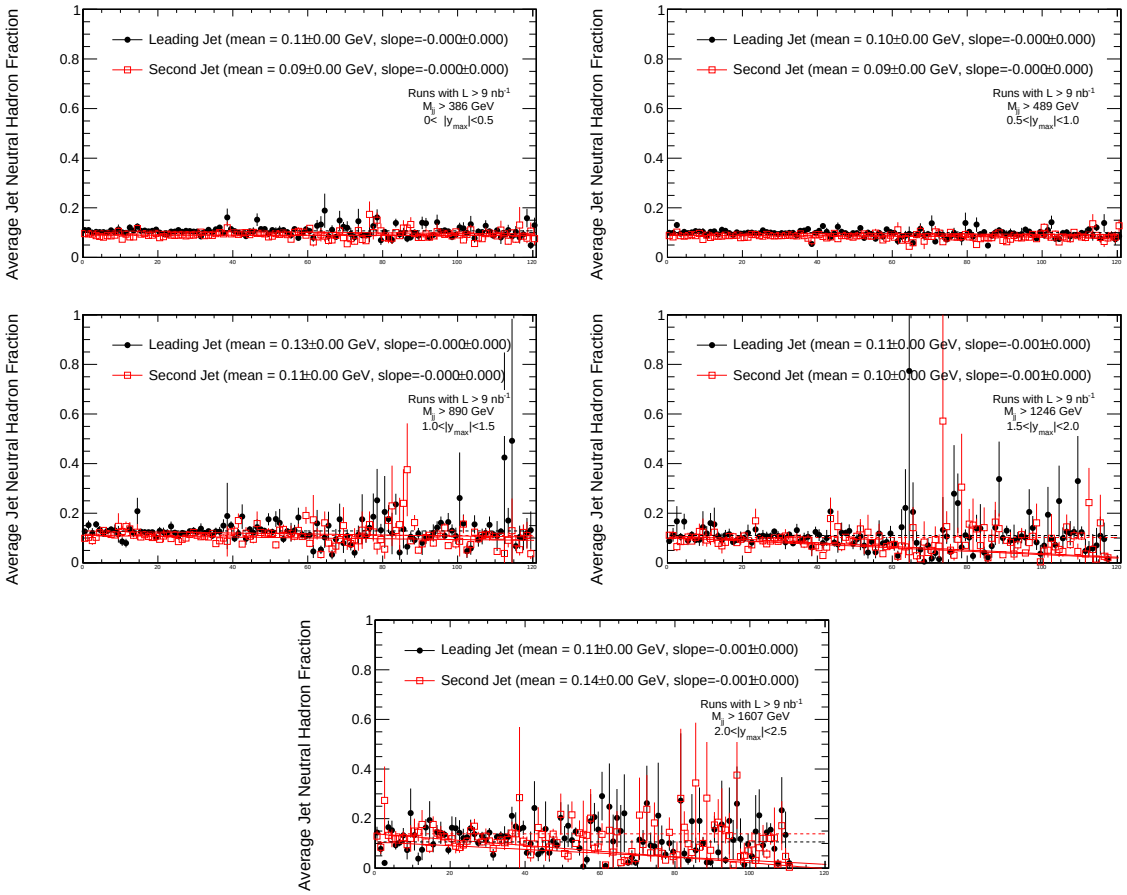

Figure B.39. The neutral hadron fraction of the leading and second jet for the five different y_{max} bins and for the HLT_Jet100U trigger as a function of time (run number), fitted with a first degree polynomial.

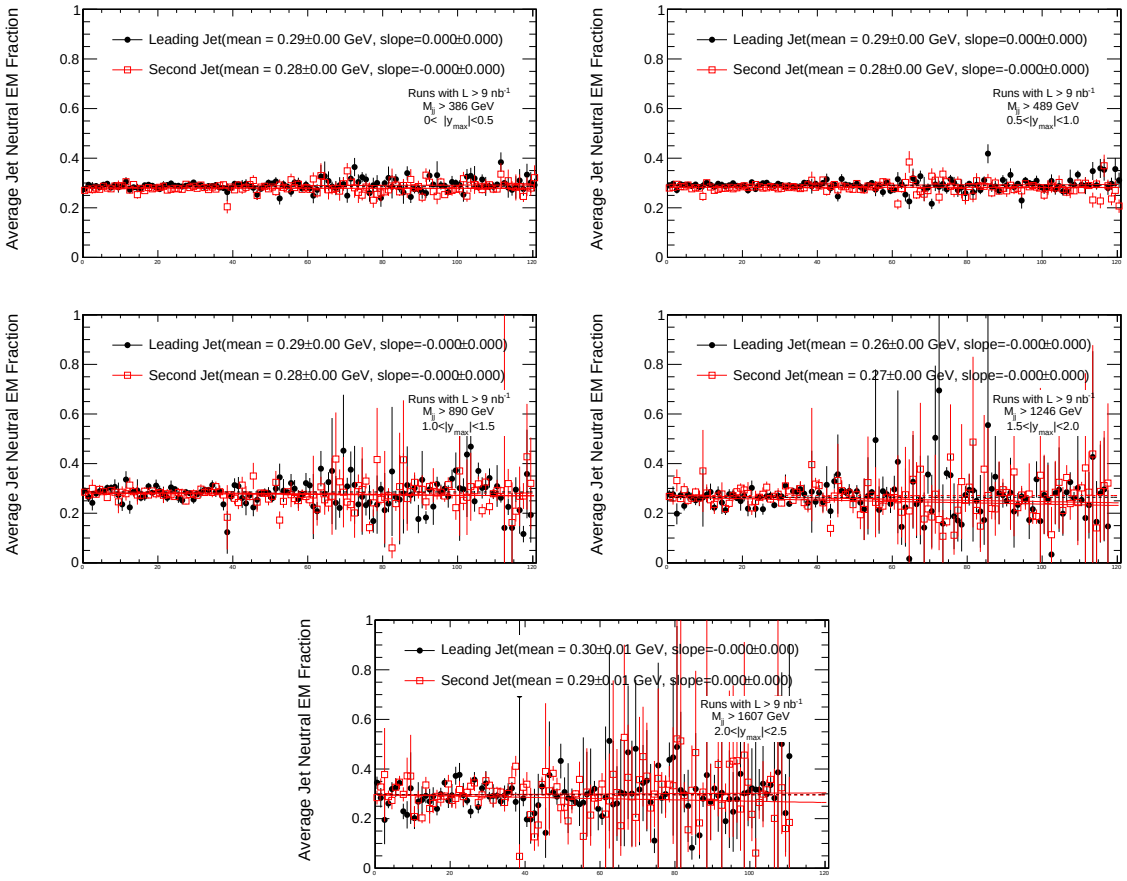

Figure B.40. The neutral electromagnetic fraction of the leading and second jet for the five different y_{max} bins and for the HLT_Jet100U trigger as a function of time (run number), fitted with a first degree polynomial.

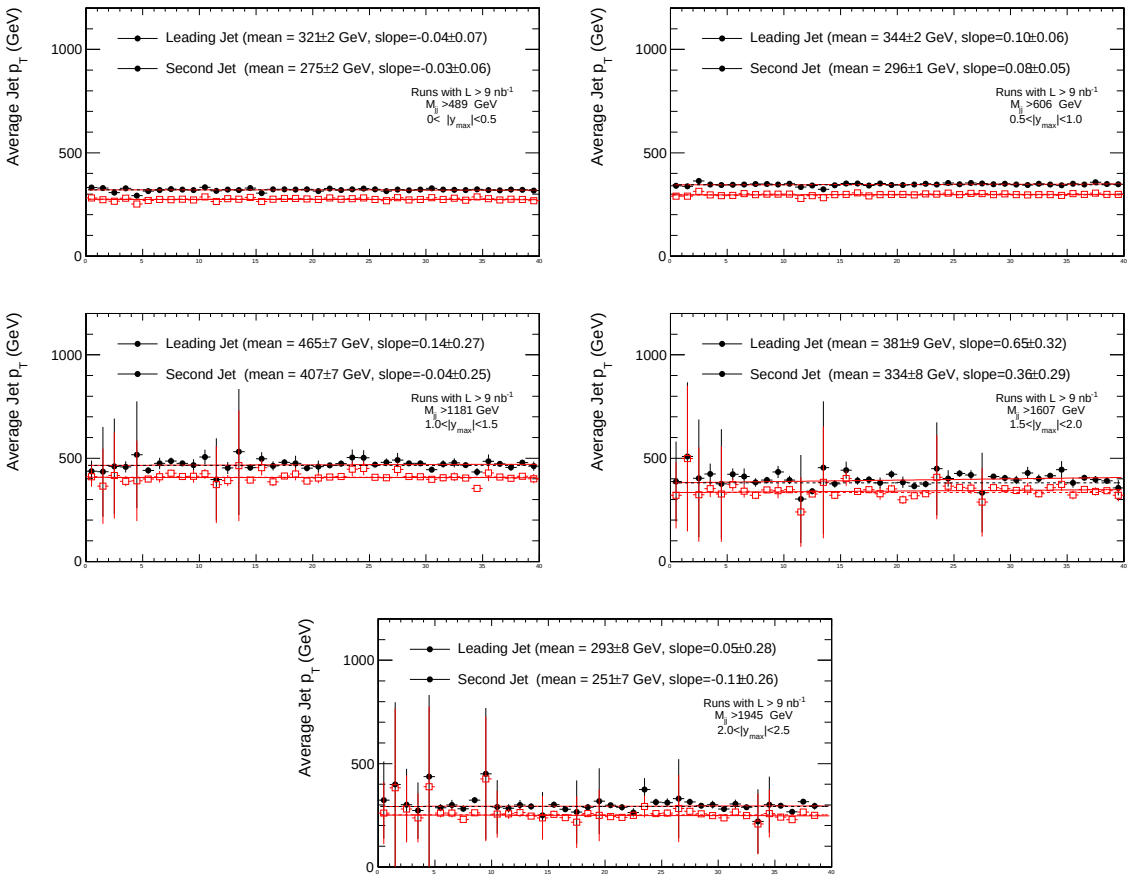

Figure B.41. The p_T of the leading and second jet for the five different y_{max} bins and for the HLT_Jet140U trigger as a function of time (run number), fitted with a first degree polynomial.

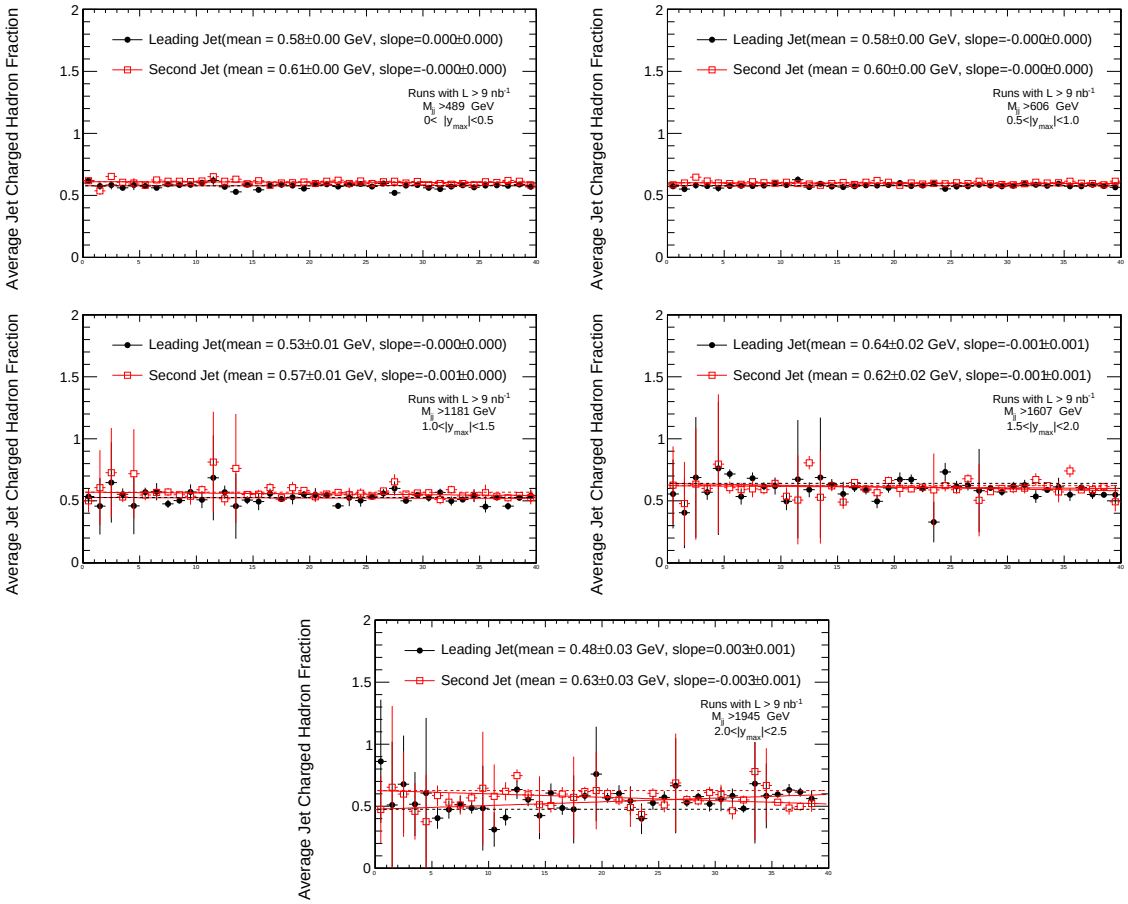

Figure B.42. The charged hadron fraction of the leading and second jet for the five different y_{max} bins and for the HLT_Jet140U trigger as a function of time (run number), fitted with a first degree polynomial.

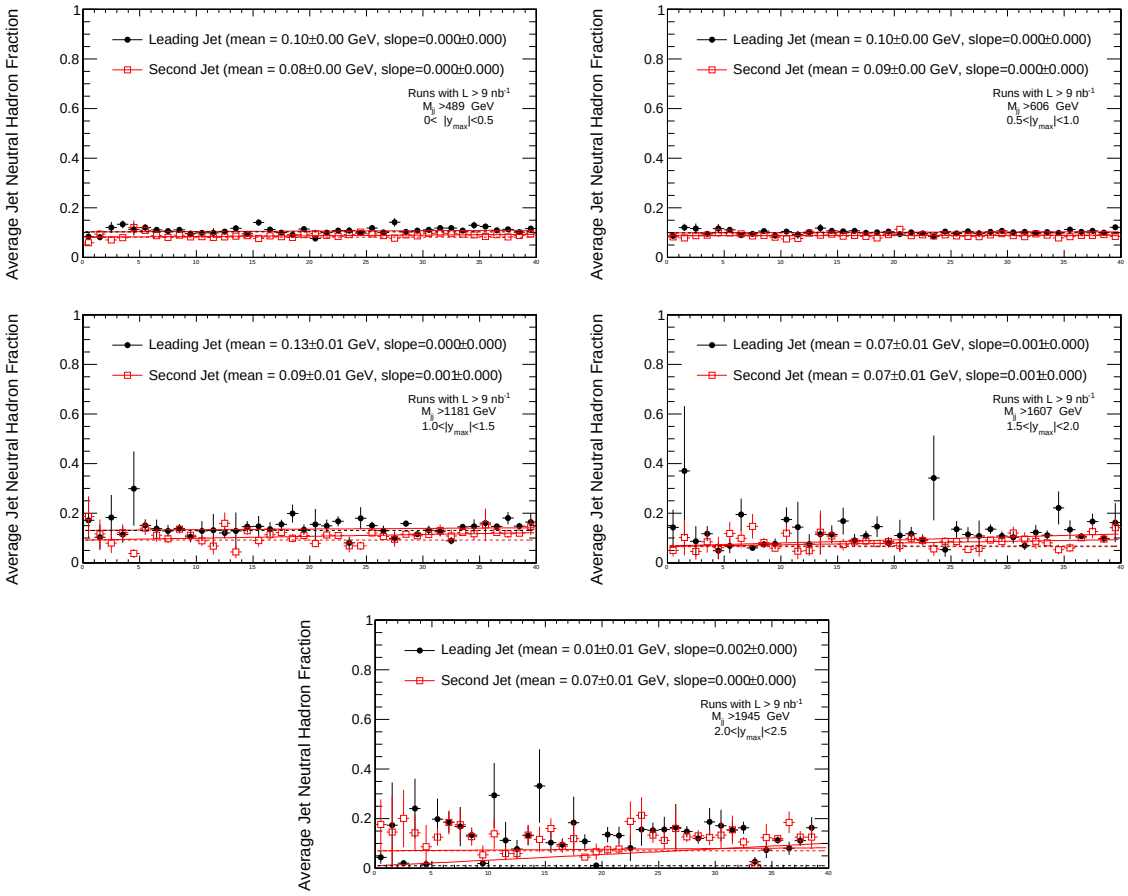

Figure B.43. The neutral hadron fraction of the leading and second jet for the five different y_{max} bins and for the HLT_Jet140U trigger as a function of time (run number), fitted with a first degree polynomial.

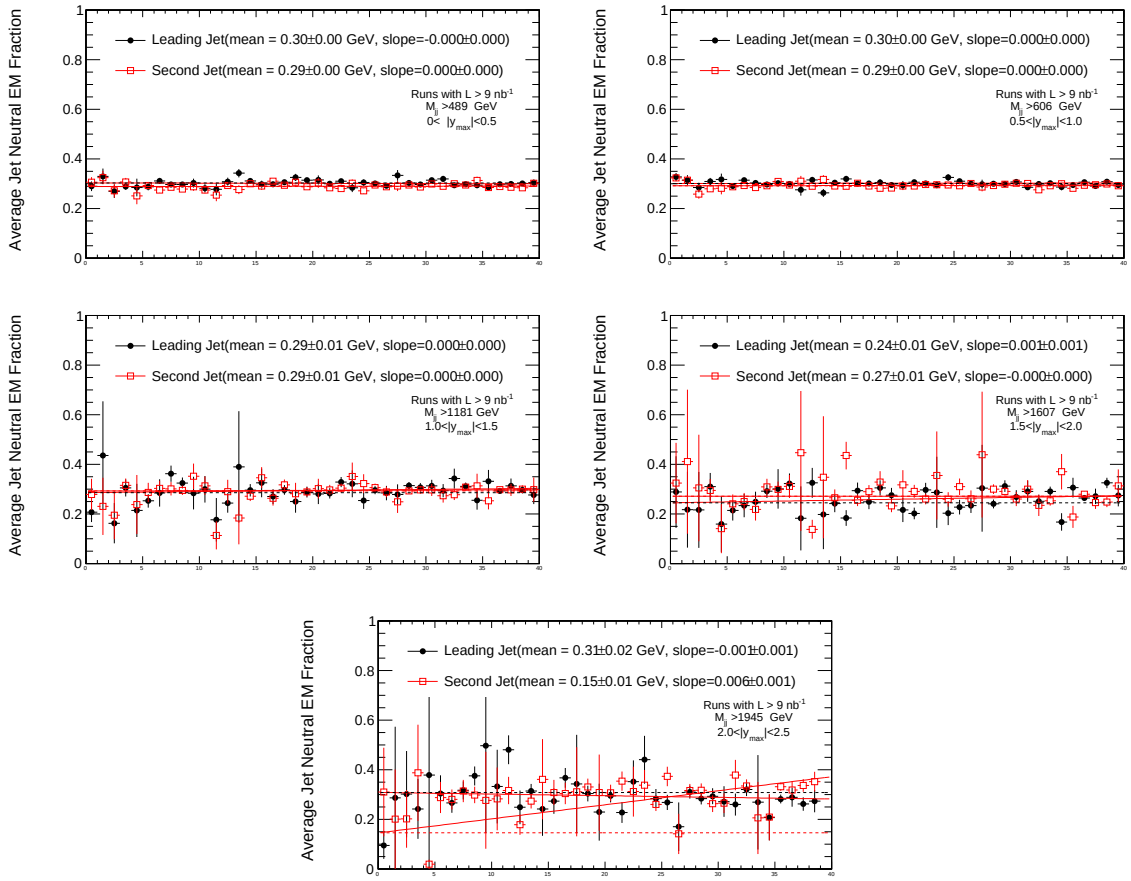

Figure B.44. The neutral electromagnetic fraction of the leading and second jet for the five different y_{max} bins and for the HLT_Jet140U trigger as a function of time (run number), fitted with a first degree polynomial.

APPENDIX C: Stability Over the Run Period

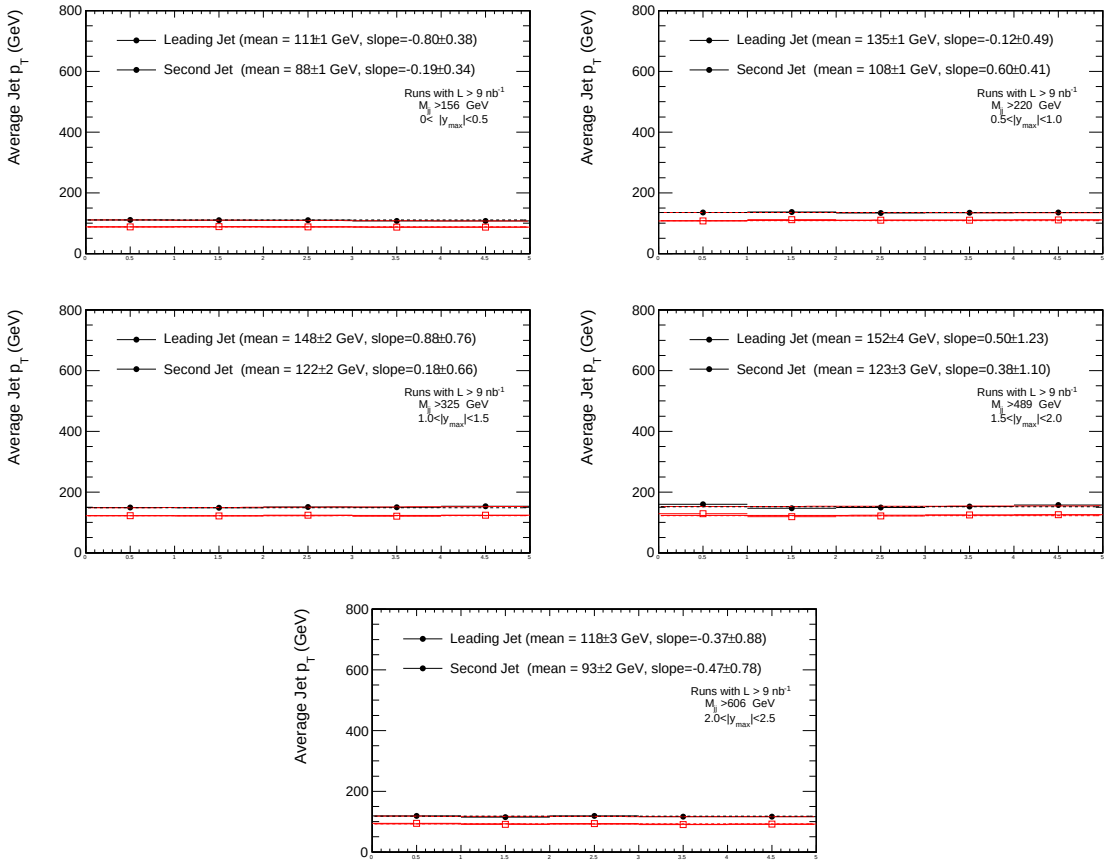

Figure C.1. The p_T of the leading and second jet for the five different y_{max} bins and for the HLT_Jet30U trigger as a function of time (run number), fitted with a first degree polynomial.

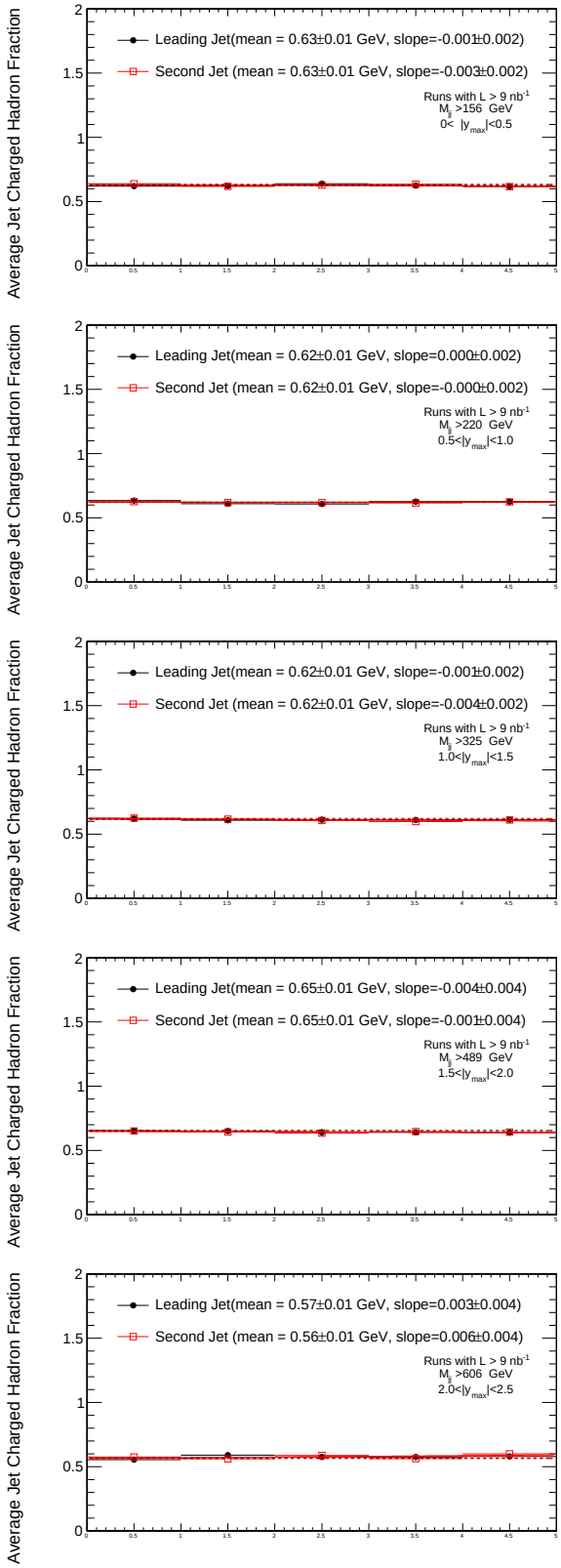

Figure C.2. The charged hadron fraction of the leading and second jet for the five different y_{max} bins and for the HLT_Jet30U trigger as a function of time (run number), fitted with a first degree polynomial.

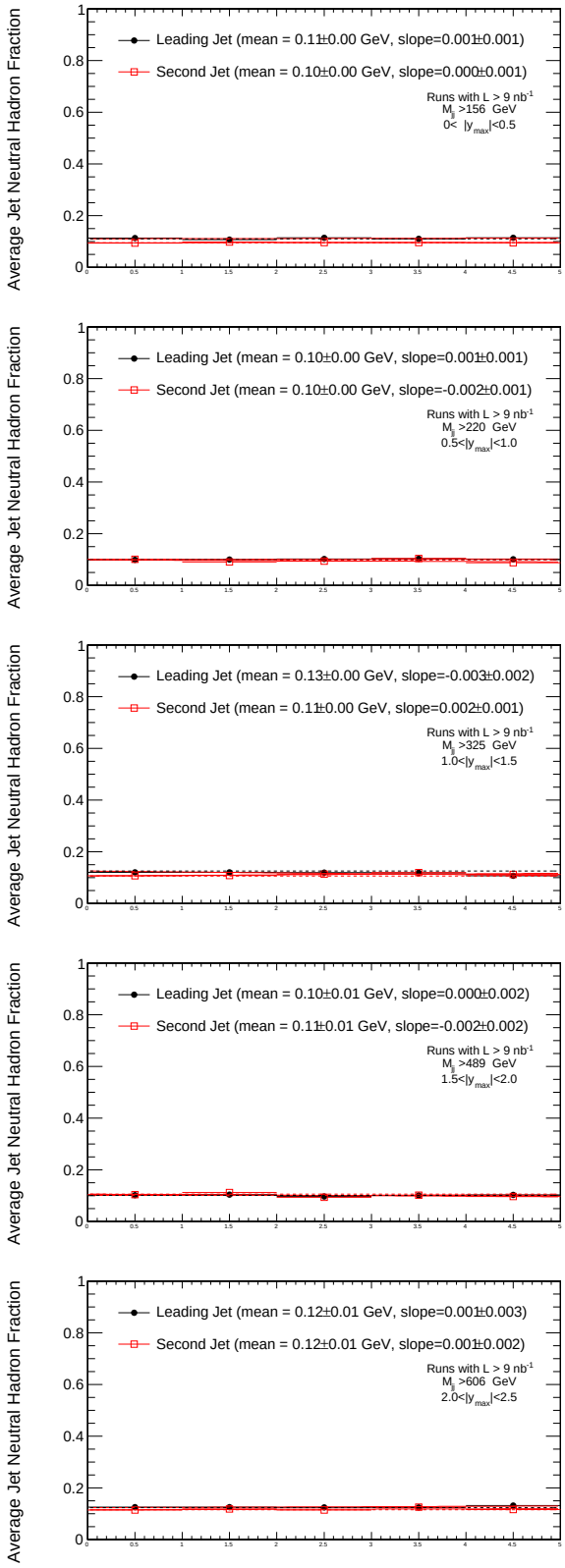

Figure C.3. The neutral hadron fraction of the leading and second jet for the five different y_{max} bins and for the HLT_Jet30U trigger as a function of time (run number), fitted with a first degree polynomial.

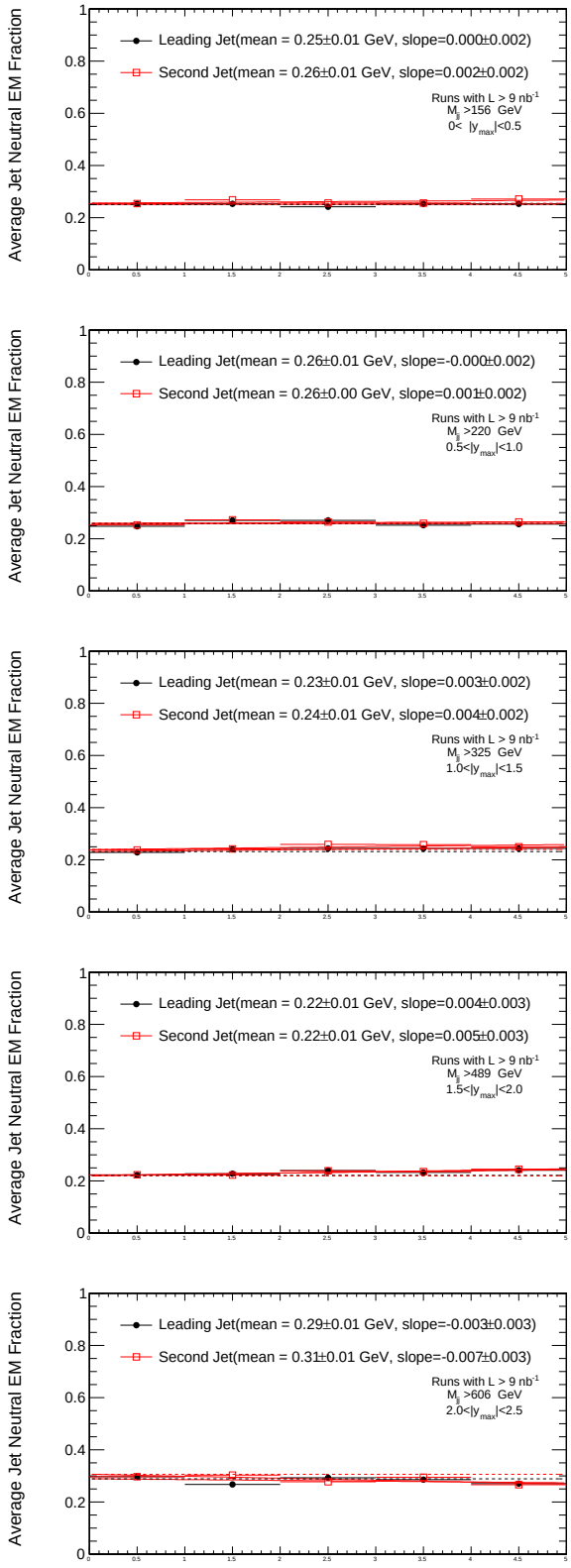

Figure C.4. The neutral electromagnetic fraction of the leading and second jet for the five different y_{max} bins and for the HLT_Jet30U trigger as a function of time (run number), fitted with a first degree polynomial.

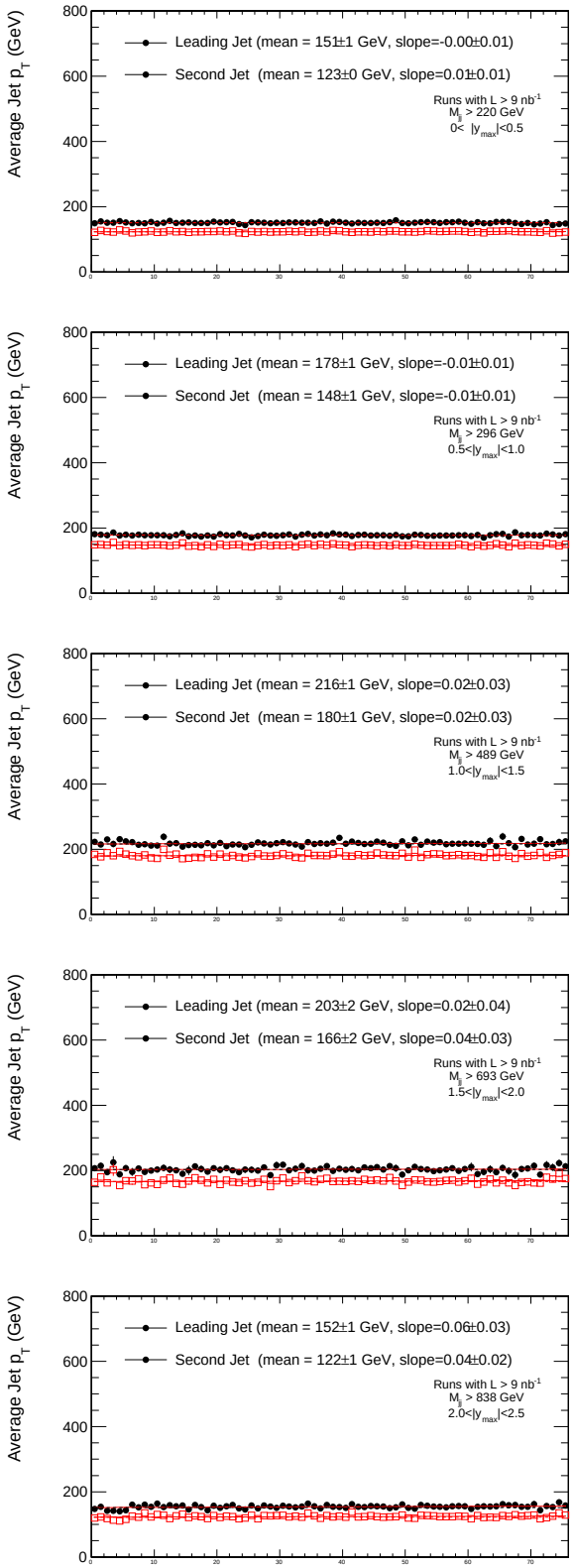

Figure C.5. The p_T of the leading and second jet for the five different y_{max} bins and for the HLT_Jet50U trigger as a function of time (run number), fitted with a first degree polynomial.

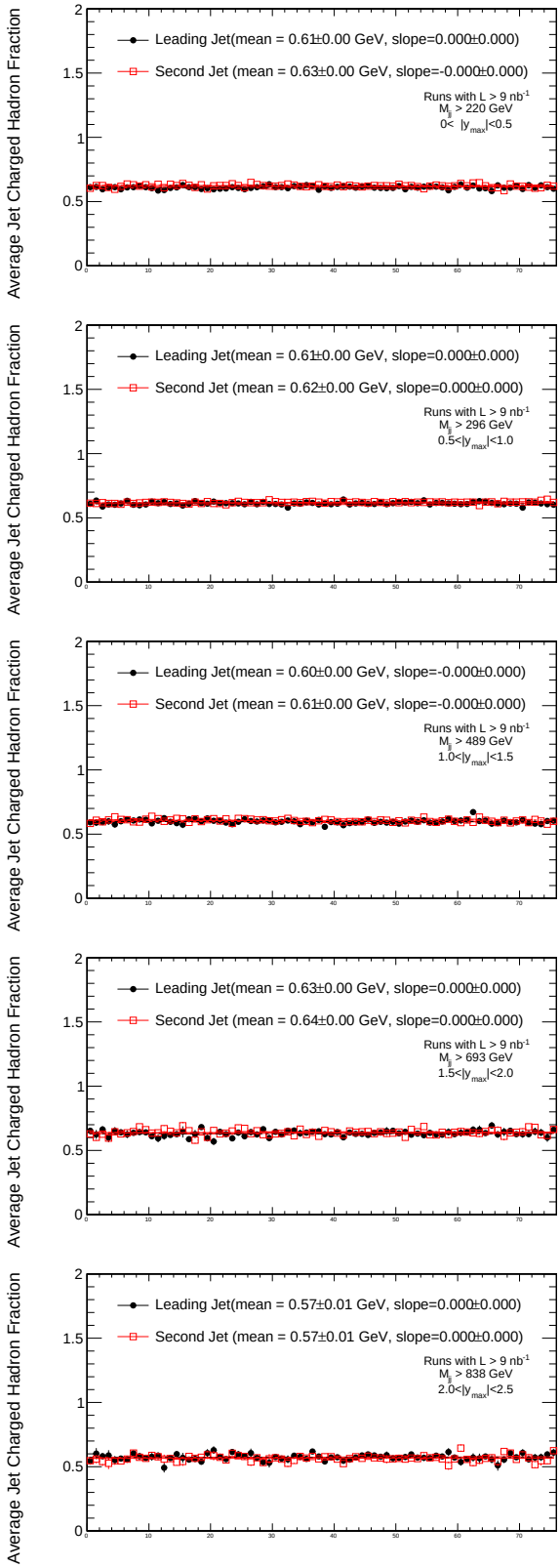

Figure C.6. The charged hadron fraction of the leading and second jet for the five different y_{max} bins and for the HLT_Jet50U trigger as a function of time (run number), fitted with a first degree polynomial.

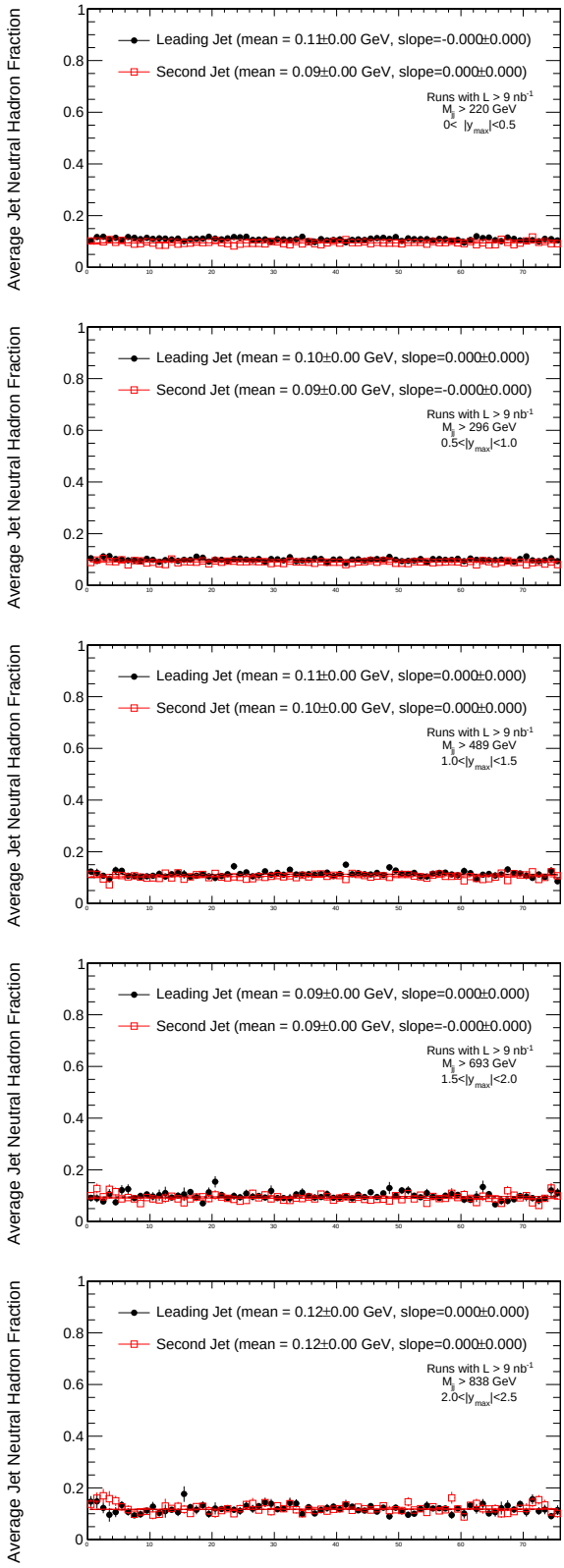

Figure C.7. The neutral hadron fraction of the leading and second jet for the five different y_{max} bins and for the HLT_Jet50U trigger as a function of time (run number), fitted with a first degree polynomial.

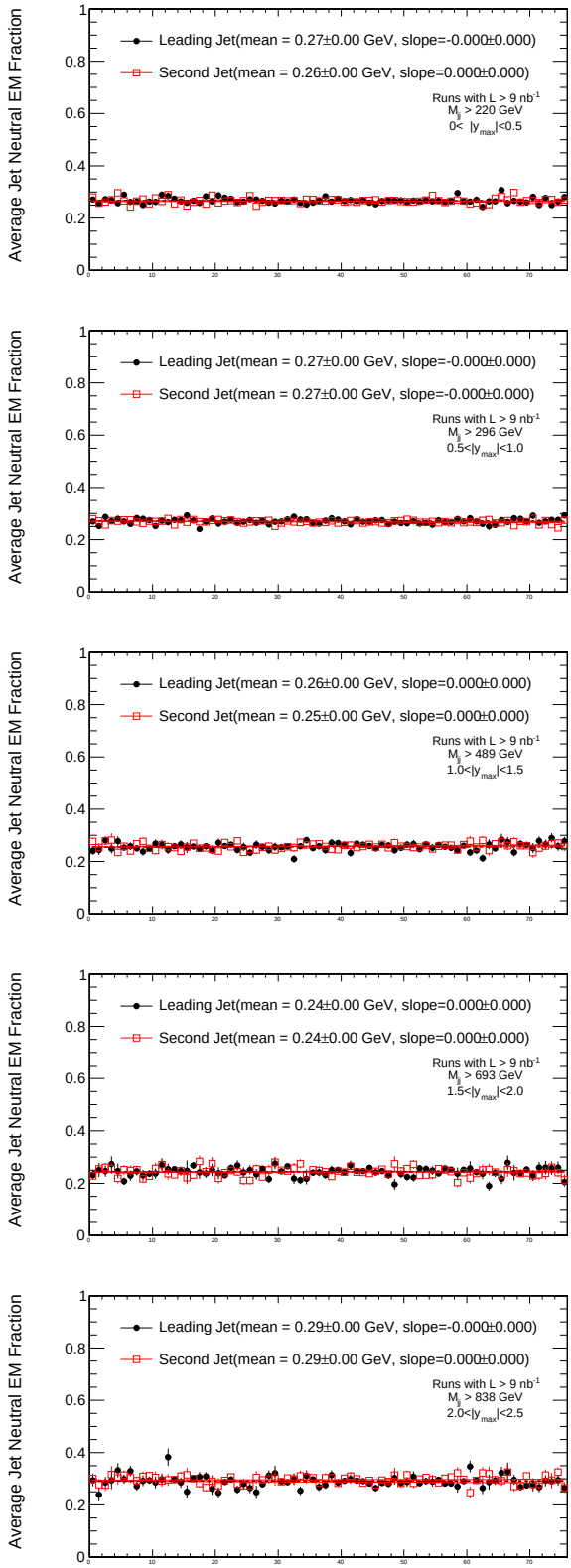

Figure C.8. The neutral electromagnetic fraction of the leading and second jet for the five different y_{max} bins and for the HLT_Jet50U trigger as a function of time (run number), fitted with a first degree polynomial.

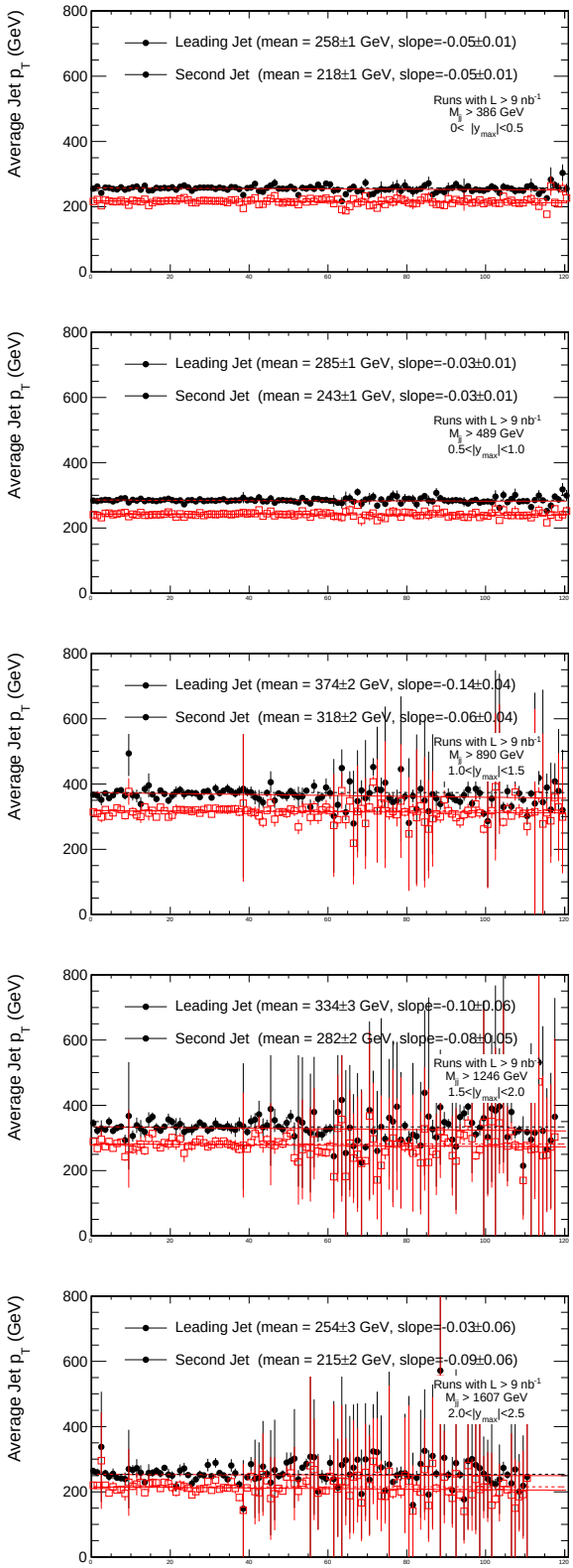

Figure C.9. The p_T of the leading and second jet for the five different y_{max} bins and for the HLT_Jet100U trigger as a function of time (run number), fitted with a first degree polynomial.

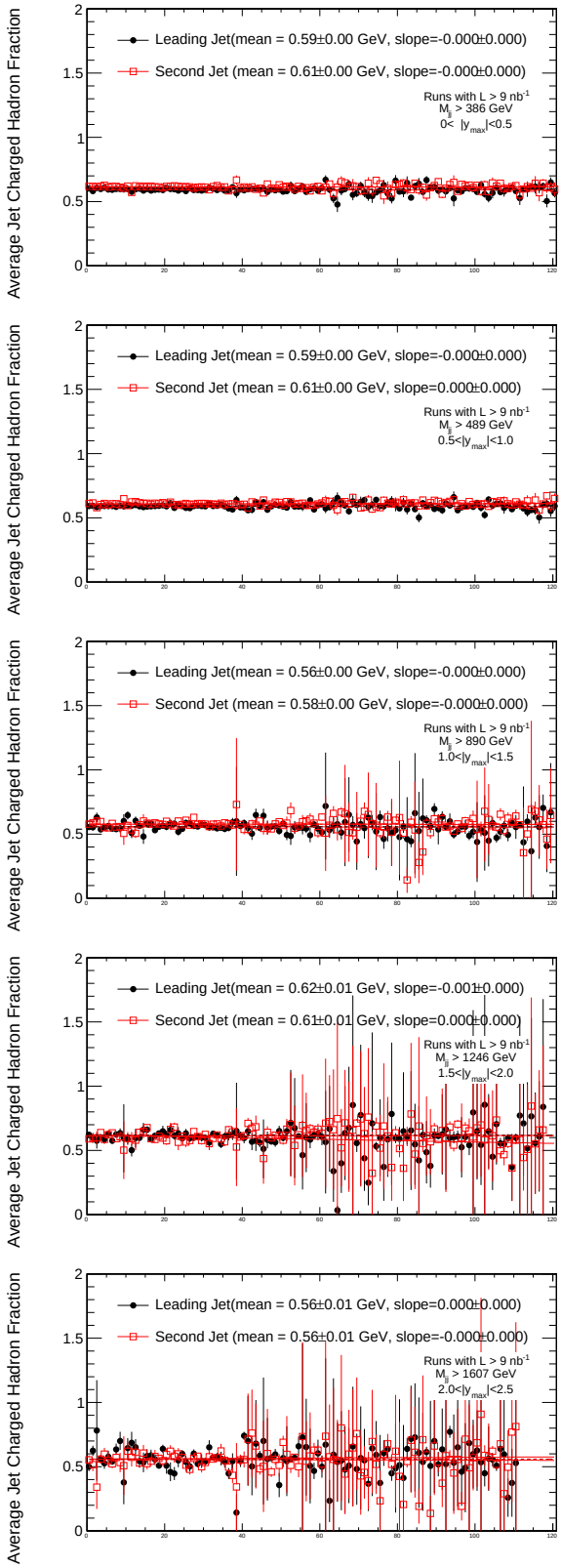

Figure C.10. The charged hadron fraction of the leading and second jet for the five different y_{max} bins and for the HLT_Jet100U trigger as a function of time (run number), fitted with a first degree polynomial.

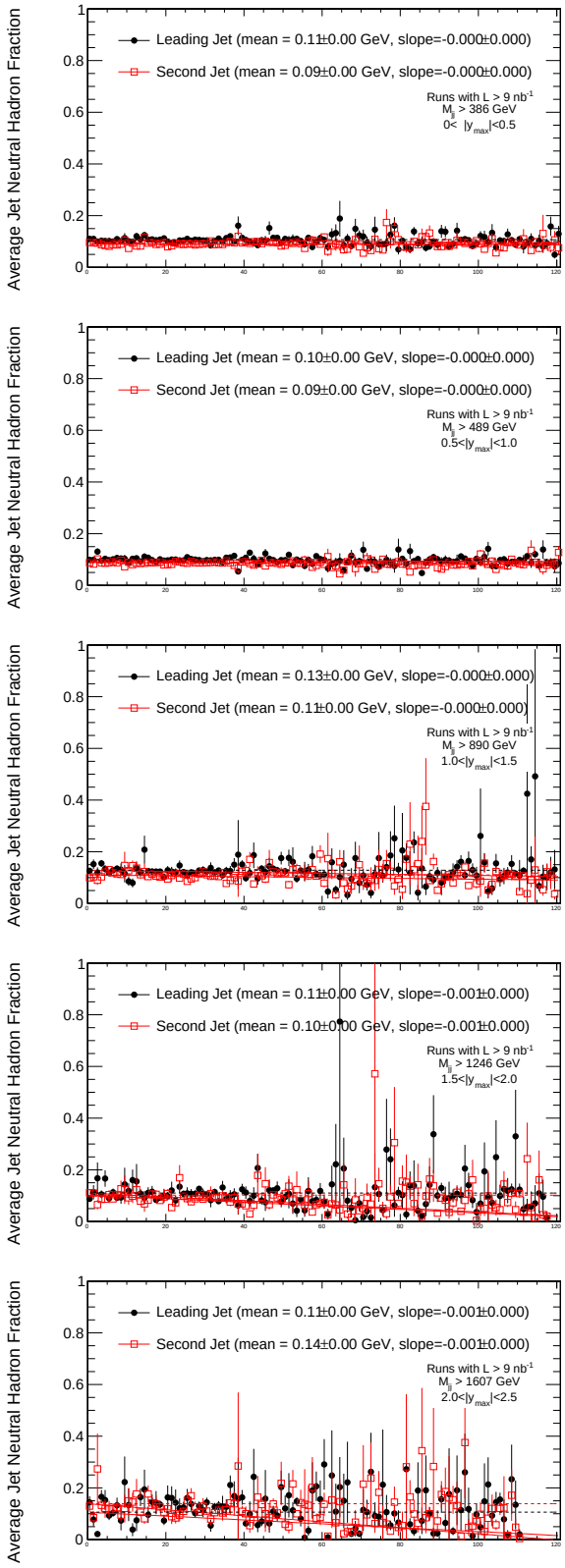

Figure C.11. The neutral hadron fraction of the leading and second jet for the five different y_{max} bins and for the HLT_Jet100U trigger as a function of time (run number), fitted with a first degree polynomial.

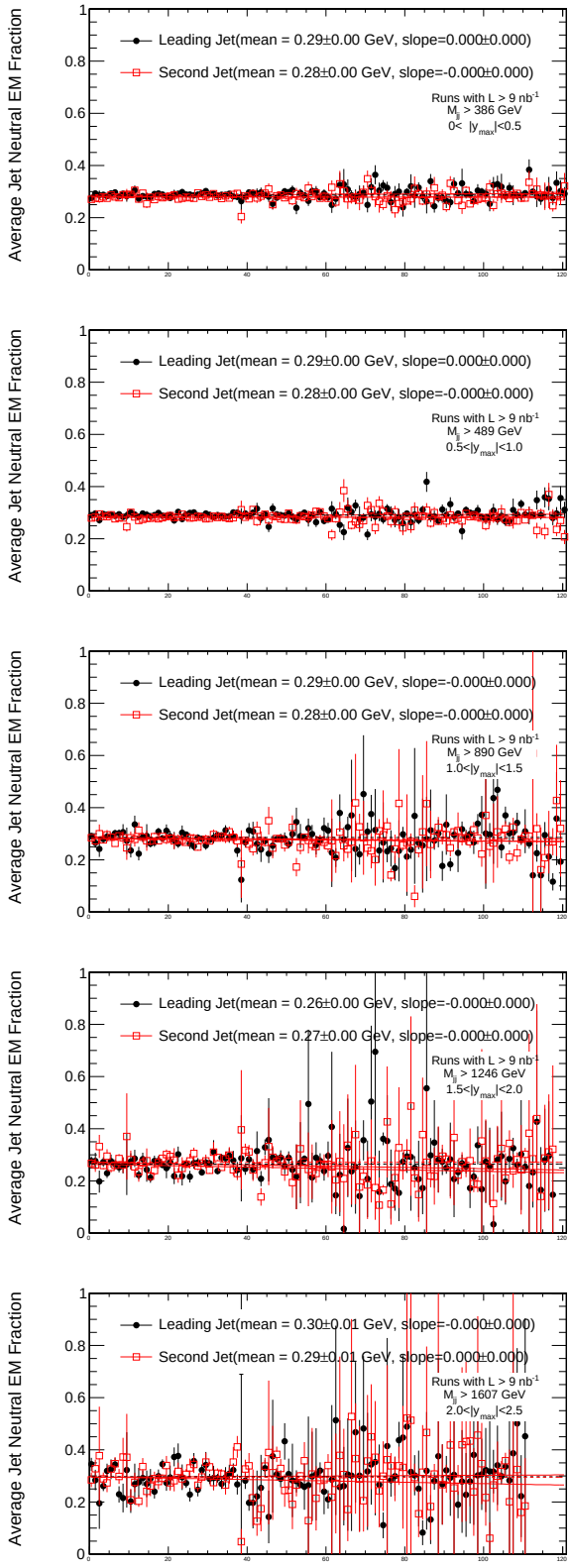

Figure C.12. The neutral electromagnetic fraction of the leading and second jet for the five different y_{max} bins and for the HLT_Jet100U trigger as a function of time (run number), fitted with a first degree polynomial.

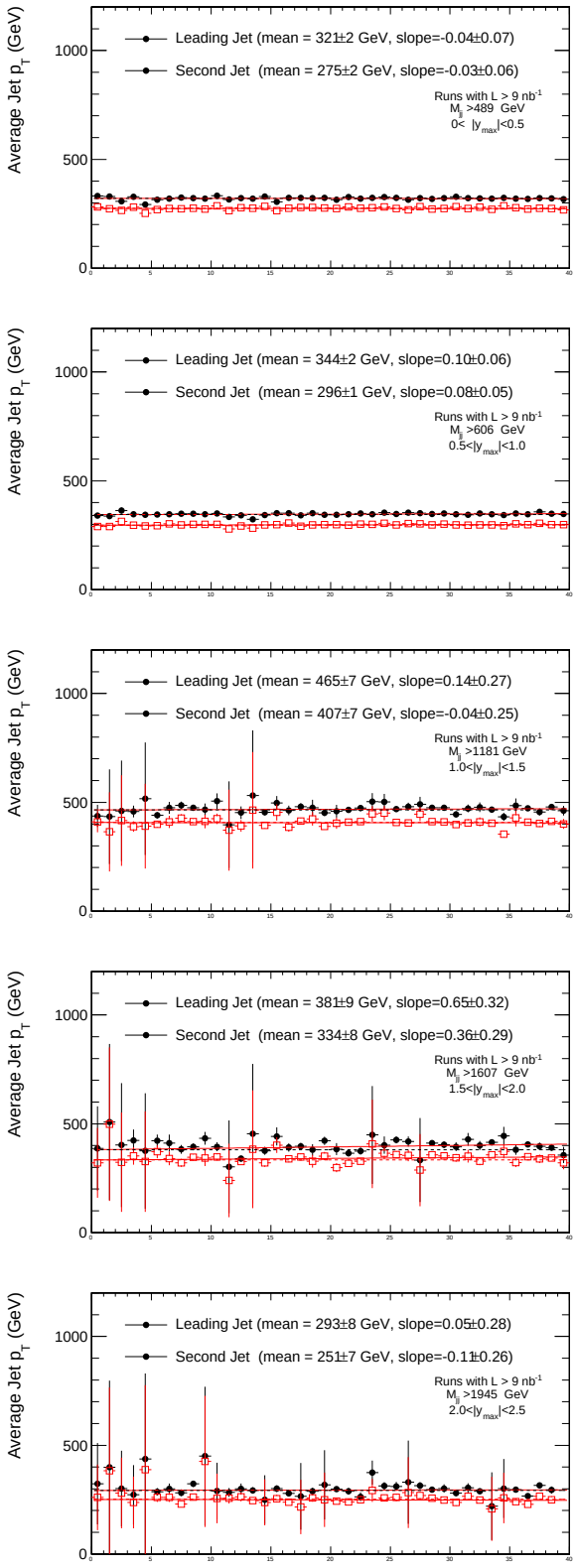

Figure C.13. The p_T of the leading and second jet for the five different y_{max} bins and for the HLT_Jet140U trigger as a function of time (run number), fitted with a first degree polynomial.

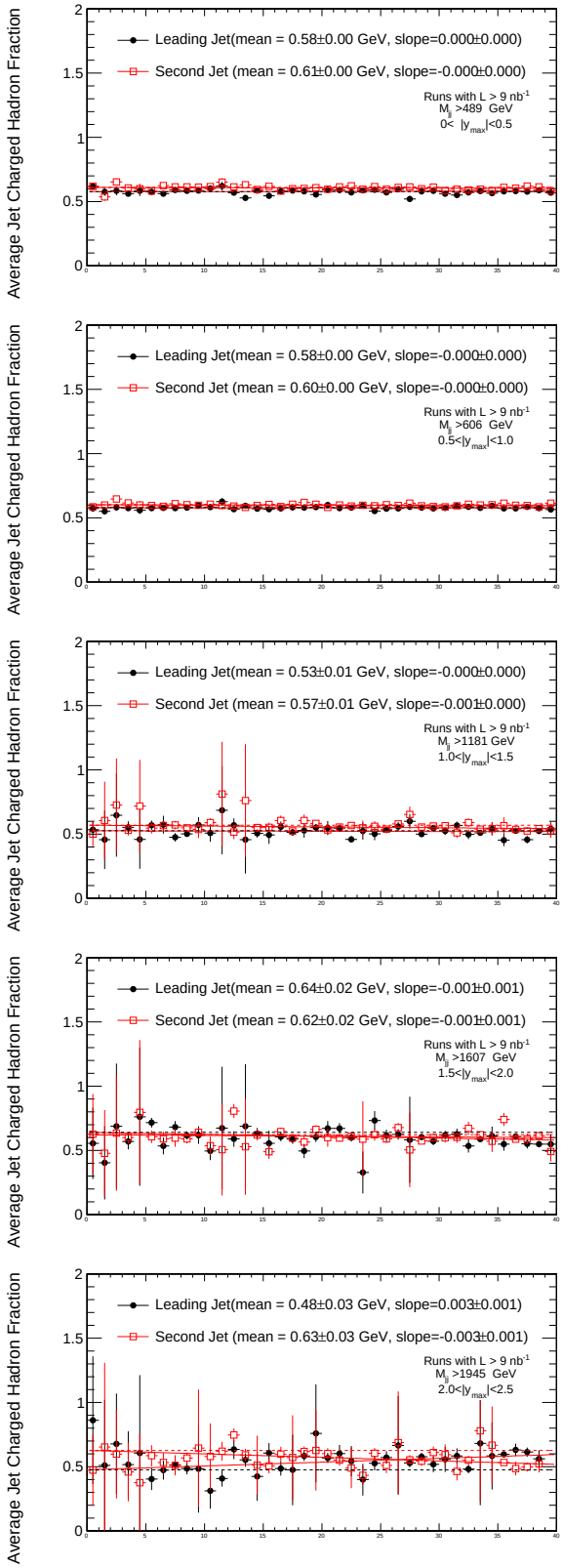

Figure C.14. The charged hadron fraction of the leading and second jet for the five different y_{max} bins and for the HLT_Jet140U trigger as a function of time (run number), fitted with a first degree polynomial.

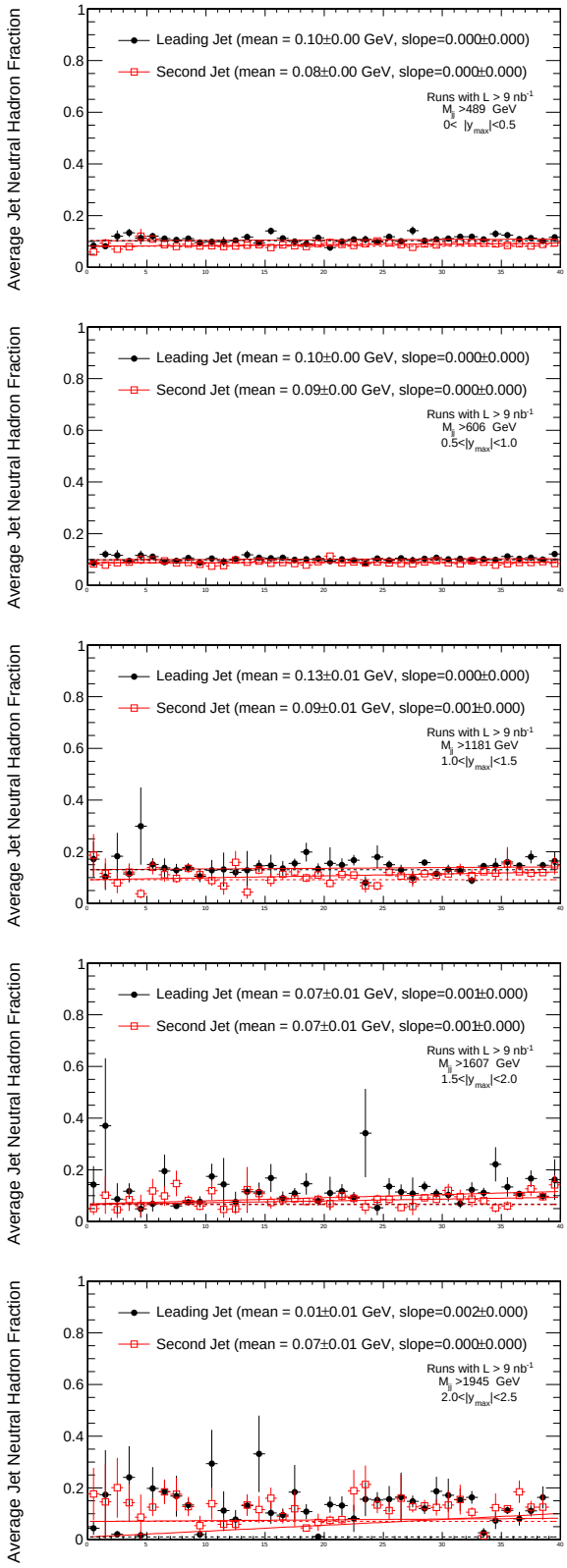

Figure C.15. The neutral hadron fraction of the leading and second jet for the five different y_{max} bins and for the HLT_Jet140U trigger as a function of time (run number), fitted with a first degree polynomial.

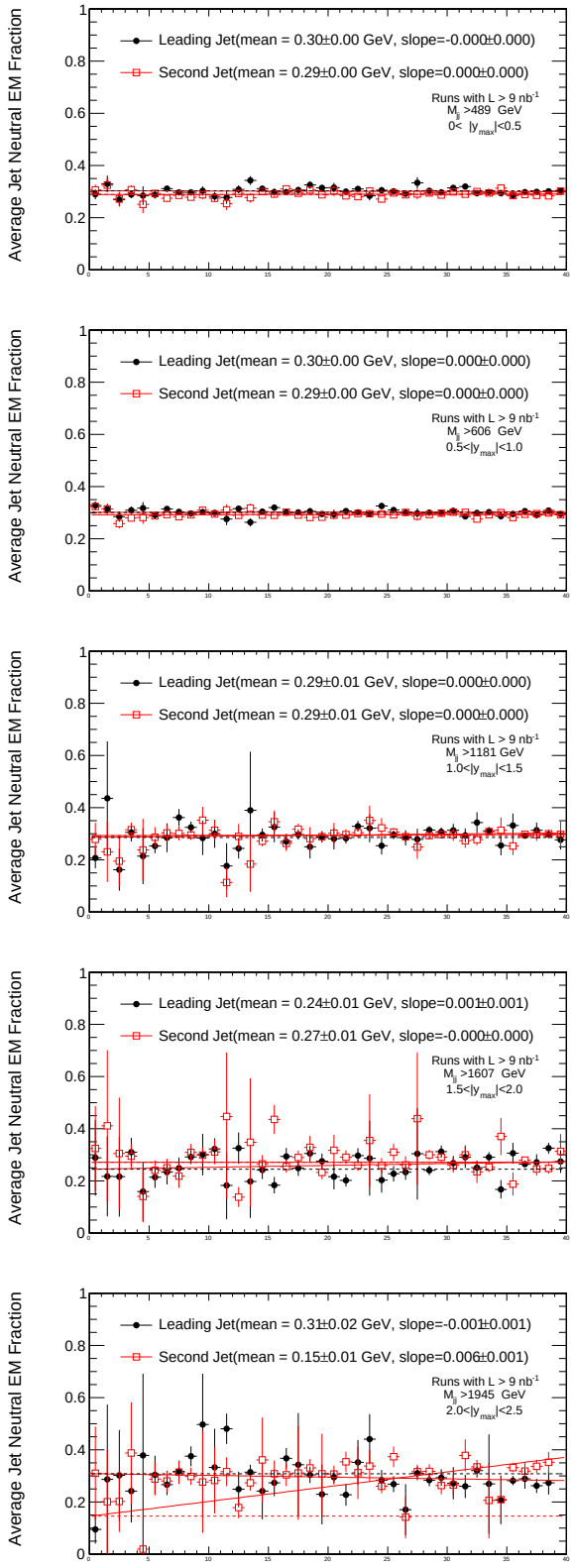

Figure C.16. The neutral electromagnetic fraction of the leading and second jet for the five different y_{max} bins and for the HLT_Jet140U trigger as a function of time (run number), fitted with a first degree polynomial.

REFERENCES

1. D0 Collaboration, "Measurement of the Dijet Invariant Mass Cross Section in ppbar Collisions at $\sqrt{s}$= 1.96 TeV", *Physics Letters D*, Vol. 693, No. 11, pp. 531-538, 2010.

2. CDF Collaboration, "Search for new particles decaying into dijets in proton-antiproton collisions at $\sqrt{s}$= 1.96-TeV", *Physical Review D*, Vol. 79, No. 11, pp. 112002, 2009.

3. The ATLAS Collaboration, "Measurement of inclusive jet and dijet cross sections in proton-proton collisions at 7 TeV centre-of-mass energy with the ATLAS detector". *The European Physical Journal C - Particles and Fields*, Vol. 71, pp. 1-59, 2011.

4. The CMS Collaboration, "Search for Dijet Resonances in 7 TeV *pp* Collisions at CMS", *Physical Review Letters*, Vol. 105, No. 2, pp. 029902, 2010.

5. The CMS Collaboration, "Search for Quark Compositeness with the Dijet Centrality Ratio in *pp* Collisions at $\sqrt{s}$ = 7 TeV", *Physical Review Letters*, Vol. 105, No. 26, pp. 262001, 2010.

6. The CMS Collaboration, "Measurement of Dijet Angular Distributions and Search for Quark Compositeness in *pp* Collisions at $\sqrt{s}$ = 7 TeV", *Physical Review Letters*, Vol. 106, No. 201804, pp. 201804, 2011.

7. The CMS Collaboration, "Measurement of the differential dijet production cross section in proton-proton collisions at $\sqrt{s}$= 7 TeV", *Physics Letters B*, Vol. 700, No.3-4, pp. 187-206, 2011.

8. Işıldak, B., "Measurement of the inclusive dijet production rate, as a function of the dijet invariant mass, with the CMS detector in proton-proton collisions at $\sqrt{s}$= 7 TeV", *LHC students poster session*, 23 March 2011, CERN Geneva, 2011.

9. Işıldak, B., "Hard QCD results from CMS", *3rd International Conference on Hadron Physics*, Çanakkale, 2011.

10. Dissertori, G., I., Knowles and M., Schmelling, *Quantum Chromodynamics: High Energy Experiments and Theory*, Oxford University Press, New York, 2009.

11. Sjostrand, T., S., Mrenna and P., Skands, "PYTHIA 6.4 physics and manual", *Journal of High Energy Phyiscs*, Vol.206, No. 05, pp. 026, 2007.

12. Bahr et al., "Herwig++ Physics and Manual", *Eurpean Physics Journal C*, Vol. 58, No. 4, pp. 639-707, 2008.

13. The CMS Collaboration, "The CMS experiment at the CERN LHC", *Journal of Instrumentation*, Vol. 3, No. 08, pp. S08004, 2008.

14. Brning, O., P., Collier, P., Lebrun, S., Myers, R., Ostojic, J., Poole and P., Proudlock, *LHC Design report*, Vol. 1, CERN Libraries, 2004.

15. The CMS Collaboration, "CMS Physics: Technical Design Report Vol. 1 Detector Performance and Software", 2006.

16. The CMS Collaboration, "The CMS experiment at the CERN LHC", *Journal of Instrumentation*, Vol. 3, No. 08, pp. S08004, 2008.

17. S. P. Martin, *A supersymmetry primer*, 1997, http://arxiv.org/abs/hep-ph/9709356, May 2011.

18. Ellis, K., R., J., Stirling and B., R., Webber QCD and Collider Physics, vol. 8, Cambridge University Press, Cambridge, 1996.

19. Feynman, R., P., R., D., Field and G., C., Fox "Quantum-chromodynamic approach for the large-transverse-momentum production of particles and jets". *Physical Review D*, Vol. 18, No. 9, pp. 3320-3343, 1978.

20. Andersson, B., G., Gustafson, G., Ingelman and T., Sjostrand, "Parton fragmentation and string dynamics", *Physics Reports*, Vol. 97, No. 2-3, pp. 31-145, 1983.

21. The CMS Collaboration, "Measurement of the underlying event activity at the LHC with $\sqrt{s} = 7$ TeV and comparison with $\sqrt{s} = 0.9$ TeV", *Journal of High Energy Physics*, Vol.2011, No. 9, pp. 1-31, 2011.

22. Field, R., *Early LHC Underlying Event Data - Findings and Surprises*,2010, http://arxiv.org/abs/1010.3558, May 2010.

23. Marchesini et al. "HERWIG: A Monte Carlo event generator for simulating hadron emission reactions with interfering gluons. Version 5.1", *Computer Physics Communications*, Vol. 67, No. 3, pp. 465-508, 1992.

24. Corcella et al. "HERWIG 6.5: an event generator for Hadron Emission Reactions With Interfering Gluons (including supersymmetric processes)", *Journal of High Energy Phyiscs*, Vol. 0101, pp. 010, 2001.

25. Amati, D., and Veneziano, G., "Preconfinement as a property of perturbative QCD", *Physics Letters B*, Vol. 83, No. 1, pp. 87-92, 1979.

26. Agostinelli et al. G4-a simulation toolkit. *Nuclear Instruments and Methods in Physics Research Section A: Accelerators, Spectrometers, Detectors and Associated Equipment*, Vol. 506, No. 3, pp. 250-303, 2003.

27. G. P. Salam, *Towards Jetography*, 2010, http://arxiv.org/abs/arXiv:0906.1833, May 2010.

28. Ellis., S., D. and Soper, E., D., "Successive combination jet algorithm for hadron collisions", *Physical Review D*, Vol. 48, No.7, pp. 3160-3166, 1993.

29. Cacciari, M., Salam, G., P. and Soyez, G., "The anti-kt jet clustering algorithm", *Journal of High Energy Physics*, Vol. 2008, No. 04, pp. 063, 2008.

30. Dokshitzer, Y., L., Leder, G., Moretti, S. and Webber, B., R., "Better jet clustering algorithms", *Journal of High Energy Physics*, Vol. 1997, No. 08, pp. 001, 1997.

31. Nagy, Z., "Three-jet cross sections in hadron hadron collisions at next-to-leading order", *Physical Review Letters*, Vol. 88, No. 12, pp. 122003, 2002.

32. Catani, S. and Seymour, M., H., "A general algorithm for calculating jet cross sections in NLO QCD", *Nuclear Physics B*, Vol. 485, No. 1-2, pp. 291-419, 1997.

33. Kluge, T., K., Rabbertz and M., Wobisch, *Fast pQCD calculations for PDF fits*, 2006, http://arxiv.org/abs/hepph/0609285, April 2010.

34. Niki Saoulidou, "Particle Flow Jet Identification Criteria", CMS AN-2010/003, 2010.

35. The CMS Collaboration, "Jet Energy Corrections determination at 7 TeV", CMS-PAS-372-JME-10-010, 2010.

36. The CMS Collaboration, "Plans for Jet Energy Corrections at CMS", CMS-PAS-JME-07-002, 2007.

37. The CMS Collaboration, "Jet Performance in pp Collisions at 7 TeV", CMS-PAS-JME-10-003, 2010.

38. Thr UA2 Collaboration, "Measurement of Production and Properties of Jets at the CERN anti-p p Collider", *Zeitschrift für Physik C*,Vol. 20, No. CERN-EP-83-94, pp. 117-134, 1983.

39. The DØ Collaboration, "Determination of the absolute jet energy scale in the DØ calorimeters", *Nuclear Instruments and Methods A*, Vol. 424, No. 2-3, pp. 352-394, 1998

40. The CDF Collaboration, "Determination of the jet energy scale at the Collider Detector at Fermilab", *Nuclear Instruments and Methods A*, Vol. 566, No.2, pp. 375-412, 2006.

41. The CMS Collaboration, "Determination of the Relative Jet Energy Scale at CMS from Dijet Balance", CMS-PAS-JME-08-003, 2008.

42. The CMS Collaboration,"Absolute luminosity normalization", *CERN Detector Performance Studies*, CMS-DP-2011-002, 2011.

43. The CMS Collaboration, "Jet Resolution Determination at sqrt(s)=7 TeV", CMS-PAS-JME-10-014, 2011.

44. Alekhin et al., *The PDF4LHC working group interim report*, 2011, http://arxiv.org/abs/1101.0536, March 2011.

45. Lafferty, G., D. and Wyatt, T., R., "Where to stick your data points: The treatment of measurements within wide bins", *Nuclear Instruments and Methods A*, Vol. 355, No. 2-3, pp. 541-547, 1995.